AD-A167 102 COMPILATION OF REPRINTS NUMBER 63(U) OREGON STATE UNIV 1/3
CORVALLIS COLL OF OCEANOGRAPHY MAR 86 REF-83-12
N00014-76-C-0067 86 PAT-APPL-825 107
UNCLASSIFIED F/G 8/10 NL

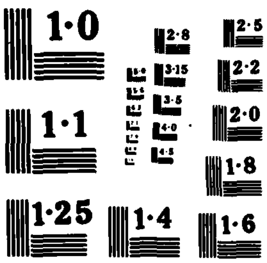
1·0
2·8
2·5
3·15
2·2
3·5
2·0
1·1
4·0
4·5
1·8
1·25
1·4
1·6

CONTENTS

PERSPECTIVE: PERSONAL OBSERVATIONS ON THE STATUS OF MARINE SCIENCES IN THE PEOPLE'S REPUBLIC OF CHINA

Chen-Tung A. Chen

LABORATORY TEST OF APPARENT ATTENUATION FORMULAS

William Menke, Dean Witte, and Rolin Chen

DISCRIMINATING INTRINSIC AND APPARENT ATTENTUATION IN LAYERED ROCK

William Menke and Bruce Dubendorff

WIND-DRIVEN MID-OCEAN BAROCLINIC GYRES OVER TOPOGRAPHY: A CIRCULATION EQUATION EXTENDING THE SVERDRUP RELATION

Roland A. de Szoeke

SECURITY CLASSIFICATION OF THIS PAGE *(When Data Entered)*

REPORT DOCUMENTATION PAGE

READ INSTRUCTIONS
BEFORE COMPLETING FORM

1. REPORT NUMBER 83-12	2. GOVT ACCESSION NO.	3. RECIPIENT'S CATALOG NUMBER
4. TITLE *(and Subtitle)* INTERNAL WAVES IN THE OCEAN: A REVIEW		5. TYPE OF REPORT & PERIOD COVERED Reprint 6. PERFORMING ORG. REPORT NUMBER
7. AUTHOR(s) MURRAY D. LEVINE		8. CONTRACT OR GRANT NUMBER(s) N00014-79-C-0004
9. PERFORMING ORGANIZATION NAME AND ADDRESS School of Oceanography Oregon State University Corvallis, OR 97331		10. PROGRAM ELEMENT, PROJECT, TASK AREA & WORK UNIT NUMBERS NR 083-102
11. CONTROLLING OFFICE NAME AND ADDRESS Office of Naval Research Ocean Science & Technology Division Arlington, VA 22217		12. REPORT DATE 1983 13. NUMBER OF PAGES [redacted] 11
14. MONITORING AGENCY NAME & ADDRESS *(if different from Controlling Office)*		15. SECURITY CLASS. *(of this report)* 15a. DECLASSIFICATION/DOWNGRADING SCHEDULE

16. DISTRIBUTION STATEMENT *(of this Report)*

17. DISTRIBUTION STATEMENT *(of the abstract entered in Block 20, if different from Report)*

18. SUPPLEMENTARY NOTES

Reprint from Reviews of Geophysics and Space Physics 21(5): 1206-1216, June 1983.

19. KEY WORDS *(Continue on reverse side if necessary and identify by block number)*

20. ABSTRACT *(Continue on reverse side if necessary and identify by block number)*

No abstract printed

DD FORM 1 JAN 73 1473 EDITION OF 1 NOV 65 IS OBSOLETE
S/N 0102-014-6601

SECURITY CLASSIFICATION OF THIS PAGE *(When Data Entered)*

Unclassified

SECURITY CLASSIFICATION OF THIS PAGE (When Data Entered)

REPORT DOCUMENTATION PAGE		READ INSTRUCTIONS BEFORE COMPLETING FORM
1. REPORT NUMBER 84-10	2. GOVT ACCESSION NO.	3. RECIPIENT'S CATALOG NUMBER
4. TITLE (and Subtitle) MESOPELAGIC FISH FAUNAL REGIONS OF THE NORTHEAST PACIFIC		5. TYPE OF REPORT & PERIOD COVERED Reprint
		6. PERFORMING ORG. REPORT NUMBER
7. AUTHOR(s) J. Marcus Willis		8. CONTRACT OR GRANT NUMBER(s) N00014-79-C-0004
9. PERFORMING ORGANIZATION NAME AND ADDRESS College of Oceanography Oregon State University Corvallis, Oregon 97331		10. PROGRAM ELEMENT, PROJECT, TASK AREA & WORK UNIT NUMBERS Project NR083-102
11. CONTROLLING OFFICE NAME AND ADDRESS Office of Naval Research Ocean Science & Technology Division Arlington, Virginia 22217		12. REPORT DATE 1984
		13. NUMBER OF PAGES 19
14. MONITORING AGENCY NAME & ADDRESS(if different from Controlling Office)		15. SECURITY CLASS. (of this report) Unclassified
		15a. DECLASSIFICATION/DOWNGRADING SCHEDULE

16. DISTRIBUTION STATEMENT (of this Report)

Approved for public release; distribution unlimited

17. DISTRIBUTION STATEMENT (of the abstract entered in Block 20, if different from Report)

18. SUPPLEMENTARY NOTES

Reprint from "Biological Oceanography," Volume 3, Number 2, 1984

19. KEY WORDS (Continue on reverse side if necessary and identify by block number)

20. ABSTRACT (Continue on reverse side if necessary and identify by block number)

Fishes from 57 Isaacs-Kidd midwater trawl collections were identified and analyzed to determine the characteristics and limits of faunal regions in Northeast Pacific Ocean. Cluster analyses of station and species groups showed three faunal regions: (1) Subarctic, the region north of the Subarctic front; (2) Central, the region south of the Subarctic front and north of the north equatorial front; and (3) Southern, the region near the Hawaiian Islands south of the north equatorial front. Temperature-salinity data show that the geographical limits of the fish faunal regions correspond with most physical

DD FORM 1 JAN 73 1473 EDITION OF 1 NOV 65 IS OBSOLETE
S/N 0102-014-6601

Unclassified

SECURITY CLASSIFICATION OF THIS PAGE (When Data Entered)

boundaries. No association was found between the subtropical front and a faunal boundary. A brief review of plankton studies in the Northeast Pacific shows that the subtropical front may be an important boundary for microplankton groups. Gradients of change in fish species composition appeared steeper and concordance in species rank order seemed lower in Central than in Subarctic waters.

Unclassified

SECURITY CLASSIFICATION OF THIS PAGE (*When Data Entered*)

REPORT DOCUMENTATION PAGE

READ INSTRUCTIONS
BEFORE COMPLETING FORM

1. REPORT NUMBER 84-11	2. GOVT ACCESSION NO.	3. RECIPIENT'S CATALOG NUMBER

4. TITLE (*and Subtitle*) THE ENERGETICS OF OVERTURNING STRUCTURES: IMPLICATIONS FOR THE THEORY OF FOSSIL TURBULENCE	5. TYPE OF REPORT & PERIOD COVERED Reprint 6. PERFORMING ORG. REPORT NUMBER
7. AUTHOR(s) DILLON, T.M.	8. CONTRACT OR GRANT NUMBER(s) N00014-79-C-0004
9. PERFORMING ORGANIZATION NAME AND ADDRESS College of Oceanography Oregon State University Corvallis, OR 97331	10. PROGRAM ELEMENT, PROJECT, TASK AREA & WORK UNIT NUMBERS NR 083-102
11. CONTROLLING OFFICE NAME AND ADDRESS Office of Naval Research Ocean Science & Technology Division Arlington, VA22217	12. REPORT DATE Nov. '83 13. NUMBER OF PAGES 9
14. MONITORING AGENCY NAME & ADDRESS(*if different from Controlling Office*)	15. SECURITY CLASS. (*of this report*) Unclassified 15a. DECLASSIFICATION/DOWNGRADING SCHEDULE

16. DISTRIBUTION STATEMENT (*of this Report*)

Approved for public release; distribution unlimited

17. DISTRIBUTION STATEMENT (*of the abstract entered in Block 20, if different from Report*)

18. SUPPLEMENTARY NOTES

Reprint from Journal of Physical Oceanography, Vol. 14, No. 3, March 1984, American Meteorological Society

19. KEY WORDS (*Continue on reverse side if necessary and identify by block number*)

20. ABSTRACT (*Continue on reverse side if necessary and identify by block number*)

A large number of oceanic and freshwater microstructure observations are analyzed to determine the energetic state of the turbulence. The total available energy and a time scale for dissipating the total energy are estimated. It is found that the time scale for dissipating the total energy in overturns is usually much shorter than the time scale for gravitational collapse found in laboratory studies. This implies that the energy being dissipated in an overturn could not be supplied fast enough to support the dissipation if gravitational collaps were the only source supplying the energy. Two criteria

DD FORM 1 JAN 73 1473 EDITION OF 1 NOV 65 IS OBSOLETE
S/N 0102-014-6601

SECURITY CLASSIFICATION OF THIS PAGE (*When Data Entered*) used in Gibson's theory of fossil turbulence for establishing the state of overturns are compared: a length scale (or available potential energy) criterion suggested by Gibson and tested in the laboratory by Stillinger and Gibson's "activity parameter" criterion. It is found that most overturns are "active" according to the available potential-energy criterion, but "fossil" according to the activity parameter criterion. A modification of the activity parameter is suggested to achieve agreement.

Unclassified
SECURITY CLASSIFICATION OF THIS PAGE (When Data Entered)

REPORT DOCUMENTATION PAGE	READ INSTRUCTIONS BEFORE COMPLETING FORM
1. REPORT NUMBER 84-15 — 2. GOVT ACCESSION NO.	3. RECIPIENT'S CATALOG NUMBER
4. TITLE (and Subtitle) MARINE SEISMIC REFRACTION STUDY BETWEEN CAPE SIMPSON AND PRUDHOE BAY, ALASKA	5. TYPE OF REPORT & PERIOD COVERED Reprint 6. PERFORMING ORG. REPORT NUMBER
7. AUTHOR(s) Beé, Michel; Johnson, Stephen H; and Chiburis, E. Chiburis, E.F.	8. CONTRACT OR GRANT NUMBER(s) N00014-76-C-0067
9. PERFORMING ORGANIZATION NAME AND ADDRESS College of Oceanography Oregon State University Corvallis, Oregon 97331	10. PROGRAM ELEMENT, PROJECT, TASK AREA & WORK UNIT NUMBERS NR083-102
11. CONTROLLING OFFICE NAME AND ADDRESS Office of Naval Research Ocean Science & Technology Division Arlington, Virginia 22217	12. REPORT DATE 10 Aug. 1984 13. NUMBER OF PAGES 20
14. MONITORING AGENCY NAME & ADDRESS(if different from Controlling Office)	15. SECURITY CLASS. (of this report) Unclassified 15a. DECLASSIFICATION/DOWNGRADING SCHEDULE

16. DISTRIBUTION STATEMENT (of this Report)

Approved for public release; distribution unlimited

17. DISTRIBUTION STATEMENT (of the abstract entered in Block 20, if different from Report)

18. SUPPLEMENTARY NOTES

Reprint from Journal of Geophysical Research, Vol. 89, No. B8, pages 6941-6960, August 10, 1984

19. KEY WORDS (Continue on reverse side if necessary and identify by block number)

20. ABSTRACT (Continue on reverse side if necessary and identify by block number)

A marine seismic refraction study conducted between Cape Simpson and Prudhoe Bay, Alaska, provides data for subsurface structural and geological cross sections of the western Beaufort Shelf. The results suggest that the western Beaufort Shelf is underlain by a sedimentary prism with beds dipping and prograding to the northeast. Correlation of the refraction data with wells drilled on land and offshore reflection profiles permits tentative identification of geologic sequences on the basis of their seismic velocity. This study

DD FORM 1 JAN 73 1473 EDITION OF 1 NOV 65 IS OBSOLETE
S/N 0102-014-6601 | Unclassified
SECURITY CLASSIFICATION OF THIS PAGE (When Data Entered)

associates near-surface velocities of 1.60-1.65 km/s with Quaternary sediments and 1.82-2.35 km/s velocities with Tertiary strata. Velocities of 1.60-3.40 km/s are correlated to Upper Cretaceous rocks, 2.10-4.14 km/s to Lower Cretaceous beds, 5.66-5.68 km/s to Mississippian-Pennsylvanian carbonates, and 4.24-6.08 km/s to the Franklinian basement composed of argillites and phyllites. West of Cape Halkett, the sedimentary section is mainly Lower Cretaceous, whereas east of Cape Halkett, Upper Cretaceous and Tertiary strata dominate. Higher velocities (6.40-7.07 km/s) are thought to represent the crystalline basement, probably silicic in composition. Although no seismic velocities typical of the upper mantle are present on the record sections, a minimum depth calculation places the Mohorovicic discontinuity no shallower than 20 km. The interpretation indicates that the stratigraphic sequence present onshore at Prudhoe continues to the offshore and implies that the western Beaufort Shelf may be a good prospect for oil. The structures derived from seismic data indicate that the Beaufort continental margin is not different from Atlantic-type margins and add further evidence to the concept of a rifted and rotated Beaufort continental margin.

Unclassified

SECURITY CLASSIFICATION OF THIS PAGE (When Data Entered)

REPORT DOCUMENTATION PAGE		READ INSTRUCTIONS BEFORE COMPLETING FORM
1. REPORT NUMBER 84-16	2. GOVT ACCESSION NO.	3. RECIPIENT'S CATALOG NUMBER
4. TITLE (and Subtitle) PRELIMINARY SEISMIC REFRACTION RESULTS USING A BOREHOLE SEISMOMETER IN DEEP SEA DRILLING PROJECT HOLE 395A		5. TYPE OF REPORT & PERIOD COVERED Reprint 6. PERFORMING ORG. REPORT NUMBER
7. AUTHOR(s) Jacobson, R.S., Adair, R. and Orcutt, J.		8. CONTRACT OR GRANT NUMBER(s) N00014-79-C-0004
9. PERFORMING ORGANIZATION NAME AND ADDRESS College of Oceanography Oregon State University Corvallis, Oregon 97331		10. PROGRAM ELEMENT, PROJECT, TASK AREA & WORK UNIT NUMBERS Project NR083-102
11. CONTROLLING OFFICE NAME AND ADDRESS Office of Naval Research Ocean Science & Technology Division Arlington, Virginia 22217		12. REPORT DATE 1983 13. NUMBER OF PAGES 10
14. MONITORING AGENCY NAME & ADDRESS(if different from Controlling Office)		15. SECURITY CLASS. (of this report) Unclassified 15a. DECLASSIFICATION/DOWNGRADING SCHEDULE

16. DISTRIBUTION STATEMENT (of this Report)

Approved for public release; distribution unlimited

17. DISTRIBUTION STATEMENT (of the abstract entered in Block 20, if different from Report)

18. SUPPLEMENTARY NOTES

Reprint from Biju-Duval, B. Moore, J.C., et al, 1984.
Initial Reports of the Deep Sea Drilling Project, Volume LXXV111,
Washington (U.S. Government Printing Office)

19. KEY WORDS (Continue on reverse side if necessary and identify by block number)

20. ABSTRACT (Continue on reverse side if necessary and identify by block number)

Three seismic refraction lines shot to the Marine Seismic System, a vertical-component borehole seismometer in DSDP Hole 395A at 609m sub-bottom depth, have been analyzed. Despite inconsistencies between various velocity determinations in the upper crust, the velocity of the uppermost 600m appears to be high, about 4.5 km/s. Between 600m and 1.8 km sub-bottom, the crust yields an apparent velocity of 4.6 km/s. This value is somewhat lower than that determined near the base of the hole using acoustic logging tools (5.0-5.5 km/s), and is also lower than the average velocity of core samples from the same depth (5.7 km/s).

DD FORM 1 JAN 73 1473 EDITION OF 1 NOV 65 IS OBSOLETE
S/N 0102-014-6601

Unclassified

SECURITY CLASSIFICATION OF THIS PAGE (When Data Entered)

The lower crust is unusually thin, only 1.8 to 2.4 km thick, and has compressional-wave velocities of 6.8 to 7.3 km/s. Mantle velocities range from 7.8 to 8.2 km/s. There is little or no velocity gradient in the uppermost kilometers of the crust, but our results indicate widespread lateral inhomogeneities, supporting the observations based on refraction profiles shot for the original site survey.

Unclassified
SECURITY CLASSIFICATION OF THIS PAGE (When Data Entered)

REPORT DOCUMENTATION PAGE		READ INSTRUCTIONS BEFORE COMPLETING FORM
1. REPORT NUMBER 84-17	2. GOVT ACCESSION NO.	3. RECIPIENT'S CATALOG NUMBER
4. TITLE (and Subtitle) LINEAR INVERSION OF BODY-WAVE DATA PART III: MODEL PARAMETERIZATION		5. TYPE OF REPORT & PERIOD COVERED Reprint
		6. PERFORMING ORG. REPORT NUMBER
7. AUTHOR(s) Beé, Michel, and Jacobson, Randal S.		8. CONTRACT OR GRANT NUMBER(s) N00014-79-C-0004
9. PERFORMING ORGANIZATION NAME AND ADDRESS College of Oceanography Oregon State University Corvallis, Oregon 97331		10. PROGRAM ELEMENT, PROJECT, TASK AREA & WORK UNIT NUMBERS NR083-102
11. CONTROLLING OFFICE NAME AND ADDRESS Office of Naval Research Ocean Science & Technology Division Arlington, Virginia 22217		12. REPORT DATE 1984
		13. NUMBER OF PAGES 6
14. MONITORING AGENCY NAME & ADDRESS(if different from Controlling Office)		15. SECURITY CLASS. (of this report) Unclassified
		15a. DECLASSIFICATION/DOWNGRADING SCHEDULE

16. DISTRIBUTION STATEMENT (of this Report)

Approved for public release; distribution unlimited

17. DISTRIBUTION STATEMENT (of the abstract entered in Block 20, if different from Report)

18. SUPPLEMENTARY NOTES

Reprint from Geophysics, Vol. 49, No. 12 (December 1984): pps. 2088-2093, 6 Figs.

19. KEY WORDS (Continue on reverse side if necessary and identify by block number)

20. ABSTRACT (Continue on reverse side if necessary and identify by block number)

A velocity gradient model parameterized with the tau-zeta inversion for seismic refraction data is examined with respect to a synthetic traveltime data set. The velocity-depth model consists of a stack of laterally homogeneous layers, each with a constant velocity gradient. The free model parameters are the velocities of the layer bounds and the number of layers.

The best velocity gradient solutions, i.e., with the least deviation from the true model, were obtained fron "constrained" models in which the velocities

DD FORM 1 JAN 73 1473 EDITION OF 1 NOV 65 IS OBSOLETE
S/N 0102-014-6601

Unclassified
SECURITY CLASSIFICATION OF THIS PAGE (When Data Entered)

of the layer bounds are the velocities of the observed refracted waves. An arbitrary selection of layer bound velocities was found to be a suboptimal choice of model parameterization for the tau-zeta inversion.

A trade-off curve between model resolution and solution variance was constructed with the constrained model parameterization from examination of numerous solutions with a diverse number of layers. A constrained model with as many layers as observed data points represents a satisfactory compromise between model resolution and solution variance. Constrained models with more layers than observed data points, however, can increase the resulution of the velocity gradient model. If model resolution is favored over solution variance, a constrained model with many more layers than observed data points is therefor the best model parameterization with the tau-zeta inversion technique.

Unclassified
SECURITY CLASSIFICATION OF THIS PAGE (When Data Entered)

REPORT DOCUMENTATION PAGE

READ INSTRUCTIONS BEFORE COMPLETING FORM

1. REPORT NUMBER
85-15

2. GOVT ACCESSION NO.

3. RECIPIENT'S CATALOG NUMBER

4. TITLE (and Subtitle)
OPTICAL ANALYSIS OF A SIMULATED IMAGE OF THE SEA SURFACE

5. TYPE OF REPORT & PERIOD COVERED
Reprint

6. PERFORMING ORG. REPORT NUMBER

7. AUTHOR(s)
Borrego, Josué Alvarez; and Machado, Marco A.

8. CONTRACT OR GRANT NUMBER(s)
N00014-84-C-0218

9. PERFORMING ORGANIZATION NAME AND ADDRESS
College of Oceanography
Oregon State University
Corvallis, Oregon 97331

10. PROGRAM ELEMENT, PROJECT, TASK AREA & WORK UNIT NUMBERS
NR083-102

11. CONTROLLING OFFICE NAME AND ADDRESS
Office of Naval Research
Ocean Science & Technology Division
Arlington, Virginia 22217

12. REPORT DATE
1984

13. NUMBER OF PAGES
9

14. MONITORING AGENCY NAME & ADDRESS(if different from Controlling Office)

15. SECURITY CLASS. (of this report)
Unclassified

15a. DECLASSIFICATION/DOWNGRADING SCHEDULE

16. DISTRIBUTION STATEMENT (of this Report)

Approved for public release; distribution unlimited

17. DISTRIBUTION STATEMENT (of the abstract entered in Block 20, if different from Report)

18. SUPPLEMENTARY NOTES
Reprint from Applied Optics, Vol. 24, page 1064-1072, April 1, 1965

19. KEY WORDS (Continue on reverse side if necessary and identify by block number)

20. ABSTRACT (Continue on reverse side if necessary and identify by block number)

A simulated sea surface with a Pierson-Neumann power specturm was generated by a numerical model. The image was recorded on photographic film by means of a microdensitometer with a writing mode. To obtain the bidimensional power spectrum of this simulated image of the sea surface, a coherent optical system was used. This power spectrum has information about frequencies in the highest energy peak and the direction that the waves have at a specific time. The Pierson-Neumann power spectrum used to generate the simulated sea surface was

Unclassified
SECURITY CLASSIFICATION OF THIS PAGE (When Data Entered)

compared with the bidimensional power spectrum obtained with the coherent optical system. Attenuation of the high frequencies in the measured spectrum was observed. This attenuation was probably caused by distribution of density values in the film or by the aperture of the detector used in the coherent optical system. Optical autocorrelations of the simulated sea surface were obtained and a high degree of correlation in the direction perpendicular to the wind was found.

Unclassified

SECURITY CLASSIFICATION OF THIS PAGE (When Data Entered)

REPORT DOCUMENTATION PAGE	READ INSTRUCTIONS BEFORE COMPLETING FORM
1. REPORT NUMBER 85-16	2. GOVT ACCESSION NO.
	3. RECIPIENT'S CATALOG NUMBER
4. TITLE (and Subtitle) INTERNAL WAVES IN THE ARCTIC OCEAN: COMPARISON WITH LOWER-LATITUDE OBSERVATIONS	5. TYPE OF REPORT & PERIOD COVERED Reprint 6. PERFORMING ORG. REPORT NUMBER
7. AUTHOR(s) Murray D. Levine and Clayton A. Paulson, and James H. Morison	8. CONTRACT OR GRANT NUMBER(s) N00014-79-C-0004
9. PERFORMING ORGANIZATION NAME AND ADDRESS College of Oceanography Oregon State University Corvallis, OR 97331	10. PROGRAM ELEMENT, PROJECT, TASK AREA & WORK UNIT NUMBERS NR083-102
11. CONTROLLING OFFICE NAME AND ADDRESS Office of Naval Research Ocean Science & Technology Division Arlington, VA 22217	12. REPORT DATE 1981 13. NUMBER OF PAGES 10
14. MONITORING AGENCY NAME & ADDRESS(if different from Controlling Office) Office of Naval Research Ocean Science & Technology Division Arlington, VA 22217	15. SECURITY CLASS. (of this report) Unclassified 15a. DECLASSIFICATION/DOWNGRADING SCHEDULE

16. DISTRIBUTION STATEMENT (of this Report)

Approved for public release;
Distribution unlimited

17. DISTRIBUTION STATEMENT (of the abstract entered in Block 20, if different from Report)

18. SUPPLEMENTARY NOTES

Reprint from Journal of Physical Oceanography, Vol. 15, No. 6
June 1985

19. KEY WORDS (Continue on reverse side if necessary and identify by block number)

20. ABSTRACT (Continue on reverse side if necessary and identify by block number)

A thermistor chain was moored below the pack ice from 50-150 m in the Arctic Ocean for five days in 1981. Oscillations in temperature are attributed to the vertical displacement of internal waves. The spectral shape of isotherm displacement is consistent with the Garrett-Munk model and other internal wave observations, but the spectral level is significantly lower. Other observations
but the spectral level is significantly lower. Other observations from the Arctic Ocean also exhibit lower internal-wave energy when compared with

DD FORM 1 JAN 73 1473 EDITION OF 1 NOV 65 IS OBSOLETE
S/N 0102-014-6601

Unclassified

SECURITY CLASSIFICATION OF THIS PAGE (When Data Entered)

historical data from lower latitudes. The lower energy may be related to the unique generation and dissipation mechanisms present in the ice-covered Arctic Ocean. Significant peaks in vertical coherence occur at 0.81 and 2.6 cph. The peak at 2.6 cph coincides approximately with the high-frequency spectral cutoff near the local buoyancy frequency; this feature has been observed in many other internal wave experiments. The coherent oscillations at 0.81 cpy exhibit a node in vertical displacement at 75-100 m. This is consistent with either the second, third or fourth vertical mode calculated from the mean buoyancy frequency profile. Evidence is presented which suggests that, contrary to the Garrett-Munk model, the frequency spectrum does not scale with the Coriolis parameter.

Unclassified

SECURITY CLASSIFICATION OF THIS PAGE (When Data Entered)

REPORT DOCUMENTATION PAGE

READ INSTRUCTIONS BEFORE COMPLETING FORM

1. REPORT NUMBER 85-17

2. GOVT ACCESSION NO.

3. RECIPIENT'S CATALOG NUMBER

4. TITLE (and Subtitle)
CALIBRATION AND COMPARISON OF THE LDGC
NEPHELOMETER AND THE OSU TRANSMISSOMETER
ON THE NOVA SCOTIAN RISE

5. TYPE OF REPORT & PERIOD COVERED Reprint

6. PERFORMING ORG. REPORT NUMBER N00014-79-C-0004

7. AUTHOR(s)
Gardner, W.D., Biscaye, P.E., Zaneveld, J.R.V. and
Richardson, M.J.

8. CONTRACT OR GRANT NUMBER(s) NR083-102

9. PERFORMING ORGANIZATION NAME AND ADDRESS
College of Oceanography
Oregon State University
Corvallis, OR 97331

10. PROGRAM ELEMENT, PROJECT, TASK AREA & WORK UNIT NUMBERS

11. CONTROLLING OFFICE NAME AND ADDRESS
Office of Naval Research
Ocean Science & Technology Division
Arlington, VA 22217

12. REPORT DATE 1979

13. NUMBER OF PAGES 22

14. MONITORING AGENCY NAME & ADDRESS(if different from Controlling Office)

15. SECURITY CLASS. (of this report) Unclassified

15a. DECLASSIFICATION/DOWNGRADING SCHEDULE

16. DISTRIBUTION STATEMENT (of this Report)
Approved for public release;
Distribution unlimited

17. DISTRIBUTION STATEMENT (of the abstract entered in Block 20, if different from Report)

18. SUPPLEMENTARY NOTES
Reprint from Marine Geology, 66 (1985) 323-344
Elsevier Science Publishers B.V., Amsterdam-Printed in The Netherlands

19. KEY WORDS (Continue on reverse side if necessary and identify by block number)

19. KEY WORDS (Continue on reverse side if necessary and identify by block number)

During the survey of the HEBBLE (High Energy Benthic Boundary Layer Experiments) area, two optical instruments were used to determine the spatial and temporal structure of the benthic nepheloid layer. Both instruments showed a linear response to suspended particle mass and volume over the typical range of concentrations found in the ocean (10-250 μg l^{-1}). At higher concentrations the transmissometer response remains linear, but, as previously noted and as shown here by theory, the nephelometer has a predictable second-order response due to multiply scattered light. At the low concentrations found in mid-water both instruments seem near their limit of sensitivity. Small

DD FORM 1 JAN 73 1473 EDITION OF 1 NOV 65 IS OBSOLETE
S/N 0102-014-6601

Unclassified

SECURITY CLASSIFICATION OF THIS PAGE (When Data Entered)

differences between instruments at low concentrations may result from variations in response to particle types found in mid-water or may be minor second-order effects of temperature or pressure on the instruments. The comparison made here shows that either instrument can be effectively used to study the nepheloid layer, and that data from different study areas using these instruments can consistently be compared. The HEBBLE region was ideal for testing the range of these instruments because it yielded the highest concentrations of particles ever recorded in the deep sea.

Unclassified

SECURITY CLASSIFICATION OF THIS PAGE (When Data Entered)

REPORT DOCUMENTATION PAGE

READ INSTRUCTIONS BEFORE COMPLETING FORM

1. REPORT NUMBER
85-18

2. GOVT ACCESSION NO.

3. RECIPIENT'S CATALOG NUMBER

4. TITLE (and Subtitle)
GEOTECHNICAL PROPERTIES OF SURFACE AND NEAR-SURFACE DEPOSITS IN THE EAST CHINA SEA

5. TYPE OF REPORT & PERIOD COVERED
reprint, 1980-82

6. PERFORMING ORG. REPORT NUMBER

7. AUTHOR(s)
Keller, George H., and Yincan , Ye

8. CONTRACT OR GRANT NUMBER(s)
N00014-79-C-0004

9. PERFORMING ORGANIZATION NAME AND ADDRESS
College of Oceanography
Oregon State Univesity
Corvallis, OR 97331

10. PROGRAM ELEMENT, PROJECT, TASK AREA & WORK UNIT NUMBERS
NR083-102

11. CONTROLLING OFFICE NAME AND ADDRESS
Office of Naval Research
Ocean Science & Technology Div.
Arlington, VA 22217

12. REPORT DATE
1980-82

13. NUMBER OF PAGES
16

14. MONITORING AGENCY NAME & ADDRESS(if different from Controlling Office)

15. SECURITY CLASS. (of this report)
unclassified

15a. DECLASSIFICATION/DOWNGRADING SCHEDULE

16. DISTRIBUTION STATEMENT (of this Report)
Distribution unlimited; approved for public release

17. DISTRIBUTION STATEMENT (of the abstract entered in Block 20, if different from Report)
Approved for public release; distribution unlimited

18. SUPPLEMENTARY NOTES
Reprint from Continental Shelf Research, Vol. 4, Nos 1/2, pp. 159-174, 1985

19. KEY WORDS (Continue on reverse side if necessary and identify by block number)

20. ABSTRACT (Continue on reverse side if necessary and identify by block number)
Shelf deposits in the East China Sea are primarily relict sands with overlying fine-grained cohesive deposits, occurring along the innermost shelf and as a more or less isolated deposit on the midshelf. Considering these surface and near-surface (0-1.5m) cohesive deposits as a unit, the innermost shelf sediments are slightly coarser (more silt) than those of the midshelf which commonly contain more clay-size material. The inner shelf sediments also display higher mean wet bulk densities (1.48 to 1.88mg m^{-3}) and shear strengths (4.0 to 9.8 kPa), but lower water contents (64 to 81%) and porosities

DD FORM 1 JAN 73 1473 EDITION OF 1 NOV 65 IS OBSOLETE
S/N 0102-014-6601

Unclassified

SECURITY CLASSIFICATION OF THIS PAGE (When Data Entered)

(62 to 66%) than those found associated with the midshelf deposits. Available data indicate that the midshelf mud deposit is primarily derived from the reworking of Huanghe (Yellow River) coastal deposits that were laid down at a time when the river debouched into the Yellow Sea to the north of the Changjiang. Some portion of the midshelf mud may be derived from the Changjiang. These midshelf 'fines' apparently are caught up in a large circulation gyre over the shelf which accounts for their isolated nature. Strong bottom and near-bottom currents, as well as winter storm wave activity, are primary mechanisms resulting in both suspended sediment and bedload transport on the shelf of theEeast China Sea.

unclassified

SECURITY CLASSIFICATION OF THIS PAGE (When Data Entered)

REPORT DOCUMENTATION PAGE		READ INSTRUCTIONS BEFORE COMPLETING FORM
1. REPORT NUMBER 85-19	2. GOVT ACCESSION NO.	3. RECIPIENT'S CATALOG NUMBER
4. TITLE (and Subtitle) SOME PERSONAL OBSERVATIONS ON THE STATUS OF MARINE SCIENCES IN THE PEOPLE'S REPUBLIC OF CHINA		5. TYPE OF REPORT & PERIOD COVERED reprint, April 1983
		6. PERFORMING ORG. REPORT NUMBER
7. AUTHOR(s) Chen-Tung A. Chen		8. CONTRACT OR GRANT NUMBER(s) N00014-79-C-0004
9. PERFORMING ORGANIZATION NAME AND ADDRESS College of Oceanography Oregon State University Corvallis, OR 97331		10. PROGRAM ELEMENT, PROJECT, TASK AREA & WORK UNIT NUMBERS NR 083-102
11. CONTROLLING OFFICE NAME AND ADDRESS		12. REPORT DATE April 1983
		13. NUMBER OF PAGES 2
14. MONITORING AGENCY NAME & ADDRESS(if different from Controlling Office)		15. SECURITY CLASS. (of this report) unclassified
		15a. DECLASSIFICATION/DOWNGRADING SCHEDULE

16. DISTRIBUTION STATEMENT (of this Report)

distribution unlimited - approved for public release

17. DISTRIBUTION STATEMENT (of the abstract entered in Block 20, if different from Report)

18. SUPPLEMENTARY NOTES

Reprint from EOS

19. KEY WORDS (Continue on reverse side if necessary and identify by block number)

20. ABSTRACT (Continue on reverse side if necessary and identify by block number)

Owing to the long hiatus in communication with the People's Republic of China (PRC) during the cultural Revolution and the inability of most westerners to read the original Chinese literature, a great deal of marine science research in PRC is not known to the outside world. I have felt that progress in marine science in general could be accelerated with better awareness of the existence of a large Chinese data base. Also, duplication of efforts caused by lags in communication could be averted if a review of the status of marine science

DD FORM 1 JAN 73 1473 EDITION OF 1 NOV 65 IS OBSOLETE
S/N 0102-014-6601

unclassified

SECURITY CLASSIFICATION OF THIS PAGE (When Data Entered)

research in PRC were available.

At the invitation of Shandong College of Oceanography in April 1983, I visited eight oceanographic institutions in PRC for a month with the primary goal of ensuring a thorough and efficient acquisition of marine chemistry in the "gray literature." A report "Marine Chemistry in the People's Republic of China" with extensive bibliography has been prepared for the Office of Naval Research (ONR) (C.-T. Chen, Marine Chemistry in the People's Republic of China, *Doc. 454 156 19338*, U.S. Government Printing Office, Washington, D.C., 1984), and a limited number of copies are available from the author. In the following report, I give only my impressions of oceanographic research in PRC obtained from my site visit and from my conversations with visiting PRC marine chemists in America. I must point out at once, however, that exceptions to my description, given below, certainly exist.

SECURITY CLASSIFICATION OF THIS PAGE (When Data Entered)

REPORT DOCUMENTATION PAGE	READ INSTRUCTIONS BEFORE COMPLETING FORM
1. REPORT NUMBER 85-20 | 2. GOVT ACCESSION NO.	3. RECIPIENT'S CATALOG NUMBER
4. TITLE (and Subtitle) PERSPECTIVE: PERSONAL OBSERVATIONS ON THE STATUS OF MARINE SCIENCES IN THE PEOPLE'S REPUBLIC OF CHINA	5. TYPE OF REPORT & PERIOD COVERED reprint, 1983 6. PERFORMING ORG. REPORT NUMBER
7. AUTHOR(s) Chen, Chen-Tung A.	8. CONTRACT OR GRANT NUMBER(s) N00014-84-C0218
9. PERFORMING ORGANIZATION NAME AND ADDRESS College of Oceanography Oregon State University Corvallis, OR 97331	10. PROGRAM ELEMENT, PROJECT, TASK AREA & WORK UNIT NUMBERS NR 083-102
11. CONTROLLING OFFICE NAME AND ADDRESS	12. REPORT DATE Winter 1983 13. NUMBER OF PAGES 3
14. MONITORING AGENCY NAME & ADDRESS(if different from Controlling Office)	15. SECURITY CLASS. (of this report) 15a. DECLASSIFICATION/DOWNGRADING SCHEDULE

16. DISTRIBUTION STATEMENT (of this Report)

approved for public release, distribution unlimited

17. DISTRIBUTION STATEMENT (of the abstract entered in Block 20, if different from Report)

18. SUPPLEMENTARY NOTES

19. KEY WORDS (Continue on reverse side if necessary and identify by block number)

20. ABSTRACT (Continue on reverse side if necessary and identify by block number)

Owing to the long hiatus in communication with the People's Republic of China (PRC) during the cultural Revolution and the inability of most westerners to read the original Chinese literature, a great deal of marine science research in PRC is not known to the outside world. I have felt that progress in marine science in general could be accelerated with better awareness of the existence of a large Chinese data base. Also, duplication of efforts caused by lags in communication could be averted if a review of the status of marine science

DD FORM 1 JAN 73 1473 EDITION OF 1 NOV 65 IS OBSOLETE
S/N 0102-014-6601

SECURITY CLASSIFICATION OF THIS PAGE (When Data Entered)

research in PRC were available.

At the invitation of Shandong College of Oceanography in April 1983, I visited eight oceanographic institutions in PRC for a month with the primary goal of ensuring a thorough and efficient acquisition of marine chemistry in the "gray literature." A report "Marine Chemistry in the People's Republic of China" with extensive bibliography has been prepared for the Office of Naval Research (ONR) (C.-T. Chen, Marine Chemistry in the People's Republic of China, *Doc. 454 156 19338*, U.S. Government Printing Office, Washington, D.C., 1984), and a limited number of copies are available from the author. In the following report, I give only my impressions of oceanographic research in PRC obtained from my site visit and from my conversations with visiting PRC marine chemists in America. I must point out at once, however, that exceptions to my description, given below, certainly exist.

Unclassified

SECURITY CLASSIFICATION OF THIS PAGE (When Data Entered)

REPORT DOCUMENTATION PAGE		READ INSTRUCTIONS BEFORE COMPLETING FORM
1. REPORT NUMBER 85-24	2. GOVT ACCESSION NO.	3. RECIPIENT'S CATALOG NUMBER
4. TITLE (and Subtitle) LABORATORY TEST OF APPARENT ATTENUATION FORMULAS		5. TYPE OF REPORT & PERIOD COVERED reprint, 1985
		6. PERFORMING ORG. REPORT NUMBER
7. AUTHOR(s) Menke, William, Witte, Dean, and Chen, Rolin		8. CONTRACT OR GRANT NUMBER(s) N00014-84C-0218
9. PERFORMING ORGANIZATION NAME AND ADDRESS College of Oceanography Oregon State Univesity Corvallis, OR 97331		10. PROGRAM ELEMENT, PROJECT, TASK AREA & WORK UNIT NUMBERS NR083-102
11. CONTROLLING OFFICE NAME AND ADDRESS Office of Naval Research Ocean Science & Technology Division Arlington, VA 22217		12. REPORT DATE 1985
		13. NUMBER OF PAGES 11
14. MONITORING AGENCY NAME & ADDRESS (if different from Controlling Office)		15. SECURITY CLASS. (of this report) unclassified
		15a. DECLASSIFICATION/DOWNGRADING SCHEDULE

16. DISTRIBUTION STATEMENT (of this Report)

Distribution unlimited; approved for public release

17. DISTRIBUTION STATEMENT (of the abstract entered in Block 20, if different from Report)

Approved for public release; distribution unlimited

18. SUPPLEMENTARY NOTES

reprint from Bulletin of the Seismological Society of America, Vol. 75, No. 5, pp. 1383-1393, October 1985

19. KEY WORDS (Continue on reverse side if necessary and identify by block number)

20. ABSTRACT (Continue on reverse side if necessary and identify by block number)

We measure the apparent attentuation of P waves propagating through a three-dimensional scattering medium (a three-dimensional aluminum block containing a random assemblage of cylindrical voids). The observed apparent attenuation is compared to that predicted by a single scattering approximation. At low frequencies, both the amount of attenuation and its variation with frequency are well predicted. At intermediate and high frequencies, the agreement is poorer. Observed phase shifts are very different from those predicted by the Kramers-Krönig relations.

DD FORM 1 JAN 73 1473 EDITION OF 1 NOV 65 IS OBSOLETE
S/N 0102-014-6601

Unclassified

SECURITY CLASSIFICATION OF THIS PAGE (When Data Entere

Unclassified

SECURITY CLASSIFICATION OF THIS PAGE (When Data Entered)

REPORT DOCUMENTATION PAGE

READ INSTRUCTIONS BEFORE COMPLETING FORM

1. REPORT NUMBER
85-25

2. GOVT ACCESSION NO.

3. RECIPIENT'S CATALOG NUMBER

4. TITLE (and Subtitle)
DISCRIMINATING INTRINSIC AND APPARENT ATTENUATION IN LAYERED ROCK

5. TYPE OF REPORT & PERIOD COVERED
reprint, 1985

6. PERFORMING ORG. REPORT NUMBER

7. AUTHOR(s)
Menke, William and Dubendorff, Bruce

8. CONTRACT OR GRANT NUMBER(s)
N00014-84C-0218

9. PERFORMING ORGANIZATION NAME AND ADDRESS
College of Oceanography
Oregon State Univesity
Corvallis, OR 97331

10. PROGRAM ELEMENT, PROJECT, TASK AREA & WORK UNIT NUMBERS
NR083-102

11. CONTROLLING OFFICE NAME AND ADDRESS
Office of Naval Research
Ocean Science & Technology Division
Arlington, VA 22217

12. REPORT DATE
1985

13. NUMBER OF PAGES
4

14. MONITORING AGENCY NAME & ADDRESS(if different from Controlling Office)

15. SECURITY CLASS. (of this report)
unclassified

15a. DECLASSIFICATION/DOWNGRADING SCHEDULE

16. DISTRIBUTION STATEMENT (of this Report)
Distribution unlimited; approved for public release

17. DISTRIBUTION STATEMENT (of the abstract entered in Block 20, if different from Report)
Approved for public release; distribution unlimited

18. SUPPLEMENTARY NOTES
reprint from GEOPHYSICAL RESEARCH LETTERS, Vol. 12, No. 10, pp 721-724, October 1985

19. KEY WORDS (Continue on reverse side if necessary and identify by block number)

20. ABSTRACT (Continue on reverse side if necessary and identify by block number)

The spectra of normal incidence transmitted compressional and shear waves are inverted to yield intrinsic (frictional) and apparent (scattering) attenuation factors as a function of frequency. This inversion is made possible by the observation that, to a first approximation, scattering and intrinsic attenuation are additive (Spencer, 1982 and Richards and Menke, 1983). Two additional assumptions are needed; that poisson's ratio is constant and that intrinsic attenuation is mainly due to shear. The technique is tested against numerical calculations, and is shown to work at least for wavelengths larger than the

DD FORM 1 JAN 73 1473 EDITION OF 1 NOV 65 IS OBSOLETE
S/N 0102-014-6601

Unclassified

SECURITY CLASSIFICATION OF THIS PAGE (When Data Entered)

scale length of the layering. The inversion requires wide-band observations and is quite sensitive to noise in the data.

Unclassified

SECURITY CLASSIFICATION OF THIS PAGE (When Data Entered)

REPORT DOCUMENTATION PAGE		READ INSTRUCTIONS BEFORE COMPLETING FORM
1. REPORT NUMBER 85-26	2. GOVT ACCESSION NO.	3. RECIPIENT'S CATALOG NUMBER
4. TITLE (and Subtitle) WIND-DRIVEN MID-OCEAN BAROCLINIC GYRES OVER TOPOGRAPHY: A CIRCULATION EQUATION EXTENDING THE SVERDRUP RELATION		5. TYPE OF REPORT & PERIOD COVERED 6. PERFORMING ORG. REPORT NUMBER
7. AUTHOR(s) de Szoeke, R. A.		8. CONTRACT OR GRANT NUMBER(s) N00014-84-C-0218
9. PERFORMING ORGANIZATION NAME AND ADDRESS College of Oceanography Oregon State Univesity Corvallis, OR 97331		10. PROGRAM ELEMENT, PROJECT, TASK AREA & WORK UNIT NUMBERS NR083-102
11. CONTROLLING OFFICE NAME AND ADDRESS Office of Naval Research Ocean Science & Technology Arlington, VA 22217		12. REPORT DATE 1985 13. NUMBER OF PAGES 32
14. MONITORING AGENCY NAME & ADDRESS(if different from Controlling Office)		15. SECURITY CLASS. (of this report) unclassified 15a. DECLASSIFICATION/DOWNGRADING SCHEDULE

16. DISTRIBUTION STATEMENT (of this Report)

Distribution unlimited; approved for public release

17. DISTRIBUTION STATEMENT (of the abstract entered in Block 20, if different from Report)

18. SUPPLEMENTARY NOTES

Reprint from Journal of Marine Research, 43:793-824, 1985.

19. KEY WORDS (Continue on reverse side if necessary and identify by block number)

20. ABSTRACT (Continue on reverse side if necessary and identify by block number)

What is the circulation driven by wind stress in a stratified ocean above topography? This question was answered by Sverdrup (1947) for vertically integrated transport over flat topography only. By applying the ideas and methods of Rhines and Young (1982a,b), a modified form of the Sverdrup transport relation can be derived for the case of stratification and topography in certain circumstances. This circulation equation is, in quasigeostrophic form,

$$J(\Psi, \beta y + \chi f_0 h'_T/H) = -\chi f_0^{-1} g A H\, J(\beta y, h'_T) + \hat{z} \cdot \nabla \times \tau/\rho_0,$$

where most symbols have their usual meanings, while χ is a parameter no larger than 1 that

DD FORM 1 JAN 73 1473 EDITION OF 1 NOV 65 IS OBSOLETE
S/N 0102-014-6601

Unclassified

SECURITY CLASSIFICATION OF THIS PAGE (When Data Entered)

depends on stratification, bottom friction and horizontal diffusivity. The effect of topography is attenuated (χ is reduced) by strong stratification, strong bottom friction, or weak horizontal diffusivity. The circulation equation applies strictly to uniform bottom slope or other topographies obeying $\nabla^2 h'_T = 0$, though it approximately holds for $\nabla^2 h'_T \simeq 0$, a criterion for which is that the scale of bottom topography greatly exceeds the baroclinic Rossby radius of deformation. It holds only above deep closed circulations. It is remarkable for the form of the characteristic lines for transport, $\beta y + \chi f_0 h'_T / H =$ constant, and the extra forcing term on the right, which depends on topography.

Examples are given of two-layer flows driven by wind-stress curl over east-west and north-south sloping topography. The determination of the boundary of the deep gyre is an implicit nonlinear problem. The solution for the case of east-west slope illustrates the general method for solving such a problem.

REVIEWS OF GEOPHYSICS AND SPACE PHYSICS, VOL. 21, NO. 5, PAGES 1206-1216, JUNE 1983
U.S. NATIONAL REPORT TO INTERNATIONAL UNION OF GEODESY AND GEOPHYSICS 1979-1982

INTERNAL WAVES IN THE OCEAN: A REVIEW

Murray D. Levine

School of Oceanography, Oregon State University, Corvallis, OR 97331

Introduction

This review documents the advances in our knowledge of the oceanic internal wave field during the past quadrennium. Emphasis is placed on studies that deal most directly with the measurement and modeling of internal waves as they exist in the ocean. Progress has come by realizing that specific physical processes might behave differently when embedded in the complex, omnipresent sea of internal waves. To understand fully the dynamics of the internal wave field requires knowledge of the simultaneous interactions of the internal waves with other oceanic phenomena as well as with themselves.

This report is not meant to be a comprehensive overview of internal waves. The focus is on topics that have been discussed most actively in the literature; subjects that may be important, but have not received recent attention, are omitted. Often only a recent reference is given; the earlier studies upon which the work is based may not be cited. Excellent reviews of internal waves are provided by Garrett and Munk (1979), Munk (1981) and Olbers (1982). Hendershott (1981) gives a useful summary of internal tides; interesting discussions by many authors on the nonlinear properties of internal waves can be found in West (1981).

The reference list is intended to be a comprehensive compilation of papers published since 1979; not all works are mentioned in the text. The list is generally confined to papers written or translated into English. A number of references from disciplines where an understanding of the internal wave field is important, such as oceanic acoustics, is also included.

Random Sea

Internal waves in the ocean exist over a sufficiently wide frequency(ω)-wavenumber(κ) band so as to obscure the identification of individual plane waves. With the rapid increase of observations during the late 1960's and early 1970's it was realized that in order to describe and model the wave field one must resort to statistical methods. Much of the research over the last decade has been directed toward measuring the statistics of time-space fluctuations of velocity and temperature and determining to what extent these observations are consistent with the fundamental properties of internal waves, such as those dictated by the dispersion relation. A major advance in describing the internal wave field has been the empirical model of Garrett and Munk (Garrett and Munk, 1972, 1975; hereafter referred to as GM). The GM model organizes many diverse observations from the deep ocean into a fairly consistent statistical representation by assuming that the internal wave field is composed of a sum of weakly interacting waves of random phase.

Paper number 3R0067.
0034-6853/83/003R-0067$15.00

Once a kinematic description of the wave field is determined, it may be possible to assess quantitatively the dynamical processes responsible for maintaining the observed internal waves. The concept of a weakly interacting system has been exploited in formulating the energy balance of the internal wave field (e.g., Olbers, 1976) in a manner analogous with the treatment of surface waves (Hasselmann, 1967). Recently, other sophisticated techniques for studying the dynamics of the random sea have been adapted from other branches of physics, such as statistical mechanics, quantum mechanics and plasma physics. The major advances have come in understanding the nonlinear interaction of internal waves with themselves. The dominant generators and dissipators of internal wave energy and momentum are still unknown, and their identification remains a challenge for theoreticians and experimentalists.

Identification: observations and verification

Deep ocean. The Garrett-Munk model is designed for the deep ocean, where the buoyancy frequency, $N(z)$, varies slowly enough with depth that the WKB approximation can be used for describing the dispersive characteristics of the internal wave field. The surprising aspect is that the energy levels and coherence structure of the GM model have been found to be remarkably constant throughout the world's oceans (Wunsch, 1976; Wunsch and Webb, 1979). A host of experiments, such as IWEX (Internal Wave Experiment), has provided much evidence which basically confirms the tenets of the GM model (Briscoe, 1975; Müller et al., 1978). Researchers now emphasize differences from the GM model in their observations. Finding significant departures from the GM universal model may lead to the identification of the most important processes that control the dynamic balance of the internal wave field (Wunsch, 1975a).

Agreement with the GM model was found to extend to low latitude (5°-10° N) in measurements of vertical wavenumber spectra (Hayes and Powell, 1980). However, very near the equator the observed spectral levels increased to ten times the GM level. Direct application of the GM model near the equator is dangerous because of the failure of the f-plane approximation. Eriksen (1980) has constructed a model of waves on an equatorial β-plane in a manner analogous to that used in formulating the GM model. Although based on limited data, the model provides a first attempt at organizing equatorial observations into a consistent framework.

At mid-latitude horizontal wavenumber spectra from towed sensors in the N. Atlantic thermocline show good agreement with the GM spectrum (Katz and Briscoe, 1979). However, there are anomalously high peaks in vertical coherence at 0.7-2 cpkm that may be due to relatively high-frequency waves that "tunnel" through a region of low N where they cannot exist as free waves. The deviation from the GM model near N is discussed in the next section.

Advances in instrumentation have made possible the measurement of small-scale vertical shear of horizontal current on vertical scales from 100 m to 1 cm, spanning the region from internal waves to turbulence (Gargett et al., 1981). The observed vertical shear spectrum is characterized as flat from 0.01 to 0.1 cpm in vertical wavenumber (β). Above 0.1 cpm the spectrum falls off as β^{-1} out to a buoyancy wavenumber $\beta_b = (N^3/\varepsilon)^{1/2}$, where there is a spectral minimum before an increase due to the dissipation of turbulent kinetic energy (ε). The level of the flat portion of the spectrum follows the WKB scaling for internal waves. The break in slope at 0.1 cpm appears to indicate the transition from internal wave motion to the increasing influence of turbulence. This is consistent with the observations and conjecture originally made by Gregg (1977).

Further effort has been made to modify, expand and explain certain consequences of the GM model especially near f (inertial frequency) and N where the WKB scaling breaks down. Munk (1980) compares peaks in the velocity spectrum near f and N that arise from using the energy distribution of the GM model with the exact solutions of the vertical wavefunctions in the neighborhood of both the horizontal and vertical turning points. The modification of the GM spectrum by a vertical turning point, where the wave frequency equals the local value of N, was first discussed by Desaubies (1973). Predicted peaks in spectra and coherences at frequencies near N are consistent with deep internal wave observations (Desaubies, 1975). In the upper ocean, however, there appears to be proportionally more energy and less wavenumber bandwidth at high frequency than in the GM energy distribution (e.g., Pinkel, 1975). The structure of the inertial spectral peak was modeled and compared with current meter data from the N. Atlantic by Fu (1981). With the effect of the turning latitude included the GM model provides a good description of the level and shape of the inertial peak in the deep ocean over smooth topography. However, at stations located in the upper ocean or in the deep ocean over rough topography, the local generation of inertial motion at the top and bottom of the ocean was found to be significant.

A deviation from the isotropic GM spectrum near topography is not necessarily an indication of a source or sink region but may be a linear distortion of the deep-ocean internal wave field. Eriksen (1982) investigated the effect of a sloping bottom on internal waves and found an intensification of velocity and temperature spectra over a frequency band centered at the local critical frequency--the frequency at which an incident ray is reflected parallel to the bottom. This linear theory predicts that these waves will be polarized with the major axis of the current ellipse oriented up-slope; there are some near-bottom observations on the continental slope that follow this behavior (Eriksen, 1982).

Another study of the effect of topography on the internal wave field was based on vertical temperature and velocity profiles near Bermuda (Johnson and Sanford, 1980). The polarization and horizontal anisotropy of the near-island current profiles are consistent with energy propagation from the ocean bottom and away from the island. These observations are in contrast to deep-ocean stations where the data indicate near-surface generation.

Upper ocean. In the upper ocean many of the assumptions of the GM model should not be valid for several reasons: 1) N varies rapidly with depth, invalidating the WKB scaling, 2) waves may be strongly forced and coupled with each other due to the proximity of atmospheric forcing, and 3) the wave field may not be stationary or homogeneous because of the large time and space variability in the upper layers. Still, the GM spectrum provides a description of the deep-ocean wave field that is useful for comparing with upper-ocean measurements.

With the increase in upper-ocean observations from experiments such as GATE (GARP Atlantic Tropical Experiment), MILE (Mixed Layer Experiment) and JASIN (Joint Air-Sea Interaction), generalizations about the upper-ocean internal wave field can begin to be made. The greatest deviations from the GM frequency spectrum are found near f, in the tidal band, and in a high-frequency band preceding the spectral roll-off. The remaining spectrum (which may not be much) sometimes follows WKB scaling (Levine et al., 1983a), but there are significant exceptions in regions where N varies rapidly (Käse and Siedler, 1980). In a summary of upper-ocean measurements Roth et al. (1981) find that spectral levels are usually equal to or above the GM spectrum. The upper-ocean wave field is hypothesized to be composed of a "base state," such as that described by GM, plus waves generated locally in the energetic upper layers.

Pinkel (1981b) discusses some of the consequences when the GM model is extended to the upper ocean. The waves of large vertical wavelength are attenuated as a result of two effects: they approach the surface boundary and the vertical waveguide where they propagate as free waves becomes thinner. This reduction of energy in the low-mode waves causes the red GM vertical wavenumber spectrum to become whiter and results in lower vertical coherence. Vertical velocity measurements from FLIP below the high-frequency band, with the semidiurnal tide and its harmonics removed, are consistent with this model (Pinkel, 1981b).

In a review of upper-ocean internal waves in the ice-covered Arctic Ocean, Morison (1983) finds frequency spectral levels to be significantly lower than those found in temperate latitudes. Although the field evidence is sparse, the spectral shapes are similar to those found in other upper-ocean experiments. The unique Arctic environment suggests many possible reasons for the low energy levels: the ice cover eliminates surface forcing by gravity waves, the tides are generally weak in the Arctic basin, and the ice sheet enhances dissipation at the surface. Additional experiments are necessary to substantiate these preliminary observations.

The deviation from the GM model at high frequency, just below the spectral roll-off, is usually evident in vertical displacement and horizontal velocity measurements as a spectral peak or shoulder accompanied by high vertical and horizontal coherence. These features appear to be due to fewer, relatively more energetic modes in this frequency band than the GM model proposes.

From a horizontal array deployed during GATE the high-frequency energy centered at 3 cph was found to be dominated by horizontally anisotropic waves of mode one, propagating to the west against a strong eastward flowing mean current (Käse and Siedler, 1980). Further analysis by Peters (1982a) indicates that the observed anisotropy cannot be explained primarily by a kinematic modification of the wave field by the mean shear flow. The implication is that the anisotropy is related to dynamic processes. The high-frequency statistics from MILE were modeled by a few low modes and incoherent noise (Levine et al., 1983a). The best fit to vertical displacement observations indicates that mode one is dominant with signal-to-noise ratios of order one. However, many features of the observed horizontal velocity spectra did not agree well with the model, such as the model-predicted 180° phase shift across the node of mode one. Some of these discrepancies are attributed to the contaminated response of a VACM (vector-averaging current meter) on a surface mooring (Halpern et al., 1981). Velocity observations in JASIN from VMCMs (vector-measuring current meter) attached to a surface mooring did show high coherence and a 180° phase shift in the high-frequency band, which is indicative of modal structure (Levine et al., 1983b). In JASIN the high-frequency band occurred over lower frequencies (0.5-3 cph) than in GATE and MILE (2-5 cph), which apparently is related to differences in the N profiles. A three-mode model was found adequate to reproduce many of the observed spectral features of both moored and towed data in JASIN (Levine et al., 1983b).

Finestructure. It is often difficult to distinguish from observations between irreversible finestructure, the signature of mixing, and reversible finestructure, the distortion due to small-scale internal waves. This problem does not solely result from our experimental inadequacies to sample densely or accurately enough but arises also from the ambiguity in defining wave-like and non-wave-like motion at small scales. In studying dynamic balances from observations it is necessary to be able to distinguish between processes that can transport mass and heat (irreversible) from those that only transport energy and momentum (reversible). This problem is usually tackled by formulating a statistical model and comparing it with observations--disagreement with internal wave statistics is blamed on irreversible finestructure (Desaubies and Gregg, 1981; Levine and Irish, 1981). Methods have also been developed to identify irreversible finestructure by attempting to remove the effect of internal wave strain on individual profiles of temperature and salinity. This is generally accomplished by removing density fluctuations (e.g., Johnson et al., 1978). However, these techniques are not unique and can lead to obscuring important processes, such as double diffusion (McDougall and Ruddick, 1982).

Indirect detection: Acoustics, Radar, Magnetometry. There is interest among acousticians to understand better the effects of the internal wave field on sound transmission through the ocean. These studies are usually undertaken from the perspective of the acoustician trying to interpret acoustic observations in terms of the sound-speed and velocity fluctuations caused by internal waves. When sound-speed fluctuations are modeled by the passive advection of a mean sound-speed profile by internal waves, the GM representation leads to a reasonable description of observed acoustic travel-time fluctuations over a fixed distance (Munk and Zachariasen, 1976; Desaubies, 1976). However, the corresponding fluctuations of the acoustic amplitude are not well predicted. Several explanations have been offered to account for this discrepancy: the effect of multiple scattering by the internal waves (Uscinski, 1980), and the strong scattering by finestructure, both reversible and irreversible (e.g., Ewart, 1980; Flatté et al., 1980; Unni and Kaufman, 1981). Whether acoustic measurements will be a useful tool for monitoring aspects of the internal wave field, such as vertical momentum flux (Munk et al., 1981a), or helping to distinguish between wave-like and non-wave-like finestructure remains unanswered.

Satellite observations have the desirable property of covering vast areas in a short time. The obvious difficulty with using this tool for the study of internal waves is that only the surface manifestations of the wave can be seen. With SAR (synthetic aperture radar) surface patterns indicative of internal waves can be detected (Vesecky and Stewart, 1982). The radar is sensitive to short surface waves (≈ 30 cm) that are believed to be modulated by internal waves through the convergence of oil films or surface wave-internal wave interactions. Internal waves are usually observed with SAR near coastal areas occurring in separate groups 10-60 km apart with crests 10-100 km long (Fu and Holt, 1982). These packets can often be associated with the interaction of tidal currents with topography and appear to exhibit characteristics of nonlinear dispersion (Apel, 1981). An attempt has also been made to use measured phase speeds of these wave packets to estimate heat content in the upper ocean (Mollo-Christensen and Mascarenhas, 1979). With increasing coverage and sampling-rate the satellite may prove useful for studying the coastal internal wave field, especially at tidal frequencies.

Internal waves propagating in the earth's magnetic field induce a secondary magnetic field. The magnetic induction spectrum for the GM model has been calculated, and magnetometry has been suggested as a potential oceanographic tool (Petersen and Poehls, 1982).

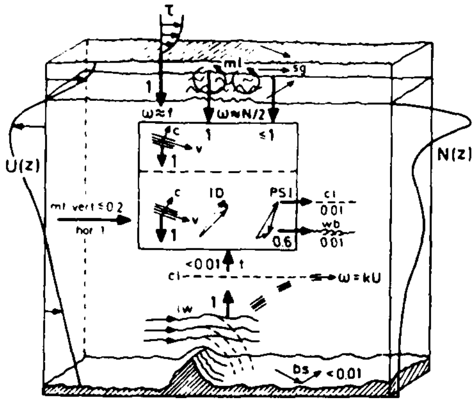

Figure 1. Sketch of interaction processes affecting the internal wave field in the upper and the deep ocean. Energy fluxes are in units of 10^{-3} W/m^2. Abbreviations and references for flux estimates are as follows: τ, wind stress (Käse, 1979; Käse and Olbers, 1980); ml, mixed layer turbulence (Bell, 1978); sg, surface gravity waves (Olbers and Herterich, 1979); cv, near-inertial waves (Käse and Olbers, 1980; Müller et al., 1978); mf, large scale mean flow (Ruddick and Joyce, 1979; Brown and Owens, 1981); t, baroclinic tides (Olbers and Pomphrey, 1981); lw, lee waves (Bell, 1975); bs, bottom scattering (Bell, 1975); cl, critical layers (Ruddick, 1980); wb, wave breaking; ID, induced diffusion; PSI, parametric subharmonic instability (Pomphrey et al., 1980). (From Olbers, 1982).

Dynamics

Great advances have been made in understanding the dynamics of the internal wave field. More realistic theoretical calculations have resulted by treating the wave field stochastically. By describing the wave field as a random process, one can more easily account for the multitude of interactions that are possible in a random sea.

The goal is to understand the flow of energy through the internal wave field: the sources, the sinks and the processes that transfer energy among the internal waves themselves. Despite the fact that the spectrum of the internal waves is nearly universal, the primary sources and sinks have still not been identified. This may not be surprising. Since the wave field is so insensitive to geographical variation, atmospheric forcing, etc., it follows that the waves spend much time as free waves and only slowly receive energy to replace the small amount lost to dissipation (e.g., Garrett and Munk, 1979; Olbers, 1982); hence, the direct link between the forcing or dissipation and the wave field itself is difficult to make. A schematic diagram from Olbers (1982) indicating some of the physical processes that may affect the internal wave field is presented in Fig. 1. Many processes, such as scattering at fronts and generation by atmospheric pressure fluctuations, were not included because their effect on the wave spectrum could not be estimated or turned out to be small (see Olbers (1982) for details).

Transfer. Much of the theoretical work has concentrated on determining the redistribution of energy among the internal waves. This calculation is the most straightforward since it depends only upon the energy distribution of the internal wave field in frequency and wavenumber--no knowledge of sources and sinks is necessary. By calculating the rate of energy transfer among the waves, the location and magnitude of the sources and sinks in frequency-wavenumber space can be inferred by assuming a steady-state internal wave field.

Most studies of nonlinear transfer in the internal wave field have used the framework of weak-interaction theory. An essential assumption of the theory is that the time scale of the nonlinear transfer of energy be slow compared with the period of the wave; the wave must maintain its integrity for at least a period or wavelength before being significantly modified. This permits the use of a two time-scale perturbation analysis, and only resonant triad interactions contribute significantly to the energy transfer. The application of weak-interaction theory to the internal wave field was pioneered by Olbers (1976) and McComas and Bretherton (1977). In these studies the internal wave field is governed by a radiative transport equation that describes the changes of the wave action density through wavenumber space. A significant contribution by McComas and Bretherton (1977) was to identify three classes of triad interactions that dominate in the internal wave field: Induced Diffusion (ID), Parametric Subharmonic Instability (PSI) and Elastic Scattering (ES). The categorizing of these interactions has facilitated the mathematical treatment as well as discussions of energy transfer. The ID mechanism represents the interaction of a high-frequency, high-wavenumber wave with a wave of low-frequency, low-wavenumber to produce another high-frequency, high-wavenumber wave. This process acts as a diffusion of wave action in vertical wavenumber space. In ES a high-frequency wave is scattered into another wave with nearly opposite vertical wavenumber (with similar horizontal wavenumber and frequency) by a low-frequency wave of twice the vertical wavenumber. This mechanism is effective in removing vertical asymmetry in the energy flux, except at frequencies near f. The PSI interaction transfers energy from a low vertical wavenumber wave into two waves of high vertical wavenumber at half the frequency. This mechanism is most efficient at near-inertial frequencies.

The most recent and complete description of the energy balance is presented by McComas and Müller (1981b) (Fig. 2). Using the GM model and an analytical simplification of the radiative transfer equation, energy is found to be generated at low vertical wavenumbers $\beta < \beta_*$ and dissipated at high wavenumbers $\beta > \beta_c$. Between β_* and β_c there is a region of constant energy flux through which the ID mechanism at high frequency ($N > \omega > 4f$) and the PSI mechanism at low frequency (2f-4f) transfers energy to high wavenumber. The constant flux region has a wavenumber spectrum with a β^{-2}

dependence, corresponding to a flat vertical shear spectrum as given by the GM model and measured directly by Gargett et al. (1981). Above $\beta_c \sim 0.1$ cpm there is a break in the slope, and the spectrum falls off more rapidly, also consistent with observations.

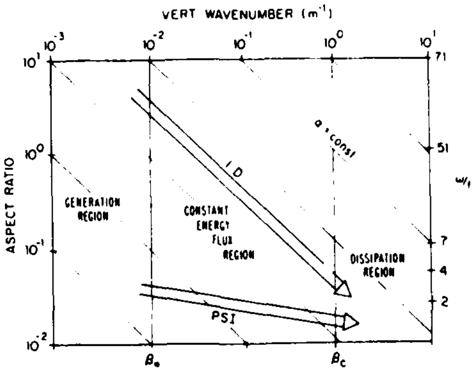

Figure 2. Schematic view of energy balance of the internal wave field. Energy is generated at low vertical wavenumbers $\beta < \beta_*$. It is transferred at high frequencies by the ID mechanism and at low frequencies by the PSI mechanism to high wavenumber $\beta > \beta_c$. Here dissipation is dominant over the weak nonlinear transfer (from McComas and Müller, 1981).

Questions have been raised as to the validity of applying weak-interaction theory to the internal wave field. It is claimed that the nonlinear transfer time is, in fact, not slow compared to the wave period for much of the high-frequency, high-wavenumber spectrum of internal waves (Holloway, 1980, 1982; Pomphrey et al., 1980). This led to recalculation of the energy transfer rates by the ID and ES mechanisms without using the assumption of weak interaction and thereby avoiding the need for time-scale separation. For the GM model the ES interactions were found to be adequately described by weak-interaction theory (Watson, 1981). However, with regard to the ID mechanism the transfer times were significantly reduced from those calculated by McComas and Müller (1981b) (Meiss and Watson, 1982). Despite this modification the scenario of the internal wave energy balance given by McComas and Müller (1981b) remains qualitatively unchanged (Pomphrey, 1982).

Recently, the ID interaction has been reexamined using eikonal theory (Henyey and Pomphrey, 1982). The high-frequency, high-wavenumber waves are modeled as a superposition of wave packets that move through a large-scale, low-frequency flow. The numerical experiments, which involve following wave packets propagating through the GM internal wave field, suggest different results from those of Meiss and Watson (1982). It is argued that ID actually behaves as diffusion in frequency-depth space rather than wavenumber-time. Further research is needed to determine the consequences on the energy balance proposed by McComas and Müller (1981b).

Another view of the energy balance is presented by Orlanski and Cerasoli (1981). Numerical experiments of a two-dimensional random internal wave field suggest strong interactions may be important in the transfer of energy. When low wavenumber energy is added to a spectrum saturated at the dissipation scales, the vertical gradient is increased in localized areas causing overturning. Hence, dissipation is increased without first transferring the energy to high wavenumber. Quantitative application of these ideas to ocean spectra would require further experimentation.

Sources. A variety of sources may be responsible for maintaining the observed internal wave field (e.g., Thorpe, 1975). Few of these have been evaluated accurately enough to determine which are the most important.

Calculations by Müller (1976) indicated that the mean shear in quasi-geostrophic flow could provide a high rate of energy input into the internal wave field. The calculated wave-induced vertical and horizontal eddy viscosities calculated from the GM model are 0.4 and 7.0 m^2/s respectively. This implies the energy gain from the vertical shear alone ($\approx 10^{-3}$ W/m^2) would be enough to maintain the internal wave field while the energy transfer rate from the horizontal shear is insignificant. However, field evidence indicates that this estimate of vertical viscosity is too high by at least a factor of 100 (Frankignoul and Joyce, 1979; Ruddick and Joyce, 1979). In contrast, results from the Local Dynamics Experiment of Polymode indicate a correlation between the horizontal shear and internal wave variance resulting in a wave-induced horizontal viscosity of 10^2 m^2/s, much larger than predicted by Müller (Brown and Owens, 1981). Further theoretical effort and more conclusive experimental evidence are needed to resolve the discrepancies.

Recent calculations by Olbers and Herterich (1979) showed that the nonlinear transfer of energy from surface waves to internal waves is relatively insignificant with the possible exception of internal waves at high frequency. The importance of this mechanism on the internal wave field is much less than originally estimated by Watson et al. (1976), where the interacting wave components were modeled by a fixed-phase relationship rather than a more reasonable random-phase representation.

The atmosphere may generate internal waves directly by fluctuating wind stress, surface pressure, and buoyancy flux. It has been established that near-inertial motion in the surface layers can be forced by the wind stress; however, the effects of the wind on the internal waves below the mixed layer are not well known. Käse (1979) estimates with a theoretical argument that the wind stress forcing is potentially strong enough at near-inertial frequencies to maintain the entire internal wave field. Measurements from GATE indicate a downward propagation of near-inertial energy into the thermocline with marginally significant correlation between the wind stress and the wave field (Käse and Olbers, 1980). These measurements are consistent with a model of Ekman suction at the base of the mixed layer providing direct linear coupling of the wind stress to the wave field in the thermocline.

The response of the ocean to an intense storm, such as a hurricane, has been studied by Price (1982 a,b) with a numerical model supported by limited field observations. The forced, near-inertial internal waves are found to transfer energy directly through the mixed layer to the thermocline more effectively than free internal waves. These waves can drain the energy in the mixed layer by 1/e in just five wave periods. These results are expected also to hold qualitatively for less severe storms.

Evidence of correlation between the wind and the high-frequency internal wave field is minimal. No significant correlation was found between the high-frequency variance in the internal wave field and the wind stress during MILE or JASIN from measurements made within 20 m of the mixed layer (Levine et al., 1983a; de Witt et al., 1982)

Using data from JASIN, Briscoe (1983) has examined the variations of the kinetic energy in the internal wave band between 0.1-2 cph away from the tidal and inertial frequencies. For a single five-day period there is a relationship between the energy flux into the atmospheric boundary layer and the changes in the vertically integrated internal wave energy. A 1.5 day lag is observed before the wave field responds to the wind stress perhaps indicating that the interaction with internal waves is accomplished indirectly through the surface wave field.

The internal tide generally contains a significant fraction of the total energy in the internal wave field. The ability of the internal tide to act as an energy source for the internal wave continuum (e.g., Bell, 1975) has been investigated theoretically using weak-interaction theory (Olbers and Pomphrey, 1981). Assuming an internal tide superimposed on the GM spectrum, the rate of energy transfer from the tide to the continuum is too low to be significant.

Sinks. The most important dissipative processes for internal waves in the ocean interior are probably shear and gravitational instabilities, or some amorphous combination of the two (Holloway, 1981). In order to describe the complete energy balance McComas and Müller (1981b) devised a simple parametrization of internal wave dissipation. By assuming that a dissipation event is localized in space and time and that the mixing in each event can be described by a vertical eddy viscosity, the time rate of change of the spectral density of the internal wave field is proportional to the spectrum of vertical shear. This is a useful result since the shear spectrum can be measured. According to this model the dissipation in the GM spectrum occurs primarily at high vertical wavenumber, where the shear is large.

A mixing model based on the random occurrences of shear instability in a stochastic representation of the internal wave field was developed by Desaubies and Smith (1982). Assuming that complete vertical mixing takes place over the depth range where the Richardson number (Ri) drops below 0.25, estimates of eddy diffusivity are comparable to those inferred from microstructure measurements (Garrett, 1979). The probability density function of Ri is found to depend only on the rms strain of the internal wave field, where strain is ∂(vertical displacement)/ ∂z, and to be very sensitive to its value. The strain is proportional to the spectral energy level and high vertical-wavenumber cutoff; an increase in either of these quantities results in a dramatic increase in the probability of instability. The model indicates that shear instabilities caused by the stretching and straining of the internal waves themselves are sufficient to result in significant internal wave dissipation.

Another possibility for removing internal wave energy and momentum is by loss to the mean flow through the mechanism of critical-layer absorption. The critical level is the location where the phase velocity of an internal wave propagating in a mean shear flow becomes equal to the mean velocity. Booker and Bretherton (1967) have demonstrated theoretically that most of the momentum of the internal wave is absorbed by the mean flow near a critical level when Ri is much greater than one. The phase speeds of oceanic internal waves of high vertical wavenumber (high mode) and low frequency can be comparable to the speeds of mean flows, thus making this mechanism a potentially important one. Ruddick (1980) has examined some of the effects on the GM spectrum, such as anisotropy and momentum loss, that could be caused by critical-layer absorption. This model, which assumes complete absorption of the wave momentum by the mean flow at a critical level, predicts a maximum wave-induced vertical eddy viscosity in a 400 m thick mean-shear layer of ~ 200 cm^2/s.

Extensive investigations into the details of critical-layer phenomena have been made theoretically with analytical and numerical studies (e.g., Brown and Stewartson, 1980, 1982a,b; Hirt, 1981) and experimentally in the laboratory (e.g., Koop, 1981; Thorpe, 1981). The application of these studies to the oceanic internal wave field has yet to be made.

Top and bottom boundaries are potential sites for internal wave dissipation as well as generation. The bottom boundary has been suggested as a sink for near-inertial internal waves to explain the often observed downward energy flux (e.g., Leaman, 1976). However, estimates of the absorption of near-inertial internal waves in the benthic boundary layer have indicated that it is probably a relatively unimportant process over smooth topography (Fu, 1981; D'Asaro, 1982b). However, Eriksen (1982) argues that near-inertial waves may be intensified after critical reflection off relatively flat slopes of 1%. The resulting strong inertial current and shear are suggested as energy sources which aid in the formation of bottom mixed layers. There is evidence that boundary layer dissipation may also be important where large amplitude internal waves encounter steep topography, such as in a submarine canyon (Hotchkiss and Wunsch, 1982).

Deterministic Waves and Specific Processes

While much of the geophysical internal wave field can only be described effectively using statistical measures, some phenomena lend themselves to a more deterministic description. This is usually only possible with oscillations at a dominant frequency or wavelength that are strong enough to be distinguished from the background. A deterministic description is also useful in theoretical models and laboratory experiments that are designed to study a specific process. This allows one to analyze a particular phenomenon in detail without the additional complications of the random sea.

Internal tides

The internal tide is an internal wave at tidal frequency that usually distinguishes itself from the background internal wave field by its large amplitude. Unlike most internal waves the source of the internal tide is known; it is generated from the barotropic tide probably by interaction with topography (see review by Hendershott, 1981).

The continental slope is a potential site of significant generation of internal tide. Theory indicates that the internal tide propagates from the slope area in beams of energy following characteristics (Rattray et al., 1969; Baines, 1982). The tide may not be observed as predicted since it can be modified as it propagates through the ocean by the spatial and temporal variations of N and mean shear (Mooers, 1975; Chuang and Wang, 1981). Current meter data from the Oregon slope and shelf were consistent with an 80 km wide beam-like structure of semidiurnal internal tide emanating from the slope where the topography was steeper than the characteristic (474-1050 m) (Torgrimson and Hickey, 1979). The beam could be traced at least 50 km from the generation area. Evidence of the beam-like nature of the tide was also found in the Rockall Trough in the N.E. Atlantic during JASIN (de Witt et al., 1982). During a one-week period, a strong tidal signal was observed, and its generation traced to Rockall Bank about 100 km away. Although the beam-like nature of the tide was observed on large space scales, locally the oscillations could be described by a dominant mode-three plane wave propagating horizontally with a wavelength of 36 km. On the W. Florida shelf a strong diurnal internal tide did not show beam-like behavior; the vertical structure was primarily composed of first and second modes (Leaman, 1980). The temporal variation of the tidal energy appeared to be related to low-frequency vertical shear. Since the diurnal tide is near the critical frequency at this location, the structure of the tide is very sensitive to changes in the slope of the characteristic caused by variation of the shear.

Far from the generator the modes are expected to become uncorrelated, the beam degenerating into uncorrelated vertical modes. The higher modes will be damped more effectively, and therefore only the lowest modes will be observed, probably with mode one dominant (Hendershott, 1981). However, recent observations in the deep ocean have indicated that higher modes, from 3-5, may dominate (Simpson and Paulson, 1979; Lyshenko and Sabinin, 1980).

Solitary waves

In addition to internal tides, flows over large ridges and sills can produce a variety of nonlinear phenomena, such as hydraulic jumps and solitary waves. Some of these phenomena that have been studied both theoretically and in the laboratory have been identified in geophysical flows. From laboratory studies Maxworthy (1979) describes a scenario of the generation of solitary waves from tidal flow: the ebb flow produces lee waves behind the sill; as flow slackens, these waves propagate upstream over the sill and develop into a series of solitary waves. Phenomenon similar to this have been seen in Massachusetts Bay (Haury et al., 1979). When the tides turned, lee waves were observed to steepen as they propagated over the sill and formed up to three wave packets, composed of 8-10 minute period waves, modulated at a period of 90 minutes. In the Andaman Sea packets of internal solitary waves that are probably generated by tidal currents have also been observed (Osborne and Burch, 1980). Interaction of the solitary waves with surface waves is demonstrated to be responsible for observed regions of short, choppy, breaking surface waves.

Internal waves generated at the sill of a fjord propagate into the fluid and when dissipated at boundaries may be responsible for vertical mixing (Stigebrandt, 1979). Extensive observations in Knight Inlet, British Columbia, indicate a large variety of responses resulting from tidally driven flow over a sill depending on the strength of the stratification and tidal currents (Farmer and Smith, 1980). The densiometric Froude number is found to be a useful quantity for characterizing whether the response will result in an internal hydraulic jump or a train of lee waves. Evidence of vertical mixing is often observed within energetic bores traveling away from the sill—this mechanism for mixing differs from Stigebrandt's model where the mixing occurs at boundaries.

Strongly nonlinear internal motion has also been observed in the thermocline of the open ocean far from the coast (100 km) over deep water (4 km) (Pinkel, 1979). Using Doppler sonar, features of 20 km horizontal scales were detected with phase velocities of 40 cm/s and water speeds >20 cm/s. Although comparison with theory is not conclusive, these features have similarities with solitary wave solutions of mode two.

It is also possible to generate solitary waves by the collapse of a localized mixed region that may be caused by turbulent overturning (e.g., Maxworthy, 1980; Kao and Pao, 1980). The geophysical significance of this mechanism is unknown.

Horizontal inhomogeneity. If the scales of the internal waves are small compared to the scales of the mean velocity and buoyancy fields, the propagation of an internal wave can be described using the WKB approximation. Olbers (1981b) applied WKB theory to internal wave propagation through a mean geostrophic flow with horizontal as well as vertical shear. Critical layers are found that exhibit a valve effect—incident waves from one side can penetrate the layer while waves from the other side are absorbed. The conditions for reflection and absorption are presented in detail for geostrophic flow with constantly sloping isopycnals.

A general theory of internal wave interaction with inhomogeneities without using WKB scaling has been developed by Olbers (1981a). The approach is to cast the equations of motion of internal waves into the form of the Schrödinger equation and adapt scattering theory from quantum mechanics. The theory is general enough to apply to scattering by topography (e.g., seamounts and continental shelves) as well as by variations in mean density and velocity fields. The theory is applied to an oceanic front and indicates that near the front the internal wave field will be anisotropic with more energy along the axis of the front than perpendicular to it.

Into the Future

The study of oceanic internal waves is at a crossroad. The extensive observations made during the past decade have been reconciled with the unforced equations of motion, and a kinematically consistent description of a "universal" internal wave field has emerged. Yet, the physical processes responsible for maintaining the pervasive oceanic internal wave field remain unidentified. While the description of the internal waves rests on a firm base of observations, the theories explaining the flow of energy through the wave spectrum are largely unsubstantiated. The path of research that will best provide the key answers is uncertain; progress in understanding the forces that drive the wave field will not be achieved easily.

Much of the recent effort by theoreticians has been directed toward describing the nonlinear energy transfer among the internal waves. Although some consensus appears to be emerging from the mathematically complicated calculations, the increasing activity by theoretical physicists from other disciplines is sure to lead to new insights and stimulate debate. The application of mathematical techniques from other branches of physics will undoubtedly be implemented in the ongoing search for the significant mechanisms of wave generation and dissipation. One of the severe theoretical limitations is the inability to treat strong nonlinear interactions. When the interaction of waves can no longer be described by weak-interaction theory, the transition to turbulence begins, and the notion of a wave itself becomes fuzzy.

Where does this leave the experimentalist? In order to make advances in understanding the dynamic balance of the internal wave field, the observationalist must be guided by theories that can be tested by measurements. As yet theoreticians have not been able to indicate such straightforward tests. The task is inherently complicated by a random sea that prevents the association of a wave of a certain frequency with its wavenumber. Indeed it is not easy even to conceive of a definitive experiment that would reveal the nature of the energy balance.

Although the prospects for breakthroughs in determining the energy balance are somewhat discouraging, there are still many topics that would benefit from further exploration. The gathering of better quality data in a variety of oceanic environments will permit the continuing refinement of the empirical description of the internal wave field and provide substance to stimulate and guide theoretical ideas. Even though the concept of a "universal" internal wave field is well founded, a closer examination of the deviations is needed. How do variations in topography, wind stress, eddy fields and fronts affect the internal wave climate? Exploratory experiments designed to investigate systematically the temporal and spatial variability of spectral level and coherence structure in diverse oceanic environments may provide useful clues.

Most recent theoretical and experimental research has been guided by the premise that internal waves exist at a continuous spectrum of frequency and wavenumber. However, most of the internal wave energy does not fit into a power law description of a spectral continuum but is, in fact, concentrated in narrow frequency bands around the inertial, tidal and buoyancy frequencies. As these are the most energetic internal waves, uncovering the details of their interactions may provide information relevant to the dynamics of the continuum. Further theoretical studies treating the interactions of these narrow-band waves with the broad-band continuum and with each other would be useful.

Internal waves occupy an intermediate time and space scale of oceanic phenomena between turbulent and geostrophic flows. Because they are ubiquitous, internal waves are familiar to investigators of microscale and mesoscale phenomena alike. Internal waves are often considered a nuisance because their complicated temporal and spatial fluctuations are blamed for obscuring and contaminating experimental observations. Consideration of the internal wave field is often necessary, if only to demonstrate their relative unimportance. However, recent work has indicated that internal waves may play a significant role in the energy and momentum balances of processes at other scales, such as an effective viscosity for mesoscale motions or as a source of shear for turbulent production at the microscale. Because internal waves can be significant participants in many physical processes in a stratified ocean, an improved understanding of their behavior is important for the specialist and for the physical oceanographer in general.

Acknowledgements. The support of the Office of Naval Research under contract N00014-79-C-0004 and the National Science Foundation under grant OCE-8117700 is gratefully acknowledged.

References

Abramov, A.A., T.M. Akivis, Yu.A. Ivanov and V.I. Ul'yanova, Behavior of internal gravity waves in the region of critical latitudes, Atmos. Ocean Phys., 17, 360-364, 1981.

Amen, R., and T. Maxworthy, The gravitational collapse of a mixed region into a linearly stratified fluid, J. Fluid Mech., 96, 65-80, 1980.

Anderson, D.L.T., and A.E. Gill, Beta dispersion of inertial waves, J. Geophys. Res., 84, 1836-1842, 1979.

Apel, J.R., Nonlinear features of internal waves as derived from SEASAT imaging radar, in Oceanography from Space, edited by J.F.R. Gower, Plenum, New York, 525-533, 1981.

Baines, P.G., Satellite observations of internal waves on the Australian north-west shelf, Aust. J. Mar. Freshwat. Res., 32, 457-463, 1981.

Baines, P.G., On internal tide generation models, Deep-Sea Res., 29, 307-338, 1982.

Basovich, A.Ya., Transformation of the surface wave spectrum due to the action of an internal wave, Atmos. Ocean Phys., 15, 448-452, 1980.

Baxter, L., III, and M.H. Orr, Fluctuations in sound transmission through internal waves associated with the thermocline: a computer model for acoustic transmission through sound velocity fields calculated from thermistor chain, CTD, XBT, and acoustic backscattering, J. Acoust. Soc. Am., 71, 61-66, 1982.

Bell, T.H., Jr., Topographically generated internal waves in the open ocean, J. Geophys. Res., 80, 320-327, 1975.

Belyayev, V.S., and A.N. Gezentsvey, Shear instability of internal waves in the ocean, Atmos. Ocean Phys., 14, 459-463, 1979.

Belyayev, V.S., and Yu.V. Mozdrin, On the vertical spectra of the temperature field fine structure in a frontal zone, Oceanology, 19, 367-372, 1980.

Benilov, A.Yu., N.I. Solntseva and B.N. Filyushkin, Relationship between the variability of the wind field and internal waves, Oceanology, 18, 257-262, 1978.

Booker, J.R., and F.P. Bretherton, The critical layer for internal gravity waves in a shear flow, J. Fluid Mech., 27, 513-539, 1967.

Briscoe, M.G., Preliminary results from the tri-moored internal wave experiment (IWEX), J. Geophys. Res., 80, 3872-3884, 1975.

Briscoe, M.G., Energy balance of internal waves, Phil. Trans. R. Soc. Lond. A, in press, 1983.

Brown, E.D., and W.B. Owens, Observations of the horizontal interactions between the internal wave field and the mesoscale flow, J. Phys. Oceanogr., 11, 1474-1480, 1981.

Brown, S.N., and K. Stewartson, On the nonlinear reflexion of a gravity wave at a critical level. Part 1., J. Fluid Mech., 100, 577-595, 1980.

Brown, S.N., and K. Stewartson, On the nonlinear reflection of a gravity wave at a critical level. Part 2., J. Fluid Mech., 115, 217-230, 1982a.

Brown, S.N., and K. Stewartson, On the nonlinear reflection of a gravity wave at a critical level. Part 3., J. Fluid Mech., 115, 231-250, 1982b.

Bukatov, A.Ye., and O.M. Bukatov, Internal waves in a zonal channel of varying depth, Atmos. Ocean Phys., 16, 944-949, 1981.

Bunimovich, L.A., Concerning certain properties of internal ocean waves with horizontally varying Vaisala-Brunt frequency, Atmos. Ocean Phys., 16, 354-359, 1980.

Cairns, J.L., Variability in the Gulf of Cadiz: internal waves and globs, J. Phys. Oceanogr., 10, 579-595, 1980.

Cartwright, D.E., The tidal signal in inverted echo-sounder records, Deep-Sea Res., 29, 767-784, 1982.

Chapman, D.C., Nearly trapped internal edge waves in a geophysical ocean, Deep-Sea Res., 29, 525-533, 1982.

Chapman, D.C., and M.C. Hendershott, Scattering of internal waves obliquely incident upon a step change in bottom relief, Deep-Sea Res., 28, 1323-1338, 1981.

Chen, H.H., and D.J. Kaup, Linear stability of internal wave solitons in a deep stratified fluid, Phys. Fluids, 23, 235-238, 1980.

Chen, H.H., and Y.C. Lee, Internal-wave solitons of fluids with finite depth, Phys. Rev. Lett., 43, 264-266, 1979.

Chen, H.H., Y.C. Lee and N.R. Pereira, Algebraic internal wave solitons and the integrable Calogero-Moser-Sutherland N-body problem, Phys. Fluids, 22, 187-188, 1979.

Chuang, W.-S., and D.-P. Wang, Effects of density front on the generation and propagation of internal tides, J. Phys. Oceanogr., 11, 1357-1374, 1981.

Cresswell, G.R., and P.M. Boland, Internal waves detected with a continental shelf current-meter array, Aust. J. Mar. Freshwat. Res., 32, 1-8, 1981.

D'Asaro, E., Velocity structure of the benthic ocean, J. Phys. Oceanogr., 12, 313-322, 1982a.

D'Asaro, E., Absorption of internal waves by the benthic boundary layer, J. Phys. Oceanogr., 12, 323-336, 1982b.

D'Asaro, E., and M. Perkins, The near-inertial internal wave spectrum in the late summer Sargasso Sea, submitted, 1982.

Davis, R.E., R. de Szoeke, D. Halpern and P. Niiler, Variability in the upper ocean during MILE. Part I: the heat and momentum balances, Deep-Sea Res., 28, 1427-1451, 1981.

de Santo, J.A., Derivation of the acoustic wave equation in the presence of gravitational and rotational effects, J. Acoust. Soc. Am., 66, 827-830, 1979.

Desaubies, Y.J.F., Internal waves near the turning point, Geophys. Fluid Mech., 5, 143-154, 1973.

Desaubies, Y.J.F., A linear theory of internal wave spectra and coherences near the Vaisala frequency, J. Geophys. Res., 80, 895-899, 1975.

Desaubies, Y.J.F., Acoustic-phase fluctuations induced by internal waves in the ocean, J. Acoust. Soc. Am., 60, 795-800, 1976.

Desaubies, Y., Note on fine structure models in underwater acoustics, J. Acoust. Soc. Am., 72, 892-895, 1982.

Desaubies, Y.J.F., and M.C. Gregg, Reversible and irreversible finestructure, J. Phys. Oceanogr., 11, 541-556, 1981.

Desaubies, Y., and W.K. Smith, Statistics of Richardson number and of instability in oceanic internal waves, J. Phys. Oceanogr., 12, 1245-1259, 1982.

de Witt, L.M., M.D. Levine and C.A. Paulson, Internal waves in JASIN: spectra, variability and internal tide, J. Phys. Oceanogr., submitted, 1982.

de Witt, R.J., and J. Wright, Self-consistent effective-medium theory of random internal waves, J. Fluid Mech., 115, 283-302, 1982.

Dillon, T.M., and D.R. Caldwell, High-frequency internal waves at ocean station P, J. Geophys. Res., 85, 3277-3284, 1980.

Dolina, I.S., S.A. Yermakov, V.V. Papko and Ye.N. Pelinovskiy, An experimental study of free-surface oscillations set up by internal waves, Atmos. Ocean Phys., 14, 859-861, 1979.

Dore, B.D., and M.A. Al-Zainaidi, On secondary vorticity in internal waves, Quart. Appl. Math., 37, 35-50, 1979.

Drazin, P.G., M.D. Zaturska and W.H.H. Banks, On the normal modes of parallel flow of inviscid stratified fluid. Part 2. Unbounded flow with propagation at infinity, J. Fluid Mech., 95, 681-705, 1979.

Dykman, V.Z., O.A. Kiseler and O.I. Yefremov, Investigations of internal wave energy in synoptic eddies, Oceanology, 21, 317-321, 1981.

Dysthe, K.B., and K.P. Das, Coupling between a surface-wave spectrum and an internal wave: modulation interaction, J. Fluid Mech., 104, 483-503, 1981.

Eriksen, C.C., Evidence for a continuous spectrum of equatorial waves in the Indian Ocean, J. Geophys. Res., 85, 3285-3303, 1980.

Eriksen, C.C., Observations of internal wave reflection off sloping bottoms, J. Geophys. Res., 87, 525-538, 1982.

Eriksen, C.C., J.M. Dahlen and J.T. Shillingford, Jr., An upper ocean moored current and density profiler applied to winter conditions near Bermuda, J. Geophys. Res., 87, 7879-7902, 1982.

Esswein, R., and S.M. Flatté, Calculation of the phase-structure function density from oceanic internal waves, J. Acoust. Soc. Am., 70, 1387-1396, 1981.

Evans, D.L., Observations of small-scale shear and density structure in the ocean, Deep-Sea Res., 29, 581-595, 1982.

Ewart, T.E., A numerical simulation of the effects of oceanic finestructure on acoustic transmission, J. Acoust. Soc. Am., 67, 496-503, 1980.

Farmer, D.M., and J.D. Smith, Tidal interaction of stratified flow with a sill in Knight Inlet, Deep-Sea Res., 27, 239-254, 1980.

Filatov, N.N., S.V. Ryanzhin and L.V. Zaytsev, Features of turbulence, Langmuir circulation and internal waves in a lake, Atmos. Ocean Phys., 16, 694-698, 1981.

Flatte, S.M., R. Dashen, W.H. Munk, K.M. Watson and F. Zachariasen, Sound Transmission through a Fluctuating Ocean, Cambridge University Press, New York, 293pp., 1979.

Flatté, S.M., R. Leung and S.Y. Lee, Frequency spectra of acoustic fluctuations caused by oceanic internal waves and other finestructure, J. Acoust. Soc. Am., 68, 1773-1779, 1980.

Frankignoul,C., and T.M. Joyce, On the internal wave variability during the internal wave experiment (IWEX), J. Geophys. Res., 84, 769-776, 1979.

Friedlander, S., and W.L. Siegmann, Internal waves in a rotating stratified fluid in an arbitrary gravitational field, Geophys. Astrophys. Fluid Dyn., 19, 267-291, 1982.

Friedlander, S., and W.L. Siegmann, Internal waves in a contained rotating stratified fluid, J. Fluid Mech., 114, 123-156, 1982.

Fritts, D.C., The transient critical-level interaction in a Boussinesq fluid, J. Geophys. Res., 87, 7997-8016, 1982.

Fu, L.-L., Observations and models of inertial waves in the deep ocean, Rev. Geophys. Space Phys., 19, 141-170, 1981.

Fu, L.-L., and B. Holt, Seasat Views Oceans and Sea Ice with Synthetic Aperture Radar, Jet Propulsion Lab., Pasadena, JPL Pub. 81-120, 200pp., 1982.

Gargett, A.E., P.J. Hendricks, T.B. Sanford, T.R. Osborn and A.J. Williams III, A composite spectrum of vertical shear in the upper ocean, J. Phys. Oceanogr., 11, 1258-1271, 1981.

Garrett, C., Mixing in the ocean interior, Dyn. Atmos. Oceans, 3, 239-265, 1979.

Garrett, C.J.R., and W.H. Munk, Space-time scales of internal waves, Geophys. Fluid Dyn., 2, 225-264, 1972.

Garrett, C.J.R., and W.H. Munk, Space-time scales of internal waves: a progress report, J. Geophys. Res., 80, 291-297, 1975.

Garrett, C., and W. Munk, Internal waves in the ocean, Ann. Rev. Fluid Mech., 11, 339-369, 1979.

Garvine, R.W., Frontal jump conditions for models of shallow buoyant surface layer hydrodynamics, Tellus, 33, 301-312, 1981.

Gordon, R.L., Tidal interactions in a region of large bottom slope near northwest Africa during JOINT-I, Deep-Sea Res., 26, 179-210, 1979.

Gordon, R.L., Boundary layer under near-inertial internal waves over a critically sloping bottom, J. Phys. Oceanogr., 10, 1032-1038, 1980.

Gordon, R.L., Internal modes in a submarine canyon, J. Geophys. Res., 87, 582-584, 1982.

Gorodtsov, V.A., and E.V. Teodorovich, On the generation of internal waves in the presence of uniform straight-line motion of local and nonlocal sources, Atmos. Ocean Phys., 16, 699-703, 1981.

Graham, E.W., and B.B. Graham, The tank wall effect on internal waves due to a transient vertical force moving at fixed depth in a density-stratified fluid, J. Fluid Mech., 97, 91-114, 1980.

Gregg, M.C., A comparison of finestructure spectra from the main thermocline, J. Phys. Oceanogr., 7, 33-40, 1977.

Grimshaw, R., Mean flow induced by internal gravity wave packets propagating in a shear flow, Phil. Trans. R. Soc., A292, 391-417, 1979.

Grimshaw, R.H.J., On resonant over-reflection of internal gravity waves from a Helmholtz velocity profile, J. Fluid Mech., 90, 161-178, 1979.

Grimshaw, R., A general theory of critical level absorption and valve effects for linear wave propagation, Geophys. Astrophys. Fluid Dyn., 14, 303-326, 1980.

Grimshaw, R.H.J., Resonant over-reflection of internal gravity waves from a thin shear layer, J. Fluid Mech., 109, 349-365, 1981.

Grimshaw, R., The effect of dissipative processes on mean flows induced by internal gravity-wave packets, J. Fluid Mech., 115, 347-377, 1982.

Halpern, D., R.A. Weller, M.G. Briscoe, R. E. Davis and J.R. McCullough, Intercomparison tests of moored current measurements in the upper ocean, J. Geophys. Res., 86, 419-428, 1981.

Hasselmann, K., Nonlinear interactions treated by the methods of theoretical physics (with application to the generation of waves by wind), Proc. Roy. Soc., A299, 77-100, 1967.

Haury, L.R., M.G. Briscoe and M.H. Orr, Tidally generated internal wave packets in Massachusetts Bay, Nature, 278, 312-317, 1979.

Hayes, S.P., The bottom boundary layer in the eastern tropical Pacific, J. Phys. Oceanogr., 10, 315-329, 1980.

Hayes, S.P., and C.J. Powell, Vertical wave number spectra of temperature fine structure in the equatorial Pacific, J. Geophys. Res., 85, 4029-4035, 1980.

Helal, M.A., and J.M. Molines, Non-linear internal waves in shallow water. A theoretical and experimental study, Tellus, 33, 488-504, 1981.

Hendershott, M.C., Long waves and ocean tides, in Evolution of Physical Oceanography, edited by B.A. Warren and C. Wunsch, MIT Press, Cambridge, 292-341, 1981.

Henyey, F.S., and N. Pomphrey, Eikonal description of internal wave interactions: a non-diffusive picture of "induced diffusion," Dyn. Atmos. Oceans, submitted, 1982.

Hirt, C.W., A numerical study of critical layer absorption,in Nonlinear Properties of Internal Waves, edited by B.J. West, AIP conference proceedings No. 76, Amer. Inst. Phys., New York, 141-157, 1981.

Holloway, G., On the spectral evolution of strongly interacting waves, Geophys. Astrophys.

Fluid Dyn., 11, 271-287, 1979.
Holloway, G., Oceanic internal waves are not weak waves, J. Phys. Oceanogr., 10, 906-914, 1980.
Holloway, G., Theoretical approaches to interactions among internal waves, in Nonlinear Properties of Internal Waves, edited by B.J. West, AIP Conference Proceedings No. 76, Amer. Inst. Phys., New York, 47-78, 1981.
Holloway, G., On interaction time scales of oceanic internal waves, J. Phys. Oceanogr., 12, 293-296, 1982.
Holyer, J.Y., Large amplitude progressive interfacial waves, J. Fluid Mech., 93, 433-448, 1979.
Hotchkiss, F.S., and C. Wunsch, Internal waves in Hudson Canyon with possible geological implications, Deep-Sea Res., 29, 415-442, 1982.
Huthnance, J.M., and P.G. Baines, Tidal currents in the northwest African upwelling region, Deep-Sea Res., 29, 285-306, 1982.
James, I.D., Tidal currents at two deep-sea moorings near the shelf edge, Deep-Sea Res., 29, 1099-1111, 1982.
Johnson, C.L., S. Cox and B. Gallagher, The separation of wave-induced and intrusive oceanic finestructure, J. Phys. Oceanogr., 8, 846-860, 1978.
Johnson, C.L., and T.B. Sanford, Anomalous behavior of internal gravity waves near Bermuda, J. Phys. Oceanogr., 10, 2021-2034, 1980.
Kantha, L.H., On generation of internal waves by turbulence in the mixed layer, Dyn. Atmos. Oceans, 3, 39-46, 1979.
Kantha, L.H., On leaky modes on a buoyancy interface, Dyn. Atmos. Oceans, 3, 47-54, 1979.
Kantha, L.H., Drift currents induced by reflection of propagating inertial and internal waves at a rigid boundary, Dyn. Atmos. Oceans, 4, 15-20, 1979.
Kao, T.W., and H.-P. Pao, Wake collapse in the thermocline and internal solitary waves, J. Fluid Mech., 97, 115-127, 1980.
Käse, R.H., Calculations of the energy transfer by the wind to near-inertial internal waves, Deep-Sea Res., 26, 227-232, 1979.
Käse, R.H., and D.J. Olbers, Wind-driven inertial waves observed during phase III of GATE, Deep-Sea Res., Suppl. to Vol. 26, 191-216, 1980.
Käse, R.H., and G. Siedler, Internal wave kinematics in the upper tropical Atlantic, Deep-Sea Res., Suppl. to Vol. 26, 161-189, 1980.
Katz, E.J., and M.G. Briscoe, Vertical coherence of the internal wave field from towed sensors, J. Phys. Oceanogr., 9, 518-530, 1979.
Kaye, G.T., Acoustic remote sensing of high-frequency internal waves, J. Geophys. Res., 84, 7017-7022, 1979.
Klostermeyer, J., On parametric instabilities of finite-amplitude internal gravity waves, J. Fluid Mech., 119, 367-377, 1982.
Koop, C.G., A preliminary investigation of the interaction of internal gravity waves with a steady shearing motion, J. Fluid Mech., 113, 347-386, 1981.
Koop, C.G., and G. Butler, An investigation of internal solitary waves in a two-fluid system, J. Fluid Mech., 112, 225-251, 1981.
Koop, C.G., and L.G. Redekopp, The interaction of long and short internal gravity waves: theory and experiment, J. Fluid Mech., 111, 367-409, 1981.
Korchashkin, N.N., I.D. Lozovatskiy and R.V. Ozmidov, Variability of the vertical finestructure of the temperature field in the western Pacific Ocean, Oceanology, 19, 121-126, 1979.
Kort, V.G., The 25th cruise of the R/V Akademik *Kurchatov (principal scientific results)*, Oceanology, 18, 242-245, 1978.
Kushnir, V.M., and Ye.G. Andryushchenko, Hydrodynamic instability in internal waves of the tidal period, Atmos. Ocean Phys., 16, 989-991, 1981.
Leaman, K.D., Observations on the vertical polarization and energy flux of near-inertial waves, J. Phys. Oceanogr., 6, 894-908, 1976.
Leaman, K.D., Some observations of baroclinic diurnal tides over a near-critical bottom slope, J. Phys. Oceanogr., 10, 1540-1551, 1980.
Leibovich, S., Waves in parallel or swirling stratified shear flows, J. Fluid Mech., 93, 401-412, 1979.
Leonov, A.I., Yu.Z. Miropolsky and R.E. Tamsalu, Nonlinear stationary internal and surface waves in shallow seas, Tellus, 31, 150-160, 1979.
Levikov, S.P., A model of the limit spectrum of internal waves, Atmos. Ocean Phys., 16, 866-870, 1981.
Levine, M.D., R.A. de Szoeke and P.P. Niiler, Internal waves in the upper ocean during MILE, J. Phys. Oceanogr., *in press*, 1983a.
Levine, M.D., and J.D. Irish, A statistical description of temperature finestructure in the presence of internal waves, J. Phys. Oceanogr., 11, 676-691, 1981.
Levine, M.D., C.A. Paulson, M.G. Briscoe, R.A. Weller and H. Peters, Internal waves in JASIN, Phil. Trans. R. Soc. Lond. A, in press, 1983b.
Lozovatskiy, I.D., On the effect of the fine structure of the temperature field on the internal wave spectra in the sea, Atmos. Ocean Phys., 14, 86-87, 1978.
Lozovatskiy, I.D., and R.V. Ozmidov, Characteristics of the vertical structure of sea turbulence, Oceanology, 18, 21-26, 1978.
Luchinin, A.G., and V.I. Titov, Concerning the feasibility of remote optical sensing of internal waves on the basis of their manifestations on the ocean surface, Atmos. Ocean Phys., 16, 950-954, 1981.
Lyashenko, A.F., and K.D. Sabinin, On the spatial structure of the internal tides on the 1970 hydrophysical test range in the Atlantic, Atmos. Ocean Phys., 15, 595-601, 1980.
Lyubitskiy, A.A., I.A. Leykin and A.D. Rozenberg, Measurement of short internal waves in a subsurface thermocline, Atmos. Ocean Phys., 14, 527-531, 1979.
Maslowe, S.A., and L.G. Redekopp, Solitary waves in stratified shear flows, Geophys. Astrophys. *Fluid Dyn., 13, 185-196, 1979.*
Maslowe, S.A., and L.G. Redekopp, Long nonlinear waves in stratified shear flows, J. Fluid Mech., 101, 321-348, 1980.
Matthews, J.B., Seasonal circulation of the Glacier Bay, Alaska fjord system, Estuarine, Coast. Shelf Sci., 12, 679-700, 1981.
Maxworthy, T., A note on the internal solitary waves produced by tidal flow over a three-dimensional ridge, J. Geophys. Res., 84, 338-346, 1979.
Maxworthy, T., On the formation of nonlinear internal waves from the gravitational collapse of mixed regions in two and three dimensions, J. Fluid Mech., 96, 47-64, 1980.
Mayer, D.A., H.O. Mofjeld and K.D. Leaman, Near-inertial internal waves observed on the outer shelf in the Middle Atlantic Bight in the wake of Hurricane Belle, J. Phys. Oceanogr., 11, 87-106, 1981.
McComas, C.H., III, and F.P. Bretherton, Resonant interaction of oceanic internal waves, J. Geophys. Res., 82, 1397-1412, 1977.
McComas, C.H., and M.G. Briscoe, Bispectra of internal waves, J. Fluid Mech., 97, 205-213, 1980.
McComas, C.H., and P. Müller, Time scales of resonant interactions among oceanic internal waves, J. Phys. Oceanogr., 11, 139-147, 1981a.
McComas, C.H., and P. Müller, The dynamic balance of internal waves, J. Phys. Oceanogr., 11, 970-986, 1981b.
McDougall, T.J., and B.R. Ruddick, The effects on finestructure measurements of correcting for internal wave strain, J. Phys. Oceanogr., 12, 495-497, 1982.
McPhaden, M.J., and R.A. Knox, Equatorial Kelvin and inertio-gravity waves in zonal shear flow, J. Phys. Oceanogr., 9, 263-277, 1979.
Meiss, J.D., N. Pomphrey and K.M. Watson, Numerical analysis of weakly nonlinear wave turbulence, Proc. Natl. Acad. Sci., 76, 2109-2113, 1979.
Meiss, J.D., and K.M. Watson, Internal-wave interactions in the induced diffusion approximation, J. Fluid Mech., 117, 315-341, 1982.
Middleton, J.H., and T.D. Foster, Fine structure measurements in a temperature-compensated halocline, J. Geophys. Res., 85, 1107-1122, 1980.
Milder, D.M., Hamiltonian dynamics of internal waves, J. Fluid Mech., 119, 269-282, 1982.
Miles, J.W., On internal solitary waves, Tellus, 31, 456-462, 1979.
Miles, J.W., Solitary waves, Ann. Rev. Fluid Mech., 12, 11-43, 1980.
Miles, J.W., On internal solitary waves II, Tellus, 33, 397-401, 1981.
Millot, C., and M. Crépon, Inertial oscillations on the continental shelf of the Gulf of Lions--observations and theory, J. Phys. Oceanogr., 11, 639-657, 1981.
Miropol'skiy, Yu.Z., Self-similar solutions of the Cauchy problem for internal waves in an unbounded fluid, Atmos. Ocean Phys., 14, 673-679, 1979.
Mofjeld, H.O., An analytic theory on how friction affects internal waves in the equatorial waveguide, J. Phys. Oceanogr., 11, 1585-1590, 1981.
Mollo-Christensen, E., and A.S. Mascarenhas Jr., Heat storage in the oceanic upper mixed layer inferred from Landsat data, Science, 203, 653-654, 1979.
Mooers, C.N.K., Several effects of a baroclinic current on the cross-stream propagation of inertial-internal waves, Geophys. Fluid Dyn., 6, 245-275, 1975.
Morison, J., Internal waves in the Arctic: a review, Proceedings of the air-sea-ice NATO *symposium, edited by N. Untersteiner*, 1983.
Morozov, Ye.G., and L.P. Pilatova, Horizontal coherence of semidiurnal fluctuations of temperature in the Poligon-70 test area, Atmos. Ocean Phys., 14, 243-245, 1978.
Muller, P., On the diffusion of momentum and mass by internal gravity waves, J. Fluid Mech., 77, 789-823, 1976.
Müller, P., A note on the variability of eddy diffusion coefficients in the ocean, Dyn. Atmos. Oceans, 3, 267-274, 1979.
Müller, P., D.J. Olbers and J. Willebrand, The IWEX spectrum, J. Geophys. Res., 83, 479-500, 1978.
Munk, W.H., Internal wave spectra at the buoyant and inertial frequencies, J. Phys. Oceanogr., 10, 1718-1728, 1980.
Munk, W.H., Internal waves and small-scale processes, in Evolution of Physical Oceanography, edited by B.A. Warren and C. Wunsch, MIT Press, Cambridge, 264-290, 1981.
Munk, W., P. Worcester and F. Zachariasen, Scattering of sound by internal wave currents: the relation to vertical momentum flux, J. Phys. Oceanogr., 11, 442-454, 1981a.
Munk, W.H., and F. Zachariasen, Sound propagation through a fluctuating stratified ocean: theory and observation, J. Acoust. Soc. Am., 59, 818-838, 1976.
Munk, W., B. Zetler, J. Clark, S. Gill, D. *Porter, J. Spiesberger and R. Spindel*, Tidal effects on long-range sound transmission, J. Geophys. Res., 86, 6399-6410, 1981b.
Nesterov, S.V., and S.Ya. Sekerzh-Zen'kovich, Purely zonal internal waves in the ocean at the equator, Atmos. Ocean Phys., 16, 789-790, 1979.
Odulo, A.B., Equations of long nonlinear waves in the ocean, Oceanology, 18, 633-636, 1979.
Odulo, A.B., and M.A. Chusov, Steady nonlinear waves in a stratified rotating fluid, Atmos. Ocean Phys., 14, 744-747, 1979.
Olbers, D.J., Nonlinear energy transfer and the energy balance of the internal wave field in the deep ocean, J. Fluid Mech., 74, 375-399, 1976.
Olbers, D.J., A formal theory of internal wave scattering with applications to ocean fronts, J. Phys. Oceanogr., 11, 1078-1099, 1981a.
Olbers, D.J., The propagation of internal waves in a geostrophic current, J. Phys. Oceanogr., 11, 1224-1233, 1981b.
Olbers, D.J., Models of the oceanic internal wave field, Rev. Geophys. Space Phys., submitted, 1982.
Olbers, D.J., and K. Herterich, The spectral energy transfer from surface waves to internal waves in the ocean. J. Fluid Mech., 92, 349-379, 1979.
Olbers, D.J., and N. Pomphrey, Disqualifying two candidates for the energy balance of oceanic internal waves, J. Phys. Oceanogr., 11, 1423-1425, 1981.
Orlanski, I., and C.P. Cerasoli, Energy transfer among internal gravity modes: weak and strong interactions, J. Geophys. Res., 86, 4103-4124, 1981.
Osborne, A.R., and T.L. Burch, Internal solitons in the Andaman Sea, Science, 208, 451-460, 1980.
Ostrovskiy, L.A., Nonlinear internal waves in a rotating ocean, Oceanology, 18, 119-125, 1978.
Ostrovskiy, L.A., and I.A. Soustova, The upper mixed layer of the ocean as a sink of internal wave energy, Oceanology, 19, 643-648, 1980.
Ou, H.W., and J.R. Bennett, A theory of the mean flow driven by long internal waves in a rotating basin, with application to Lake Kinneret, J. Phys. Oceanogr., 9, 1112-1125, 1979.
Peters, H., On the kinematics of a stochastic field of internal waves modified by a mean shear current, Deep-Sea Res., submitted, 1982a.
Peters, H., On the dispersion characteristics of high-frequency internal waves in a mean shear current, Deep-Sea Res., submitted, 1982b.
Petersen, R.A., and K.A. Poehls, Model spectrum of magnetic induction caused by ambient internal waves, J. Geophys. Res., 87, 433-440, 1982.
Petrov, V.V., Interaction of internal waves with small-scale surface turbulence in the ocean, Atmos. Ocean Phys., 14, 246-249, 1978.
Phillips, O.M., The structure of short gravity waves on the ocean surface, in Spaceborne Synthetic Aperture Radar for Oceanography, edited by R.C. Beal, P. DeLeonibus and I. Katz, John Hopkins Press, Baltimore, Maryland, 1981.
Pinkel, R., Upper ocean internal wave observations, J. Geophys. Res., 80, 3892-3910, 1975.
Pinkel, R., Observations of strongly nonlinear internal motion in the open sea using a range-gated Doppler sonar, J. Phys. Oceanogr., 9, 675-686, 1979.
Pinkel, R., On the use of Doppler sonar for internal wave measurements, Deep-Sea Res., 28, 269-289, 1981a.
Pinkel, R., Observations of the near-surface internal wavefield, J. Phys. Oceanogr., 11, 1248-1257, 1981b.
Podney, W., and R. Sager, Measurement of *fluctuating magnetic gradients* originating from internal waves, Science, 205, 1381-1381, 1979.
Pollard, R.T., Properties of near-surface inertial oscillations, J. Phys. Oceanogr., 10, 385-398, 1980.
Pomphrey, N., Review of some calculations of energy transport in a Garrett-Munk ocean, in Nonlinear Properties of Internal Waves, edited

by B.J. West, AIP conference proceedings No. 76, Amer. Inst. Phys., New York, 113-128, 1981.

Pomphrey, N., J.D. Meiss and K.M. Watson, Description of nonlinear internal wave interactions using Langevin methods, J. Geophys. Res., 85, 1085-1094, 1980.

Price, J.F., Internal wave wake of a moving storm. Part I, scales, energy budget and observations, J. Phys. Oceanogr., submitted, 1982a.

Price, J.F., Internal wave wake of a moving storm. Part II, parameter dependence, J. Phys. Oceanogr., submitted, 1982b.

Rattray, M., Jr., J.G. Dworski and P.E. Kovala, Generation of long internal waves at the continental slope, Deep-Sea Res., Suppl. to Vol. 16, 179-195, 1969.

Renouard, D.P., An experimental study of gravity-inertial waves and wind-induced Kelvin-type upwellings in a rotating system, J. Phys. Oceanogr., 11, 1100-1112, 1981.

Ripa, P., On the theory of nonlinear wave-wave interactions among geophysical waves, J. Fluid Mech., 103, 87-115, 1981.

Roth, M.W., M.G. Briscoe and C.H. McComas III, Internal waves in the upper ocean, J. Phys. Oceanogr., 11, 1234-1247, 1981.

Ruddick, B.R., Critical layers and the Garrett-Munk spectrum, J. Mar. Res., 38, 135-145, 1980.

Ruddick, B.R., and T.M. Joyce, Observations of interaction between the internal wavefield and low-frequency flows in the North Atlantic, J. Phys. Oceanogr., 9, 498-517, 1979.

Sabinin, K.D., and V.A. Shulepov, Spatial characteristics of the semidiurnal internal tides in the hydrophysical test range-70, Oceanology, 18, 253-256, 1978.

Sabinin, K.D., and V.A. Shulepov, Model of the frequency spectrum of internal waves in the ocean, Atmos. Ocean Phys., 17, 48-54, 1981.

Segur, H., and J.L. Hammack, Soliton models of long internal waves, J. Fluid Mech., 118, 285-304, 1982.

Shaub, Ya.B., and V.N. Demenok, Measurement of internal waves with an electrical-contact device, Oceanology, 18, 95-98, 1978.

Simpson, J.J., and C.A. Paulson, Observations of upper ocean temperature and salinity structure during the POLE experiment, J. Phys. Oceanogr., 9, 869-884, 1979.

Sokolov, V.A., L.M. Fomin and A.D. Yampol'skiy, On the linear mechanism of internal wave spectrum generation in the ocean, Atmos. Ocean Phys., 16, 735-738, 1981.

Spiesberger, J.L., and P.F. Worcester, Fluctuations of resolved acoustic multipaths at long range in the ocean, J. Acoust. Soc. Am., 70, 565-576, 1981.

Spigel, R.H., Coupling of internal wave motion with entrainment at the density interface of a two-layer lake, J. Phys. Oceanogr., 10, 144-155, 1980.

Stigebrandt, A., Observational evidence for vertical diffusion driven by internal waves of tidal origin in the Oslofjord, J. Phys. Oceanogr., 9, 435-441, 1979.

Sturova, I.V., Internal waves generated by local perturbations in a two-layer stratified liquid, Atmos. Ocean Phys., 15, 865-869, 1979.

Sturova, I.V., and V.A. Sukharev, Generation of internal waves by local disturbances in a fluid with a specified vertical density profile, Atmos. Ocean Phys., 17, 457-461, 1981.

Suvorov, A.M., A.S. Tananayev and L.V. Cherkesov, Development of three-dimensional internal waves in a fluid flow with velocity shear, Atmos. Ocean Phys., 16, 438-441, 1981.

Teodorovich, E.V., and V.A. Gorodtsov, On some singular solutions of internal wave equations, Atmos. Ocean Phys., 16, 551-553, 1981.

Thompson, R.O.R.Y., Efficiency of conversion of kinetic energy to potential energy by a breaking internal gravity wave, J. Geophys. Res., 85, 6631-6635, 1980.

Thomson, R.E., and W.S. Huggett, M2 baroclinic tides in Johnstone Strait, British Columbia, J. Phys. Oceanogr., 10, 1509-1539, 1980.

Thorpe, S.A., The excitation, dissipation, and interaction of internal waves in the deep ocean, J. Geophys. Res., 80, 328-338, 1975.

Thorpe, S.A., An experimental study of critical layers, J. Fluid Mech., 103, 321-344, 1981.

Torgrimson, G.M., and B.M. Hickey, Barotropic and baroclinic tides over the continental slope and shelf off Oregon, J. Phys. Oceanogr., 9, 945-961, 1979.

Unni, S., and C. Kaufman, Spectrum of intensity fluctuations in the internal wave frequency range, J. Acoust. Soc. Am., 67, 1384-1385, 1980.

Unni, S., and C. Kaufman, Acoustic fluctuations due to the temperature finestructure of the ocean, J. Acoust. Soc. Am., 69, 676-680, 1981.

Uscinski, B.J., Parabolic moment equations and acoustic propagation through internal waves, Proc. Roy. Soc. Lond., A372, 117-148, 1980.

van Duin, C.A., and H. Kelder, Reflection properties of internal gravity waves incident upon a hyperbolic tangent shear layer, J. Fluid Mech., 120, 505-522, 1982.

Vesecky, J.F., and R.H. Stewart, The observation of ocean surface phenomena using imagery from the SEASAT synthetic aperture radar: an assessment, J. Geophys. Res., 87, 3397-3430, 1982.

Volkov, Yu.A., and Yu.M. Kuftarkov, Thermal effect of internal gravity waves on the free surface of the ocean, Atmos. Ocean Phys., 16, 795-798, 1981.

Voronovich, A.G., Hamiltonian formalism for internal waves in the ocean, Atmos. Ocean Phys., 15, 52-57, 1979.

Watson, J.G., W.L. Siegmann and M.J. Jacobson, Consistent environmental acoustics: application to stochastic internal-wave models, J. Acoust. Soc. Am., 67, 1207-1221, 1980.

Watson, K.M., Internal wave transport at high vertical wavenumbers: the elastic scattering mechanism, in Nonlinear Properties of Internal Waves, edited by B.J. West, AIP conference proceedings No. 76, Amer. Inst. Phys., New York, 201-216, 1981.

Watson, K.M., B.J. West and B.I. Cohen, Coupling of surface and internal gravity waves: a mode coupling model, J. Fluid Mech., 77, 185-208, 1976.

Weller, R.A., The relation of near-inertial motions observed in the mixed layer during the JASIN (1978) experiment to the local wind stress and to the quasi-geostrophic flow field, J. Phys. Oceanogr., 12, 1122-1136, 1982.

Weller, R.A., and D. Halpern, The velocity structure of the upper ocean in the presence of surface forcing and mesoscale oceanic eddies, Phil. Trans. R. Soc. Lond. A, in press, 1983.

West, B.J., editor, Nonlinear Properties of Internal Waves, AIP conference proceedings No. 76, Amer. Inst. Phys., New York, 351pp., 1981.

Wilson, H.L., and F.D. Tappert, Acoustic propagation in random oceans using the radiation transport equation, J. Acoust. Soc. Am., 66, 256-274, 1979.

Winant, C.D., and A.W. Bratkovich, Temperature and currents on the Southern California shelf: a description of the variability, J. Phys. Oceanogr., 11, 71-86, 1981.

Woods, J.D., Do waves limit turbulent diffusion in the ocean?, Nature, 288, 219-224, 1980.

Worcester, P.F., Reciprocal acoustic transmission in a midocean environment: fluctuations, J. Acoust. Soc. Am., 66, 1173-1181, 1979.

Worcester, P.F., G.O. Williams and S.M. Flatte, Fluctuations of resolved acoustic multipaths at short range in the ocean, J. Acoust. Soc. Am., 70, 825-840, 1981.

Wunsch, C., Deep ocean internal waves: what do we really know?, J. Geophys. Res., 80, 339-343, 1975a.

Wunsch, C., Internal tides in the ocean, Rev. Geophys. Space Phys., 13, 167-182, 1975b.

Wunsch, C., Geographical variability of the internal wave field: a search for sources and sinks, J. Phys. Oceanogr., 6, 471-485, 1976.

Wunsch, C., and S. Webb, The climatology of deep ocean internal waves, J. Phys. Oceanogr., 9, 235-243, 1979.

Yermakov, S.A., Ye.N. Pelinovskiy and T.G. Talipova, Influence of surface films on changes in wind-wave spectra under the action of internal waves, Atmos. Ocean Phys., 16, 788-794, 1981.

Young, W.R., P.B. Rhines and C.J.R. Garrett, Shear-flow dispersion, internal waves and horizontal mixing in the ocean, J. Phys. Oceanogr., 12, 515-527, 1982.

Zaytsev, A.A., Induced long waves in a rotating stratified fluid layer, Oceanology, 20, 5-7, 1980.

(Received October 18, 1982;
accepted January 13, 1983.)

Mesopelagic Fish Faunal Regions of the Northeast Pacific

J. Marcus Willis

School of Oceanography
Oregon State University
Corvallis, Oregon

Abstract Fishes from 57 Isaacs-Kidd midwater trawl collections were identified and analyzed to determine the characteristics and limits of faunal regions in the Northeast Pacific Ocean. Cluster analyses of station and species groups showed three faunal regions: (1) Subarctic, the region north of the Subarctic front; (2) Central, the region south of the Subarctic front and north of the north equatorial front; and (3) Southern, the region near the Hawaiian Islands south of the north equatorial front. Temperature-salinity data show that the geographical limits of the fish faunal regions correspond with most physical boundaries. No association was found between the subtropical front and a faunal boundary. A brief review of plankton studies in the Northeast Pacific shows that the subtropical front may be an important boundary for microplankton groups. Gradients of change in fish species composition appeared steeper and concordance in species rank order seemed lower in Central than in Subarctic waters.

Introduction

The currents, water masses, fronts, and gyres in the North Pacific delineate environments, or habitats, with different physical, chemical, and biological characteristics (Sverdrup, Johnson,

Biological Oceanography, Volume 3, Number 2
0196-5581/84/010167-00$02.00/0

and Fleming, 1942; Reid, 1962; Roden, 1970; McGowan and Williams, 1973; Reid et al., 1978). Distribution patterns and oceanic communities of plankton animals and plants have the same spatial extent as these oceanic habitats (e.g., Johnson and Brinton, 1963; Fager and McGowan, 1963; McGowan, 1971; Reid et al., 1978). Although studies of nektonic groups are not as numerous as those of plankton, there are similar associations with water masses (e.g., Haffner, 1952; Parin, 1961; Aron, 1962; King and Iversen, 1962; Barnett, 1975; Wormuth, 1976; Jahn and Backus, 1976). Most zoogeographic studies of fishes concern particular families as part of systematic work (e.g., Ebeling, 1962; R. K. Johnson, 1974), or they consider commercially important species (e.g., Laurs and Lynn, 1977). Few have considered assemblages of mesopelagic fishes or the faunal transitions as related to physical structure of the North Pacific.

In this paper, I will present data on faunal regions of mesopelagic fishes in the Northeast Pacific and relate those regions to physical oceanographic features. I will also discuss the subtropical front as a zoogeographical barrier.

Materials and Methods

Between February 1965 and February 1980, fishes were collected on four cruises made in the Northeast Pacific Ocean (Figure 1). These included three long cruise tracks across the Subarctic boundary at various places (YALOC, WELOC, SICSPAC) and one to a restricted area of the Central gyre (FRONTS). Table 1 summarizes the data, types of gear used, depths sampled, and number of tows taken on these four cruises. All 57 tows were made in the upper 200 m at night, and each lasted about 60 minutes. Thus the following analysis applies primarily to the vertically migrating mesopelagic species. All samples were preserved at sea in 10% Formalin in seawater and returned to the laboratory for analysis.

For the analysis of similarity between stations, only those species occurring in more than one tow were included (83 out of 124 species). Similarity between stations was calculated using the presence-absence index proposed by Ochiai (1957): similar-

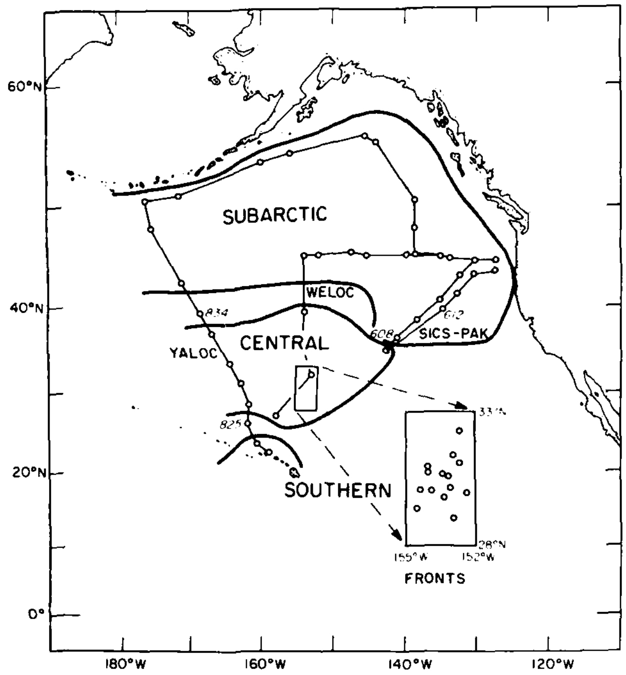

FIGURE 1. Boundaries of the three station groups in the Northeast Pacific Station groups are based on nearest-neighbor grouping of the stations. Values of the Ochiai index ≥0.500 determined the groups.

Table 1

Summary of cruises on which mesopelagic fishes were collected for this study. Trawl locations for each cruise are shown in Figure 1.

Cruise	Dates	Gear (IKMT)	Depths Sampled	Number of Tows
SICS-PAC	22 Feb–10 Mar 1965	1.8 m and 3 m	0–200 m	11
YALOC	30 May–27 July 1966	1.8 m	0–200 m	21
WELOC	10 Aug–27 Aug 1976	1.8 m	0–50 m, 0–200 m	11
FRONTS	15 Jan–16 Feb 1980	3 m	0–200 m	14

ity = $J/\sqrt{AB}$, where J = the number of species in common between the two samples under consideration and A and B are the numbers of species in each of the two samples being compared. An evaluation of the Ochiai index and other presence-absence similarity indices can be found in Hubalek (1982). Stations were grouped by a nearest-neighbor strategy, and a similarity level of 0.500 or higher determined station groups.

The Ochiai index was also used to group the species. Again, a nearest-neighbor strategy was used, a similarity level of 0.500 determined species groups, and only species occurring in more than one sample were included. Based on the species present in each group and their distributions, species groups were named according to their locations (Subarctic, Central, "southern"). Not all species were included in these three groups. Some rare species did not occur often enough with others to be included in any species group.

Hydrographic data are available for SICS-PAC (Wyatt et al., 1967), YALOC (Barstow et al., 1968), and FRONTS (University of Washington, 1980). No hydrographic data were taken during WELOC. Data for the upper 1,500 m were used to draw temperature-salinity (T-S) curves for each tow. Temperature-salinity envelopes were then constructed for each station group using the extreme curves for each group. The curves and envelopes were plotted to depths much greater than depths of tows in order to include the range of vertical migration of the species considered and also to identify the salinity minimum in deep water characteristic of North Pacific intermediate water (Reid, 1965), an important physical feature of the Central North Pacific.

Results

Two large station groups, representing the two major faunal provinces in the Northeast Pacific, and one smaller group were determined by the station similarity analysis (Figure 1). The larger station groups, Subarctic and Central, represent the faunas of the Eastern Subarctic and Central North Pacific, respectively. Their boundaries agree well with those of planktonic groups (e.g., Brinton, 1962; Fager and McGowan, 1963; McGowan, 1971).

Temperature-salinity relationships (Figure 2) indicate that the Central and Subarctic tows were from waters of different physical character. In general, Subarctic stations had low surface temperatures and salinity minima at the surface. Temperature inversions were common. Central stations, on the other hand, had higher surface temperatures and salinities, with salinity minima at depths of 400–600 m. No temperature inversions were noted.

The boundary between the Central and Subarctic groups was well correlated with the Subarctic front (34‰ surface salinity), which was observed just north of station 834 (Figure 1) along the YALOC transect (Figure 3) and near the southwest end of the SICS-PAC transect. Faunal changes at the Subarctic front along the YALOC transect were associated with steep gradients of salinity, temperature (Figure 3), chlorophyll *a* (Park, Curl, and Glooshenko, 1967), various chemical properties (Park, 1967), sound scattering layers, and animal biomass (Donaldson and Pearcy, 1972). The "transition zone" endemic fauna found in previous studies was not identified in these samples, possibly because of the small number of endemic "transitional" fish species or because the ranges of these "transitional" species overlap broadly with those of Subarctic species (Parin, 1961).

The Subarctic and Central station groups had very different species compositions (Table 2). The Subarctic group was strongly dominated numerically by *Stenobrachius leucopsarus*, which comprised nearly 50% of the individuals captured in this region. The Central group was weakly dominated by *Ceratoscopelus warmingi* (19.7%), and the top six species total 50% of the individuals captured. A total of 39 species were captured in two or more Subarctic tows, while 65 species were captured in two or more Central tows. The number of tows was comparable in the two station groups (29 Subarctic, 24 Central). Thus there are differences in species equitability and species richness between these two regions.

The Central station group included tows taken in several

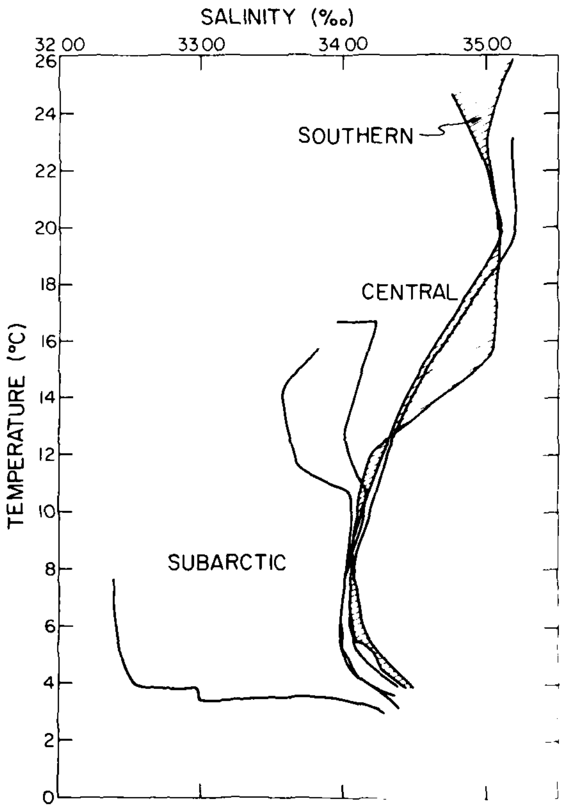

FIGURE 2. Temperature-salinity (T-S) envelopes for the three station groups shown in Figure 1. The shaded envelope is that for the "southern" station group. Envelopes are for the 0–1,500 m depth interval.

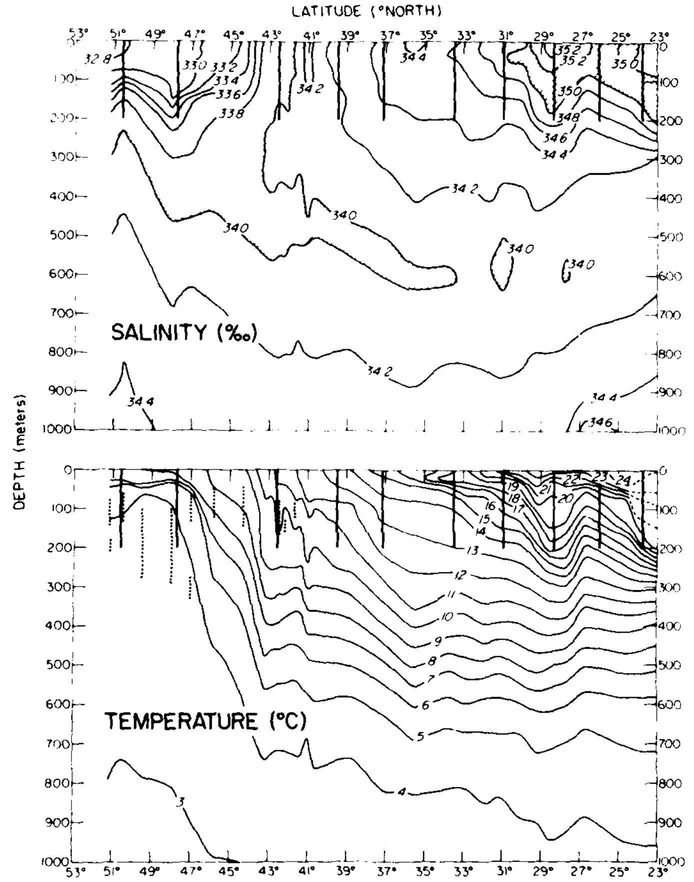

FIGURE 3. Salinity (upper) and temperature (lower) sections for the Hawaii to Aleutian leg of YALOC (see Figure 1). Section was occupied 31 May–24 June 1966. Vertical dotted lines indicate temperature inversions associated with subarctic water. Bars originating at the surface represent tow locations. There were several hydrographic stations between tows.

Table 2

Rank order of abundance of the ten most abundant species (numerically) in each station group and in the two ungrouped tows. Percentage of total number of individuals captured are given in parentheses.

Subarctic
Stenobrachius leucopsarus (46.8)
Diaphus theta (12.9)
Cyclothone pseudopallida (7.4)
Lampanyctus ritteri (4.9)
Tactostoma macropus (4.0)
Bathylagus ochotensis (3.8)
Tarletonbeania crenularis (3.5)
Ceratoscopelus townsendi (2.1)
Protomyctophum crockeri (1.5)
Protomyctophum thompsoni (1.5)

Central
Ceratoscopelus warmingi (19.7)
Notolychnus valdiviae (6.6)
Diogenichthys atlanticus (5.6)
Vinciquerria poweriae (5.3)
Bathylagus ochotensis (4.9)
Lampanyctus "no pectorals" (4.5)
Lampanyctus tenuiformis/festivus (4.3)
Diaphus anderseni (4.2)
Triphoturus nigrescens (4.0)
Melamphaes simus? (3.9)

"Southern"
Diaphus schmidti (13.7)
Notolychus valdiviae (11.8)
Vinciquerria nimbaria (11.8)
Benthosema suborbitale (11.8)
Vinciguerria poweriae (9.8)
Ceratoscopelus warmingii (7.8)
Hygophum proximum (7.8)
Gonostoma ebelingi (7.8)
Melamphaes simus? (3.9)
Lampanyctus nobilis (3.9)

Station 834
Diaphus fulgens (50.0)
Lestidium sp. (13.3)
Argyropelecus sladeni (10.0)
Melamphaes simus? (10.0)
Vinciguerria nimbaria (6.7)
Cololabis saira (3.3)
Nemichthys scolopaceus (3.3)
Electrona rissoi (3.3)

Station 825
Vinciquerria poweriae (31.2)
Melamphaes simus? (12.5)
Lampanyctus tenuiformis/festivus (12.5)
Ceratoscopelus warmingii (6.2)
Bolinichthys longipes (6.2)
Lampanyctus nobilis (6.2)
Hygophum proximum (6.2)
Bregmaceros sp. (6.2)
Triphoturus nigrescens (6.2)
Gonostoma elongatum (6.2)

months in different years (cf. Table 1, Figure 1), indicating a lack of seasonal and yearly variation in species composition in this area (mean Ochiai similarity = 0.472, range = 0.073–0.778), as shown by previous investigators (Barnett, 1975; McGowan, 1977; Loeb, 1979; McGowan and Walker, 1980). Within the area sampled during FRONTS (Figure 1), the mesopelagic fish fauna was relatively homogeneous in composition on scales of 10 to 200 km (FRONTS mean similarity = 0.661, range = 0.400–0.778). It appears from these data, as well as those presented by McGowan (1977), that variations in species composition in this area are on scales greater than 200 km. The Subarctic station group also included tows made in different years and seasons, but species composition was more variable than in Central waters (mean similarity = 0.406, range = 0.0–1.000).

The ungrouped station between the Subarctic and Central groups (station 834, Figure 1) contained primarily Central species, with some species which had ranges extending into both Subarctic and Central waters. Of the eight species captured at station 834, one was found only in the Subarctic group, three were found only in the Central group, and four were found in both groups. None of the species present at this station ranked higher than 10th in either the Subarctic or Central groups. Therefore, it does not appear to represent the endemic "transition zone" fauna. Although it contained mostly Central species, it did not group with the Central stations. The composition of this tow was different from the other Central tows. Certain Central species may have broader ranges than others and may thus be found in unusual combinations at the peripheries of this faunal region (Geynrikh, 1975).

Jahn and Backus (1976) studied fish faunal transitions across the Gulf Stream and found that shallower collections in the Gulf Stream axis grouped with the Sargasso Sea collections while deeper tows grouped with slope water collections. Likewise, the Sargasso Sea water overlies the slope water in the Gulf Stream. An analogous situation may pertain at the Subarctic front. In this region, Subarctic water (cold, low salinity) subsides beneath Central water (warm, high salinity) (Reid, 1965). This may explain the presence of primarily Central species in a shallow collection (station 834) in the Subarctic frontal region.

The two-station group near Hawaii ("southern," Figure 1) was apparently related to the northern boundary of the north equatorial current. This group was in a region of higher surface temperatures (>24°C) and lower surface salinities (<35‰) than the Central group (Figures 2 and 3). Chlorophyll *a* values were somewhat higher at the southern end of the YALOC transect than in Central waters (Park, Curl, and Glooshenko, 1967). The temperature and salinity front associated with this boundary occurred at about 26°N on the YALOC transect, extending from the surface to about 250 m (Figure 3). The usual situation in May and June is for surface temperatures to be 22–24°C and surface salinities to be greater than 35.2‰ (Seckel, 1968; Sverdrup, Johnson, and Fleming, 1942). The data of Figures 2 and 3 show that water of equatorial character was present north of Hawaii during the YALOC cruise. Similar northward intrusions of equatorial water in this area have been reported by Seckel (1968), Roden (1970), and Sverdrup, Johnson, and Fleming (1942).

This northward intrusion of warm, low-salinity water may have carried with it species of equatorial origin. Species composition of the "southern" tows was different from that of the Central group tows (Table 2). Of the 10 most abundant species in the "southern" group catches, only four were among the most abundant 10 in the Central group. The numerically dominant species in the "southern" area *(Diaphus schmidti)* was not captured in any Central group tow.

The ungrouped station at 26°N (station 825) was in the north equatorial boundary zone. Species composition of this tow was intermediate between the "southern" and Central groups (Table 2). Of the 10 species captured at station 825, five were among the top 10 Central species, and five were among the top 10 "southern" species. The north equatorial frontal zone appears to be a region of faunal mixing between species of central and Hawaiian or equatorial origin.

Contours of species groups as determined by the species similarity analysis were similar to the boundaries of the station groups (Figure 4). Two large species groups (Central and Subarctic) and one smaller one ("southern") were found at a similar-

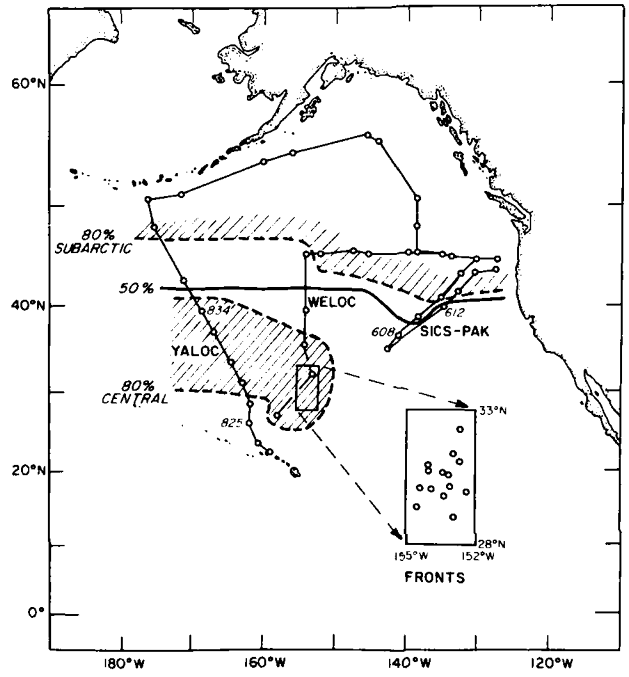

FIGURE 4. Boundaries of the mesopelagic fish faunal regions in the Northeast Pacific. Lines are contours of percentage of fish species captured which belonged to either the Subarctic or Central species group. Solid line represents the 50% contour; dashed lines and shading represent the 80% regions.

ity level of 0.500. No "transitional" species group was found in these samples. The contours in Figure 4 outline the areas where 50% or 80% of the species captured belonged to either the Subarctic or Central species groups. The shaded (80%) areas in Figure 4 can be considered as the "cores" of the faunal provinces and agree well with the regions outlined by McGowan (1974). As indicated above for station groups, intrusion of equatorial-type water from the south is probably responsible for the Hawaiian Islands area being excluded from the 80% Central region in this data. Station 834, which was ungrouped in the station similarity analysis (see above), was included in the 80% Central region in Figure 4. This lends further support to the conclusion that the fauna sampled at this station was primarily Central in character.

To investigate the spatial variability in species composition in the Subarctic and Central station groups, product-moment correlation coefficients between similarity value and distance were calculated. The two data sets (Subarctic and Central) were further broken down into north-south and east-west station pairs based on station compass bearings to one another. Thus each similarity value has an associated compass bearing and distance. The resulting correlations give a measure of the steepness of the gradients of change in species composition (Haury, 1976). All correlations were significant ($p < 0.01$). Overall correlations were significantly different at the 0.01 level (within Subarctic $r = -0.371$, within Central $r = -0.764$). North-south and east-west correlations likewise showed differences at the 0.01 level between Subarctic and Central groups (north-south: Subarctic $r = -0.581$, Central $r = -0.827$; east-west: Subarctic $r = -0.473$, Central $r = -0.783$).

A further comparison of variability may be made by testing for concordance in species ranks by cruise within each station group. In the present data, it is not possible to separate spatial and temporal variability, so in the subsequent discussion, "coherence" refers to both spatial and temporal coherence. Rank concordance tests (Tate and Clelland, 1957) were performed on the three cruises in each station group (the single SICS-PAC station in the Central group, station 609 in Figure 1, was not included) to test for coherence in species rankings in space and time. Concordance was significant for Subarctic cruises ($W = 0.615$, $p < 0.025$) but was not significant for the Central tows ($W = 0.395$, $p > 0.25$). This suggests that rank order of abundance of fish species is more stable, in space and time, in Subarctic than in Central waters. Again, the data may be biased by the collection scheme, particularly by the relatively large number of 3-m IKMT tows from the FRONTS area.

Discussion

The results presented above for concordance of species ranks and the correlations between similarity and geographic distance seem contrary to those presented by McGowan (1977) and McGowan and Williams (1973). In these papers, as well as others, the Subarctic is considered a more variable environment than the Central gyre. The correlations presented above indicate that gradients of change in species composition are steeper in Central-gyre waters than in Subarctic waters. There are at least two possible explanations for this: (1) The Central tows may be biased by the relatively large number of tows from the restricted FRONTS region, or (2) the Subarctic tows cover most of the eastern Subarctic Pacific, whereas the Central tows are from near the periphery of the Central gyre, where gradients of change might be steeper. This second possibility may explain the higher east-west correlation in the Central than in the Subarctic group.

These results further suggest that studies of variations in species composition on scales greater than 200 km may be needed before any confidence can be placed in extrapolations from site-oriented studies. Recent physical studies of the Central North Pacific have revealed greater spatial and temporal variations in properties than was previously thought (e.g., Bernstein and White, 1974; White, 1977; Roden and Paskausky, 1978; Roden, 1980a).

Barnett (1975) noted the presence of species of equatorial origin near the Hawaiian Islands and attributed it to the higher productivity in this area relative to the rest of the North Pacific Central gyre. This higher productivity may also account for the differences in species composition observed at the southern end of the YALOC transect. Further evidence for a unique combination of species around Hawaii comes from a comparison of the myctophid and stomiatoid species reported by Clarke (1973, 1974) with those reported by Barnett (1975) from the Northeast Central and Equatorial Pacific. These two studies are more comparable in spatial and temporal coverage than the present data are to either. Of the 90 species reported by Clarke (1973, 1974), 18 were not listed by Barnett (1975), and five were listed by Barnett but not captured by him in the Northeast Central or Equatorial Pacific. Of the remaining 67 species, 45 either were captured by Barnett only in the Northeast Central Pacific or were ranked higher there than in the Equatorial samples, and 22 species either were captured only in the Equatorial samples or were ranked higher in the Equatorial than in the Northeast Central samples. From this comparison, there appear to be significant Equatorial elements in the mesopelagic fish fauna of the Hawaiian Islands region. The geographic limits of this fauna and the associated physical structure merit further study.

The relationship of faunal boundaries to oceanic fronts was clear in some cases but did not hold in others. Station-group boundaries along the SICS-PAC and YALOC cruise tracks were related to the Subarctic boundary (as indicated by 34‰ surface salinity) at about 40°N in the central Subarctic (YALOC, Figure 3) and at about 35°N in the California Current region (SICS-PAC). Another station-group boundary occurred at the northern boundary of the north equatorial current at the southern end of the YALOC transect. The subtropical front (as indicated by 35‰ surface salinity) occurred at about 30°N on the YALOC transect (Figure 2) and also ran roughly along 31°N through the area sampled during FRONTS (Roden, 1981). On neither of these cruises, nor on WELOC, was a fish faunal boundary detected which could be related to the subtropical front. The subtropical front varies on scales of tens of km and 1–2 weeks, and it changes its character seasonally (Roden, 1975, 1980a, 1980b). The front is coupled on long time scales to the convergence of Ekman transports in this region. On shorter time scales, the position and nature of the front are influenced by local, fast-moving atmospheric systems (Roden, 1980b). The front may be single or multiple, depending on the frequency and intensity of these atmospheric disturbances. In addition, the front is an upper ocean feature, rarely extending below 200 m, even in winter when the thermocline is deep (Roden, 1981). These characteristics of the subtropical front may make it an ineffective zoogeographical barrier to micronektonic fishes, particularly for vertically migrating species which would be influenced by the front only at night.

Since planktonic organisms are more dependent on the movement of water for their own movements than fishes, does the subtropical front affect the distributions of planktonic organisms? This question has not been directly addressed by plankton biogeographers for the North Pacific, but some large-scale studies of meridional plankton distributions have been made. Most of these studies have included the taking of temperature and salinity data, so that the distributions presented can be correlated with physical features.

Shaw and Mapes (1979) identified convergent zones along a transect at 158°W from 56°N to 22°N and found peaks in surface-collected tar and plastic at these convergences. One of these (near 32°N) is probably the subtropical front, which is also a convergence (Roden, 1981). Therefore, planktonic or neustonic organisms, which might be carried in a similar manner, may also be aggregated at the subtropical front. Honjo and Okada (1974) presented data on abundance and species richness of coccolithophores along a transect at 155°W from 50°N to 15°S. They took samples within the upper 200 m. The highest diversity along this transect was found in subsurface waters (40 m) at 30°N, near the subtropical front (Marumo, 1970, his Figure 3). They also found that coccosphere abundance was higher in subsurface than in surface waters in the region of the subtropical front.

Distributional sections along 155°W for coccolithophores (Okada and Honjo, 1973; Honjo and Okada, 1974) and radiolarians (Kling, 1976) show some species which appear to have northern or southern limits associated with the subtropical front. Those radiolarians with northern boundaries near the subtropical front were called "Central water mass species" by Kling (1976). The "Salinity maximum zone species" of Kling (1976) were those associated with the shallower waters between the subarctic and subtropical fronts (transition zone of Roden, 1970). Honjo and Okada (1974) show changes in species composition in the area of the subtropical front. The data presented in these studies suggests that the subtropical front may be a biogeographic feature of importance, at least for these microplanktonic groups, in the North Pacific Central gyre. It apparently has no effect on fish distributions in the gyre.

Venrick (1971) studied distribution patterns of diatoms on meridional transects at 155°W from Hawaii to Alaska. She found distinct Subarctic, Transitional, and Central species groups but no boundaries which were related to the subtropical front.

In conclusion, I have presented data which indicate that (1) zoogeographical regions for fishes in the Northeast Pacific agree well with those published for planktonic groups; (2) the limits of the zoogeographical regions are correlated with observed temperature and salinity fronts; (3) there appear to be significant differences between the Hawaiian Islands area and the Central gyre in fish species composition, probably in part because of equatorial elements in the Hawaiian fauna; (4) scales of variation in fish species composition in the Central gyre are greater than 200 km; and (5) although the data may be biased, species rank concordance in space and time appears lower and gradients of change in species composition appear steeper in Central than in Subarctic regions. This final result suggests that studies of species composition and community structure on scales greater than 200 km are needed before the results of the many site-oriented studies can be used to generalize processes in the entire Central gyre system.

Acknowledgments

The author wishes to thank W. G. Pearcy for patient support during this work. R. D. Brodeur, J. Kern, P. Scott, K. Walters, and especially C. B. Miller provided helpful comments. I enjoyed fruitful discussions with K. Walters and E. W. Hogue. D. L. Stein, B. Zahuranec, and K. Kawaguchi assisted with taxonomic problems. G. Roden assisted with interpretation of the YALOC hydrographic section. Samples were collected from the research vessels *Wecoma*, *Yaquina*, and *Thomas Washington* by D. L. Stein, H. Donaldson, L. R. Coleman, and the author. The assistance of the scientists and crews of the vessels is most appreciated. Collection was supported by the National Science Foundation, the Atomic Energy Commission, and the Office of Naval Research. Final writing support was provided by the Office of Naval Research through contract N00014-79-C-0004, under project NR083-102.

References

Aron, W., 1962. The distribution of animals in the eastern North Pacific and its relation to physical and chemical conditions. J. Fish. Res. Board Can. 19: 271–314.

Barnett, M. A., 1975. Studies on the patterns of distribution of mesopelagic fish faunal assemblages in the central Pacific and their temporal persistence in the gyres. Ph.D. thesis, University of California, San Diego. 145 pp.

Barstow, D., W. Gilbert, K. Park, R. Still, and B. Wyatt, 1968. Hydrographic data from Oregon waters,1966. Oregon State University, Department of Oceanography, Reference 68–34, Data Report 33. Corvallis. 109 pp.

Bernstein, R. L., and W. B. White, 1974. Time and length scales of baroclinic eddies in the Central North Pacific Ocean. J. Phys. Oceanogr. 4: 613–624.

Brinton, E., 1962. The distribution of Pacific euphausiids. Bull. Scripps Inst. Oceanogr. 8: 51–270.

Clarke, T. A., 1973. Some aspects of the ecology of lanternfishes (Myctophidae) in the Pacific Ocean near Hawaii. Fish. Bull., U.S. 71: 401–434.

Clarke, T. A., 1974. Some aspects of the ecology of stomiatoid fishes in the Pacific Ocean near Hawaii. Fish. Bull., U.S. 72: 337–351.

Donaldson, H. A., and W. G. Pearcy, 1972. Sound scattering layers in the northeast Pacific. J. Fish. Res. Board Can. 29: 1419–1423.

Ebeling, A. W., 1962. Melamphaeidae. I. Systematics and zoogeography of the species in the bathypelagic fish genus *Melamphaes* Gunther. Dana Rep. Carlsberg Found. 58: 1–64.

Fager, E. W., and J. A. McGowan, 1963. Zooplankton species groups in the North Pacific. Science 140: 453–460.

Geynrikh, A. K., 1975. Boundaries of the oceanic plankton communities. Okeanologiya 15:1097–1100 (in Russian, translation by the American Geophysical Union, Washington, D.C.).

Haffner, R. E., 1952. Zoogeography of the bathypelagic fish *Chauliodus*. Syst. Zool. 1: 112–133.

Haury, L. R., 1976. Small-scale pattern of a California Current zooplankton assemblage. Mar. Biol. 37: 137–157.

Honjo, S., and H. Okada, 1974. Community structure of coccolithophores in the photic layer of the mid-Pacific. Micropaleontology 20: 209–230.

Hubalek, S., 1982. Coefficients of association and similarity, based on binary (presence-absence) data: An evaluation. Biol. Rev. 57: 669–689.

Jahn, A. E., and R. H. Backus, 1976. On the mesopelagic fish fauna of slope water, Gulf Stream, and northern Sargasso Sea. Deep-Sea Res. 34: 223–234.

Johnson, M. W., and E. Brinton, 1963. Biological species, water masses and currents. In: M. N. Hill (ed.), The Sea. Interscience Publ., New York, 2: 381–414.

Johnson, R. K., 1974. A revision of the alepisauroid family Scopelarchidae (Pisces, Myctophiformes). Fieldiana Zool. 66: 1–249.

King, J. E., and R. T. B. Iversen, 1962. Midwater trawling for forage organisms in the Central Pacific 1951–1956. Fish. Bull., U.S. 62: 271–321.

Kling, S. A., 1976. Relation of radiolarian distributions to subsurface hydrography in the North Pacific. Deep-Sea Res. 23: 1043–1058.

Laurs, R. M., and R. J. Lynn, 1977. Seasonal migration of North Pacific albacore, *Thunnus alalunga*, into North American coastal waters: Distribution, relative abundance, and association with Transition zone waters. Fish. Bull., U.S. 75: 795–822.

Loeb, V. J., 1979. Larval fishes in the zooplankton community of the North Pacific central gyre. Mar. Biol. 53: 173–191.

Marumo, R. (ed.), 1970. Preliminary report of the *Hakuho-Maru* cruise KH-69-4. Ocean Research Institute, University of Toyko, 1–68.

McGowan, J. A., 1971. Oceanic biogeography of the Pacific. In: B. H. Funnel and W. R. Riedel (eds.), The Micropaleontology of the Oceans. Cambridge University Press, Cambridge: 3–74.

McGowan, J. A., 1974. The nature of oceanic ecosystems In: C. B. Miller (ed.), Biology of the Oceanic Pacific. Oregon State University Press, Corvallis: 9–28.

McGowan, J. A., 1977. What regulates pelagic community structure in the Pacific? In: N. R. Andersen and B. J. Zahuranec (eds.), Oceanic Sound Scattering Prediction. Plenum Press, New York: 423–443.

McGowan, J. A., and P. W. Walker, 1980. Structure in the copepod community of the North Pacific Central gyre. Ecol. Monogr. 49: 195–226.

McGowan, J. A., and P. M. Williams, 1973. Oceanic habitat differences in the North Pacific. J. Exp. Mar. Biol. Ecol. 12: 187–217.

Ochiai, A., 1967. Zoogeographic studies of the soleid fishes found in Japan and its neighboring regions. Bull. Jpn. Soc. Sci. Fish. 22: 526–5[illegible].

Okada, H., and S. J. Honjo, 1973. The distribution of oceanic coccolithophores in the Pacific. Deep-Sea Res. 20: 355–374.

Parin, N. V., 1961. The distributions of deep-sea fishes in the upper bathypelagic layer of the Subarctic waters of the northern Pacific Ocean. Tr. Inst. Okeanol. Akad. Nauk SSSR 45: 359–378 (in Russian, translation by Bureau of Commercial Fisheries).

Park, K., 1967. Chemical features of the Subarctic Boundary near 170°W. J. Fish. Res. Board Can. 24(5): 899–908.

Park, K., H. C. Curl, Jr., and W. A. Glooshenko, 1967. Large surface carbon dioxide anomalies in the North Pacific Ocean. Nature 215(5099): 380–381.

Reid, J. L., Jr., 1962. On circulation, phosphate-phosphorous content and zooplankton volumes in the upper part of the Pacific Ocean. Limnol. Oceanogr. 7: 287–306.

Reid, J. L., Jr., 1965. Intermediate waters of the Pacific Ocean. Johns Hopkins Oceanogr. Stud. 2: 1–85.

Reid, J. L., Jr., E. Brinton, A. Fleminger, E. L. Venrick, and J. A. McGowan, 1978. Ocean circulation and marine life. In: H. Charnock and G. Deacon (eds.). Advances in Oceanography. Plenum Press, New York: 65–130.

Roden, G. I., 1970. Aspects of the mid-Pacific transition zone. J. Geophys. Res. 75: 1097–1109.

Roden, G. I., 1975. On North Pacific temperature, salinity, sound velocity and density fronts and their relation to the wind and energy flux fields. J. Phys. Oceanogr. 5: 557–571.

Roden, G. I., 1980a. On the variability of surface temperature fronts in the western Pacific, as detected by satellite. J. Geophys. Res. 85: 2704–2710.

Roden, G. I., 1980b. On the subtropical frontal zone north of Hawaii during winter. J. Phys. Oceanogr. 10: 342–362.

Roden, G. I., 1981. Mesoscale thermohaline, sound velocity and baroclinic flow structure of the Pacific subtropical front during the winter of 1980. J. Phys. Oceanogr. 11: 658–675.

Roden, G. I., and D. F. Paskausky, 1978. Estimation of rates of frontogenesis and frontolysis in the North Pacific Ocean using satellite and surface meteorological data from January 1977. J. Geophys. Res. 83: 4545–4550.

Seckel, G. R., 1968. A time-sequence oceanographic investigation in the North Pacific trade-wind zone. Trans. Am. Geophys. Union 49: 377–387.

Shaw, D. G., and G. A. Mapes, 1979. Surface circulation and the distribution of pelagic tar and plastic. Mar. Pollut. Bull. 10: 160–162.

Sverdrup, H. V., M. W. Johnson, and R. H. Fleming, 1942. The Oceans. Prentice-Hall, New York. 1,087 pp.

Tate, M. W., and R. C. Clelland, 1957. Nonparametric and shortcut statistics in the social, biological, and medical sciences. Interstate Printers and Publishers, Danville, Ill. 171 pp.

University of Washington, Department of Oceanography, 1980. FRONTS Expedition CTD data report, 15 January–16 February, 1980. Technical Report 384. University of California, San Diego. 300 pp.

Venrick, E. L., 1971. Recurrent groups of diatom species in the North Pacific. Ecology 52: 614–625.

White, W. B., 1977. Secular variability in the baroclinic structure of the interior North Pacific from 1950–1970. J. Mar. Res. 35: 587–607.

Wormuth, J. H., 1976. The biogeography and numerical taxonomy of the oegopsid squid family Ommastrephidae in the Pacific Ocean. Bull. Scripps Inst. Oceanogr. 23: 1–90.

Wyatt, B., R. Still, D. Barstow, and W. Gilbert, 1967. Hydrographic data from Oregon waters, 1965. Oregon State University, Department of Oceanography, Reference 67-28, Data Report 27. Corvallis. 56 pp.

Reprinted from JOURNAL OF PHYSICAL OCEANOGRAPHY, Vol. 14, No. 3, March 1984
American Meteorological Society
Printed in U. S. A.

The Energetics of Overturning Structures: Implications for the Theory of Fossil Turbulence

T. M. DILLON

School of Oceanography, Oregon State University, Corvallis, OR 97331

(Manuscript received 30 August 1982, in final form 21 November 1983)

ABSTRACT

A large number of oceanic and freshwater microstructure observations are analyzed to determine the energetic state of the turbulence. The total available energy and a time scale for dissipating the total energy are estimated. It is found that the time scale for dissipating the total energy in overturns is usually much shorter than the time scale for gravitational collapse found in laboratory studies. This implies that the energy being dissipated in an overturn could not be supplied fast enough to support the dissipation if gravitational collapse were the only source supplying the energy. Two criteria used in Gibson's theory of fossil turbulence for establishing the state of overturns are compared: a length scale (or available potential energy) criterion suggested by Gibson and tested in the laboratory by Stillinger and Gibson's "activity parameter" criterion. It is found that most overturns are "active" according to the available potential-energy criterion, but "fossil" according to the activity parameter criterion. A modification of the activity parameter is suggested to achieve agreement.

1. Introduction

Vertical overturns, regions of fluid containing small-scale density inversions, are a commonly observed feature of the ocean. Most microstructure observations consist of vertical or horizontal transects, and it is usually impossible to define the horizontal position of a typical overturning patch sufficiently well to sample it more than once. Even if a given patch could be sampled a second time, it would not be found in a pristine state, because the fluid would have been stirred during the first observation. Each observation must be treated as a single realization, a "snapshot," of a random process. Consequently, there is no way to directly determine the time evolution of overturns. Yet assumptions about the unobserved history and subsequent evolution of overturns play a crucial role for the interpretation of microstructure observations.

Several possible evolutionary scenarios can be imagined. The overturn may be growing and rapidly entraining fluid. It may be gravitationally decaying, with the kinetic energy of the internal motions supplied by the potential energy released by restabilization. An overturn may be in an approximate steady-state equilibrium with its environment. Gibson (1980, 1981a,b, 1982a,b,c) maintains that the kinetic-energy dissipation rates observed in the ocean are underestimates of the actual space–time averages, because almost all observed patches of turbulence in the ocean can be classified as "fossil turbulence," and that the dissipation rates were much larger when the patches were "active."

The purpose of this report is to compare the potential energy content of overturns with the rate of dissipation of kinetic and potential energy, and determine the relation between "fossil turbulence" and "gravitationally collapsing turbulence." Most of the observations presented below satisfy a fossil turbulence criterion. We will see whether or not the observations satisfy a "collapsing turbulence" criterion. The reasoning is by contradiction: it will first be assumed that the observed overturns are gravitationally collapsing, and that no turbulent energy is produced in the overturns; if a contradiction emerges, the assumption must be wrong. It is hoped that conclusions drawn from the analysis will lead to a better understanding of the fossil turbulence theory.

In Section 2, the potential energy content of an overturning patch is defined. In Section 3, the equations of motion are discussed. In Section 4, the potential energy content of overturning patches is compared to their rate of energy dissipation, and in Section 5, the theory of fossil turbulence is briefly discussed. In Section 6, some ideas from the theory of fossil turbulence are combined with ideas commonly held by a number of investigators (no claim of originality is made for this discussion), in an attempt to foster a synthesis of the theory of fossil turbulence and other common interpretations.

2. The potential energy of an overturn

Available potential energy (APE) can be defined as the energy which would be released if a density perturbation were returned to its equilibrium depth. This definition assumes implicitly a reference state for the system, i.e., a definition of "equilibrium depth." In some cases, a time-averaged density profile may be used as a reference state. This state is not very useful for studying the energetics of small-scale density inversions in a stably stratified ocean, because the largest contribution to the APE relative to the time-averaged density profile comes from internal wave displacements, not from the inversions themselves. A study of the potential energy content of small-scale density inversions must use a reference state which is independent of internal wave displacements.

The available potential energy of density inversions can be found using a Thorpe-ordered density profile (Thorpe, 1977; Dillon, 1982). We will assume that temperature and density fluctuations are proportional, $\rho'/\rho = -\alpha T'$, where ρ' is a density fluctuation, T' is a temperature fluctuation, and α is a coefficient of expansion, a function of salinity and temperature (Dillon, 1982). If temperature $T(z_n)$ is sampled at discrete depths z_n, a monotonic profile $T_0(z_n)$, called the Thorpe or ordered profile, can be formed using a simple bubble-sort algorithm (Dillon, 1982).

The Thorpe profile has a unique physical meaning: it represents the state of lowest potential energy to which an observed profile can evolve without exchanging heat with the surrounding fluid. The profile $T_0(z_n)$ represents the state to which $T(z_n)$ would adiabatically collapse under the influence of gravitational forces; "adiabatic collapse" here means that no sample experiences heat transfer, although density and temperature may change slightly because water is not incompressible. If the mean temperature gradient is much greater than the adiabatic temperature gradient, compressibility can be ignored, but if the mean gradient is small, the potential temperature must be used.

A Thorpe-ordered density profile is a state of minimum potential energy, because if any two density samples from the ordered profile are exchanged, the potential energy change is zero if the two samples have identical density, or positive, if the sample densities differ. Because any arrangement of a finite number of density samples may be accomplished by a finite number of two-sample exchanges, and because molecular diffusion of heat cannot decrease the potential energy of a system, all states to which an observed state can evolve must have potential energy greater than that of the ordered profile, unless heat crosses the system boundary. It follows that when an isolated observed state evolves to some final state, the potential energy released must be less than or equal to the difference in potential energy of the observed state and the ordered state. Define the potential energy difference per unit mass as the available potential energy of the fluctuations, (APEF)

$$\mathrm{APEF} = \sum_{n=M_1}^{M_2} \alpha g z_n [T(z_n) - T_0(z_n)](M_2 - M_1)^{-1}. \quad (1)$$

Here, M_1 and M_2 are depth indices completely enclosing some complete overturn. The APEF is conceptually similar to the available potential energy, except that nonoverturning internal-wave potential energy is removed. The APEF is insensitive to the choice of M_1 and M_2 as long as the interval encloses complete overturns. By "complete overturn," we mean that no temperatures in the interval are found outside of the interval, and no temperatures outside of the interval are found inside.

Density overturns are three-dimensional features, but it is impossible to measure the density in three dimensions on the small scales demanded by a study of density fluctuations. Although a vertical density profile is only one random example of the many profiles that might be measured in a given overturn, the Thorpe profile resulting from that measurement may be the best estimate that can be realistically made of the reference state of an overturn.

3. Equations of motion

The velocity field in a volume of fluid may be formally decomposed into mean and fluctuating parts, $u = \langle u \rangle + u'$, the Reynolds decomposition, where $\langle\ \rangle$ is a volume average enclosing some overturning event. Gargett *et al.* (1981) have shown that the shear spectrum of internal waves extends to the length scale of overturns and that the oceanic velocity spectrum may be always red, with no spectral gap separating the microstructure and internal wave bands. In contrast to the APEF, a volume average of kinetic energy may not always separate turbulence and internal waves, because averaged quantities may depend on the averaging scale. Yet there is a clear, fundamental difference between the velocity field of internal waves and the velocity field of an overturning structure: a distinct change in the spectral slope of the vertical shear (Gargett *et al.*, 1981) occurs at a wavenumber closely related to the length scale characteristic of overturning intervals (Dillon, 1982).

The size of an overturning region provides a natural averaging scale since the break in spectral slope occurs at a wavenumber corresponding to the "size" of the overturning region. Although not strictly necessary, the Reynolds decomposition, with all its possible ambiguities, will be employed here because of its familiarity, using an averaging scale related to the patch size.

Conservation of energy for an overturn may be expressed as

$$\frac{1}{2}\left\langle \frac{\partial}{\partial t} u'_i u'_i \right\rangle = S - \epsilon - g\rho^{-1}\langle w'\rho' \rangle, \quad (2)$$

where $\langle\ \rangle$ is a volume average, u'_i is a velocity fluctuation, w' is explicitly a vertical velocity fluctuation, and ρ' a density fluctuation. The left side of (2) is the rate of change of the kinetic energy of the fluctuations;

S is the rate of supply of kinetic energy to the overturn due to i) shear production, ii) turbulent and mean advection and iii) pressure–velocity correlations (cf. Osborn, 1980; Dillon, 1982; or any standard turbulence text). It is often assumed that shear production is the dominant contributor to S, but no such restriction is needed here, and other possible sources and sinks of turbulent kinetic energy are included for the sake of completeness. The rate of dissipation of turbulent kinetic energy is ϵ, and $g\rho^{-1}\langle\rho' w'\rangle$ is the buoyancy flux.

In highly stratified regions of the sea, turbulence is usually intermittent, and regions containing overturns are surrounded by completely stable water. We will term such regions "overturning patches," or simply "patches." For the present, the discussion will be limited to overturning patches; later, the argument will be extended to surface mixing layers, where a clear-cut decomposition into overturning patches and completely stable fluid cannot be made.

The temperature equation for a fluid is

$$\frac{\partial T}{\partial t} = -u_i\frac{\partial T}{\partial x_i} + D\frac{\partial}{\partial x_i}\frac{\partial T}{\partial x_i}, \tag{3}$$

where u_i is the velocity, and D is the molecular diffusivity of temperature. Multiplying (3) by a temperature fluctuation T', integrating over a volume V having a surface Σ with unit normal vector $\mathbf{n}$, assuming that the rate of change of $\langle T\rangle$ is much less than the rate of change of T' and using the divergence theorem, yields the temperature variance equation

$$\int_V T'\frac{\partial T'}{\partial t}dv = -\int_V u_i T'\langle\partial T/\partial x_i\rangle dv - D\int_V \frac{\partial T'}{\partial x_i}\frac{\partial T'}{\partial x_i}dv + \int_\Sigma [T'^2\mathbf{u}\cdot\mathbf{n} + T'D(\nabla T')\cdot\mathbf{n}]d\sigma. \tag{4}$$

The last term on the right of (4) is a surface integral, and Σ completely encloses the overturning region. Strictly speaking, the surface integral is not necessarily zero, because we have defined the temperature fluctuations T' relative to the volume-averaged temperature $\langle T\rangle$, $T = \langle T\rangle + T'$. But this term will be small because on Σ there are no overturns. The second term on the right of (4) is proportional to the temperature variance dissipation rate χ_T

$$\chi_T = 2D\left\langle\frac{\partial T'}{\partial x_i}\frac{\partial T'}{\partial x_i}\right\rangle = 6D\left\langle\left(\frac{\partial T'}{\partial z}\right)^2\right\rangle \tag{5}$$

(the last equality is assigned by assuming isotropy on the small, dissipation-range scales).

The first term on the right of (4), a sum of one vertical and two horizontal components, is the rate at which temperature variance is created. The most important part of this term will be $\langle wT'\rangle\langle\partial T/\partial z\rangle$, because in the observations with which we are concerned, vertical temperature gradients are orders of magnitude larger than horizontal gradients. Because the only velocities we are concerned with are correlated with density fluctuations inside a patch, we can also write $w = w'$; then, dividing (4) by the volume and using (5) gives

$$\frac{1}{2}\left\langle\frac{\partial}{\partial t}(T'^2)\right\rangle = -\langle w'T'\rangle\langle\partial T/\partial z\rangle - \frac{1}{2}\chi_T. \tag{6}$$

The buoyancy frequency is given by

$$N^2 = -g\rho^{-1}\left\langle\frac{\partial\rho}{\partial z}\right\rangle = \alpha g\left\langle\frac{\partial T}{\partial z}\right\rangle, \tag{7}$$

where the expansion coefficient α depends on temperature and salinity, and is positive for stable stratification. The Cox number (Osborn and Cox, 1972) is

$$C = \chi_T(2D)^{-1}\langle\partial T/\partial z\rangle^{-2}. \tag{8}$$

Using (7) and (8) in (6) yields a potential energy equation,

$$\frac{1}{2}\left\langle\frac{\partial}{\partial t}(\alpha g T')^2\right\rangle N^{-2} = -\alpha g\langle w'T'\rangle - N^2DC. \tag{9}$$

The term on the left of (9) is the rate of change of potential energy within the averaging region, relative to a linear density gradient. The first term on the right is the rate of production of potential energy, and the last term is the rate of dissipation of potential energy.

The integral of the temperature variance spectrum, from which χ_T and the potential energy dissipation rate N^2DC are calculated, is dominated by the high-wavenumber microstructure peak, if such a peak exists. We also know that the microstructure spectral peak can be found when, and only when, small-scale density inversions exist (Dillon, 1982), that is, when nonzero Thorpe displacements are found. If the fluid has no small-scale inversions, the Cox number is of order 10 or smaller, and the temperature gradient spectrum has a shape at high wavenumbers characteristic of well stratified finestructure, falling off as (wavenumber)$^{-1}$.

This suggests an intimate relation between the potential energy contained in the density inversions (i.e., the potential energy relative to the Thorpe profile), and the potential-energy dissipation rate. Since N^2DC is dominated by the high-wavenumber microstructure peak in all examples examined below, we can think of the potential energy relative to a linear density profile as being composed of two parts: that contributed by the mean gradient and the low-wavenumber finestructure, and that contributed by the density inversions. Though the finestructure contribution may be larger than the contribution of the inversions, the *rate of change* of the potential energy relative to a constant density gradient must be dominated by the rate of change of the potential energy relative to the Thorpe profile. We therefore approximate the rate of potential energy change by the rate of change of the potential energy *relative to the Thorpe profile.*

Approximating $\frac{1}{2}\alpha g T'^2 N^{-2}$ by the APEF, and using (9) to eliminate $g\rho^{-1}\langle \rho' w' \rangle$ in (2) results in a total-energy conservation equation:

$$\frac{1}{2}\left\langle \frac{\partial}{\partial t} u_i' u_i' \right\rangle + \frac{1}{2}\frac{\partial}{\partial t}(\mathrm{APEF}) = S - \epsilon - N^{-2}DC. \qquad (10)$$

The left side of (10) is just the volume average of the rate of change of the *total* energy of the fluctuations, kinetic plus potential. The first term on the right is the net rate at which turbulent energy is put into the system, and includes local production and advection of energy. This term is positive only if the local rate of turbulent energy production is greater than the rate at which energy is advected and radiated from the system, i.e., if the direction of net energy flow is into the system. There may exist some cases where the local production is small and is exceeded by the rate of flow out of the system, in which case S is a sink rather than a source. The next two terms, the rates of kinetic and potential energy dissipation, are always energy sinks.

We are now ready to make a fundamental assumption—that all observations represent a state of gravitational collapse—and we shall later see whether this assumption leads to any contradictions. The definition we will use of "gravitational collapse" is $S \leqslant 0$, i.e., there is no net mechanical energy source. There may be mechanical energy sinks (other than ϵ), perhaps arising from the radiation of internal waves. Gravitationally collapsing turbulence cannot persist indefinitely because (10) demands that the total turbulent energy always decrease when $S \leqslant 0$. The turbulent kinetic energy is constantly drained by ϵ, and there is only one term in the turbulent-kinetic energy equation (2), $-g\rho^{-1}\langle w'\rho' \rangle$, that can supply the energy necessary to drive internal motions. But while $\langle w'\rho' \rangle$ may be a kinetic energy source in (2), it is a potential energy sink in (9). It is shown below that the rate of change of the total energy when $S \leqslant 0$ is always negative.

When the fluid is in a state of gravitational collapse, energy is transformed from potential to kinetic energy. Fluid parcels with a greater density (lower temperature) than that of the immediately surrounding fluid may be correlated with downward vertical-velocity fluctuations, i.e., $\langle w'T' \rangle$ may be positive ($\langle w'\rho' \rangle$ negative). The APEF will be decreased by this restratification and also decreased by N^2DC; the "mean" potential energy of the system will in turn be increased at the rate N^2DC. Eventually, parcels of fluid will rise or sink to their equilibrium depth, the density difference of the fluctuations will be dissipated, and there will be no more potential energy available to drive internal motions.

The assumption of $S \leqslant 0$ in (10) leads to the inequality

$$\frac{1}{2}\left\langle \frac{\partial}{\partial t} u_i' u_i' \right\rangle + \frac{\partial}{\partial t}(\mathrm{APEF}) \leqslant -\epsilon - N^2DC. \qquad (11)$$

Both terms on the right of (11) can be measured, but only one quantity on the left, the APEF, can be found from field measurements; the time derivative of the kinetic and potential energies cannot be measured. The kinetic energy in the fluctuating field can, however, be estimated. If the parcels of fluid in a gravitationally collapsing overturn behaved as a one-dimensional, undamped, simple harmonic oscillator with each parcel having a random phase, the average kinetic energy would equal the average potential energy. But the fluid is viscous, motions in the patch are damped and the motions are three-dimensional. Therefore, the APEF is not equal to, but an upper bound on, the energy contained in the vertical velocity fluctuations in a collapsing overturn. Because the patch (by assumption) is collapsing, energy in the horizontal velocity components must originate from vertical motions. Since isotropic velocity fluctuations are an extreme case for collapsing turbulence, the total kinetic energy might be as large as $3\langle w'^2 \rangle/2$. An upper bound on the *kinetic* energy is therefore 3APEF, and an upper bound on the *total* energy is 4APEF.

We cannot measure the time rate of change of the energy, but we can compare the rate of change of the energy to the energy divided by a natural time scale of the system, i.e., the inverse of the buoyancy frequency. There exists a number m such that

$$4\mathrm{APEF} > m(\epsilon + N^2DC)N^{-1}. \qquad (12)$$

The largest such number m can be considered the time scale for the dissipation of the total energy in a gravitationally collapsing overturn, in units of $1/N$. If it is assumed that the rate of change of energy in gravitational collapse follows an exponential decay law, m is the e-folding time, in units of $1/N$. However, in general, (12) should be considered as a "scaling rule" suggested by (11), because the rate of change of energy is not known. If a patch is collapsing, the energy dissipated is drawn from the APEF. The time scale for collapse must be at least as small as the time scale for dissipation, else the density fluctuations would dissipate before their energy could be transformed from potential to kinetic. The test of whether or not an observed patch is collapsing is whether or not the value of m necessary to satisfy (12) is a realistic time scale for collapse.

4. The evidence

The data examined here, from the same observations described by Dillon (1982), were collected at Ocean Station P during the MILE experiment, and in a freshwater lake, Green Peter Reservoir. The data include observations from several different regimes: 1) the seasonal thermocline at Station P and at Green Peter Reservoir, 2) a mixing layer interior strongly forced by the wind at Station P, 3) a mixing layer in the presence of dying winds at Station P, and 4) the energetic near-surface layer of a lake. Temperature was sampled at approximately 0.1 cm intervals. A preliminary average, with 1 cm bins for the lake data and 2 cm for the oceanic data, was first used to reduce electronic noise, resulting in a sequence of temperatures at equally spaced depths. These temperatures were then Thorpe-ordered by a bubble-sort algorithm to yield a stable, ordered, monotonic profile (Dillon, 1982).

The choice of averaging interval in the seasonal thermoclines was straightforward. Here, patches of overturning structures were isolated by regions of undisturbed water. Above and below the patches, no temperature fluctuations were found. The situation was not so clear-cut in the mixing layer, where large regions of undisturbed water could not be found. However, distinct, easily identifiable structures were often found in the mixing layers. The Thorpe displacement signature of these structures was a large "reverse-Z" shape with sharp edges. Water immediately above and below the structure had displacements much smaller than that inside the structure (cf. Figs. 2–5 of Dillon, 1982). When these structures were found, the averaging interval was the entire extent of the structure. At other times, distinct structures were not found. An averaging interval was then chosen so that the buoyancy frequency, dissipation rate, and Thorpe scale (the rms displacement) did not change much within an average. For all averaging intervals, the mean temperature fluctuation was zero.

Not all portions of the surface layer could be usefully analyzed. Water above 10 m depth in the oceanic data may have been stirred by a ship's wake, and so samples above 10 m were discarded. At times turbulence was so intense near the surface that the complete temperature gradient spectrum could not be resolved; these segments were neglected.

It may seem that one of the assumptions leading to (12) is violated in surface layers. Can the advection terms in (4) really be neglected in surface layers? If the surface layer turbulence is not collapsing, advection cannot be neglected *a priori*. However, if the patches are collapsing, as the fundamental assumption states, there are excellent reasons to believe that advection is not important. A close examination of the data reveals that Thorpe displacements are organized in such a manner that there exist distinct intervals, where no displacement in a particular region references a depth outside of the region; we will call such intervals "complete overturns." All temperatures in a complete overturn lie between the minimum and maximum temperature of the interval, and temperatures found within are found nowhere else. The rms size of complete overturns is about the same as the Thorpe scale.

The averaging intervals used in the analysis correspond to at least one, and sometimes several, complete overturns. If the fluctuations within an overturn are driven solely by gravitational collapse, parcels of fluid within a region cannot escape that region by moving vertically. The region can shrink in the vertical, but cannot expand because there is no energy source to drive vertical entrainment; therefore, vertical advection of temperature variance may be neglected when the vertical averaging interval corresponds to one or more complete overturns.

Temperature was sampled only in the vertical, not in the horizontal. A pointwise horizontal integration cannot be made—but pointwise integrations are not the only way to form an average. Each vertical average may be viewed as one realization of a random process, one sample in the horizontal plane. The collection of all vertical averages amounts to an ensemble average, or equivalently, a Monte Carlo integration in the horizontal, since the horizontal position of a cast is a random variable. Any single realization from the ensemble may contain horizontal temperature-variance advection contributions, but the advection term cannot always have the same sign, because a quantity advected into some region must have come from somewhere else. Therefore, if one wishes to minimize errors resulting from horizontal advection in the temperature variance equation, all vertical averages should be ensemble-averaged (after an appropriate nondimensionalization has been done).

Mean temperature gradients were calculated in a manner essentially equivalent to dividing the maximum temperature difference within a patch by the patch size (see Dillon, 1982 for details). Kinetic energy and temperature variance dissipation rates have been estimated from the temperature gradient spectrum (Dillon and Caldwell, 1980). The only difference between the dissipations used here and the Dillon (1982) estimates is that here a temperature-dependent kinematic viscosity is used. This changes the dissipation estimates by a factor of the same order as the systematic uncertainty in the estimates, and is not of great importance.

The physical meaning of (12) is a comparison of the amount of energy which would be dissipated in a time $m\,N^{-1}$ to the total energy contained in the fluctuations. In a log-log plot of $(\epsilon + N^2DC)N^{-1}$ versus APEF (Fig. 1), m is represented by a family of straight lines. For all points below the line $m = 1$, an amount of energy equal to 4APEF could be dissipated in a time shorter than $1/N$. Only a few of the points lie above the $m = 1$ line (Fig. 1). This means that the time scale for dissipating the total energy for most of the samples is much shorter than $1/N$ ($1/N$ is about 15% of a buoyancy period). In order to satisfy (12) in an average of all the data, m would have to be 0.07 or less, that is, the time scale for dissipation in an average sense is at most $0.07/N$, or 1% of a buoyancy period.

How does this time scale compare with the time scale for collapse? Lange (1982) measured the growth characteristics of dye injected into the wake of a biplanar grid towed in a salt-stratified tank. He found

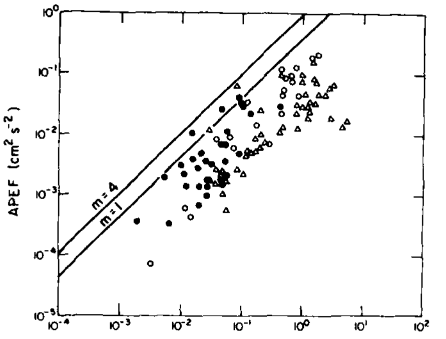

FIG. 1. A comparison of the APEF, the available potential energy, and the amount of kinetic and potential energy that could be dissipated in a time N^{-1}, where N is the buoyancy frequency, in units of radians per second. If the turbulence is gravitationally decaying, an estimate of the total energy in the fluctuations is 4 APEF. The time scale for dissipation (the *e*-folding time if the turbulence is exponentially dissipating in units of N^{-1} is a family of diagonal lines. Two such lines are drawn, labeled $m = 1$ and $m = 4$, corresponding to dissipation time scales of N^{-1} and $4N^{-1}$. All dissipation time scales are shorter than $4N^{-1}$, and most are shorter than N^{-1}. The time scale for gravitational collapse estimated from laboratory studies is longer than N^{-1}, indicating that the time scale for dissipation is usually shorter than the time scale for gravitational collapse. Closed circles are from MILE data, weak winds; open circles are from MILE data, strong winds; triangles are from a freshwater lake.

that the estimated mean-square wake width grew in time for ½ of a buoyancy period, then began to collapse. About ½ a buoyancy period (or $3/N$) after collapse began, the wake width was half as large as its maximum value. The *e*-folding time scale for collapse for Lange's experiment is then roughly $4/N$.

Stillinger *et al.* (1983, hereafter SHV) measured turbulence in the wake of a grid in a stratified water tunnel (this experiment will be discussed later), finding that the length scale of the turbulence (and therefore the APE) increased to a maximum value, then began to decrease. The time necessary to fall from the maximum APE to $1/e$ of the maximum (i.e., an *e*-folding time for restratification and diffusion) was greater than $3/N$ in all cases, a result consistent with Lange's experiment. A very conservative estimate for the time scale for gravitational collapse would be $1/N$, or $m = 1$ in (12).

Lange's and SHV's experiments are consistent with a collapse time scale of 3–4 (in units of $1/N$), while the time scale for dissipating density fluctuations in the sea and in lakes is usually much smaller than 1. This means that most of the energy in temperature and velocity fluctuations would be dissipated before gravitational collapse could occur, a contradiction of the fundamental assumption. We therefore conclude that gravitational collapse is usually not the sole source of energy driving internal motions in overturning patches. In order to sustain the observed level of turbulence, energy must be supplied to the overturning patch from the environment. For most disturbances, S must be greater than zero, a source of energy, not a sink.

The essence of the above argument can be summarized by an analogy: Suppose one measures the rate at which energy flows into an electric motor as, say, 100 watts. If the motor is found to dissipate heat at the rate of 1000 watts, the motor must be receiving energy from some unmeasured source. Since the rate of decrease of kinetic and potential energy due to gravitational collapse cannot supply energy at a rate sufficient to balance the rate at which it is dissipated, energy must be flowing into the turbulence from another source.

5. Some elements of the theory of fossil turbulence

Gibson (1982c) maintains that most, if not all, patches of small-scale temperature inversions observed in the ocean and in lakes are not active turbulence but are instead fossils of previously active mixing events. In Gibson's scheme, active turbulence is synonymous with "isotropic," "3-dimensional" and "overturning" turbulence, and is defined as "a random, isotropic, eddy-like motion in which inertial forces dominate both buoyancy and viscous forces . . .". In contrast, fossil temperature turbulence consists of "temperature fluctuations produced by active turbulence which persists after the fluid has ceased to be actively turbulent at the scale of the fluctuation" (Gibson, personal communication, 1982). The velocity field of a fossil patch should not be assumed zero, but may be fossil vorticity turbulence, which is defined as "the buoyancy-dominated velocity field left after the turbulence has been damped by stratification." Fossil vorticity turbulence is motion that is ". . . random, rotational, and strongly non-linear . . . qualitatively quite different from the overturning turbulence from which its energy derives and should not be classified as turbulence but as a form of internal wave." Gibson's (1980) quantitative criterion for active turbulence is

$$A_T = [\epsilon(13N^2DC)^{-1}]^{1/2} > 1, \qquad (13a)$$

where A_T is called the activity parameter. The state of turbulence is scale-dependent, and a given patch of turbulence might be fossil on some large scale and active on a smaller scale. The turbulence is said to be active at a wavelength λ, if λ satisfies (Gibson, 1981b, 1982a)

$$1.2L_0 > \lambda > 15L_k, \qquad (13b)$$

where L_k is the Kolmogorov or viscous scale $(\nu^3/\epsilon)^{1/4}$, ν is the kinematic viscosity, and L_0 is $(\epsilon/N^3)^{1/2}$ (Gibson [1982a] uses the symbol L_R for this quantity; L_0 is used here because the common name for it is the "Ozmidov scale"). The scale dependance of the fossil-active state originates from the assumption that following some initial instability, a disturbance will grow and produce overturns until restraining or damping forces become as large as the internal inertial forces.

Buoyancy forces increase with increasing length scale in a stratified fluid, and $1.2L_o$ is, approximately, the wavelength at which inertial and buoyancy forces are equal (Gibson, 1981b). Consequently, Gibson (1981b) assumes that the wavelength of overturning for active turbulence can only be as large as $1.2L_o$, and if an overturn with wavelength larger than $1.2L_o$ is observed, it is assumed to be a remnant left from a previous time, when L_o and the dissipation rate were larger (note that N is not allowed to change in time, since it is measured on a length scale larger than the disturbance). Overturns cannot occur at very small wavelength, because the motion would be damped by viscosity (Gibson, 1981b, 1982a).

Gibson's theory appears plausible. It is possible to imagine a disturbance, perhaps created from the wake of a body, such that the input of energy occurs in a very short time. Initially, the disturbance grows until an upper bound is reached. The upper bound on the size of the disturbance will be determined by density stratification, viscous forces, the boundaries of fluid or perhaps something else. For a stratified fluid of infinite extent, the upper bound may well depend on L_o because L_o contains information relating inertial stirring and buoyant restoring forces. After the upper bound is reached, the fluid must begin to restratify and gravitationally collapse, unless there is a continuing source of energy.

The SHV experiment involved measurements of turbulence in the wake of a mesh in a salinity-stabilized water tunnel. The kinetic-energy dissipation rate and density fluctuations were measured at several fixed points downstream from the mesh. The mean disturbance size was estimated as twice the rms density fluctuation divided by the mean density gradient. This disturbance size will be referred to below as L_S. For a constant mean density gradient, L_S will be approximately twice as large as the Thorpe scale L_T used by Dillon (1982). The $2L_T$ and L_S are not exactly the same because a measurement of the Thorpe scale requires a vertical density profile, whereas L_S is measured at a fixed point in space. Thorpe displacements contain no contributions from internal wave displacements, while measurement of density fluctuations at a fixed point in space may contain contributions from internal waves.

Near the mesh, SHV found that the turbulent length scale increased downstream (i.e., increased in time) in accord with the unstratified results of Montgomery (1974). Farther downstream L_S departed from the unstratified prediction and began to decrease. At the point where L_S first departed from the unstratified prediction, L_S/L_o was found to be 1.4, in reasonably good agreement with a prediction by Gibson (1981b) of 1.2. At the point of departure from the unstratified prediction, gravitational forces are large enough to significantly constrain the turbulent motions, and the turbulence may be termed "at the point of fossilization." Downstream from the point of fossilization, i.e., later in time, L_S/L_o was greater than 1.4, and the turbulence can there be called "fossil."

It remains to be seen whether or not oceanic turbulence can be easily related to water tunnel turbulence. The source of turbulent energy in SHV's experiment was very localized because the turbulence was initiated by a mesh. The kinetic-energy dissipation rate was highest near the mesh and decreased monotonically downstream. It is not clear that this situation is analogous to oceanic turbulence, where many different processes may simultaneously occur. Some, perhaps most, oceanic turbulence is generated by shear instabilities—can this be modeled as wake turbulence, where a sudden instability causes rapid growth and soon after, a gravitational collapse? A possible occurrence in the ocean is that the large-scale shear from an inertial wave increases until a critical gradient Richardson number is reached and turbulence is initiated. The time scale of an inertial wave may be much longer than the time scale of dissipation or the time scale of collapse.

6. Toward a synthesis

Some care should be used when comparing Dillon's (1982) Thorpe scale calculation with SHV's results. A direct length-scale comparison may not be the best way to proceed because of nonlinearity in the oceanic density profiles. However, other comparisons can be made. Here L_S is defined as

$$L_S = 2\langle\rho'^2\rangle^{1/2}\left\langle\frac{\partial\rho}{\partial z}\right\rangle^{-1}, \tag{14a}$$

and may be expressed in terms of the APEF as

$$L_S = 8(\mathrm{APEF})N^{-2}. \tag{14b}$$

The square of the ratio of L_o to L_S is

$$\left(\frac{L_o}{L_S}\right)^2 = \frac{1}{8}\epsilon N^{-1}(\mathrm{APEF})^{-1}, \tag{15}$$

i.e., it is the ratio of the amount of kinetic energy dissipated in a time $1/N$, to 8 times the potential energy in the fluctuating field (note that this relation holds only if the density gradient is linear, as it was in the water tunnel); (15) is similar to lines of constant slope in Fig. 1, the difference being that SHV did not measure the potential energy dissipation rate, and so could not include it in the calculation. When the APEF from both SHV's data and the field data are plotted versus ϵ/N, the result is striking (Fig. 2). In SHV's data (Fig. 2a), points can be temporally connected. Points nearest the mesh have the largest kinetic energy dissipation, which monotonically decreases in time. The temporal track is along lines of nearly constant APEF, finally converging near the line ϵ/N = APEF which is approximately followed thereafter.

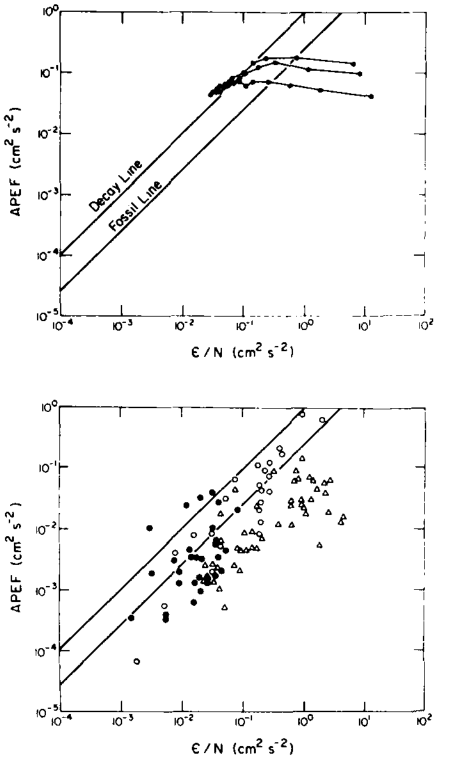

FIG. 2. (a) A comparison of the available potential energy in the fluctuations, APEF and the amount of kinetic energy that could be dissipated in a time N^{-1}. Data points are from SHV's stratified water tunnel experiment. Points joined by solid lines are sequential in time from right to left. Three runs, with initial buoyancy frequencies of 0.97 s^{-1}, 0.79 s^{-1} and 0.50 s^{-1} are shown. Points to the right of the fossil line were classified as active turbulence. The correlation of density and vertical velocity, $\langle \rho' w' \rangle$, approached zero near the decay line. (b) Field data points from the ocean and from a freshwater lake as in Fig. 1. All points to the left of the fossil line satisfy the SHV criterion for fossil turbulence; points to the right of the fossil line are active. Few points are found to the left of the decay line.

SHV found the velocity–density correlation $\langle \rho' w' \rangle$ largest near the mesh or not far from it. Downstream from the maximum, $\langle \rho' w' \rangle$ approached zero, then became negative, indicating that restratification was beginning to occur. The line ϵ/N = APEF in Fig. 2a might be termed the "decay line", because the convergence of points to the line corresponds to the time when $\langle \rho' w' \rangle$ approached zero. The decay line seems to represent a limit which the SHV data cannot exceed by a significant amount; it corresponds to $L_S = 2L_o$. The same effect can be seen in the field data (Fig. 2b), where the decay line is an edge to the distribution which only a few points cross by a small amount. The agreement between Fig. 2a and Fig. 2b (i.e., both distributions seem to have an edge on or about the line ϵ/N = APEF) suggests that both data sets are measures of the same process.

The point of fossilization is represented in the SHV data by $L_S = 1.4L_o$, or by ϵ/N = 4APEF. In Fig. 2b, the point of fossilization is labeled the "fossil line." All points above the fossil line qualify as fossil by (13b), and all points below qualify as active.

SHV could not estimate Gibson's activity parameter because the density gradient spectrum could not be fully resolved. We must look to the oceanic data to estimate A_T. For consistency, one would like to see the activity parameter approach unity as L_S approaches $1.4L_o$. That is, does "the point of fossilization," as found by SHV, correspond to $A_T = 1$? The comparison can be made in the field data by noting that the criterion $L_S = 1.4L_o$ corresponds to

$$\epsilon^{1/2}N^{-1/2} = 2(\text{APEF})^{1/2}. \tag{13c}$$

The two fossil turbulence criteria, (13a) and (13b), are not equivalent. In Fig. 3 the relation (13c) is a dotted vertical line, and the $A_T = 1$ is a solid horizontal line. The criteria are both satisfied where the two lines cross. The middle of the distribution of data points along the vertical line corresponds to the horizontal line A_T = 0.4–0.5, rather than $A_T = 1$.

The states of "gravitationally collapsing turbulence" and "fossil turbulence" are not identical. While few data points have dissipation time scales as large as the time scale required for gravitational collapse, many of the points are fossil by both turbulence criteria, (13a) and (13b). It may be concluded that energy is often

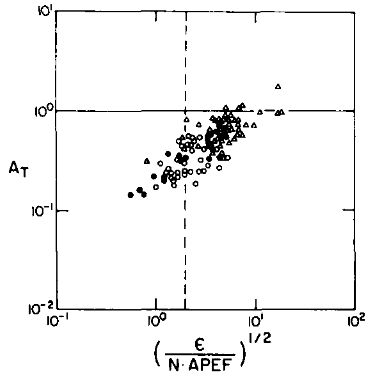

FIG. 3. A comparison of the fossil turbulence criterion, suggested by Gibson and tested by SHV, and Gibson's activity-parameter criterion. Points below the solid horizontal line are fossil by the activity parameter criterion, and points to the right of the dashed vertical line are fossil according to the SHV criterion. Many points are active by SHV criterion, but fossil according to the activity parameter criterion. Agreement between the two criteria may require a change in the definition of the activity parameter.

produced in, or advected into, fossil overturns. Fossil turbulence may be productive and may entrain fluid. Fossil overturns are not necessarily quiescent remnants of previously active events. The evidence indicates fluctuations in fossil patches are being supported by energy drawn from the environment.

Since (13b) has the support of the SHV data and because SHV could not test (13a), it may be that (13a) is in some way in error. The inconsistency between (13a) and (13b) can be removed if the factor of 13 in the definition of the activity parameter is replaced by a smaller number.

Consider the implications of such a change to formalisms other than the fossil formalism: There is a body of evidence that indicates that the flux Richardson number R_f has an upper limit in the range 0.1–0.2 [cf. Osborn, 1980; the limiting value of atmospheric boundary-layer stability functions for high stability (cf. Businger, 1980, and many others) also corresponds to a flux Richardson number in this range]. A number related (perhaps remotely!) to R_f is the "dissipation" Richardson number R_D

$$R_D = N^2DC(\epsilon + N^2DC)^{-1}. \qquad (16)$$

The activity parameter can be written as a function of R_D

$$A_T = [\epsilon/(xN^2DC)]^{1/2} = \left[\frac{1 - R_D}{xR_D}\right]^{1/2}. \qquad (17)$$

Here, x is an adjustable parameter which has the value 13 in (13a). If a turbulent patch has a production–dissipation–buoyancy flux balance (it is not clear that all or even most overturning patches exhibit this balance, but surely some turbulence has this characteristic, and any theory of turbulence must account for this case), the flux Richardson number and dissipation Richardson numbers are equivalent. It is reasonable to suppose that the critical flux Richardson number represents the point at which buoyant restoring forces become important. If this is so and if at the same time a production–dissipation–buoyancy flux balance exists, the activity parameter could be forced to unity (approximately) at $R_f = 0.2$ by choosing $x = 4$. If x is set equal to 4, rather than 13, there would be little disagreement between the theory of fossil turbulence and critical Richardson number theory. With this change, the theory of fossil turbulence would be in substantial agreement with most observations and with much of the existing turbulence literature.

The actual history and evolution of mixing events in the ocean may never be well known. Turbulence in the ocean is not necessarily so well behaved as in the laboratory. The time scale of the forcing that initially produces the instability may be much longer in the sea than in the laboratory. It is conceivable that if the forcing time scale is long compared to the time of growth, a disturbance could be maintained indefinitely in an active state. A few oceanic mixing patches may be gravitationally decaying, some may be in a steady state and others may be rapidly growing. Yet viewed collectively, a large number of patches may be in a statistically steady state (Caldwell, 1983).

Acknowledgments. The entire past and present cast of the OSU Microstructure group, including D. Caldwell, P. Newberger, M. Brown, S. Wilcox, M. Matsler, J. Cantey, M. Park, and H. Dannelongue deserve a vote of thanks. S. Thorpe, J. Imberger, W. Crawford, A. Gargett, and C. Gibson, among others, were the source of many helpful and stimulating dialogues. The author expressly wishes to thank C. Gibson for many helpful discussions regarding the theory of fossil turbulence, and for instigating a stimulating and fruitful controversy. The collection and analysis of the freshwater data were sponsored by the National Science Foundation, Contract OCE-8018444. The collection and analysis of the oceanic data were supported by the Office of Naval Research, Contract N00014-79-c-0004.

REFERENCES

Businger, J. A., 1973: Turbulent transfer in the atmospheric surface layer. *Workshop on Micrometeorology*, D. A. Haugen, Ed., Amer. Meteor. Soc., 390 pp.

Caldwell, D. R., 1983: Oceanic turbulence: Big bangs or continuous creation? *J. Geophys. Res.*, **88**, 7543–7550.

Dillon, T. M., 1982: The mixing length of vertical overturns: a comparison of the Thorpe and Ozmidov length scales. *J. Geophys. Res.*, **87**, 9601–9613.

——, and D. R. Caldwell, 1980: The Batchelor spectrum and dissipation in the upper ocean. *J. Geophys. Res.*, **85**, 1910–1916.

Gargett, A. E., P. J. Hendricks, T. B. Sanford, T. R. Osborn and A. J. Williams, 1981: A composite spectrum of vertical shear in the upper ocean. *J. Phys. Ocean.*, **11**, 1258–1271.

Gibson, C. H., 1980: Fossil temperature, salinity and vorticity turbulence in the ocean. *Marine Turbulence*, J. C. J. Nihoul, Ed., Elsevier, 221–257.

——, 1981a: Buoyancy effects in turbulent mixing: sampling the stratified ocean. *AIAA J.*, **19**, 1394–1400.

——, 1981b: Fossil turbulence and internal waves, in AIP Conf. Proc. No 76, *Nonlinear Properties of Internal Waves*, B. West, Ed., pp. 159–179.

——, 1982a: Alternative interpretations for microstructure patches in the thermocline. *J. Phys. Oceanogr.*, **12**, 374–383.

——, 1982b: Fossil turbulence in the Denmark Strait. *J. Geophys. Res.*, **87**, 8039–8046.

——, 1982c: On the scaling of vertical temperature gradient spectra. *J. Geophys. Res.*, **87**, 8031–8038.

Lange, R. E., 1982: An experimental study of turbulence behind towed biplanar grids in a salt-stratified fluid. *J. Geophys. Res.*, **12**, 1506–1513.

Montgomery, R. D., 1974: An experimental study of grid turbulence in a thermally stratified flow. Ph.D. thesis, University of Michigan, 215 pp.

Osborn, T. R., 1980: Estimates of the local rate of vertical diffusion from dissipation measurements. *J. Phys. Oceanogr.*, **10**, 83–89.

——, and C. S. Cox, 1972: Oceanic finestructure. *Geophys. Fluid Dyn.*, **3**, 321–345.

Stillinger, D. C., K. N. Helland and C. W. Van Atta, 1983: Experiments on the transition of homogeneous turbulence to internal waves in a stratifited fluid. *J. Fluid Mech.*, **131**, 91–122.

Thorpe, S. A., 1977: Turbulence and mixing in a Scottish Loch. *Phil. Trans. Roy. Soc. London*, **A286**, 125–181.

JOURNAL OF GEOPHYSICAL RESEARCH, VOL. 89, NO. B8, PAGES 6941-6960, AUGUST 10, 1984

MARINE SEISMIC REFRACTION STUDY BETWEEN CAPE SIMPSON AND PRUDHOE BAY, ALASKA

M. Bee

College of Oceanography, Oregon State University, Corvallis

S. H. Johnson

Amoco Production Research, Tulsa, Oklahoma

E. F. Chiburis

Aramco, Texas City, Texas

Abstract. A marine seismic refraction study conducted between Cape Simpson and Prudhoe Bay, Alaska, provides data for subsurface structural and geological cross sections of the western Beaufort Shelf. The results suggest that the western Beaufort Shelf is underlain by a sedimentary prism with beds dipping and prograding to the northeast. Correlation of the refraction data with wells drilled on land and offshore reflection profiles permits tentative identification of geologic sequences on the basis of their seismic velocity. This study associates near-surface velocities of 1.60-1.65 km/s with Quaternary sediments and 1.82-2.35 km/s velocities with Tertiary strata. Velocities of 1.60-3.40 km/s are correlated to Upper Cretaceous rocks, 2.10-4.14 km/s to Lower Cretaceous beds, 5.66-5.68 km/s to Mississippian-Pennsylvanian carbonates, and 4.24-6.08 km/s to the Franklinian basement composed of argillites and phyllites. West of Cape Halkett, the sedimentary section is mainly Lower Cretaceous, whereas east of Cape Halkett, Upper Cretaceous and Tertiary strata dominate. Higher velocities (6.40-7.07 km/s) are thought to represent the crystalline basement, probably silicic in composition. Although no seismic velocities typical of the upper mantle are present on the record sections, a minimum depth calculation places the Mohorovicic discontinuity no shallower than 20 km. The interpretation indicates that the stratigraphic sequence present onshore at Prudhoe continues to the offshore and implies that the western Beaufort Shelf may be a good prospect for oil. The structures derived from seismic data indicate that the Beaufort continental margin is not different from Atlantic-type margins and add further evidence to the concept of a rifted and rotated Beaufort continental margin.

Introduction

A wealth of knowledge exists concerning the onshore geology of the Arctic Slope of northern Alaska from geological [Brosgé and Tailleur, 1970; Martin, 1970; Tailleur and Brosgé, 1970; Alaska Geological Society, 1971, 1972, 1977; Young et al., 1976; Carter et al., 1977; Grantz et al., 1981; and others], geophysical [Dana, 1951; Woolson et al., 1962; National Oceanic and Atmospheric Administration, (NOAA), 1982; and others], and borehole data [Robinson, 1959; Robinson and Collins, 1959; Collins, 1961; Rickwood, 1970; Morgridge and Smith, 1972; Witmer et al., 1981b; NOAA, 1982; and others], but very little data are available north of the coast because of the limits imposed on offshore studies by the harsh environment of the Beaufort Sea. The sparsity of published seismic reflection and well data on the north side of the Barrow Arch requires that the geologic structure of the western Beaufort Shelf be extrapolated from onshore test wells, geological structure, and seismic data on land in combination with a handful of offshore geophysical studies [Hunkins, 1966; Wold et al., 1970; Grantz et al., 1974, 1975, 1979, 1981; Eittreim and Grantz, 1979].

Existing marine seismic surveys conducted on the western Beaufort Shelf are, for the most part, reflection profiles which provide information on shallow structures from the midshelf to the continental slope. Published seismic information from the shoreline to the midshelf is rare perhaps because of the considerable economic interest in the area. The data gap contributes to a lack of information necessary to resolution of arguments concerning a relationship between the continental margins of northern Alaska and the Canadian Arctic Archipelago.

The study reported here provides seismic data obtained from the near-offshore region (Figure 1). The data are sonobuoy refraction profiles collected in 1976 from an icebreaker on the western Beaufort Sea portion of the Alaskan Shelf. We describe some unusual (for this area) data acquisition techniques, an interpretation of the data, and implications of our refraction results on the offshore continuation of onshore stratigraphy and to the origin of the Canada Basin. We limit our discussions to the broad structures permitted by the nature of the refraction data.

Tectonic, Stratigraphic, and Geologic Setting

The following brief summary of the geology and tectonics of the western Beaufort Shelf is included to acquaint the reader to the tectonic framework of the North Slope of Alaska in preparation for later discussions. For a more comprehensive review the reader is referred to Grantz et al. [1975, 1979, 1981].

Existing evidence suggests that the continental shelf of northern Alaska is composed of a sedimentary prism which progrades to the northeast and contains mainly Tertiary and Cretaceous

Paper number 4B0658.
0148-0227/84/004B-0658$05.00

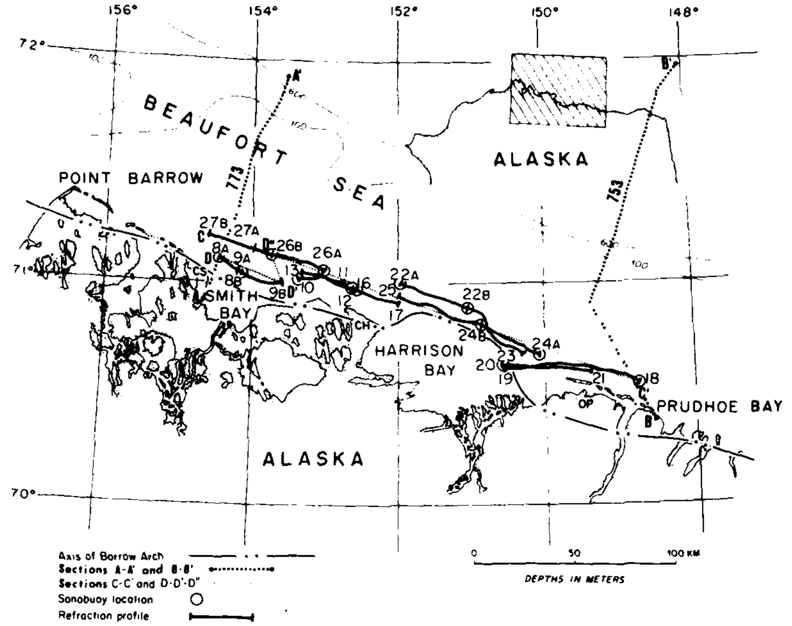

Fig. 1. Location map showing the locations of sonobuoys and seismic refraction profiles, together with the locations of section AA' (Figure 7), section BB' (Figure 8), section CC' (Figure 9), and section DD'D" (Figure 10). CS, Cape Simpson; CH, Cape Halkett; OP, Oliktok Point.

material and possibly local thin truncated Mississippian to Jurassic beds. Onshore, a significant stratigraphic change occurs near Cape Halkett where the Upper Cretaceous and Tertiary prism thins from the east and disappears and is replaced by Lower Cretaceous material to the west. On the south the prism is bounded by the Barrow Arch, a southeastward plunging anticline whose crest follows the coast of our study area from Point Barrow in the west to Prudhoe Bay in the east. The Barrow Arch forms a hinge line between the northward tilted basement surface of pre-Mississippian rocks which underlie the continental shelf of the western Beaufort Sea and the southward tilted Arctic Platform of northern Alaska [Grantz et al., 1981].

The geologic formations of northern Alaska can be conveniently grouped into the Franklinian, Ellesmerian, and Brookian sedimentary sequences [e.g., Lerand, 1973; Grantz et al., 1975, 1981; Carter et al., 1977]. These sequences with their component formations are shown in Figure 2 together with a geologic cross section from Morgridge and Smith [1972] based upon onshore well data. Their cross section is parallel to the axis of the Barrow Arch but on its southern flank and summarizes in a simple manner the onshore stratigraphy. For a more extensive stratigraphic column the reader is referred to Grantz et al. [1981] and for more detailed geologic cross sections to the Alaska Geological Society [1971, 1972, 1977], Witmer et al. [1981a], and NOAA [1982].

Franklinian Sequence. These strongly deformed Cambrian to Devonian argillites and phyllites constitute the economic basement for petroleum exploration and the acoustic basement for reflected waves on the North Slope. These rocks result from an orogenic uplift in what is now extreme northern Alaska. In most areas this sequence is severely altered, and locally it is intruded by plutonic rocks. Franklinian rocks are 0.8 km deep near Point Barrow and deepen eastward along the axis of the Barrow Arch to depths of about 3.5 km at Prudhoe Bay. Seismic reflection profiles suggest that north of the Barrow Arch, these rocks slope seaward to depths of at least 8.0 km beneath the continental slope [Grantz et al., 1979, 1981].

Ellesmerian Sequence. Unconformably overlying the Franklinian rocks are the Mississippian to Lower Cretaceous (Neocomian) clastic and carbonate rocks of the Ellesmerian Sequence. These sediments appear to have been derived from a northern source area. The Ellesmerian beds are good seismic reflectors, especially the top of the Triassic Shublik Formation and the Pebble Shale unit of Neocomian age. At Prudhoe Bay the Ellesmerian rocks contain giant oil and gas accumulations within structures near the Barrow Arch. The Ellesmerian strata wedge out to the west, due to thinning and truncation, from thicknesses of about 1.6 km at Prudhoe Bay to a few hundred meters near Point Barrow. They also wedge out to the north where pre-Jurassic Ellesmerian formations extend probably to the south-

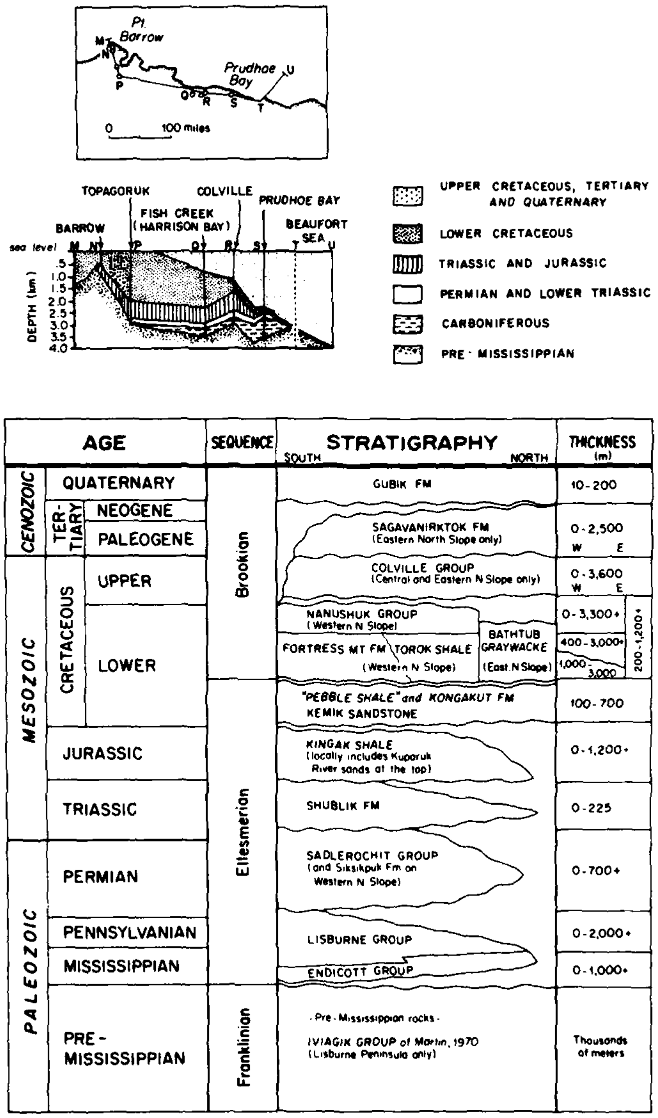

AGE			SEQUENCE	STRATIGRAPHY SOUTH NORTH	THICKNESS (m)
CENOZOIC	QUATERNARY		Brookian	GUBIK FM	10-200
	TERTIARY	NEOGENE		SAGAVANIRKTOK FM (Eastern North Slope only)	0-2,500 W E
		PALEOGENE			
MESOZOIC	CRETACEOUS	UPPER		COLVILLE GROUP (Central and Eastern N Slope only)	0-3,600 W E
		LOWER		NANUSHUK GROUP (Western N Slope)	0-3,300+ 200-1,200+
				FORTRESS MT FM TOROK SHALE (Western N Slope) BATHTUB GRAYWACKE (East. N Slope)	400-3,000+ 1,000-3,000
			Ellesmerian	"PEBBLE SHALE" and KONGAKUT FM KEMIK SANDSTONE	100-700
	JURASSIC			KINGAK SHALE (locally includes Kuparuk River sands at the top)	0-1,200+
	TRIASSIC			SHUBLIK FM	0-225
PALEOZOIC	PERMIAN			SADLEROCHIT GROUP (and Siksikpuk Fm on Western N Slope)	0-700+
	PENNSYLVANIAN			LISBURNE GROUP	0-2,000+
	MISSISSIPPIAN			ENDICOTT GROUP	0-1,000+
	PRE-MISSISSIPPIAN		Franklinian	- Pre-Mississippian rocks - IVIAGIK GROUP of Martin, 1970 (Lisburne Peninsula only)	Thousands of meters

Fig. 2. Geologic cross section from onshore well data [Morgridge and Smith, 1972] and the stratigraphic column of northern Alaska [Grantz et al., 1979].

ernmost part of the shelf. These pre-Jurassic strata are overlapped by thick upper Ellesmerian Jurassic and Neocomian beds which might extend to the central part of the shelf, where they rest unconformably over Franklinian rocks [Grantz et al., 1975, 1979, 1981]. Worth noting are the presence of sandstone beds of the Lisburne Group as far as the midshelf areas east of Cape Halkett [Bird and Jordan, 1977] and the near absence of Jurassic Kingak Shale under the Beaufort Shelf west of Prudhoe Bay [Grantz et al., 1981].

Brookian Sequence. The Lower Cretaceous (Albian) to Quaternary sediments of the Brookian Sequence were derived from a southern source, the Brooks Range. The sequence as thick as 1.0 km near Point Barrow and approximately 2.5 km thick at Prudhoe Bay. The Brookian rocks extend across the Barrow Arch and dominate the sedimentary prism of the western Beaufort Shelf. Their thickness beneath the outer shelf and slope is as much as 6.0 km [Grantz et al., 1979, 1981]. However, differential subsidence created two regions with marked differences in stratigraphy: between Point Barrow and Cape Halkett, dominantly Albian Cretaceous rocks constitute most of the sequence except for a thin Tertiary wedge which extends beneath the outer shelf. Between Cape Halkett and Prudhoe Bay, Tertiary and Upper Cretaceous strata make up almost the entire section beneath the shelf with the Tertiary becoming dominant near Prudhoe Bay. The Brookian Sequence, in most part, unconformably overlies the Ellesmerian Sequence. This unconformity is most pronounced in the Prudhoe Bay area where it is a major trapping element of the field. Upper Cretaceous sandstones in the Prudhoe Bay field and Lower Cretaceous (late Albian) sandstones in the Simpson area provide reservoirs for oil [Jamison et al., 1980]. These sandstone beds are thought to extend seaward under the shelf, where the fading and weakening of these seismic reflectors suggest that they pinch out [Grantz et al., 1975]. Quaternary clastic sediments of the Gubik Formation, locally as much as a few hundred meters thick, constitute the uppermost blanket of sediments on the western Beaufort Shelf.

Refraction Measurement

Location

The marine seismic refraction data described here were collected in the western Beaufort Sea to obtain structural and velocity information on the continental shelf. In contrast to most previous refraction studies in the region, which were made from stations located on the ice, our data were obtained during the Arctic summer using standard marine seismic techniques with sonobuoys and explosive charges. This was made possible by a zone of ice-free or semi-ice-free water which frequently exists along the northern continental shelf area out to the 2000 m bathymetry contour for 1 month's time (usually August). Thirteen profiles were completed between Cape Simpson and Prudhoe Bay in August 1976 from the U.S. Coast Guard icebreaker Burton Island with helicopter support. The profiles, ranging in length from 23 to 75 km, were roughly parallel to the coastline at a distance of about 15 km from it in approximately 20 m of water. As the Barrow Arch is situated roughly along the coast in our study area, all the refraction profiles were run over the northern flank of the Barrow Arch. The seismic lines shown on Figure 1 were shot along the southern edge of the floating ice pack which explains the crookedness of the lines. Also shown are the locations of the 13 sonobuoys used as receivers.

Techniques

The lines were shot in the standard marine fashion; charges with powder fuses were dropped into the water from the fantail of the icebreaker using a tilt table while the ship was underway. Rotor-mounted Yagi antennas were used to receive the sonobuoy signals which were recorded on a four-channel analog tape recorder. Two of the four channels recorded sonobuoy signals, one a clock signal, and one a shot-break signal from a streamer 3 m long which was towed close behind the ship. When radio contact with the sonobuoys was lost, at a distance of about 30 km because of earth curvature, a portable recording unit consisting of a radio receiver, an amplifier, and strip chart and tape recorders installed in a helicopter monitored the sonobuoy. The helicopter remained within radio reception range of the sonobuoy during shooting at far ranges. The timing of the helicopter recordings was synchronized with the shooting ship by comparing the times of the ship laboratory crystal clock to the helicopter crystal clock before helicopter takeoffs and after helicopter landings.

Expendable naval sonobuoys of the type AN/SSQ 41A were modified for extended time operation by addition of dry cell batteries which worked well in spite of the cold water. Explosive charges of less than 10 lbs (4.5 kg) were made up of nitrocarbonitrate (Nitromon) in 1-lb (0.4 kg) metal cans. Explosive charges between 30 and 660 lbs (13.6 and 299.4 kg) were made up of Tovex in 30-lb (13.6 kg) plastic bags.

Shots were detonated every 3 min at a ship speed of about 10 knots (18.5 km/h) which was slightly variable because of ice conditions. This procedure resulted in shots spaced at nominal intervals of 0.7 km. During the helicopter operations, shots were detonated at intervals varying from 5 to 15 min resulting in a shot spacing of 1.4-4.3 km.

A special sonobuoy deployment was used in our study: two sonobuoys were dropped at the beginning of each line and for a long line an intermediate sonobuoy was deployed in the middle of the line. This resulted in a special line numbering with letter A for the first sonobuoys and letter B for the intermediate one (for example, lines 22A-23 and 22B-23).

The ship's satellite navigation equipment was inoperative during the time of the experiment; therefore all the navigation was by radar fixes to land points at 15-min intervals. We estimated the navigational precision to 500 m. The ice coverage ranged from 0 to 100% during the course of the experiment and required frequent course changes and caution on the part of the shooter not to hit floating ice during the explosive drops.

The water currents were not negligible and affected the sonobuoy drift. The direction and magnitude of the drift was estimated by combining water wave travel time and navigation. The in-line component of drift ranged from 0 to 1.65 m/s and was variable from line to line.

For detailed information regarding these reconstructions the reader is referred to a technical report [Bée et al., 1979] which gives track line maps, shot locations, radar navigation points, sonobuoy drifts, input data files, data analysis techniques, computer program listings, and output data files.

Data Reduction

The refraction profiles were run parallel to the coast in a general east-west direction. Figures 3-6 show the 13 profiles plotted as reduced record sections where the reducing velocity is

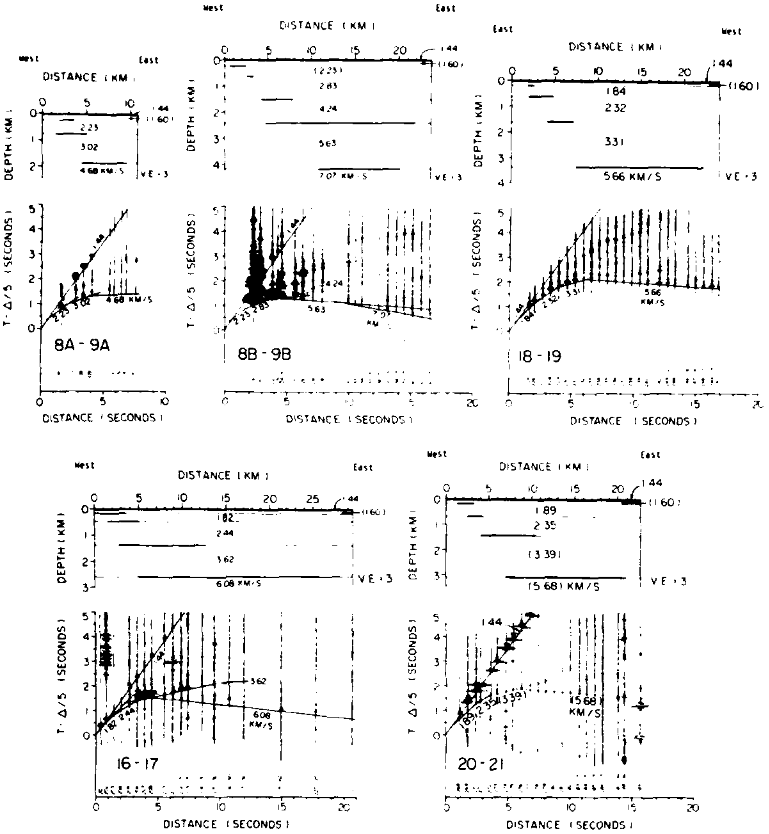

Fig. 3. Lines 8A-9A, 8B-9B, 16-17, 18-19, and 20-21 record sections and velocity-depth model interpretations. The lines are single ended, and the velocities are apparent velocities. Below each seismogram is listed the shot number and the charge weight in pounds. Line 18-19 record section shows second arrivals, between 6 and 14 s, which do correspond to any good refractor but may be sideswipe arrivals from the nearby Barrow Arch.

5.0 km/s. The distance is in water wave travel time seconds where the water velocity was 1.44 km/s. All the velocities are in kilometers per second. Because of the ice problem only three lines were approximately reversed. These reversed pairs are lines 10-11 and 12-13, lines 22A-23 and 24B-25, and lines 24A-25 and 22B-23, where the numbers indicate the end points of the lines. The seven remaining lines (lines 8A-9A, 8B-9B, 16-17, 18-19, 20-21, 26A-27A, and 26B-27B) were interpreted as single-ended lines. The poor quality of the records of line 20-21 did not permit a reversal with line 18-19, as initially planned. We interpreted the data with a classical slope-intercept method (layer solution). The assumptions of the layer solution approach are that the structure is composed of thick, homogeneous layers and that any lateral inhomogeneity takes the form of dip. The choice of this interpretation technique was greatly determined by the quality of our data and the apparent alignment of the arrivals along straight lines. The data are of mediocre quality as a result of the difficult conditions of data acquisition and the limited frequency response of the sonobuoys. Other limitations in the interpretation arise from the fact that the data are not in digitized form and the automatic gain control (AGC) cannot be removed from the seismograms. In light of these limitations and the mediocre quality of the data we did not attempt any amplitude or waveform modeling, and we simply interpreted travel times with a layer solution. We do not preclude the existence of velocity gradients, but our error analysis confirms that a structure with homogeneous plane horizontal or dipping layers is an appropriate physical model. The seismic models determined from slope intercept interpretations of the re-

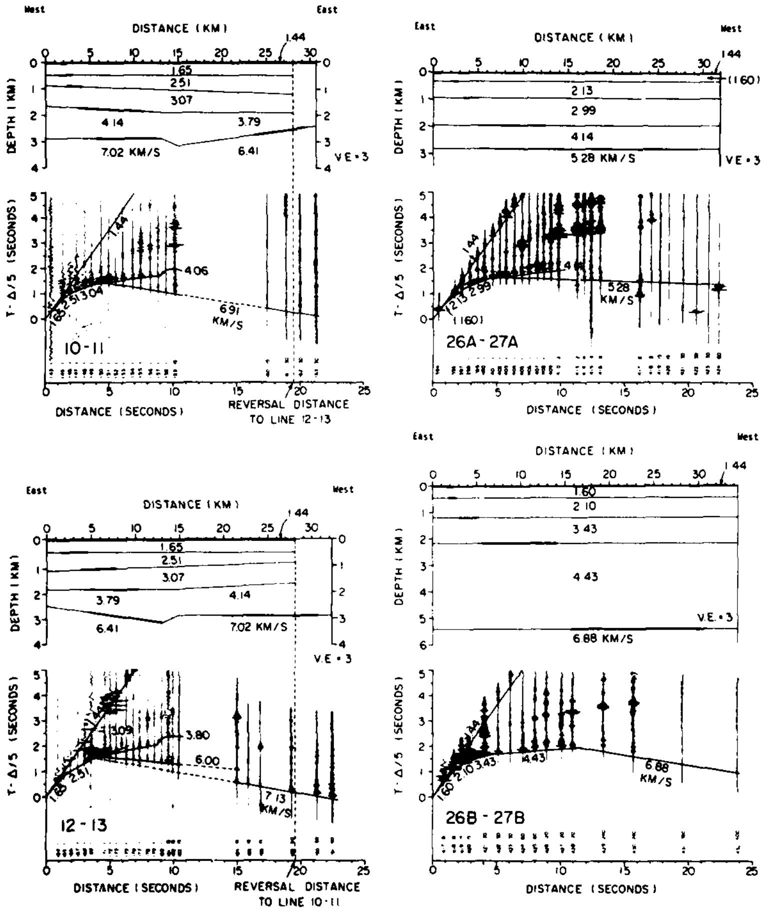

Fig. 4. Lines 10-11, 12-13, 26A-27A, and 26B-27B record sections and velocity-depth model interpretations. Line 10-11 reverses line 12-13, and the corresponding velocity-depth model includes true velocities. Lines 26A-27A and 26B-27B are single ended, and the corresponding velocities are apparent velocities.

duced record sections are shown above the record sections with a vertical exaggeration of 3:1. Heavy lines on the refractors indicate the interfaces responsible for observed arrivals and contain the horizontal offsets for upgoing rays. Only the reversed profiles resulted in true velocities, and on all the single-ended profiles, apparent velocities are assumed to be true velocities. Arrivals from a thin upper sediment layer generally were not detected as first arrivals because of the wide shot spacing, but its presence is required to obtain the observed water depth (about 20 m). Velocities of 1.60 km/s on line 26B-27B and 1.65 km/s on lines 10-11 and 12-13 were obtained for this layer from the arrival on the first seismogram. For other lines the velocity for this layer was assumed to be 1.60 km/s. All estimated velocities are in parentheses. The velocities and thicknesses obtained at each sonobuoy station are listed in Table 1. Table 2 lists apparent velocities obtained from interpretations of the record sections and calculated depths to the refracting interfaces. Where a sufficient number of arrivals existed on a travel time segment, the statistical variation of apparent velocity was calculated using the method of Steinhart and Meyer [1961]. Calculated, and estimated errors of the velocities and intercept times translate into statistical errors in the computed depths of the interfaces; variations of velocity and depth are given in Table 2. The small values of the errors in velocity suggest a strong linear relationship between time and distance and lend confidence to our assumption of the plane-dipping-layer model. This analysis does not address depth errors as-

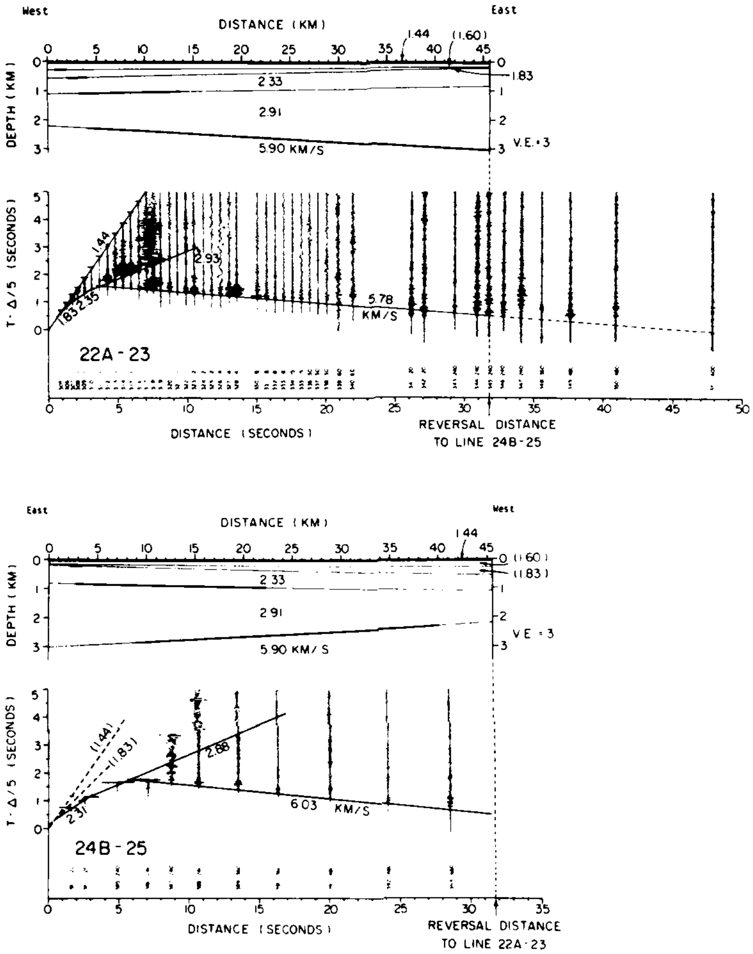

Fig. 5. Lines 22A-23 and 24B-25 record sections and velocity-depth model interpretations. Line 22A-23 reverses line 24B-25, and the velocity-depth model includes true velocities.

sociated with incorrect arrival picks, horizontal velocity variations, and vertical velocity inversions. With reference to the record sections presented in Figures 3-6 the following paragraphs describe the basis for the interpretation of each line and the velocity-depth section computed.

Line 8A-9A was shot to the east close to Cape Simpson and is only 11 km long. The records presented in Figure 3 indicate a poorly determined velocity of 2.23 km/s based on first and second arrivals and two well-determined velocities of 3.02 and 4.68 km/s.

Line 8B-9B (Figure 3) continues line 8A-9A to the east and runs close to and parallel to the coast. The velocity structure is a seven-layer model with refractor velocities of 2.23, 2.83, 4.24, 5.63, and 7.07 km/s. The absence of data at the beginning of the line forced the inclusion of a velocity of 2.23 km/s based on the interpretation of line 8A-9A.

Situated between Cape Simpson and Cape Halkett, line 10-11 (Figure 4) from west to east reversed line 12-13 (Figure 4) from east to west. On both lines the upper layers are well determined and easily reversed resulting in true velocities of 1.44, 1.65, 2.51, and 3.07 km/s. The deeper layers were more difficult to interpret and required manual ray tracing using the formulation of Adachi [1954]. Very strong second arrivals indicate velocities of 4.06 km/s on line 10-11 and 3.80 km/s on line 12-13. Unfortunately, these two apparent velocities do not satisfy

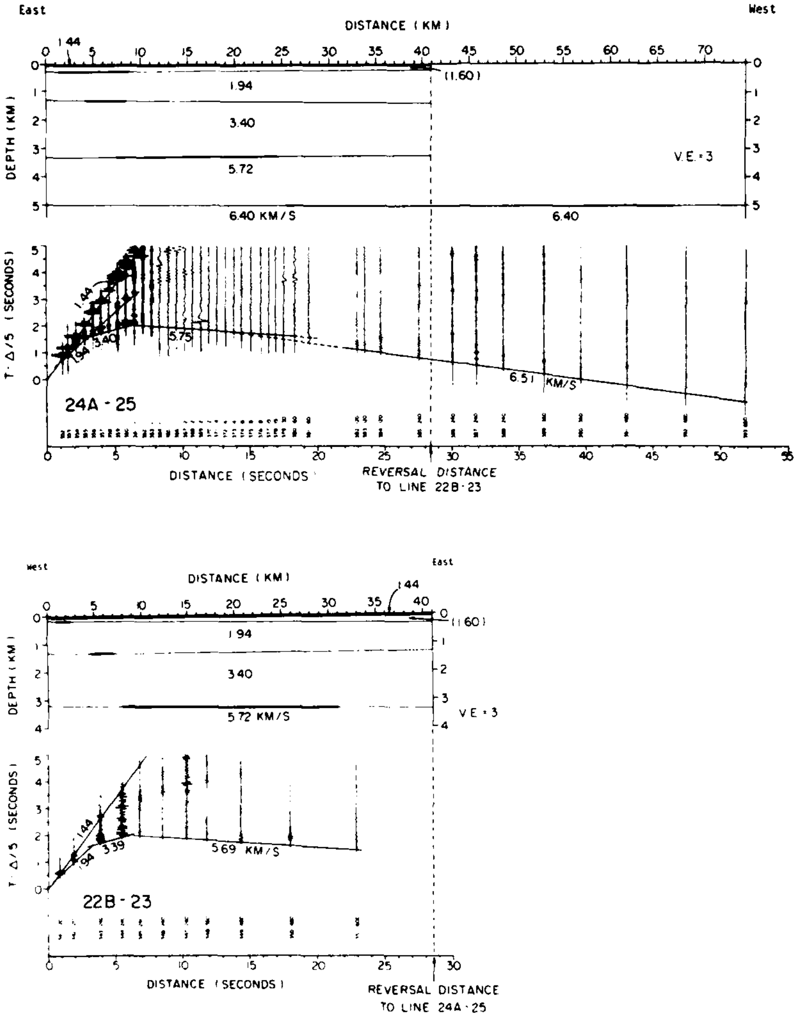

Fig. 6. Lines 24A-25 and 22B-23 record sections and velocity-depth model interpretations. Line 24A-25 reverses line 22B-23, and the velocity-depth model includes true velocities.

the reciprocity condition and both layer velocity and layer dip were required to account for apparent velocities along the profile. The arrivals have been attributed to a 4.14 km/s velocity layer with a downdip of 1° to the west on line 10-11 and to a horizontal refractor with a velocity of 3.79 km/s on line 12-13. For the deepest layer the layer dip and velocity for the western end were adjusted to obtain the observed 6.91 km/s apparent velocity to the east on line 10-11 and the 7.13 km/s apparent velocity to the west on line 12-13. The result is a refractor at about 2.8 km depth with a true velocity of 7.02 km/s which dips up to the east at 0.08°. Repeating this procedure at the eastern end, a 6.00 km/s apparent velocity on line 12-13 and 6.91 km/s apparent velocity on line 10-11 result in a 6.41 km/s refractor at depths of 2.4-3.0 km with a large dip of 3.2° down to the west. This interpretation of the deep layers is not esthetically pleasing because the 6.91 km/s velocity arrivals seem to be continuous on line 10-11 and hence should form a single continuous layer. However, there appears to be no other easy way to explain the lack of 7.13 km/s arrivals in the middle of line 12-13. The reversal travel time

TABLE 1. Table of Velocities and Thicknesses Obtained From Interpretation of the Seismic Refraction Data (see Figures 3-6)

Sonobuoy Station	Position		Velocity (km/s)							Thickness (km)					
	Latitude N	Longitude W	Water	1	2	3	4	5	6	Water	1	2	3	4	5
8A	71°06.34	154°29.90	1.44	(1.60)	2.23	3.02	4.68	----	----	0.02	0.23	0.52	1.10	----	----
8B	71 04.27	154 18.34	1.44	(1.60)	(2.23)	2.83	4.24	5.63	7.07	0.02	0.23	0.39	0.89	0.91	1.75
10	71 01.07	153 23.77	1.44	1.65	2.51	3.07	4.14[a]	7.02[a]	----	0.01	0.47	0.40	0.79	1.22	----
12	70 58.46	152 39.57					3.79[b]	6.41[b]	----	0.01	0.47	0.72	0.70	0.66	----
16	70 58.65	152 36.55	1.44	(1.60)	1.82	2.44	3.62	6.08	----	0.02	0.14	0.31	0.91	1.23	----
18	70 32.49	148 42.78	1.44	(1.60)	1.84	2.32	3.31	5.66	----	0.02	0.18	0.43	0.98	1.76	----
20	70 37.53	150 38.68	1.44	(1.60)	1.89	2.35	(3.39)	(5.68)	----	0.02	0.17	0.51	0.74	1.63	----
22A	71 00.10	152 00.20	1.44	(1.60)	1.83	2.33	2.91	5.90	----	0.02	0.27	0.28	0.54	1.10	----
24B	70 48.52	150 51.40								0.02	0.14	0.03	0.64	2.20	----
22B	70 53.30	151 03.56	1.44	(1.60)	1.94	3.40	5.72	6.40	----	0.02	0.28	1.00	2.03	1.67	----
24A	70 40.85	150 04.40								0.02	0.15	1.16	1.87	1.81	----
26A	71 03.33	153 01.68	1.44	(1.60)	2.13	2.99	4.14	5.28	----	0.02	0.31	0.62	1.01	0.87	----
26B	71 07.55	153 40.20	1.44	1.60	2.10	3.43	4.43	6.88	----	0.02	0.42	0.76	0.96	3.24	----

Brackets indicate reversed line. The reversed lines have true velocities. The single-ended lines have apparent velocities.
Parentheses indicate estimated velocity.
[a] For west half of reversed line only.
[b] For east half of reversed line only.

for the model agrees with the observed travel time to within 0.05 s. The absence of data in the middle of these two lines is due to helicopter launches while the ship continued underway.

Line 16-17 shown in Figure 3 lies close to Cape Halkett and extends for a distance of 30 km to the east. The records are slightly noisy, and the only two velocities really well-determined are a 1.82 km/s velocity based on first arrivals and a 3.62 km/s velocity based on strong first and second arrivals. An intermediate 2.44 km/s velocity and a higher 6.08 km/s velocity are suggested, but the evidence is weaker.

Line 18-19 (Figure 3) is the easternmost line of the study and extends from nearly Prudhoe Bay toward the west. On line 18-19, first arrivals close to the origin with an apparent velocity of 1.84 km/s are followed by strong first arrivals which indicate apparent velocities of 2.32 and 3.31 km/s. These are followed by a long segment with a velocity of 5.66 km/s.

Line 20-21, shown in Figure 3, runs from west to east close to Oliktok Point. The records are very noisy because of a substandard sonobuoy; most velocities have been estimated by comparison to line 18-19.

In Harrison Bay, line 22A-23 (Figure 5) from west to east and line 24B-25 (Figure 5) from east to west are reversed over a distance of 46 km. Line 22A-23 shows strong arrivals over its total length of 69 km (the last 35 km of the line are helicopter records) and first seen are two first arrival apparent velocities of 1.83 and 2.35 km/s. The apparent velocity of 2.93 km/s is based mainly on strong second arrivals, and the highest apparent velocity of 5.78 km/s can be seen almost over the entire remaining length of the line.

Line 24B-25 has less data but shows strong arrivals for the determination of 2.31, 2.88, and 6.03 km/s apparent velocities. A 1.83 km/s velocity had to be estimated because no data exist close to the origin. The large amplitude and high frequency of the waves at the beginning of the line overdrove the recorder, but the water waves visible later on individual seismograms permitted calculation of the shot distance for the reduced section. The corresponding velocity structure with true velocities and dipping layers is a six-layer model with layers of velocities 1.83, 2.33, and 2.91 km/s. The deepest layer has a velocity of 5.90 km/s, and the interface dips down to the east with a 1° dip from a depth of 2.20-3.03 km.

Also situated in Harrison Bay, line 24A-25 (Figure 6) from east to west and line 22B-23 (Figure 6) from west to east reverse over a distance of 41 km. On line 24A-25, first arrivals close to the origin and second arrivals at greater distances show a 1.94 and a 3.40 km/s velocity. Evidence for a higher velocity of 5.75 km/s is less convincing on these records because of noisy traces and a lack of strong clear arrivals. Line 24A-25 out to a distance of 75 km is the longest line of the study, and helicopter records on the most distant portion show a 6.51 km/s velocity. The corresponding velocity on line 22B-23 was not seen, and hence the interpretation had to be treated with manual ray tracing. The strong first arrivals of line

TABLE 2. Table of Apparent Velocities Obtained From Interpretations of the Record Sections (see Figures 3-6) and Their Standard Deviations, Together With the Calculated Depths to the Refracting Interfaces and Their Standard Deviations

Sonobuoy Station	Apparent Velocity (km/s) ± Standard Deviation						Depth (km) ± Standard Deviation					
	1	2	3	4	5	6	Water	1	2	3	4	5
8A	(1.60)	2.23	3.02	4.68	----	----	0.02	0.24	0.76	1.86	----	----
	(±.03)	(±.03)	±.02	±.19				±.04	±.06	±.07		
8B	(1.60)	(2.23)	2.83	4.24	5.63	7.07	0.02	0.24	0.63	1.52	2.43	4.18
	(±.03)	(±.03)	(±.03)	(±.03)	±.02	±.16		±.04	±.07	±.09	±.09	±.13
10	1.65	2.51	3.04	4.06	6.91	----	0.01	0.48	0.88	1.67	2.89	----
	(±.03)	(±.03)	(±.03)	±.02	±.05			±.03	±.07	±.08	±.08	
12	1.65	2.51	3.09	3.80	6.00	7.13	0.01	0.48	1.20	1.89	2.55	----
	(±.03)	(±.03)	±.03	(±.02)	±.03	±.17		±.03	±.08	±.08	±.08	
16	(1.60)	1.82	2.44	3.62	6.08	----	0.02	0.16	0.47	1.37	2.60	----
	(±.03)	(±.03)	(±.03)	±.01	±.04			±.05	±.07	±.07	±.07	
18	(1.60)	1.84	2.32	3.31	5.66	----	0.02	0.20	0.62	1.60	3.36	----
	(±.03)	(±.03)	(±.03)	(±.03)	±.08			±.05	±.07	±.08	±.09	
20	(1.60)	1.89	2.35	(3.39)	(5.68)	----	0.02	0.18	0.69	1.43	3.06	----
	(±.03)	(±.03)	(±.03)	(±.20)	(±.20)			±.05	±.07	±.34	±.54	
22A	(1.60)	1.83	2.35	2.93	5.78	----	0.02	0.28	0.56	1.10	2.20	----
	(±.03)	(±.03)	(±.03)	(±.03)	±.06			±.05	±.07	±.09	±.10	
24B	(1.60)	(1.83)	2.31	2.88	6.03	----	0.02	0.16	0.19	0.83	3.03	----
	(±.03)	(±.03)	(±.03)	(±.03)	±.12			±.05	±.07	±.09	±.10	
22B	(1.60)	1.94	3.39	5.69	----	----	0.02	0.30	1.30	3.33	5.00	----
	(±.03)	(±.03)	(±.03)	±.05				±.04	±.06	±.06	±.14	
24A	(1.60)	1.94	3.40	5.75	6.51	----	0.02	0.16	1.32	3.19	5.00	----
	(±.03)	(±.03)	(±.03)	±.03	±.08			±.04	±.06	±.06	±.15	
26A	(1.60)	2.13	2.99	4.14	5.28	----	0.02	0.32	0.94	1.95	2.82	----
	(±.03)	(±.03)	(±.03)	±.01	(±.03)			±.04	±.06	±.09	±.13	
26B	1.60	2.10	3.43	4.43	6.88	----	0.02	0.44	1.20	2.16	5.40	----
	(±.03)	(±.03)	(±.03)	±.01	±.09			±.04	±.06	±.06	±.06	

Water layer velocity = 1.44 km/s. Parentheses indicate estimated velocity. Standard deviations of velocities and associated depths obtained using the method of Steinhart and Meyer [1961].

22B-23 show clearly 1.94, 3.39, and 5.69 km/s velocities. This seismic model (Figure 6) shows velocities different from those of other lines situated in Harrison Bay (see lines 22A-23 and 24B-25 in Figure 5). For example, the 2.33 km/s velocity (Figure 5) is not seen in Figure 6 and the 1.83 and 2.91 km/s velocities (see Figure 5) increase to 1.94 and 3.40 km/s, respectively, in Figure 6. Although the 5.90 km/s velocity (see Figure 5) is similar to the 5.72 km/s of model 22B-24A (see Figure 6), there is an additional higher velocity of 6.40 km/s present in Figure 6. The apparent velocity of 6.51 km/s had to be explained by ray tracing through the two reversed models, where the downgoing ray travels through model 24A-22B (obtained from reversing lines 24A-25 and 22B-23) and upgoing ray travels through model 22A-24B (obtained from reversing lines 22A-23 and 24B-25). The best fit is a horizontal layer at a depth of 5.0 km with a true velocity of 6.40 km/s. The travel time at the reversal distance from the model agrees with the observed travel time to within 0.04 s.

Line 26A-27A shown in Figure 4 profiles from east to west and lies at the western end of the study area close to Cape Simpson but more offshore than lines 8A-9A and 8B-9B. A 1.60 km/s velocity is weakly determined but is based on one first arrival and one second arrival. The subsequent first arrivals are strong and clear, and they show apparent velocities of 2.13 and 2.99 km/s. Strong second arrivals have a 4.14 km/s apparent velocity, while 5.28 km/s apparent velocity arrivals are weak because of the noisy traces of the end of the line. The seismic model extends to a distance of 32 km and to a depth of about 3.0 km. The general ringing nature of the traces is typical of shelf profiles due to uniform layering, shallow water, and the bubble pulse associated with the explosion. There are two packets of high-energy second arrivals at 10-15 s range, one at 3 s reduced time and the second at about 4 s reduced time, both with apparent velocities around 4.14 km/s. These arrivals are reverberations which probably are P wave that have been multiply reflected within the basement layer (within the two layers with apparent velocities of 2.13 and 2.99 km/s).

Line 26B-27B (Figure 4) is 34 km long and is the western extension of line 26A-27A. It shows velocities of 2.10, 3.43, and 4.43 km/s for the upper layers similar to the velocities of line 26A-27A. A higher velocity of 6.88 km/s at a depth of 5.4 km is poorly determined by weak first arrivals. It indicates an increase in velocity and depth for the deeper layers compared to line 26A-27A.

Data Interpretation

Comparison of the refraction profiles to other data was done by correlating refraction veloci-

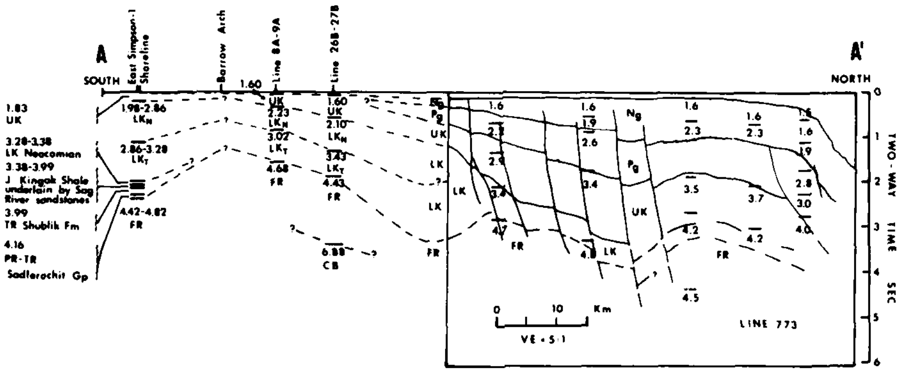

Fig. 7. Section AA', geologic cross section tentatively interpreted from seismic refraction data (lines 8A-9A and 26B-27B of this study), seismic reflection data (line 773 in Figure 13C of Grantz et al. [1981], and well data (East Simpson 1 test well from Witmer et al. [1981a] and NOAA [1982]. Section AA' extends north of Cape Simpson across the western Beaufort Shelf (see Figure 1 for location). Inferred rock units are Ng, Neogene; Pg, Paleogene; UK, Upper Cretaceous; LK, Lower Cretaceous; LK_N, Lower Cretaceous Nanushuk Group; LK_T, Lower Cretaceous Torok Formation; J, Jurassic; TR, Triassic; PR-TR, Permo-Triassic; FR, Franklinian Sequence; CB, crystalline basement.

ties and depths to interpreted common depth point reflection data [Grantz et al., 1981], vibroseis data [Cobb, 1974], onshore well data [Alaska Geological Society, 1971, 1972, 1977; Morgridge and Smith, 1972; Cobb, 1974; Witmer et al., 1981a; NOAA, 1982], other seismic surveys near the study area [Dana, 1951; Woolson et al., 1962; Hunkins, 1966; Hofer and Varga, 1972; Grantz et al., 1975; Johnson and Chiburis, 1977], and the geological information summarized earlier in this paper. The amplitude information was not used for the interpretation since the receivers were military sonobuoys with nonlinear response. Four cross sections shown in Figures 7-10 describe the velocity-depth-age information of the western Beaufort Shelf.

Section AA'

Section AA' (see Figure 1 for location) is situated near Cape Simpson at the western end of our study area and extends across the Barrow Arch from south to north through the East Simpson 1 test well [Witmer et al., 1981a; NOAA, 1982], refraction lines 8A-9A and 26B-27B of this study and reflection line 773 of Grantz et al. [1981, Figure 13C]. When correlating seismic velocities, one has to keep in mind that the sonobuoy refraction velocities tend to be somewhat higher than the interval velocities derived from common depth point stacking velocities and from borehole sonic logs [Eittreim and Grantz, 1979]. Also, it is not certain that velocity correlations across the Barrow Arch indicate stratigraphic correlations. Such correlations can only be demonstrated conclusively by offshore wells. Nevertheless, section AA', shown in Figure 7, demonstrates that sedimentary thicknesses and velocities obtained from the refraction and reflection surveys and from the test wells are in good agreement. The 1.60 km/s velocity of lines 8A-9A and 26B-27B is interpreted to represent the Upper Cretaceous rocks present near the surface onshore and offshore. Grantz et al. [1981] reported that on the western part of the Beaufort Shelf the Tertiary is present only from the midshelf areas to the continental slope (as indicated by their reflection profile line 773 in section AA'). However, as the 1.60 km/s velocity seen on lines 8A-9A and 26B-27B does not exclude the possibility of the presence of a thin layer of Tertiary age, our refraction data do not show how far south the Tertiary beds extend under the shelf in section AA'. A thick (~1.6 km) section of Lower Cretaceous rocks is present under lines 8A-9A and 26B-27B. The upper part of the section has velocities of 2.23 and 2.10 km/s at depths of about 0.2-0.4 km and is associated to rocks of the Nanushuk Group. The lower part of the section with velocities of 3.02 and 3.43 km/s at depths of 0.8-1.2 km is interpreted to represent beds of the Torok Formation. The Jurassic, Triassic, and Permian strata present onshore at East Simpson 1 are not detected by our refraction study on the southern part of the shelf. Our seismic data do not show to what extent these rocks continue across the crestal zone of the arch to underlie the western Beaufort Shelf, but they are probably truncated along the flank of the Barrow Arch. Velocities of 4.68 and 4.43 km/s are associated to Franklinian argillites and phyllites. The Franklinian basement lies at depths of 1.9 km under line 8A-9A and 2.2 km under line 26B-27B, suggesting an apparent seaward dip. A deeper refractor (5.4 km depth) with a high velocity of 6.88 km/s is detected only under line 26B-27B and is interpreted as crystalline basement, probably granite, by comparison with velocities and depths observed by others: a 6.2 km/s velocity at 6.0-km depth underlying the Franklinian basement at Point Barrow [Hunkins, 1966], a velocity of 6.4 km/s interpreted as granite underlaying Franklinian rocks at Cape Simpson [Dana, 1951] and on the shelf west of Point Barrow a 6.4 km/s veloc-

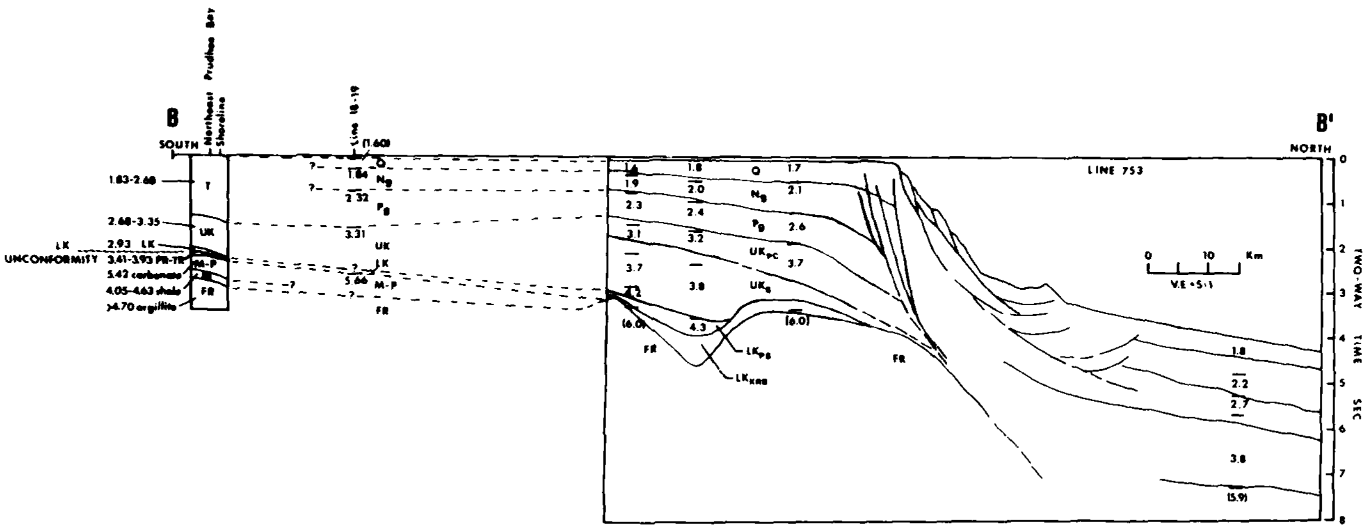

Fig. 8. Section BB', geologic cross section tentatively interpreted from seismic refraction data (line 18-19 of this study), seismic reflection data (line 753 in Figure 13B of Grantz et al. [1981], and vibroseis data (Figure 8 of Cobb [1974]). Section BB' extends north of Prudhoe Bay across the western Beaufort Shelf (see Figure 1 for location). Inferred rock units are Q, Quaternary; T, Tertiary; Ng, Neogene; Pg, Paleogene; UK, Upper Cretaceous; UK_{PC}. Upper Cretaceous Prince Creek Formation; UK_S, Upper Cretaceous Schrader Bluff Formation; LK, Lower Cretaceous; LK_{PS}, Lower Cretaceous "Pebble Shale"; LK_{KRS}, Lower Cretaceous Kuparuk River Sandstone; PR-TR, Permo-Triassic; M-P, Mississippian-Pennsylvanian; M, Mississippian; FR, Franklinian Sequence.

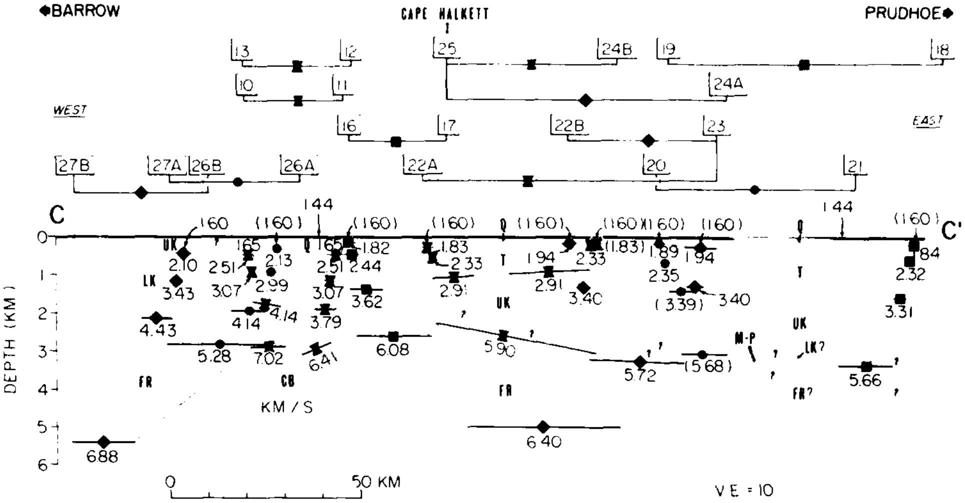

Fig. 9. Section CC', geologic cross section tentatively interpreted from seismic refraction data and the interpretations of sections AA' and BB' (Figures 7 and 8). Section CC' extends along the western Beaufort Shelf parallel to the coastline from the west near Cape Simpson to the east near Prudhoe Bay (see Figure 1 for location). The different shaped symbols along each interface correspond to the appropriate refraction lines shown at the top of the figure. Heavy lines on the refractors indicate the interfaces responsible for observed arrivals and contain the horizontal offsets for upgoing rays. Inferred rock units are Q, Quaternary; T, Tertiary; UK, Upper Cretaceous; LK, Lower Cretaceous; M-P, Mississippian-Pennsylvanian; FR, Franklinian Sequence; CB, crystalline basement.

ity at a depth of 3.0 km thought to be granite [Johnson and Chiburis, 1977]. Reflection profile line 773 in section AA' does not suggest any crystalline basement rocks, probably indicating that the crystalline basement lies deeper than the maximum reflection penetration of 4.0 s of two-way travel time. In section AA' the thicknesses and depths of the sedimentary beds directly above the Barrow Arch are not constrained.

Section BB'

At the eastern end of our study area, near Prudhoe Bay, section BB' (see Figure 1 for location) extends from south to north through a vibroseis profile from the northeast part of the Prudhoe Bay field interpreted with seismic and stratigraphic results from a nearby test well [Figure 8 of Cobb, 1974], through refraction line 18-19 of this study and reflection line 753 of Grantz et al. [1981, Figure 13B]. Section BB', shown in Figure 8, is situated on the northern flank of the Barrow Arch and indicates that north of Prudhoe Bay the sedimentary strata dip gently seaward. The interpretation of line 18-19 associates velocities of 1.60 km/s to quaternary rocks, 1.84 km/s to Neogene beds, 2.32 km/s to Paleogene beds, 3.31 km/s to Upper Cretaceous strata, and 5.66 km/s to Mississippian-Pennsylvanian carbonates. Under line 18-19 the Tertiary section is 1.4 km thick, and the Upper Cretaceous beds have a thickness of approximately 1.8 km. The possible presence of thin Lower Cretaceous beds at the base of the Upper Cretaceous rocks is discussed later in the discussion section. The vibroseis profile indicate that the Permo-Triassic oil-rich Prudhoe Bay rocks are truncated by erosion near the shoreline where they are unconformably overlain by the Lower Cretaceous beds. This is consistent with offshore results obtained from our refraction study near the coast and the reflection study of Grantz et al. [1981] near the continental slope, since neither seismic surveys detected any Permo-Triassic beds. The Franklinian basement was not detected under line 18-19 probably because its velocity (4.70 km/s for upper Franklinian beds onshore at a Prudhoe Bay test well) is lower than the highly compacted overlying carbonates of the Lisburne Group (5.42 km/s onshore and 5.66 km/s on the southern shelf). The thickness and the exact seaward extent of the Mississippian-Pennsylvanian layer is not constrained, but the layer probably pinches out in the midshelf area since it is not seen on the reflection profile line 753 of Grantz et al. [1981].

Section CC'

Section CC' shown in Figure 9 extends from the west, near Point Barrow, to the east, near Prudhoe Bay, and summarizes the subsurface velocity and depth information calculated from the refraction data. The heavy lines on the interfaces, corresponding to the observed arrivals as shown in Figures 3-6, were projected onto

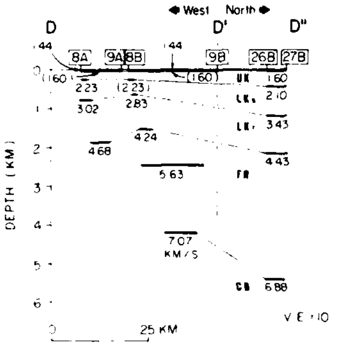

Fig. 10. Section DD'D", Geologic cross section tentatively interpreted from seismic refraction data and the interpretation of section AA' (Figure 7). Section DD'D" is located north of Smith Bay (see Figure 1 for location). Inferred rock units are UK, Upper Cretaceous; LK_N, Lower Cretaceous Nanushuk Group; LK_T, Lower Cretaceous Torok Formation; FR, Franklinian Sequence; CB, crystalline basement.

a composite section which passes through the profiles (see Figure 1 for location). The small symbols along each interface correspond to the appropriate refraction lines shown at the top of the figure. Section AA' (Figure 7) at the west end of section CC' and section BB' (Figure 8) at the east end constrain the correlation between the seismic velocities and the age of the formations. The refraction layers from adjacent lines have been correlated on the basis of velocity, as indicated in section CC' by light lines. The surface layer with velocities of 1.60-1.65 km/s and a thickness of 0.2-0.4 km is associated with the Gubik Formation of Quaternary age. These Quaternary rocks are underlain by Tertiary strata with seismic velocities of 1.82-2.35 km/s. This agrees with the results of Grantz et al. [1975] from an air gun sonobuoy profile parallel to the western Beaufort coast 48 km offshore where an observed 1.8-2.9 km/s velocity layer is correlated with the Tertiary section observed in the Prudhoe Bay wells. In section CC' the Tertiary beds have thicknesses of 1.4 km near Prudhoe Bay, and as they are not seen in the western part of the profiles, they probably pinch out just west of Cape Halkett. A layer which dips down and thickens from near-surface depths and thicknesses of nearly 0.4 km in the western part of the profiles to depths of around 1.6 km and thicknesses of approximately 1.8 km in the eastern part of the profiles is correlated with Upper Cretaceous sediments. The Upper Cretaceous velocities range from 1.6 to 2.5 km/s west of Cape Halkett and are higher (2.91-3.40 km/s) east of Cape Halkett. In the western part of the profiles the Upper Cretaceous beds are underlain by a thick (1.0 to 2.5 km) sedimentary section from depths of about 0.5 to 2.8 km. This layer with velocities ranging from 2.10 to 4.14 km/s is correlated to Lower Cretaceous rocks. The Lower Cretaceous layer is not seen east of station 17 either because it is truncated by erosion or it is too thin to be detected with these data. However, the interpretation of section BB' north of Prudhoe Bay (Figure 8) suggests that in the eastern part of the profiles, thin (probably less than 250 m) Lower Cretaceous strata are present at the base of the thick Upper Cretaceous section. The velocities (1.60-4.14 km/s) of the thick Cretaceous section are in good agreement with previous sonobuoy refraction work done near the western Beaufort continental slope [Grantz et al., 1975] where, north of Point Barrow, velocities of 3.1-3.2 km/s were associated with Albian shales and sands and, north of Prudhoe Bay, velocities nominally 3.8 km/s were associated with Upper Cretaceous rocks. The velocities of the Cretaceous beds also agree with a velocity of 3.0 km/s attributed to Cretaceous shales and sands in a long reversed refraction line trending northwestward from Point Barrow [Hunkins, 1966] and with interval velocities obtained from a reflection survey conducted east of Prudhoe Bay in the Mackenzie Bay where a thick section of shales and sands largely Cretaceous is characterized by velocities ranging from 1.67 to 4.27 km/s [Hofer and Varga, 1972]. Geologic information indicates that the Franklinian basement dips eastward and lies at a depth of 0.8 km at Point Barrow [Dana, 1951; Morgridge and Smith, 1972], 2.0 km at Cape Simpson [Robinson, 1959], and approximately 3.5 km at Prudhoe Bay [Brosgé and Tailleur, 1970; Rickwood, 1970; Morgridge and Smith, 1972]. Hence the layer which dips eastward at about these depths is probably the Franklinian basement composed of argillite and phyllite with P wave velocities ranging from 4.43 to 6.08 km/s. These velocities are in agreement with velocities reported by other authors and interpreted to represent the Franklinian basement: 4.9-5.9 km/s offshore near the western Beaufort continental slope [Grantz et al., 1975], 5.2 km/s at Cape Simpson [Dana, 1951], 5.5-6.1 km/s at Point Barrow [Woolson et al., 1962], 4.9 km/s north of Point Barrow [Hunkins, 1966], and 5.1 km/s west of Point Barrow [Johnson and Chiburis, 1977]. In the eastern part of the profiles, velocities of 5.66-5.68 km/s are correlated with Mississippian-Pennsylvanian compacted high-velocity carbonates as pointed out earlier in the interpretation of section BB'. A higher velocity layer of 6.40-7.02 km/s shallows beneath stations 10-12 but is not detected beyond station 20 to the east. This high-velocity layer is thought to be a crystalline basement and is tentatively identified as silicic in character (see section AA' interpretation; see also crystalline basement arch interpretation in the discussion section).

Section DD'D"

Section DD'D" in Figure 10 is a section at the west end of section CC' which shows velocity and depth changes between two nearshore lines and the midshelf areas. Section DD'D" indicates that on the north side of the Barrow Arch, sediments dip to the northeast.

Discussion

Figures 7-10 demonstrate that the beds of the sedimentary prism dip and prograde to the northeast. This was expected as our study area lies

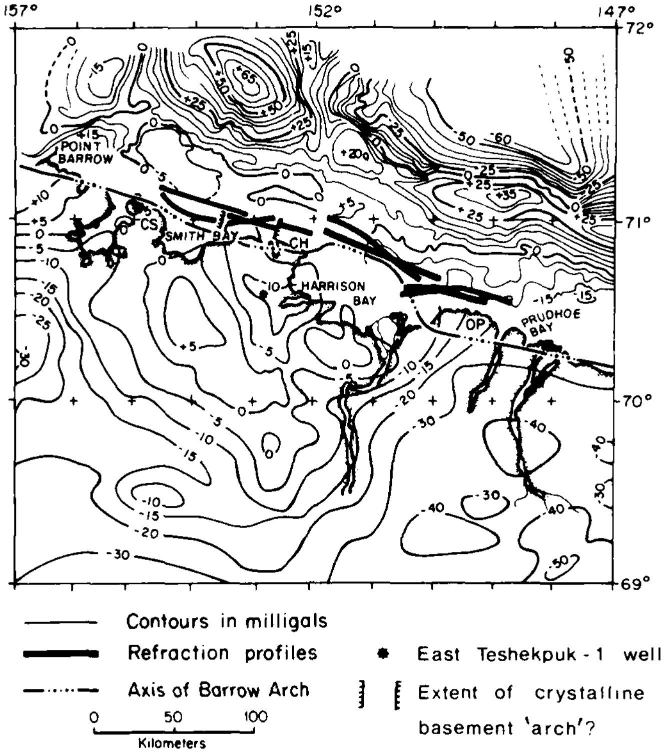

Fig. 11. Gravity anomaly map of northern Alaska together with the locations of refraction profiles. Offshore free air gravity anomalies from Dehlinger [1978] and land Bouguer anomalies from Woolson et al. [1962]. CS, Cape Simpson; CH, Cape Halkett; OP, Oliktok Point.

seaward of the northern flank of an east-southeasterly plunging anticline (Barrow Arch). A northeasterly dipping progradational sedimentary prism under the western Beaufort Shelf is in agreement with earlier geological and geophysical studies in the same area [Woolson et al., 1962; Hunkins, 1966; Rickwood, 1970; Wold et al., 1970; Morgridge and Smith, 1972; Grantz et al., 1975, 1979, 1981; and others].

The refraction profiles lie in a region of low-gravity gradient between moderate gravity highs on land and a series of substantial gravity highs at the edge of the upper continental slope (Figure 11). The near absence of drastic changes in the gravity anomalies under the western Beaufort Shelf is in accord with the linearity and uniformity of the structure as shown in Figures 7-10. The only feature which disturbs this linearity is a crystalline basement arch (see Figure 9) that is discussed later in this section.

A minimum depth estimate for the Mohorovicic discontinuity along the line of profiles is 20 km because velocities higher than 6.40 km/s are not detected to distances of 75 km (line 24A-25) and because the upper mantle velocity in the region has been measured at about 8.3 km/s [Mair and Lyons, 1981]. The minimum crustal thickness of 20 km under the western Beaufort Shelf determined from this study adds no new information on how the crust thins seaward from a continental level of approximately 35 km assumed from gravity [Wold et al., 1970] to crustal thicknesses of 13-17 km in the Canada Basin obtained from refraction studies [Milne, 1966; Baggeroer and Falconer, 1982] and from gravity measurements [Wold et al., 1970]. Seaward thinning of the crust has been reported to the east on the Canadian side of the Canada Basin from gravity and refraction surveys. These studies find crustal thicknesses of 35-38 km on the continent near the coast [Sander and Overton, 1965; Overton, 1970; Sobczak and Weber, 1973], around 23 km under the shelf [Sobczak and Weber, 1973], and thicknesses of about 18 km in the Canada Basin [Berry and Barr, 1971]. Therefore there seems to be evidence for thinning of the crust from the continent to the Canada Basin which would indicate a transition from continental to oceanic crust. Thin crust, water depths exceeding 3.5 km [Grantz et al., 1975] together with dispersion patterns of Lg phase seismic waves [Oliver et al., 1955] suggest that the Canada Basin is underlain by oceanic crust. The suggestion is that it formed by seafloor spreading.

As reported above, geophysical data tend to support the idea that the western Beaufort continental margin is linear and progradational at least in its shallower sedimentary beds and that it faces the Canada Basin, a deep basin underlain by oceanic crust. The Beaufort continental margin is therefore not different from continental margins of Atlantic type.

A major feature on section CC' shown in Figure 9 is an anomalous basement feature, which rises to a minimum depth of 3.0 km under the reversed lines 10-11 and 12-13. The arch is at least 20 km wide and is characterized by high seismic velocities of 6.41-7.02 km/s. It is uncertain whether this basement high represents the variability of seismic velocity within material of the same composition or whether there is a change in composition. However, a gravity low extending northerly to line 10-12 (Figure 11; see also National Petroleum Reserve in Alaska gravity maps from NOAA, [1982] suggests that the change in velocity under line 10-12 is the result of a change in composition (from argillite and phyllite to crystalline rocks). Approximately 40 km south of line 10-12 on the southern flank of the Barrow Arch, an onshore well (see Figure 11 for location of East Teshekpuk 1 well) bottomed in granite at about 3.2 km depth [Bird et al., 1978]. This granite was the first in situ granite found in the subsurface north of the Brooks Range. In northern Alaska, granite batholiths are characterized by gravity lows [Bird et al., 1978], and thus the gravity low contours delineate the aeral extent of the batholith. In Figure 11 the gravity low (-5 mGal contour) between Smith Bay and Harrison Bay is irregularly shaped but elongates northerly over the Barrow Arch toward line 10-12. The anomalous basement feature shown in section CC' (Figure 9) could possibly be the northern extension of a granitic batholith at depths around 3.0 km. If this correlation is valid, it implies that the crystalline basement is granitic and favors, as discussed below, a rifted and rotated Beaufort continental margin. The possible implications of this previously unknown basement arch regarding offshore petroleum potential are discussed later. The fact that the sedimentary beds overlying the crystalline basement arch seem to be structurally undisturbed (see Figure 9) supports a pre-Franklinian age for the basement high.

The origin of the Canada Basin, of which the Beaufort Sea occupies the southeastern part, is of prime importance for the evaluation of the petroleum potential of the continental shelf north of Alaska. Carey [1955], Tailleur [1969, 1973], and Rickwood [1970] suggested that the Canada Basin was formed by a relative rotation of northern Alaska away from the Canadian Arctic Islands about a pole near the Mackenzie Delta or in Alaska. This theory implies that the Beaufort Sea margin is a rifted and rotated margin. Other hypotheses have been proposed for the origin of the Canada Basin and have implied that the Beaufort continental margin is a rifted and simply translated margin, a subduction margin, or a sheared or transformed margin [Churkin, 1973; Herron et al., 1974; Vogt and Avery, 1974; Yorath and Norris, 1975; Bally, 1976; Churkin and Trexler, 1980; Jones, 1980]. However, the idea of rifting involving a counterclockwise rotation of Alaska away from Canada now generally has been accepted [Sweeney et al., 1978; Newman et al., 1979] (for a summary see Grantz et al., [1979]). The main uncertainty remaining is the time of formation of the Canada Basin. Depending on the geological and the geophysical data used, proposed ages of opening vary from Early Jurassic [Tailleur, 1969, 1973; Grantz et al., 1979], to Late Jurassic to Early Cretaceous [Rickwood, 1970; Newman et al., 1979; Taylor et al., 1981], and Early Cretaceous [Sweeney et al., 1978; Baggeroer and Falconer, 1982]. Grantz et al. [1979] have reported geological similarities between northern Alaska and the Canadian Arctic Islands; they noted that the Ellesmerian strata are closely correlative and lithologically similar and, in both areas, the Paleozoic rocks extend to the upper continental slope. The sediments of the western Beaufort Shelf and the Canadian Shelf prograde seaward; sediment thicknesses under the western Beaufort shelf increase from 1.0-3.0 km at the coast [Grantz et al., 1981; this study] to about 6.0-8.0 km at the base of the continental slope [Grantz et al., 1981] and are comparable to thicknesses of sediments under the Canadian Shelf: a few kilometers at the coast and 3.5-6.5 km under the continental slope [Berry and Barr, 1971; Sobczak and Weber, 1973]. In this section we will compare the western Beaufort Shelf seismic velocities obtained from our study to seismic velocities obtained from refraction experiments conducted in the Canadian Arctic Archipelago [Hobson, 1962; Sander and Overton, 1965; Hobson and Overton, 1967; Overton, 1970; Berry and Barr, 1971; Sobczak and Weber, 1973] in order to add seismic similarities to the geologic similarities noted above. The velocities (1.60-4.14 km/s) and the depths (a few hundred meters to 3.3 km) of the Mesozoic layer of the western Beaufort Shelf are in good agreement with velocities around 4.00 km/s down to 4.0 km depths reported by Sander and Overton [1965] for Mesozoic beds in the Canadian Arctic Archipelago. The Franklinian basement composed of argillite and phyllite with P wave velocities ranging from 4.24 to 6.08 km/s dipping from depths of 1.5 km to the west to depths of 3.5 km to the east correlates well with velocities interpreted to represent the Franklinian basement in the Canadian Arctic Archipelago: 6.0 km/s at depths greater than 4.0 km [Sander and Overton, 1965], 5.72 km/s at 5.0 km depth [Berry and Barr, 1971], and 5.80 km/s at 3.0 km depth [Overton, 1970]. The velocities (6.40-7.07 km/s) of the crystalline basement (probably granite), which underlies the Franklinian basement at depths of 3.0-5.4 km, are a little higher but similar to velocities reported in the Canadian Arctic Archipelago and associated with a crytalline basement probably granitic in character: 6.25 km/s at depths of 4.0-7.0 km [Hobson, 1962] and 6.00-6.25 km/s at depths of 10.0 km or more [Hobson and Overton, 1967; Overton, 1970; Sobczak and Weber, 1973]. There is a perhaps coincidental agreement between crustal velocities observed in this study and those observed in the Canadian Arctic Archipelago. If this comparison is valid, the theory of opening of the Canada Basin by a rotation of Alaska away from Canada [Carey, 1955;

Tailleur, 1969, 1973; Rickwood, 1970; Freeland and Dietz, 1973; Grantz et al., 1979; Newman et al., 1979; Sweeney et al., 1978; Taylor et al., 1981; Baggeroer and Falconer, 1982] provides an adequate explanation of the seismic observations and implies that the continental crystalline basement is silicic in character. This is consistent with the above observation of a crystalline basement arch probably of granitic composition. A rifted and rotated Beaufort margin is also consistent with the indication reported earlier that the Canada Basin is underlain by oceanic crust.

The evaluation of the western Beaufort Shelf as a potential petroleum province is particularly timely because of recent offshore lease sales in the Beaufort Sea. In the Prudhoe Bay field the main reservoirs where oil was found are the Mississippian-Pennsylvanian carbonates and the Permo-Triassic sandstones and to a less extent the Lower Cretaceous Kuparuk River sandstones and Upper Cretaceous West Sak sands [Jones and Speers, 1976; Jamison et al., 1980]. Onshore farther west, in the Simpson area, oil was found in Lower Cretaceous (late Albian) sandstones of the Nanushuk Group [Jamison et al., 1980]. The refraction data, together with the correlation with reflection profiles and test well information, indicate that the Lower Cretaceous beds of the Nanushuk Group present onshore in the Simpson wells cross over the Barrow Arch and extend northward on the Beaufort Shelf where they are truncated by Upper Cretaceous beds (see Figures 7 and 10); the Lower Cretaceous strata of the Nanushuk Group extend to about 40 km north of the Barrow Arch with thicknesses of 0.5-0.8 km. North of Prudhoe Bay, the refraction data indicate thick (>1.5 km) Upper Cretaceous beds which extend to the continental slope where they are truncated by normal faults (Figure 8). Even though there are indications of the presence of Lower Cretaceous beds on both sides of refraction line 18-19 (see Figure 8), they could not be detected with the refraction method. This is certainly due to the fact that these Lower Cretaceous strata are thin (probably less than 250 m) and that their propagation velocity of 2.93 km/s is similar to the range of interval velocities (2.68-3.35 km/s) of the overlaying Upper Cretaceous rocks. These thin Lower Cretaceous should probably be included at the base of the thick Upper Cretaceous section detected by the refraction method. Reflection profile line 753, shown in Figure 8, suggests that north of Prudhoe Bay the Lower Cretaceous Kuparuk River sandstones extend to distances of approximately 100 km from the shoreline. The refraction and reflection data in section BB' (Figure 8) give no indication that the oil-rich Permo-Triassic beds present in the Prudhoe Bay field extend much farther north than the coastline where they are truncated by the Lower Cretaceous beds. The carbonate rocks of Mississippian-Pennsylvanian age are hard to detect seismically because their propagation velocities are similar to those of the basement. However, as discussed earlier in the interpretation, the velocities and depths of the deeper refractors at the eastern end of the profiles (Figure 8) correlate well with Mississippian-Pennsylvanian carbonates present onshore near the coast in a Prudhoe Bay test well. This suggests that the Mississippian-Pennsylvanian beds of the Lisburne Group (with a thickness of about 1.0 km at the coast) extend seaward to the midshelf areas where they pinch out. This is in agreement with the distribution of the Lisburne Group reported by Bird and Jordan [1977, Figure 1]. The western Beaufort Shelf is shown to be a major offshore sedimentary province with sufficient thicknesses of sedimentary rocks to be prospective for oil. The presence of oil under the Beaufort Shelf has been recently established when more than 30 exploratory wells drilled in the Beaufort Sea have produced oil, but no information regarding these wells has yet been released by the oil companies involved. Another interesting result of this study toward oil potential is the possible presence of an anomalous crystalline basement between Smith Bay and Harrison Bay. As the Prudhoe Bay oil and gas fields and the South Barrow gas field are structural and combination traps along the trend of the Barrow Arch, there is also the possibility of truncated beds containing trapped oil and gas along the side of the anomalous basement detected by this refraction study.

Conclusions

1. The data were gathered under difficult experimental conditions using standard marine refraction techniques with explosive charges and sonobuoys. Legal problems associated with protection of marine mammals and Native American jurisdiction probably mean that this type of experiment will be difficult to reconduct on the Alaskan Shelf, making our data set unique.

2. The western Beaufort Shelf is underlain by a sedimentary prism with beds dipping and prograding to the northeast. Near-surface refraction velocities of 1.60-1.65 km/s are associated with Quaternary sediments and 1.82-2.35 km/s velocities with Tertiary sediments. Velocities of 1.60-3.40 km/s are correlated to Upper Cretaceous rocks, 2.10-4.14 km/s to Lower Cretaceous beds, 5.66-5.68 km/s to Mississippian-Pennsylvanian carbonates, and 4.24-6.08 km/s to the Franklinian basement. A deeper crystalline basement is represented by higher velocities of 6.40-7.07 km/s. West of Cape Halkett the sedimentary section is mainly Lower Cretaceous overlain by a thin layer of Upper Cretaceous, whereas east of Cape Halkett, Upper Cretaceous and Tertiary strata dominate the sedimentary section.

3. Our refraction data indicate the existence of a crystalline basement feature between Smith Bay and Harrison Bay. The crystalline basement is thought to be granitic in composition, although its seismic velocities (6.40-7.07 km/s) do not categorically permit its identification as silicic or mafic.

4. The western Beaufort Shelf has sufficient thicknesses of sedimentary rocks to be a good prospect for oil. Our geophysical data indicate that most of the beds which contain oil onshore extend to the offshore area as well. The crystalline basement feature may provide associated fluid traps along its sides.

5. A minimum depth estimate for the Mohorovicic discontinuity under the nearshore western Beaufort Shelf is 20 km. This is not in disagreement with data from the eastern Beaufort Sea

which suggest that the Canada Basin is underlain by oceanic crust.

6. The continental margin north of Alaska is not different from Atlantic type margins. Our data are compatible with a rifted and rotated Beaufort continental margin, as proposed by Carey [1955], Tailleur [1969, 1973], Rickwood [1970] and many others.

7. There is still a lack of data concerning the composition and age of the seismic units identified. To fill these data gaps, additional data (borehole drilling and high-resolution geophysical surveys) are required, but with the current economic interest and exploration activities in the region, new and crucial information should be forthcoming.

Acknowledgments. It is our pleasure to acknowledge the assistance we received from both Office of Polar Operations and the Eleventh District of the U.S. Coast Guard and to the divisions of Marine Geology and Geophysics (code 480) and Arctic Programs (code 461) of the Office of Naval Research for permission and encouragement to undertake these experiments. We express our sincere appreciation to Captain Fournier, the officers and crew of the USCG *Burton Island* in 1976 for their assistance and cooperation during data gathering at sea under difficult arctic conditions. We appreciate the use of the facilities at the Naval Arctic Research Laboratories at Barrow and assistance from laboratory personnel under the direction of Warren Denner for invaluable help with logistics. LCDR Bill Vinson directed and assisted in the essential helicopter operations. S. Trombly, R. O. Ahner, T. Graham, E. F. Chiburis, Jr., M. [illegible]ain and R. E. McAlister provided invaluable assistance and pleasant company during the field operations. Specialized instrumentation was designed and constructed by R. E. McAlister. This research was supported under ONR grants N00014-76-C-0067 to Oregon State University and N00014-75-C-0714 to the University of Connecticut.

References

Adachi, R., Fundamental relations on the seismic prospecting, *Kumamoto J. Sc. Ser. A*, *2*, 18-23, 1954.

Alaska Geological Society, West to east stratigraphic correlation section, Point Barrow to Ignek Valley, Arctic North Slope, Alaska, North Slope Stratigraphic Committee (1970-1971), report, Anchorage, Alaska, 1971.

Alaska Geological Society, Norhtwest to southwest stratigraphic correlation section, Prudhoe Bay to Ignek Valley, Arctic North Slope, Alaska, North Slope Stratigraphic Committee (1971-1972), report, Anchorage, Alaska, 1972.

Alaska Geological Society, North to south stratigraphic correlation section, Beaufort Sea-Prudhoe Bay-Nora No. 1, Arctic Slope, Alaska, North Slope Stratigraphic Committee, report, Anchorage, Alaska, 1977.

Baggeroer, A. B., and R. Falconer, Array refraction profiles and crustal models of the Canada Basin, *J. Geophys. Res.*, *87*, 5461-5476, 1982.

Bally, A. W., Canada's passive continental margins--A review, *Mar. Geophys. Res.*, *2*, 327-340, 1976.

Bée, M., S. H. Johnson, E. F. Chiburis, and R. E. McAlister, Marine seismic refraction data between Wainwright Inlet and Prudhoe Bay, Alaska, *Tech. Rep. 79-9*, Sch. of Oceanogr., Oreg. State Univ., Corvallis, 1979.

Berry, M. J., and K. G. Barr, A seismic refraction profile across the polar continental shelf of the Queen Elizabeth Islands, *Can. J. Earth Sci.*, *8*, 347-360, 1971.

Bird, K. J., and C. F. Jordan, Lisburne Group (Mississippian and Pennsylvanian), potential major hydrocarbon objective of Arctic Slope, Alaska, *Am. Assoc. Petrol. Geol. Bull.*, *61*, 1493-1512, 1977.

Bird, K. J., C. L. Connor, I. L. Tailleur, M. L. Silberman, and J. L. Christie, Granite on the Barrow Arch, northeast NPRA, *U.S. Geol. Surv. Circ.*, *772-B*, B24-B25, 1978.

Brosgé, W. P., and I. L. Tailleur, Depositional history of northern Alaska, in *Proceedings of the Geological Seminar on the North Slope of Alaska*, edited by W. L. Adkinson and M. M. Brosgé, pp. D1-D18, Pacific Section, American Association of Petroleum Geologists, Los Angeles, Calif., 1970.

Carey, S. W., Orocline concepts in geotectonics, *Pap. Proc. R. Soc. Tasmania*, *89*, 255-288, 1955.

Carter, R. D., C. G. Mull, K. J. Bird, and R. B. Powers, The petroleum geology and hydrocarbon potential of Naval Petroleum Reserve No. 4, North Slope, Alaska, *U.S. Geol. Surv. Open File Rep.*, *77-475*, 1977.

Churkin, M., Jr., Geologic concepts of Arctic Ocean Basin, in *Arctic Geology*, *Mem. 19*, edited by M. G. Pitcher, pp. 485-499, American Association of Petroleum Geologists, Tulsa, Okla., 1973.

Churkin, M., Jr., and J. H. Trexler, Jr., Circum-Arctic plate accretion--Isolating part of a Pacific plate to form the nucleus of the Arctic Basin, *Earth Planet. Sci. Lett.*, *48*, 356-362, 1980.

Cobb, A. T., "Vibroseis" applications in the Arctic, in *Proceedings of the 1973 National Convention*, pp. 115-140, Canadian Society of Exploration Geophysicists, Calgary, Alberta, 1974.

Collins, F. R., Core test and test wells Barrow area, Alaska, Exploration of Naval Petroleum Reserve No. 4 and adjacent areas, northern Alaska, 1944-53, *U.S. Geol. Surv. Prof. Pap.*, *305-K*, 1961.

Dana, S. W., Geology of the Arctic Slope of Alaska, *Map OM 126*, sheet 2, U.S. Geol. Surv., Reston, Va., 1951.

Dehlinger, P., *Marine Gravity*, 322 pp., Elsevier, New York, 1978.

Eittreim, S., and A. Grantz, CDP seismic sections of the western Beaufort continental margin, *Tectonophysics*, *59*, 251-262, 1979.

Freeland, G. L., and R. S. Dietz, Rotation history of Alaskan tectonic blocks, *Tectonophysics*, *18*, 379-389, 1973.

Grantz, A., A. G. McHendrie, T. H. Nilsen, and C. J. Yorath, Seismic reflection profiles, 1973, on the continental shelf and slope between Bering Strait and Barrow, Alaska, and McKenzie Bay, Canada, *U.S. Geol. Surv. Open File Rep.*, *74-42*, 49 sheets seismic reflection profiles, 2 index maps, 1974.

Grantz, A., M. L. Holmes, and B. A. Kososki, Geologic framework of the Alaskan continental terrace in the Chukchi and Beaufort seas, in Canada's Continental Margins and Offshore Petroleum Exploration, Mem. 4, edited by C. J. Yorath, E. R. Parker and D. J. Glass, pp. 669-700, Canadian Society of Petroleum Geologists, Calgary, Alberta 1975.

Grantz, A., S. Eittreim, and D. A. Dinter, Geology and tectonic development of the continental margin north of Alaska, Tectonophysics, 59, 263-291, 1979.

Grantz, A., S. Eittreim, and O. T. Whitney, Geology and physiography of the continental margin north of Alaska and implications for the origin of the Canada Basin, in The Ocean Basins and Margins, vol. 5, The Arctic Ocean, edited by A. E. M. Nairn, M. Churkin, Jr., and F. G. Stehli, pp. 439-492, Plenum, New York, 1981.

Herron, E. M., J. F. Dewey, and W. C. Pitman III, Plate tectonics model for the evolution of the Arctic, Geology, 2, 377-380, 1974.

Hobson, G. D., Seismic exploration in the Canadian Arctic Islands, Geophysics, 27, 253-273, 1962.

Hobson, G. D., and A. Overton, A seismic section of the Sverdrup Basin, Canadian Arctic Islands, in Seismic Refraction Prospecting, edited by A. W. Musgrave, pp. 550-562, Society of Exploration Geophysicists, Tulsa, Okla.,1967.

Hofer, H., and W. Varga, Seismologic experience in the Beaufort Sea, Geophysics, 37, 605-619, 1972.

Hunkins, K., The Arctic continental shelf north of Alaska, Can. Geol. Surv. Pap., 66-15, 197-205, 1966.

Jamison, H. C., L. D. Brockett, and R. A. McIntosh, Prudhoe Bay--A 10 year perspective, in Giant Oil and Gas Fields of the Decade 1968-1978, Mem. 30, edited by M. T. Halbouty, pp. 289-314, American Association of Petroleum Geologists, Tulsa, Okla., 1980.

Johnson, S. H., and E. F. Chiburis, Marine refraction profiles west of Point Barrow, Alaska (abstract), Eos Trans. AGU, 58, 165, 1977.

Jones, H. P., and R. G. Speers, Permo-Triassic reservoirs of Prudhoe Bay field, North Slope, Alaska, in North American Oil and Gas Fields, Mem. 24, edited by J. Braunstein, pp. 23-50, American Association of Petroleum Geologists, Tulsa, Okla., 1976.

Jones, P. B., Evidence from Canada and Alaska on plate tectonic evolution of the Arctic Ocean Basin, Nature, 285, 215-217, 1980.

Lerand, M., Beaufort Sea, in The Future Petroleum Provinces of Canada--Their Geology and Potential, Mem. 1, edited by R. G. McCrossan, pp. 315-386, Canadian Society of Petroleum Geologists, Calgary, Alberta, 1973.

Mair, J. A., and J. A. Lyons, Crustal structure and velocity anisotropy beneath the Beaufort Sea, Can. J. Earth Sci., 18, 724-741, 1981.

Martin, A. J., Structure and tectonic history of the western Brooks Range, De Long Mountains and Lisburne Hills, northern Alaska, Geol. Soc. Am. Bull., 81, 3605-3622, 1970.

Milne, A. R., A seismic refraction measurement in the Beaufort Sea, Bull. Seismol. Soc. Am., 56, 775-779, 1966.

Morgridge, D. L., and W. B. Smith Jr., Geology and discovery of Prudhoe Bay field, eastern Arctic Slope, Alaska, in Stratigraphic Oil and Gas Fields, Classification, Exploration Methods and Case Histories, Mem. 16, edited by R. E. King, pp. 489-501, American Association of Petroleum Geologists, Tulsa, Okla., 1972.

Newman, G. W., C. G. Mull, and N. D. Watkins, Northern Alaska paleomagnetism, plate rotation, and tectonics, in Relationship of Plate Tectonics to Alaskan Geology and Resources, edited by A. Sisson, pp. C1-C7, Alaska Geological Society, Anchorage, 1979.

National Oceanic and Atmospheric Administrtion, Catalog of geological and geophysical data for the National Petroleum Reserve in Alaska, report, Natl. Geophys. Data Cent., Boulder, Colo., 1982.

Oliver, J., M. Ewing, and F. Press, Crustal structure of the Arctic regions from the Lg-phase, Geol. Soc. Am. Bull., 66, 1063-1074, 1955.

Overton, A., Seismic refraction surveys, western Queen Elizabeth Islands, and Polar continental margin, Can. J. Earth Sci., 7, 346-360, 1970.

Rickwood, F. K., The Prudhoe Bay field, in Proceedings of the Geological Seminar on the North Slope of Alaska, edited by W. L. Adkinson, and M. M. Brosgé, pp. L1-L11, Pacific Section, American Association of Petroleum Geologists, Los Angeles, Calif., 1970.

Robinson, F. M., Test wells Simpson area, Alaska, Exploration of Naval Petroleum Reserve no. 4 and Adjacent Areas, Northern Alaska, 1944-53, U.S. Geol. Surv. Prof. Pap., 305-J, 1959.

Robinson, F. M., and F. R. Collins, Core test, Sentinel Hill area and test well Fish Creek area, Alaska, Exploration of Naval Petroleum Reserve no. 4 and Adjacent Areas, Northern Alaska, 1944-53, U.S. Geol. Surv. Prof. Pap., 305-I, 1959.

Sander, G. W., and A. Overton, Deep sesimic refraction investigation in the Canadian Arctic Archipelago, Geophysics, 30, 87-96, 1965.

Sobczak, L. W., and J. R. Weber, Crustal structure of Queen Elizabeth Islands and polar continental margin, Canada, in Arctic Geology, Mem. 19, edited by M. G. Pitcher, pp. 517-525, American Association of Petroleum Geologists, Tulsa, Okla., 1973.

Steinhart, J. S., and R. P. Meyer, Minimum statistical uncertainty of the seismic refraction profile, Geophysics, 26, 574-587, 1961.

Sweeney, J. F., E. Irving, and J. W. Geuer, Evolution of the Arctic Basin, in Arctic Geophysical Review, edited by J. F. Sweeney, Publ. Earth Phys. Branch, 45, 91-100, 1978.

Tailleur, I. L., Rifting speculation on the geology of Alaska's North Slope, Oil Gas J., 67, 128-130, 1969.

Tailleur, I. L., Probable rift origin of Canada Basin, Arctic Ocean, in Arctic Geology, Mem. 19, edited by M. G. Pitcher, pp. 526-535, American Association of Petroleum Geologists, 1973.

Tailleur, I. L., and W. P. Brosgé, Tectonic history of northern Alaska, in Proceedings of the Geological Seminar on the North Slope of Alaska, edited by W. L. Adkinson and M. M.

Brosgé, pp. E1-E20, Pacific Section, American Association of Petroleum Geologists, Los Angeles, Calif., 1970.

Taylor, P. T., L. C. Kovacs, P. R. Vogt, and G. L. Johnson, Detailed aeromagnetic investigation of the Arctic Basin, 2, J. Geophys. Res., 86, 6323-6333, 1981.

Vogt, P. R., and O. E. Avery, Tectonic history of the Arctic Basin: Partial solutions and unsolved mysteries, in Marine Geology and Oceanography of the Arctic Seas, edited by Y. Herman, pp. 83-117, Springer-Verlag, New York, 1974.

Witmer, R. J., M. B. Mickey, and H. Haga, Biostratigraphic correlations of selected test wells of National Petroleum Reserve in Alaska, U.S. Geol. Surv. Open File Rep., 81-1165, 1981a.

Witmer, R. J., H. Haga, and M. B. Mickey, Biostratigraphic report of thirty-three wells drilled from 1975 to 1981 in National Petroleum Reserve in Alaska, U.S. Geol. Surv. Open File Rep., 81-1166, 1981b.

Wold, R. J., T. L. Woodzick, and N. A. Ostenso, Structure of the Beaufort Sea continental margin, Geophysics, 35, 849-861, 1970.

Woolson, J. R., et al., Seismic and gravity surveys of Naval Petroleum Reserve no. 4 and adjoining areas, Alaska, U.S. Geol. Surv. Prof. Pap., 304-A, 1962.

Yorath, C. J., and D. K. Norris, The tectonic development of the southern Beaufort Sea and its relationship to the origin of the Arctic Ocean Basin, in Canada's Continental Margins and Offshore Petroleum Exploration, Mem. 4, edited by C. J. Yorath, E. R. Parker and D. J. Glass, pp. 589-611, Canadian Society of Petroleum Geologists, Calgary, Alberta, 1975.

Young, F. G., D. W. Myhr, and C. J. Yorath, Geology of the Beaufort-MacKenzie Basin, Can. Geol. Surv. Pap., 76-11, 65 pp., 1976.

M. Bée, College of Oceanography, Oregon State University, Corvallis, OR 97331.

E. F. Chiburis, Aramco, 1964 1 St. N., Texas City, TX 77590.

S. H. Johnson, Amoco Production Research, P.O. Box 591, Tulsa, OK 74102.

(Revised November 14, 1983;
revised April 11, 1984;
accepted April 25, 1984.)

Reprinted from Biju-Duval, B., Moore, J. C., et al., 1984
Initial Reports of the Deep Sea Drilling Project, Volume LXXVIII, Washington (U.S. Government Printing Office)

13. PRELIMINARY SEISMIC REFRACTION RESULTS USING A BOREHOLE SEISMOMETER IN DEEP SEA DRILLING PROJECT HOLE 395A[1]

R. S. Jacobson, College of Oceanography, Oregon State University
R. Adair and J. Orcutt, Geological Research Division, Scripps Institution of Oceanography[2]

ABSTRACT

Three seismic refraction lines shot to the Marine Seismic System, a vertical-component borehole seismometer in DSDP Hole 395A at 609 m sub-bottom depth, have been analyzed. Despite inconsistencies between various velocity determinations in the upper crust, the velocity of the uppermost 600 m appears to be high, about 4.5 km/s. Between 600 m and 1.8 km sub-bottom, the crust yields an apparent velocity of 4.6 km/s. This value is somewhat lower than that determined near the base of the hole using acoustic logging tools (5.0–5.5 km/s), and is also lower than the average velocity of core samples from the same depth (5.7 km/s). The lower crust is unusually thin, only 1.8 to 2.4 km thick, and has compressional-wave velocities of 6.8 to 7.3 km/s. Mantle velocities range from 7.8 to 8.2 km/s. There is little or no velocity gradient in the uppermost kilometers of the crust, but our results indicate widespread lateral inhomogeneities, supporting the observations based on refraction profiles shot for the original site survey.

INTRODUCTION

For the past 30 years, seismic refraction results have described in general terms the oceanic crustal velocity structure, its variation with age, and its relation to the spreading rate at the time of formation (Raitt, 1963; Shor et al., 1971; Bibee and Shor, 1976; Spudich and Orcutt, 1980a). Until a few years ago, correlation of compressional-wave velocities with lithology has been determined primarily on the basis of measurements on rocks dredged from the sea floor (e.g., Christensen and Salisbury, 1975). Velocity measurements on dredge samples show a systematic bias toward higher velocities than may be expected on the basis of seismic refraction velocities. Since seismic refraction techniques are wavelength-limited (~200 m), they must also average such features as large-scale fractures, voids, vugs, and joints, all of which profoundly affect the porosity and velocity of the rock. Further, many different lithologies can be averaged together, making correlation of refraction velocities with lithology even more difficult.

With the advent of deep drilling into igneous ocean crust, it may be possible to resolve and quantify the differences between velocity determinations made by seismic refraction, laboratory studies on dredge or core samples, and downhole acoustic logs. A large portion of these differences must be related to the scale of measurement and the wavelengths over which velocity determinations are made, varying from less than a meter to many hundreds of meters (Salisbury et al., 1979). Important questions need to be addressed and answered. Under what conditions do laboratory and log velocities converge? Can seismic refraction velocities be predicted from acoustic logs? Is there a smooth velocity increase with depth in the uppermost crust, and if so, is it controlled by porosity changes or lithologic changes, or both?

There exist significant difficulties in measuring the velocity structure in the uppermost 500 m of ocean crust by seismic refraction methods (White and Matthews, 1980; Ewing and Purdy, 1982). These difficulties arise because of the geometry of the experiment, usually involving near-surface explosive charges as sources and either near-surface hydrophones or ocean-bottom seismometers as receivers. The thick water layer acts to mask refracted waves, which penetrate only through the uppermost crust, making identification of arrivals tenuous at best.

One possible way of improving the resolution of upper crustal velocity structure is to use a borehole seismometer as a receiver. The effective use of a borehole seismometer in seismic refraction studies has been demonstrated at DSDP Site 417 (Stephen, 1979; Stephen et al., 1980). Another borehole seismometer has been deployed in DSDP Holes 482C and 494A, but the results are not yet published. More recently, the Defense Advanced Research Projects Agency (DARPA) and the Naval Ocean Research and Development Activity (NORDA) cosponsored the development of a borehole seismometer called the Marine Seismic System (MSS). The long-range objective of this system is to monitor man-made and natural seismicity over long periods of time. Before Leg 78B, the system was untested in a borehole situation, and a series of engineering tests was needed to ensure operational capability. The Deep Sea Drilling Project had planned to re-enter Hole 395A (Fig. 1), in the central Atlantic, to measure geophysical properties—using downhole logging instruments—to a sub-bottom depth of 600 m in the igneous crust. Hole 395A was selected as an optimal location for testing the MSS, combining downhole geophysical logging with a series of seismic refraction profiles in a coherent geophysical investigation. This experiment would provide a

---

[1] Hyndman, R. D., Salisbury, M. H., et al., *Init. Repts. DSDP*, 78B: Washington (U.S. Govt. Printing Office).

[2] Present addresses: (Jacobson) College of Oceanography, Oregon State Univ., Corvallis, OR 97331; (Adair and Orcutt) Geological Research Div., A-015, Scripps Institution of Oceanography, La Jolla, CA 92093.

unique opportunity to answer some of the questions we have raised here.

DSDP Hole 395A was re-entered in March and April of 1981. This hole, at 22°45′N, 46°05′W, is near the Mid-Atlantic Ridge in 7.2-Ma-old crust formed at a half-spreading rate of 1.7 cm/y. (Hussong et al., 1979). Hussong et al. (1979) observed in their site survey of the area that the geology appears to be very complex. Their seismic refraction results show a diverse range of crustal structure and varying thicknesses and seismic velocities. It was hoped that these results could be improved upon by using the borehole seismometer (BHS) of the Marine Seismic System.

Since it was planned to monitor the BHS in real time aboard the *Challenger*, it was necessary to have an additional ship, the *USNS Lynch*, deploy the explosive charges. In addition, the *Lynch* deployed four University of Texas ocean-bottom seismometers (OBS's) around Hole 395A. Comparison of the OBS and borehole seismometer data would determine whether burial would reduce absolute noise levels, thus increasing the signal-to-noise ratio, and whether there are any advantages in using a sub-bottom instrument in inversion techniques and velocity determinations. Unfortunately, none of the data collected by the ocean-bottom seismometers was usable for travel-time inversion, owing to mechanical and electrical failures. A noise comparison between one of the OBS's and the MSS (Adair et al., this volume) demonstrated, however, that the ambient noise was lower at the bottom of the hole by almost two orders of magnitude.

This paper presents the velocity structure determined around Hole 395A using a variety of simple travel-time inversion techniques. We will compare the results presented here with those obtained from the original site survey using OBS's and sonobuoys (Hussong, et al., 1979), and with other regional surveys, core samples, and the acoustic log.

FIELD OPERATIONS

Four seismic refraction lines were shot to the borehole seismometer (Fig. 1). These lines were originally planned on the basis of previously published bathymetry (Hussong et al., 1979, their figure 3) to reduce the effects of topography. Topographic corrections to the refraction data were expected to be on the order of 0.5 s.

A shot calibration profile was performed to determine the shot size necessary to overcome ambient background noise. This was accomplished by monitoring the BHS in real time aboard the *Challenger* and relaying the results back to the shooting party aboard the *Lynch*. The real-time monitoring also made possible adjustment of charge sizes during the refraction profiles themselves.

Information necessary for reducing the refraction data was collected by the *Lynch* personnel. This information included shot detonation times as recorded by a shot-break streamer, time checks to WWV (a universal time code), depth under the shot, charge size, fuse length, sinking time, and the position, speed, and heading of the *Lynch*. Clock calibrations were also performed aboard the *Challenger*.

The topography under the four seismic lines was sufficiently rough to strain the assumptions made in using most travel-time inversion methods. A few sediment ponds were encountered, the thickest pond (apparently) being at Site 395. The seismic reflection system aboard the *Lynch* was inoperative, making sediment thickness corrections impossible.

The borehole seismometer data proved to be of exceptionally high quality. Background noise levels were comparable to the quietest OBS sites yet observed, and seismic signal-to-noise ratios were very high (Adair et al., this volume). A total of 112 shots were recorded at a sampling rate of 75 samples/second at six different gain settings. One shot, number 23, was located directly over the borehole, and will be used to calculate an interval velocity from the seabed to the instrument at 609 m sub-bottom.

DATA PROCESSING

Data recorded by the BHS instrument were digitized downhole at 75 samples/second and sent to the *Challenger* via a cable, where they were recorded on digital tape. Real-time playback was performed in order to ensure system operation. The raw data have been transcribed into ROSE format (Latraille et al., 1982) by Teledyne Geotech, but not without some problems. Pseudo-random timing errors on the order of 0.5 s were observed when comparing the transcribed digital data with the real-time playback recordings. A systematic process of comparing times of numerous peaks and troughs from both data sets has reconciled the timing inaccuracy to less than 0.05 s.

Shot detonation times were adjusted for distance offset to the shot-break streamer, and corrected to WWV, as were the borehole data. Shot depths were then corrected to the sea surface and shot-receiver ranges were computed on the basis of *Lynch* navigation. Topographic corrections were applied to a flat datum, defined by the depth of the seafloor at Hole 395A. The depth used for the topographic correction was measured at the point the waves entered the seafloor, although allowance was made for picking a nearby strong reflector on the echo-sounder recording as the probable location for the signal to enter the seafloor. The topographic correction was designed to replace igneous crust of velocity 6.8 km/s above the datum level with water of velocity 1.5 km/s. It is thus assumed that the upper crust is of constant thickness, and that all topography is the result of undulations in the top of Layer 3. Topographic corrections were as much as 0.82 s. The use of dipping-bottom datum planes could reduce this amount considerably, but would have made it difficult to compare profiles. Finally, the data were filtered from 2 to 20 Hz, using a fourth-order Chebyshev filter, and plotted in reduced record sections.

Seven record sections have been prepared for travel-time analysis. For each of the three lines (Line 3 has not been corrected for timing discrepancies, and will not be discussed further), a true amplitude plot and an autoscaled plot have been prepared. For the true amplitude plot, signal levels have been adjusted for shot size and range, according to the formula

$$A = A_0\,(R/R_0)^{Rexp}(W_0/W)^{Wexp}$$

where A is the true amplitude, A_0 is the measured amplitude, R and W are the shot range and weight, R_0 and W_0 are reference ranges and weights, and *Rexp* and *Wexp* are empirical constants equal to 1.75 and 0.65, respectively. A seventh record section, from range zero to 10 km, depicts the autoscaled combined short-range refracted arrivals from Lines 1, 2, and 4.

The autoscaled plots are of channel L1, which had sufficiently high gain to show clearly the first refracted arrivals. Unfortunately, *the high gain on this channel clipped the later-arriving high-amplitude* arrivals. Channel L2, with a gain about 0.02 that of channel L1, was used to produce the true amplitude plots. No clipping of signals is evident, but at large ranges, the amplitude only barely exceeded the system noise level. The autoscaled and the true amplitude plots for refraction lines 1, 2, and 4 are shown in Figures 2, 3, and 4, respectively. The autoscaled record section of the combined short-range shots is shown in Figure 5.

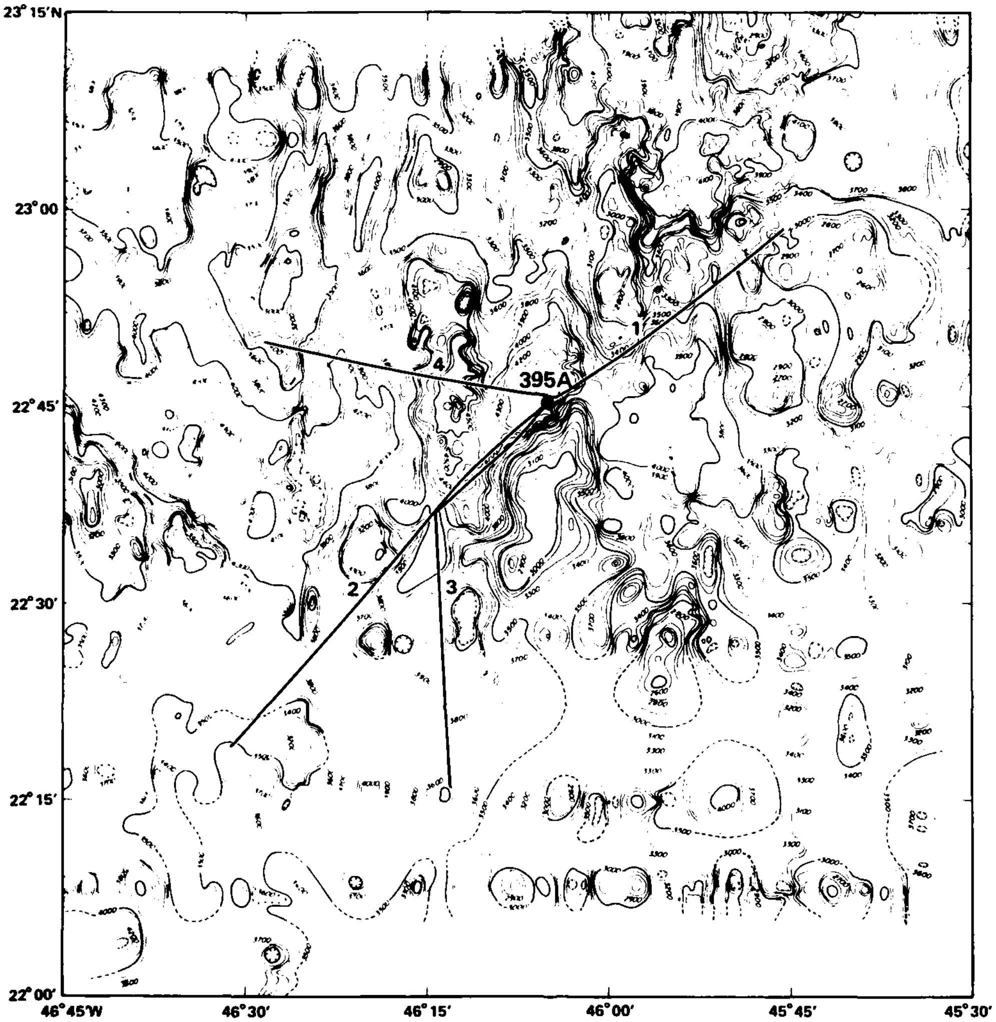

Figure 1. Bathymetric chart of the area surrounding DSDP Hole 395A (reprinted from Hussong et al., 1979), showing the locations of the seismic refraction profiles shot to the borehole seismometer. Depths shown in corrected meters.

The most prominent arrivals are the secondary arrivals, seen in the true-amplitude record sections. These arrivals are interpreted as vertically polarized converted shear waves. The coherence of the arrival times of these waves in the record sections is seriously degraded, since the topographic corrections were made assuming a high refraction velocity to correct the compressional-wave arrivals. The velocities of the shear-wave arrivals vary between 2.5 and 4.7 km/s.

The first refracted arrivals show a change of polarity at a range of 2.8 km (Fig. 5), corresponding to a change in propagation direction of the seismic energy at the instrument from above to just below the horizontal. The phase velocity of the seismic energy just beyond this range yields the seismic velocity (at low frequencies) at the depth of the instrument, since the seismic waves have just reached horizontal propagation. This will be discussed later in more detail. The first arrivals at all ranges show clear onset times, as recorded on channel L1.

TRAVEL-TIME ANALYSIS

The first attempt to analyze travel times was to visually fit straight-line segments to the first arrivals of the travel-time curve. This approach yields the classical plane-layer solution of Officer (1958) and Ewing (1963). Each record section has three distinct travel-time branches, corresponding to the classical Layer 2, Layer 3, and mantle arrivals. Breaks in the travel-time curve were de-

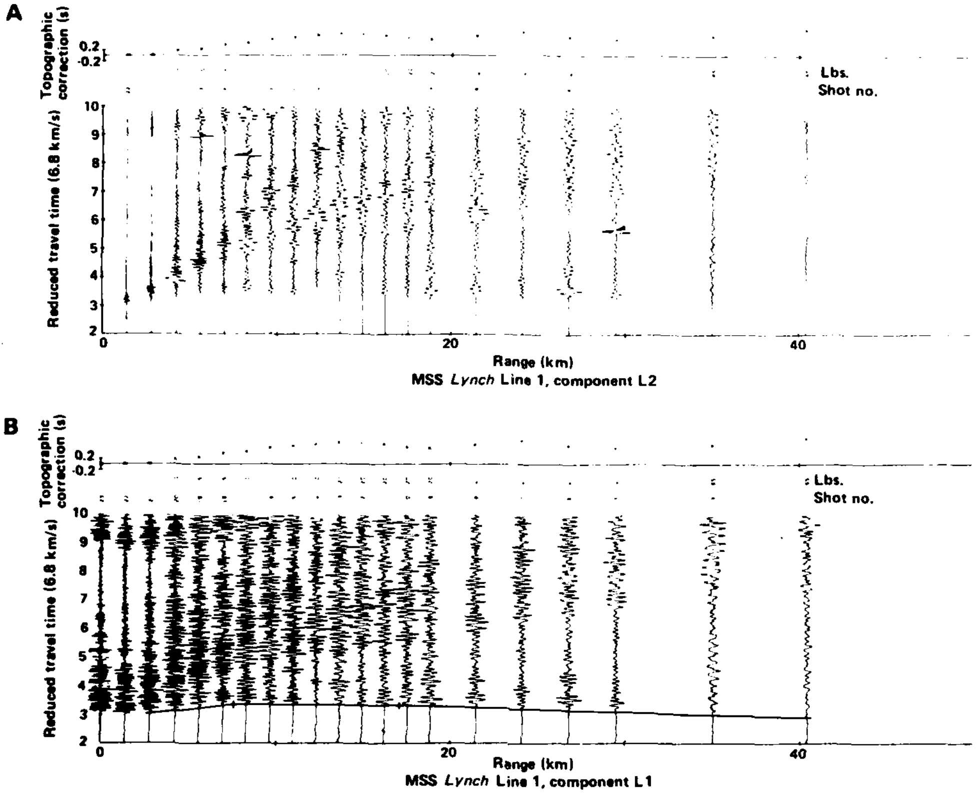

Figure 2. True amplitude (A) and autoscaled (B) record sections for Line 1, located in Figure 1. Both plots are reduced using a velocity of 6.8 km/s. The true amplitude plot, using component L2, has a weighting applied to each trace to adjust for charge size and receiver-source offset. The autoscaled plot, using component L1, has clipped signal levels beyond the first refracted arrival. Also shown are the straight-line segments used for the velocity analysis.

termined by slope changes and verified by amplitude increases corresponding to critical reflections. The increase of amplitudes in the range of 15 to 25 km corresponds to the critical reflections of the mantle. The location and character of the critical reflections differed among the record sections, reflecting lateral inhomogeneity in the crust surrounding Site 395.

Plane-layer solutions were calculated for each of the three available lines, assuming flat layers. The uppermost crustal structure was combined for all three profiles. The record section in Figure 5, combining all refracted arrivals available out to 10 km within the sediment pond, yields an apparent velocity of 4.62 km/s. Because of the geometry of the receiver and source locations, the polarity of the arrivals detected by the vertical-component seismometer is negative at near zero ranges, changing to positive just when the waves start to refract upward from the horizontal. The polarity change of the first arrivals serves to separate the "oblique refraction branch" of the travel-time curve from the standard head-wave refracted branch, the break occurring at an offset of 2.8 km. The refraction velocity of 4.62 km/s observed at the offset range of 3 to 10 km is inferred to be the average seismic velocity at the depth of the seismometer (609 m sub-bottom). No curvature of the travel-time branch just beyond the range of 3 km is readily apparent, indicating that upper crustal velocity gradients below 600 m are extremely low.

Before proceeding to a discussion of the deeper velocity structure, we must first describe the velocity structure in the uppermost 609 m. Shot 23, located directly above the borehole, enables us to determine an average interval velocity to the instrument. Our best determination of this interval velocity is 5.30 km/s. The velocity of 5.30 km/s averages 93 m of sediment and 516 m of igneous crust, implying that the uppermost crust has an even higher velocity. The value of the average interval velocity is inconsistent with the inferred velocity at 609 m depth of 4.62 km/s. The velocity inconsistency is probably caused by measurement error or lateral refraction of shot 23 into the surrounding hill of igneous crust near the borehole, bypassing the sedimen-

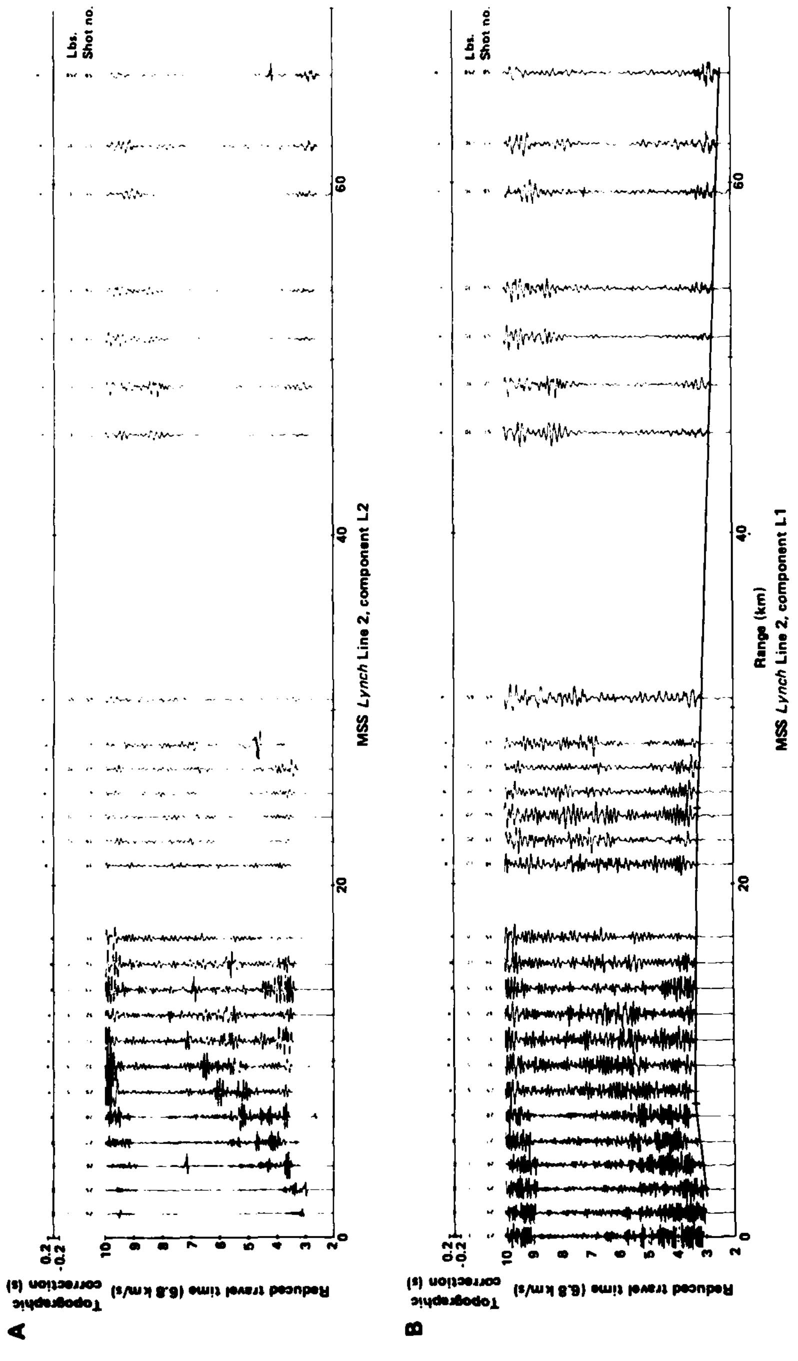

Figure 3. True amplitude (A) and autoscaled (B) record sections for Line 2.

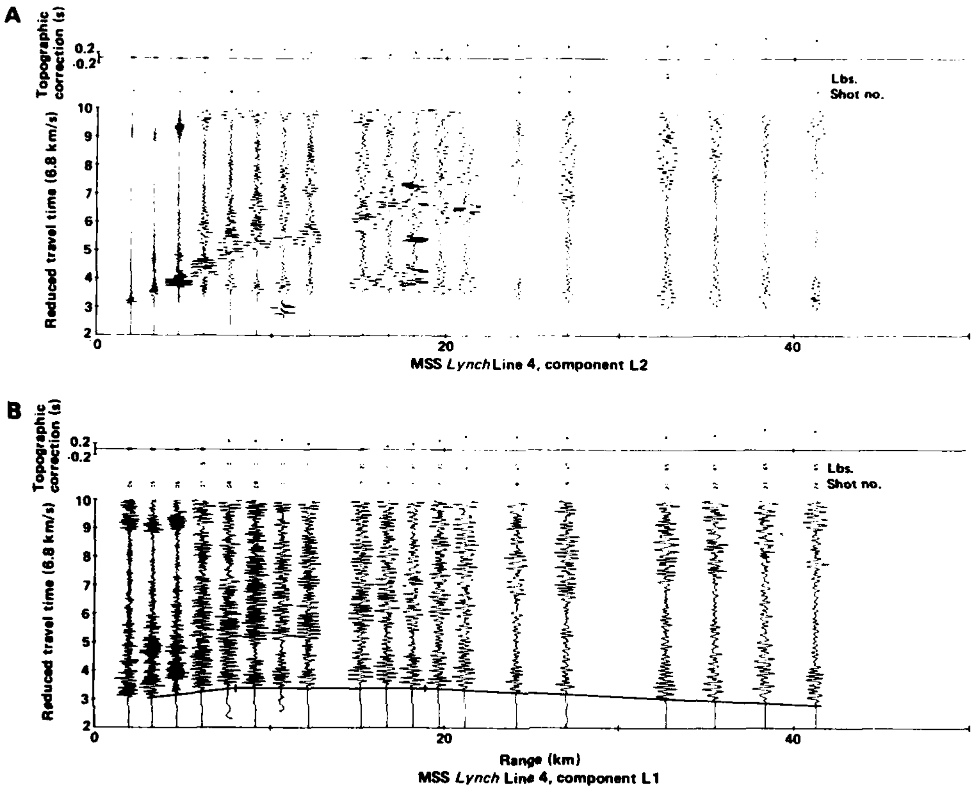

Figure 4. True amplitude (A) and autoscaled (B) record sections for Line 4.

tary layer. Further, our apparent velocity of 4.62 km/s may be low, since the sediment thickness increases away from Hole 395A along our shot lines. If we could correct for the sediment thickness along the shot lines, the apparent velocity at short ranges would be close to 5.0 km/s. That the compressional-wave velocity in the uppermost crust is quite high is indicated by the observed high amplitude of the converted shear-wave arrivals seen in Figures 2, 3, and 4. Spudich and Orcutt (1980b) have noted that *P*- to *S*-wave conversion is efficient across boundaries with a high velocity contrast, that is, when the uppermost crust displays a high compressional-wave velocity. They also infer that the shear-wave amplitude should decrease as the apparent velocity of the shear waves approaches the compressional-wave velocity at the top of the basement. A *P*-wave velocity of around 5.0 km/s near the seafloor, shear-wave velocities of 2.7 to 4.7 km/s, and the observed high amplitudes, are consistent with this hypothesis.

We still need to determine an appropriate velocity for the upper-most crust around Site 395. The shallow crustal structure at Hole 395A includes 93 m of sediment. Elsewhere in the sediment pond, the sediment thicknesses can exceed 0.3 s (Hussong et al., 1979). Outside the pond, little sediment cover was observed, suggesting that lateral inhomogeneity should be taken into consideration. We need to determine a refraction velocity for the upper crust outside the pond, such that the delay time to the 4.62-km/s layer is satisfied. Knowing the thickness of this layer (609 m), a velocity of 4.47 km/s was calculated. Figure 6 depicts the upper crustal structure used for the modified plane-layer solution.

The velocity structure inferred below the level of the seismometer differs between the three profiles, as outlined in Table 1. The thickness of Layer 2, of velocity 4.62 km/s, was rather uniform, varying between 1.14 and 1.25 km. Layer 3 velocities vary significantly, from 6.81 to 7.32 km/s, as did thicknesses, from 1.92 to 2.39 km. Total crustal thickness ranged from 3.67 to 4.25 km. Mantle velocities also showed a wide range of values, between 7.75 and 8.18 km/s, with V_p fast parallel to the spreading direction.

Much of the velocity variation could be the result of dipping layers. We applied the data to a dipping-layer model, solving for the dip and strike of plane layers. The solution indicated that the dips were severe enough

AD-A167 102   COMPILATION OF REPRINTS NUMBER 63(U) OREGON STATE UNIV   2/3
CORVALLIS COLL OF OCEANOGRAPHY MAR 86 REF-83-12
N00014-76-C-0067 86 PAT-APPL-825 107

UNCLASSIFIED   F/G 8/10   NL

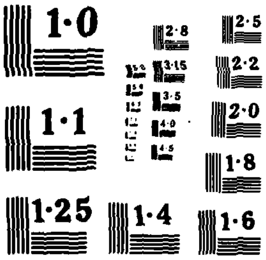
1·0
2·8
2·5
3·2
3·15
2·2
3·5
2·0
1·1
4·0
4·5
1·8
1·25
1·4
1·6

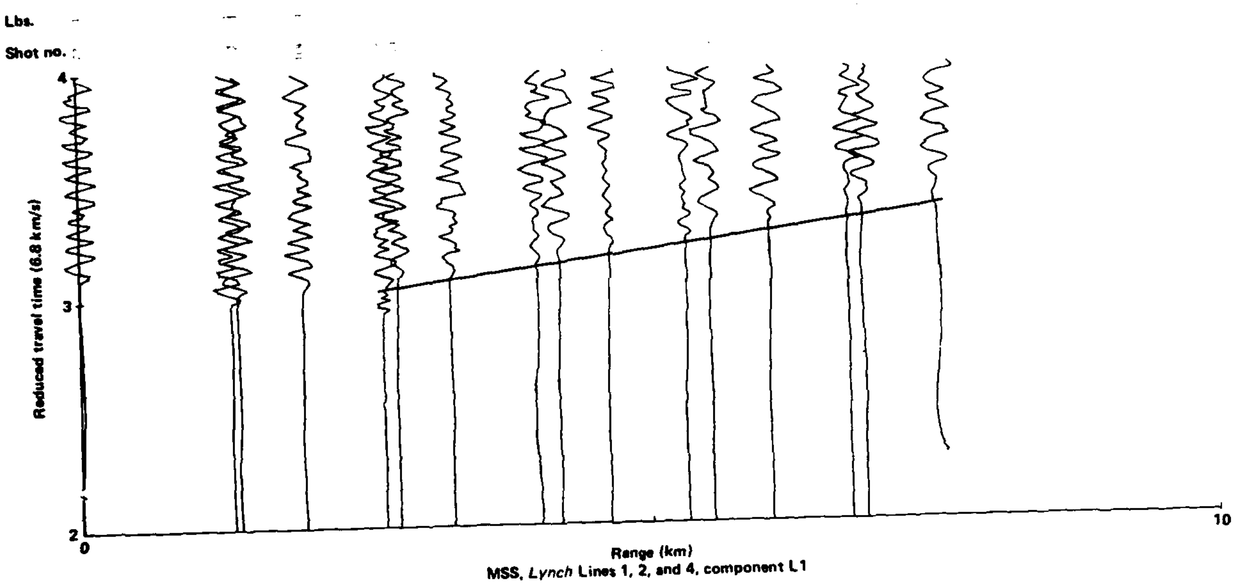

Figure 5. Combined autoscaled record section for all shots from Lines 1, 2, and 4 with an offset of less than 10 km.

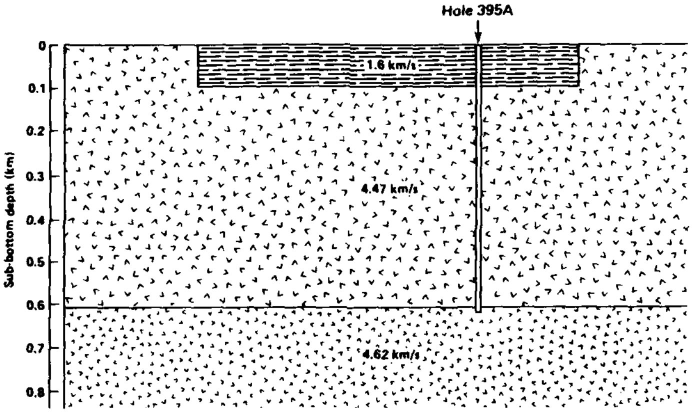

Figure 6. Model of upper crustal velocity structure immediately surrounding DSDP Hole 395A, as deduced from the seismic refraction data. Velocities not corrected for dip.

Table 1. Plane-layer regional solution assuming flat datums.

	Line 1			Line 2			Line 4		
Layer	V_p (km/s)	Thickness (km)	Total thickness (km)	V_p (km/s)	Thickness (km)	Total thickness (km)	V_p (km/s)	Thickness (km)	Total thickness (km)
0	1.509	4.483		1.509	4.483		1.509	4.483	
1	4.47[a]	0.609	0.609	4.47[a]	0.609	0.609	4.47[a]	0.609	0.609
2	4.62	1.140	1.749	4.62	1.247	1.858	4.62	1.178	1.787
3	7.04	1.921	3.670	7.32	2.393	4.251	6.81	2.368	4.155
4	7.75			7.81			8.18		

Note: Drilling results indicate that the uppermost 0.093 km consists of 1.6 km/s sediment.
[a] Assumed velocity.

that the refracting plane layers crossed each other, a physically unrealizable model. A more complex geometry for the refracting horizons would produce an even more unstable solution. However, a somewhat satisfactory model with flat, non-dipping layers is proposed, having velocities of 4.47 (assumed), 4.62, and 7.11 km/s, and a mantle velocity of 7.89 km/s, and thicknesses of 0.609, 1.24, and 1.85 km, respectively, for the three uppermost layers. Systematic residuals in travel times were evident for all layers, indicating either the presence of dipping layers or lateral variations in velocity.

Comparison with Earlier Refraction Studies

In the original site survey by Hussong et al. (1979), it was emphasized that the crustal velocity structure exhibited inhomogeneity which reflected the complex geology of the area. Our results certainly support this conclusion. The great variability in Layer 3 and mantle velocities and crustal thicknesses cannot be attributed solely to timing errors. The close-range arrivals, out to 10 km, show fairly good coherence and exhibit unusually well-behaved travel times (Fig. 5), considering the lack of sediment-thickness corrections. All shots within 10 km of Hole 395A were within the sediment pond, an obviously downfaulted piece of oceanic crust. The crust under the sediment pond at Site 395 may be laterally homogeneous, but it may also be anomalous when compared with the surrounding crust. The sediment pond is deeper than any other seafloor within a radius of 100 km, and also has the thickest sediment cover. The most important evidence of lateral inhomogeneities are the ranges where critical mantle reflections become most prominent. These ranges vary between 15 and 25 km, indicating major structural changes in the crust surrounding Site 395.

It is instructive to examine the differences between the results of this study and those of Hussong et al. (1979). Figure 7 shows a comparison of our lines with profiles of Hussong et al. having similar geographic placement. Very little agreement exists, either in velocities or crustal thicknesses. The exception is Layer 2: the profiles of Hussong et al. show a range in Layer 2 velocities of 3.9 to 4.8 km/and a fairly uniform thickness. It appears that Layer 2 is more homogeneous in this area than is the more deep-seated structure.

The results of this experiment, compared with the regional structure given by Hussong et al. (1979), are more encouraging (Fig. 8). The agreement between velocities and lower crustal layer thicknesses are good. Perhaps more surprising is the greater similarity between our three lines than between those of Hussong et al. This must be the result of our only having one seismometer location in an area of lateral complexity, whereas Hussong et al. had more than 10 receivers.

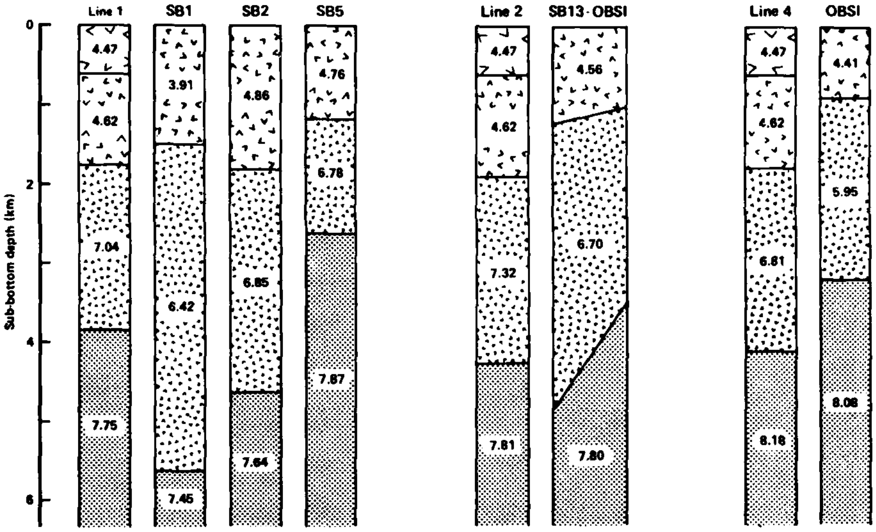

Figure 7. Comparison of crustal velocity structure near Site 395 determined from the DARPA borehole seismometer experiment (Lines 1, 2, and 4) with co-located seismic refraction profiles run by Hussong et al. (1979) using sonobuoys and OBS's. Layer velocities in km/s.

Other crustal velocity structure determinations have been made reasonably close to Site 395. Barrett and Purdy (1979) report on the seismic structure at Site 396, situated to the east of the same ridge crest at 23°50′N, 44°30′W. This site is on 10-Ma-old crust formed at a half-spreading rate of 1.5 cm/y. (Purdy, Rabinowitz, and Schouten, 1979). These authors determined a total crustal thickness of 6.8 km, with a 4.6-km-thick Layer 3 (Purdy, Schouten, et al., 1979), shown in Figure 8.

Detrick and Purdy (1980) have reported a series of crustal determinations across the Kane Fracture Zone at 44°W. The crust south of the fracture zone, created at the same ridge that created the crust at Site 395, is 7 Ma old, and formed at a half-spreading rate of 1.4 cm/y. Their results from OBH2, within 40 km of the fracture zone, are shown in Figure 8, and more closely resemble ours.

Detrick and Purdy (1980) also mention the possible existence of several small-scale fracture zones south of the Kane Fracture Zone which trend WNW. Hussong et al. (1979) also noted two possible fracture zones trending WNW which offset magnetic anomaly patterns around Site 395. The existence of fracture zones may explain the unusually thin crust under Hole 395A. The well-developed Kane Fracture Zone, just to the north, shows a complete absence of Layer 3 (Detrick and Purdy, 1980).

Comparison with Laboratory and Logging Velocities

Melson, Rabinowitz, et al. (1979) reported selected laboratory sonic velocity determinations for crustal rocks from Site 395. Their results, for samples from a depth of 609 m sub-bottom, indicate an average velocity of 5.69 km/s for doloritic basalt, greater than our 4.62 km/s determination of apparent velocity. It is well known that velocities determined on core samples represent maximum velocities because of a sampling bias toward coherent material. A better indication of *in situ* velocities may often be obtained by using downhole acoustic logs. The log for Hole 395A (Mathews et al., this volume) recorded reliable velocities only in the deepest part of the hole. The results indicate an interval velocity of 5.26 km/s. Unfortunately, the acoustic log was unreliable for the shallower structure, and could not be used to verify the lack of velocity gradients deduced above.

SUMMARY

The preliminary results from three out of four seismic refraction lines shot to the DARPA borehole seismometer implanted in DSDP Hole 395A support the results obtained by Hussong et al. (1979) using ocean-bottom seismometers and sonobuoys. Major lateral inhomogeneities are evident in the lower crustal velocity structure, whereas the Layer 2 velocities and thicknesses are more uniform from profile to profile. The gross features of the crust include a 1.85-km-thick Layer 2 overlying a 1.9-km-thick Layer 3 or lower oceanic crust. This crustal section is considerably thinner than that normally expected for Atlantic-type crust. There is little evidence to indicate the existence of velocity gradients within Layer 2, but if gradients do exist, they must be small. Velocity determinations from the sonic logs are considerably higher than the observed refraction velocities, and are somewhat lower than the sonic velocities of discrete samples from the borehole.

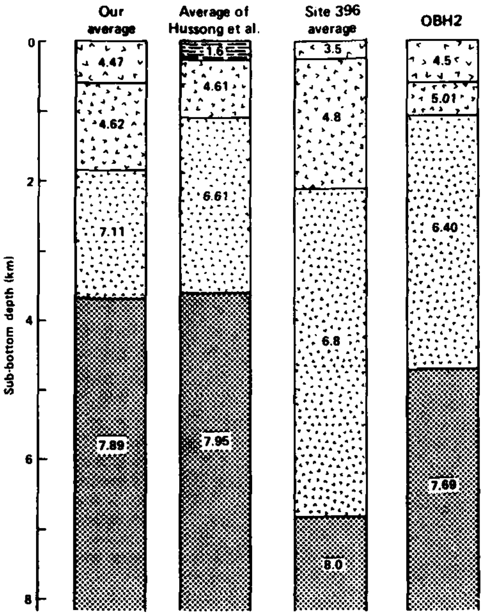

Figure 8. Comparison of the results presented here and the average velocity structure near Site 395 deduced by Hussong et al. (1979). Also shown are the crustal structure near Site 396 (Purdy, Schouten, et al., 1979) and the velocity structure near the Kane Fracture Zone (OBH2), determined by Detrick and Purdy (1980). Layer velocities in km/s.

The results of the data collected from the borehole seismometer are more self-consistent than those obtained using many OBS's, but this may be the result of having a single sensor in a geologically complicated structure. The use of a borehole seismometer offers considerable advantages in travel-time analysis, especially for determining the velocity at the depth of the sensor. Nonetheless, we expect that the conclusions reached in this chapter will change little with further analysis. Because amplitudes are strongly dependent on vertical and horizontal velocity gradients, the use of synthetic seismograms to refine the compressional- and shear-wave velocity structure any further will prove extremely difficult.

ACKNOWLEDGMENTS

We would like to thank the crew of the *USNS Lynch* for their cooperation and patience. We especially appreciate the fine effort put forth by the master, E. Maier, without whom many of our results could not have been obtained. We also thank the UT Galveston crew, headed by D. McGowan and P. Donoho, for their efforts in working with the OBS's. We also wish to thank the NORDA Code 360 personnel aboard the *Lynch* for making the cruise function smoothly. Finally, we with to express our thanks to L. Dorman, F. Duennebier, and M. Salisbury for reviewing this manuscript.

This work was supported by NORDA Code 543, ONR (N00014-79-C-0004), the School of Oceanography at Oregon State University, and by a grant from the Defense Advanced Research Projects Agency (F49620-79-C-0019).

REFERENCES

Barrett, D. L., and Purdy, G. M., 1979. IPOD survey area AT-6: Seismic refraction results. *In* Melson, W. G., Rabinowitz, P. D., et al., *Init. Repts. DSDP*, 45: Washington (U.S. Govt. Printing Office), 49-53.

Bibee, L. E., and Shor, B. B., Jr., 1976. Compressional wave anisotropy in the crust and upper mantle of the Pacific. *Geophys. Res. Lett.*, 3:639-642.

Christensen, N. I., and Salisbury, M. H., 1975. Structure and constitution of the lower oceanic crust. *Rev. Geophys. Space Phys.*, 13: 57-86.

Detrick, R. S., Jr., and Purdy, G. M., 1980. The crustal structure of the Kane Fracture Zone from seismic refraction studies. *J. Geophys. Res.*, 85:3759-3777.

Ewing, J. I., 1963. Elementary theory of seismic refraction and reflection measurements. *In* Hill, M. N. (Ed.), *The Sea* (Vol. 3): New York (Interscience), pp. 3-19.

Ewing, J. I., and Purdy, G. M., 1982. Upper crustal velocity structure in the ROSE area of the East Pacific Rise. *J. Geophys. Res.*, 87: 8397-8402.

Hussong, D. M., Fryer, P. B., Tuthill, J. D., and Wipperman, L. K., 1979. The geological and geophysical setting near DSDP Site 395, North Atlantic Ocean. *In* Melson, W. G., Rabinowitz, P. D., et al., *Init. Repts. DSDP*, 45: Washington (U.S. Govt. Printing Office), 23-37.

LaTraille, S. L., Gettrust, J. F., and Simpson, M. E., 1982. The ROSE seismic data storage and exchange facility. *J. Geophys. Res.*, 87: 8359-8363.

Melson, W. G., Rabinowitz, P. D., et al., 1979. Site 395: 23°N, Mid-Atlantic Ridge. *In* Melson, W. G., Rabinowitz, P. D., et al., *Init. Repts. DSDP*, 45: Washington (U.S. Govt. Printing Office), 131-264.

Officer, C. B., 1958. *Introduction to the Theory of Sound Transmission:* New York (McGraw-Hill).

Purdy, G. M., Rabinowitz, P. D., and Schouten, H., 1979. The Mid-Atlantic Ridge at 23°N: Bathymetry and magnetics. *In* Melson, W. G., Rabinowitz, P. D., et al., *Init. Repts. DSDP*, 45: Washington (U.S. Govt. Printing Office), 119-128.

Purdy, G. M., Schouten, H., Crowe, J., Barrett, D. L., Falconer, R. K. H., Udintsev, G. B., Marova, N. A., Litvin, V. M., Vlayashko, G. M., Markushevich, V. M., and Zdorovenin, V. V., 1979. IPOD survey area AT-6: A site survey. *In* Melson, W. G., Rabinowitz, P. D., et al., *Init. Repts. DSDP*, 45: Washington (U.S. Govt. Printing Office), 39-48.

Raitt, R. W., 1963. The crustal rocks. *In* Hill, M. N. (Ed.), *The Sea* (Vol. 3): New York, (Interscience), pp. 85-102.

Salisbury, M. H., Stephen, R., Christensen, N. I., Francheteau, J., Hamano, Y., Hobart, M., and Johnson, D., 1979. The physical state of the upper levels of Cretaceous oceanic crust from the results of logging, laboratory studies and the oblique seismic experiment at DSDP Sites 417 and 418. *In* Talwani, M., Harrison, C. G., and Hayes, D. E., (Eds.) *Deep Drilling Results in the Atlantic Ocean: Ocean Crust*, Am. Geophys. Union, p. 113-134.

Shor, G. G., Jr., Menard, H. W., and Raitt, R. W., 1971. Structure of the Pacific basin. *In* Maxwell, E. (Ed.), *The Sea* (Vol. 4): New York (Wiley), pp. 3-27.

Spudich, P., and Orcutt, J., 1980a. A new look at the seismic velocity structure of the oceanic crust. *Rev. Geophys. Space Phys.*, 18: 627-645.

_______, 1980b. Petrology and porosity of an oceanic crustal site: results from wave form modeling of seismic refraction data. *J. Geophys. Res.*, 85:1409-1433.

Stephen, R. A., 1979. The oblique seismic experiment in oceanic crust—equipment and technique. *Mar. Geophys. Res.*, 4:213-226.

Stephen, R. A., Louden, K. E., and Matthews, D. H., 1980. The oblique seismic experiment on Deep Sea Drilling Project Leg 52. *In* Donnelly, T. Francheteau, J., Bryan, W., Robinson, P., Flower, M., Salisbury, M., et al., *Init. Repts. DSDP*, 51, 52, 53, Pt. 1: Washington (U.S. Govt. Printing Office), 675-704.

White, R. S., and Matthews, D. H., 1980. Variations in oceanic upper crustal structure in a small area of the north-eastern Atlantic. *Geophys. J. R. Astron. Soc.*, 61:401-435.

Date of Initial Receipt: January 5, 1983
Date of Acceptance: June 24, 1983

GEOPHYSICS, VOL. 49, NO. 12 (DECEMBER 1984); P. 2088-2093, 6 FIGS.

Linear inversion of body-wave data—Part III: Model parameterization

M. Bée* and R. S. Jacobson‡

ABSTRACT

A velocity gradient model parameterized with the tau-zeta inversion for seismic refraction data is examined with respect to a synthetic traveltime data set. The velocity-depth model consists of a stack of laterally homogeneous layers, each with a constant velocity gradient. The free model parameters are the velocities of the layer bounds and the number of layers.

The best velocity gradient solutions, i.e., with the least deviation from the true model, were obtained from "constrained" models in which the velocities of the layer bounds are the velocities of the observed refracted waves. An arbitrary selection of layer bound velocities was found to be a suboptimal choice of model parameterization for the tau-zeta inversion.

A trade-off curve between model resolution and solution variance was constructed with the constrained model parameterization from examination of numerous solutions with a diverse number of layers. A constrained model with as many layers as observed data points represents a satisfactory compromise between model resolution and solution variance. Constrained models with more layers than observed data points, however, can increase the resolution of the velocity gradient model. If model resolution is favored over solution variance, a constrained model with many more layers than observed data points is therefore the best model parameterization with the tau-zeta inversion technique.

INTRODUCTION

The tau-zeta traveltime inversion method of Dorman and Jacobson (1981) for seismic refraction data has been successfully used to obtain velocity-depth profiles for sediments (Jacobson et al., 1981; Jacobson et al., 1984) and the oceanic crust (Stephen and Harding, 1983; Stephen et al., 1983). For this inversion technique, traveltime-range data $T(X)$ are reparameterized into the form $\tau(p) = T - pX$ and $\zeta(p) = T + pX$, where p is the slowness, or inverse velocity. The linear relationship of τ and ζ to a velocity gradient model results when one assumes a stack of laterally homogeneous layers, each containing a constant velocity gradient (Dorman and Jacobson, 1981). Linear inverse theory (Wiggins, 1972) can be used to obtain the velocity gradient solution and the covariance of the gradient model. The velocity-depth function can then be obtained from an integration of the velocity gradient solution. Linear inverse theory also permits one to trade off model resolution with error estimates of the velocity gradient model. Once this inversion scheme is selected, we can adjust the parameterization of the velocity gradient model to maximize the quality of the solution. The quality of the solution is therefore a function of the manner of choosing the layer bounds for the gradient model. Dorman and Jacobson (1981) found that the model with the smallest variance had the velocities of the layer bounds take on the corresponding values of the observed apparent velocities (inverse slownesses) of the refracted waves (Figure 1a). We call such a model a "constrained" model. Dorman and Jacobson (1981) also tried a fine-layered solution, where the velocity gradient model has many more layers than observed traveltime data. They were unsuccessful in their attempt to obtain a solution, attributing their lack of success to a poor treatment of the model parameter covariance matrix.

Other model parameterizations are possible but have not been fully investigated. Values of velocities for the layer bounds can be arbitrarily selected. For example, layer bounds can be equally spaced between the minimum and maximum observed velocities (Figure 1b). The parameterization of such a model, which we call "arbitrary," would be more independent of the data than the constrained model. For either model, the number of layers chosen is dependent upon one's desire for more resolution of the model or for smaller solution variance.

We present here the results of an investigation into many possible combinations of velocity gradient models and their parameterizations for the tau-zeta inversion using a synthetic traveltime data set. Our intent was to find the best parameterized model. With any inverse problem, determination of a best model is impossible without some a priori or subjective criteria. Since we have used a velocity model to construct our synthetic data, we can use the criterion of the least deviation of the velocity gradient solution from the starting model to determine the best model parameterization. Furthermore, we can alter the number of layers in the model to satisfy the degree of

Manuscript received by the Editor February 24, 1984; revised manuscript received June 7, 1984.
*Chevron Geosciences Company, P. O. Box 42832, Houston, TX 77242-2832.
‡College of Oceanography, Oregon State University, Corvallis, OR 97331.

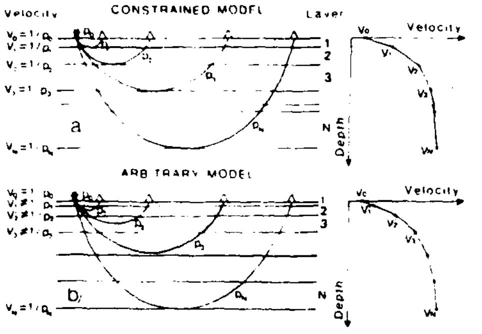

FIG 1. Model layer bound parameterizations for the tau-zeta traveltime inversion (a) Constrained models in which the layers consist of constant velocity gradients and are defined by the velocities $V_0, V_1, V_2, \ldots, V_N$ equal to the inverses of the observed slownesses $p_0, p_1, p_2, \ldots, p_N$ (b) Arbitrary models in which the layers consist of constant velocity gradients and are defined by the velocities $V_0, V'_1, V'_2, \ldots, V_N$ arbitrarily selected and independent from the inverses of the observed slownesses (but with $V_0 = 1/p_0$ and $V_N = 1/p_N$) The linear inversion procedure solves for the depths to these velocities from the traveltime and range data.

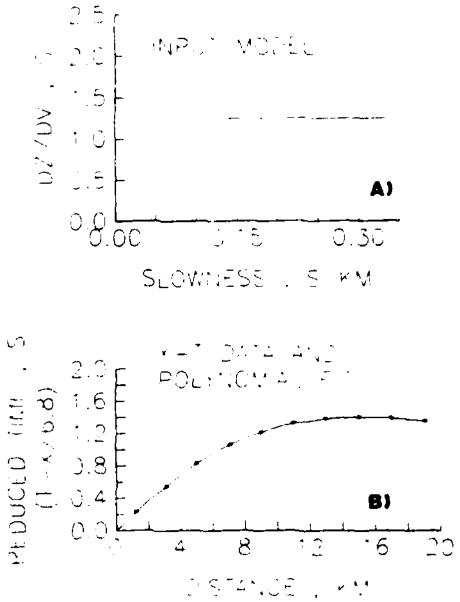

FIG. 2. (a) Starting, or true, model (constant inverse velocity gradient of 1.25 s). (b) Corresponding traveltime and range data generated by a forward method, together with the polynomial fit to the data. Note that the traveltime data have been reduced with a velocity of 6.8 km/s.

resolution we seek. We demonstrate a quantitative description of this trade-off between resolution and variance.

STARTING MODEL AND DATA REPARAMETERIZATION

The model for which the tau-zeta method will be tested is chosen to be one with a constant inverse velocity gradient of 1.25 s, shown in Figure 2a. The slowness bounds for this model are 0.330 s/km and 0.125 s/km, corresponding to a velocity-depth model of $V = V_0 + 0.8z$, where V_0 is the initial velocity, equal to 3.0 km/s, and the maximum velocity is 8.0 km/s. This starting, or true, model was used to generate ten noise-free T-X data points equally spaced in distance (Figure 2b). The data set is thus similar to what is usually obtained in a conventional marine seismic refraction profile with a constant ship speed and equal time intervals between shots. We have also generated three other data sets containing data points equally spaced in time, slowness, and velocity, but the solutions obtained were not significantly different from solutions derived from traveltime data equally spaced in distance. For this reason, we only present solutions which use data equally spaced in distance. At this point, we ignore our knowledge of the true velocity model and now consider the traveltime data as real data with unknown velocities associated with them.

An estimate of the slowness appropriate to each datum point is necessary so that the reparameterization of the data from $X(T)$ to $\tau(p)$ and $\zeta(p)$ can be accomplished. Dorman and Jacobson (1981) used low-order polynomials of $X(T)$, whose derivative at the datum yields the apparent velocity (inverse slowness) for that point. Other methods considered were cubic splines and running averages. In this study, however, we fitted different types of polynomials to the data, trying to minimize the root-mean-square (rms) error between the polynomial and the data. We also investigated the effects of these polynomials upon the velocity gradient solution and its variance. Time or distance (as independent variables) and the order of the polynomial were the parameters we varied in the polynomial regression. The order of the polynomial was increased until the rms error between the data and the polynomial did not decrease significantly. We also examined whether forcing the polynomial through the origin (justified by having both the source and receiver located at the same depth) significantly improved the quality of the solution. For our particular example, the best solution (in terms of the least deviation of the velocity gradient solution from the true model) was obtained with a polynomial of the fourth order in time forced through the origin (Figure 2b). Better velocity solutions could be obtained if the initial velocity at the origin could be constrained by being treated as an additional datum, but in this case, a priori knowledge of the initial velocity is required.

Once the values of slowness are determined for each traveltime datum, the data can be reparameterized into $\tau(p)$ and $\zeta(p)$. The data covariance matrix was derived from the covariance of the polynomial regression coefficients, according to Jacobson et al. (1984). The rms errors in τ and ζ were, respectively, 0.91×10^{-3} s and 0.26×10^{-2} s. These errors are due

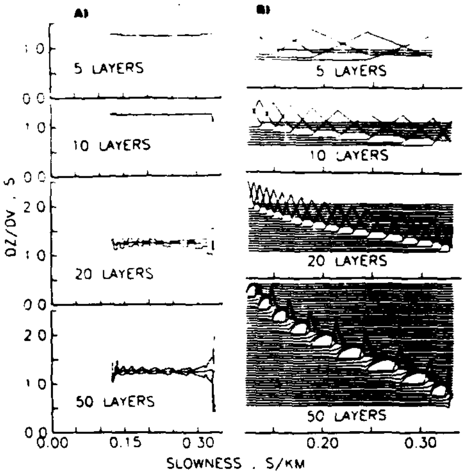

FIG. 3. (a) Constrained inverse velocity gradient solutions with their 96 percent confidence limits, for 5-, 10-, 20-, and 50-layered constrained models. (b) Corresponding constrained model resolutions. The vertical axis represents the layer number.

entirely to the misfit of the polynomial regression, since the traveltime data were calculated without noise.

CONSTRAINED MODELS

The constrained models (Figure 1a) have some of their layers chosen with velocity bounds equal to the inverse observed horizontal slownesses of the data. The slownesses used were those determined from the polynomial fit to the data. The layer bounds are placed where the observed rays turn horizontally, and the model parameters are therefore dependent upon the data. We then varied the number of layers and investigated the following constrained models, each having ten traveltime data points:

1. overdetermined model: 5 layers, with the layer bound slownesses equal to every other observed slowness;
2. evendetermined model: 10 layers, with the layer bound slownesses equal to the observed slownesses;
3. underdetermined models, with 20, 30, 40, 50, and 100 layers. [The layer bound slownesses were the ten observed slownesses and the slownesses obtained by dividing by two, three, four, five, and ten between the observed slownesses.]

The inverse velocity gradient solutions $dz/dV(p)$ with their 96 percent confidence limits for the 5-, 10-, 20-, and 50-layered models are shown in Figure 3a. The overdetermined and evendetermined solutions differ little from the true or starting model. As the number of layers increases the underdetermined solutions depart more and more from the true model. Accordingly, the model error bounds grow with increasing number of layers. The first or uppermost layer (largest slowness) is characterized by a large departure from the true model and has large error bounds (Figure 3a). This situation is possibly caused by imperfections near the origin in the polynomial fitting technique and creates a problem which we have not solved yet but which needs to be addressed.

The model resolutions for each layer of the constrained solutions with 5, 10, 20, and 50 layers are plotted in Figure 3b. The resolution of each layer is derived from the resolution matrix, $\underline{V}\underline{V}^T$ of the generalized linear inverse (Wiggins, 1972). The layers for the 5-, 10-, and 20-layered solutions are determined completely independently, as seen by the sharp narrow peaks in the model resolution matrix. Models with more than 20 layers have layers that are not independently resolved (Figure 3b). A surprising result (Figure 3b) is that the 20-layered solution has velocity gradients that are independently determined. This observation can be explained by the manner in which the data are reparameterized in the tau-zeta inversion. Most traveltime inversion methods (e.g., Bessonova et al., 1974) transform the observed X and T data into τ and p data, retaining only one observable quantity (τ) as a dependent variable. The slowness (p) appropriate for each τ is estimated from the $X(T)$ data and becomes the independent variable. In the tau-zeta inversion, the observed X and T data are transformed into τ, ζ, and p data where τ and ζ are orthogonal, dependent variables of slowness. The values of the slownesses (p) are derived from the original observed $X(T)$ data by a process of smoothing the traveltime data (i.e., the polynomial regression) and treated as the independent parameter. The process of estimating the slowness introduces errors into the data, caused by the imprecision in the knowledge of p. For each $X(T)$ observation, two data, $\tau(p)$ and $\zeta(p)$, are obtained. The values of the tau and zeta data are partially controlled by the type of smoothing employed and are therefore not exactly determined by the $X(T)$ observations. *In principle, in the presence of noise-free data and* exact measurements of slowness, only one-half of these [$\tau(p)$, $\zeta(p)$] data are needed to obtain a velocity-depth function that can reproduce the $X(T)$ data. But selecting the best 50 percent of real data (in terms of finding a solution with smallest possible variance) in the presence of noise is difficult. The tau-zeta inversion technique therefore utilizes all (τ, ζ) data and can tolerate a solution which has an artificially fine resolution. The zeta datum provides most of the constraint upon the layer which contains the horizontally turning ray, whereas the tau datum provides nearly equal constraint on the other layers (Dorman and Jacobson, 1981).

Strictly speaking, there are not twenty, but rather fourteen independent data derived from the ten traveltime data points. As Jacobson et al. (1984) pointed out, the ten tau data are independent of each other and of the zeta data. The ten zeta data are related to one another by their covariance matrix, ultimately derived from the fourth-order polynomial regression to the traveltime data. The covariance matrix of the zeta data is rank deficient; that is, since the covariance of the zeta data is of rank four, only four of all the zeta data are independent. Since the generalized inverse matrix used to solve the inverse problem is weighted by the covariance of the data, the solution can have at most fourteen independent parameters.

Rather than apply the sharp cut-off criterion of Wiggins (1972), we forced the rank of the covariance matrix of the data to be twenty. We did this by adjusting the eigenvalues to be greater than some arbitrary, small value when we performed the eigenvalue decomposition of the data covariance matrix. This procedure also serves to restrict the maximum variance of the solution, if the solution has more than fourteen parameters, as we show later. Further, the 20-layered solution will have velocity gradients that are independently determined, now that the generalized inverse matrix used to solve the inverse problem is of rank twenty, instead of rank fourteen.

A repetitive pattern exists in the constrained velocity-gradient-underdetermined solutions (e.g., the 50-layered solution). There are ten rays corresponding to the ten observed data points and the ten layers in which these rays turn have maximum resolution. Maximum resolution is characterized by sharp peaks in the resolution matrix and very small variance of the solution in these layers. The resolution maxima are a consequence of choosing the layer-bound slownesses equal to the observed slownesses of the rays. The information about the inverse velocity gradient at a particular slowness (or depth) is carried mostly by the ray that bottoms at that depth, since that ray spends a great amount of time in that layer (Dorman and Jacobson, 1981). A layer whose lower bound slowness is an observed slowness contains the maximum information about the bottoming ray traveling with that observed slowness. In between these ten layer bounds are layers where no ray bottoms, and the information about the inverse velocity gradient is then an "average" of the nearby well-constrained layers. The layers where no ray bottoms are characterized by wider and flatter peaks in the model resolution matrix and larger variances in the solution (Figure 3).

ARBITRARY MODELS

Arbitrary models have slownesses of the layer bounds which are chosen to be equally spaced between the maximum (inverse of initial velocity) and minimum observed slownesses (Figure 1b). In these cases, the model parameterization is independent of the data distribution. As the number of layers increases, the highly underdetermined arbitrary solution should asymptotically approximate the highly underdetermined constrained solution.

The $dz/dV(p)$ solutions with arbitrary layer bounds and associated error bounds are shown in Figure 4a. An overdetermined solution consisting of five layers is a reasonable approximation to the true solution. As the number of layers increases, the solutions depart more from the true solution, while the corresponding error bounds grow. The 10-layered and 20-layered solutions sometimes contain two or more consecutive layers with large variances and large departures from the true model, caused by the independent distribution of layer bounds with respect to the observed data distribution. These solutions are in contrast to the constrained solutions where consecutive layers alternate with large and small variances, resulting in a more even distribution of information to the solution.

The resolutions ($\mathbf{V}\mathbf{V}^T$) of each layer for the arbitrary models are displayed in Figure 4b. The results indicate maximum resolution for some layers for the overdetermined and evendetermined solutions and very poor resolutions for most layers of the underdetermind solutions (e.g., Figure 4b, 20-layered solution, between slownesses of 0.22 to 0.28 s/km). When the layer bound slownesses are chosen independently of the observed slownesses, parts of the model are very poorly resolved because no observed rays turn horizontally near the bottom of these layers.

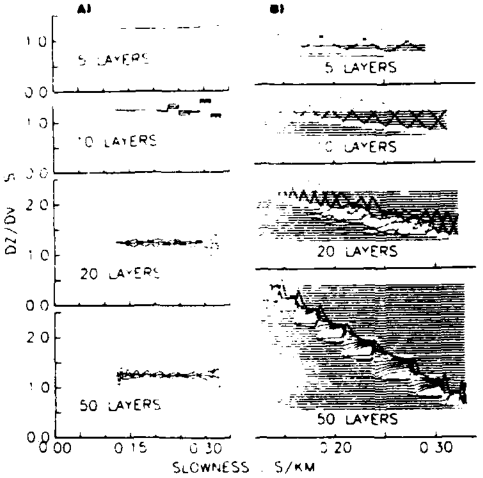

FIG. 4. (a) Arbitrary inverse velocity gradient solutions with their 96 percent confidence limits, for 5-, 10-, 20-, and 50-layered arbitrary models. (b) Corresponding constrained model resolutions. The vertical axis represents the layer number.

QUANTITATIVE MEASUREMENT FOR BEST MODELS

In an effort to quantify the goodness of fit and the differences between the two methods of model parameterization, we have quantitatively examined the departure from the true model curve and the model resolution versus solution variance trade-off curve. The trade-off curve is an empirical determination of the compromise of model resolution and solution errors, analogous to the Backus and Gilbert (1970) trade-off curves. We can select the best way of parameterizing the model layer bounds (constrained versus arbitrary) using the criterion of the least deviation of the solution from the starting velocity model. Once the parameterization of the layer bounds is chosen, the trade-off curve allows us to investigate the effects of varying the number of layers for the model upon model resolution and solution variance.

We define a criterion called "departure from true model" as

$$\sum_{i=1}^{N}\left[\left(\frac{dz}{dV}\right)_{i\,\mathrm{solution}} - \left(\frac{dz}{dV}\right)_{i\,\mathrm{true}}\right]^2,$$

where N is the number of layers. The departure from the true model is used to determine the best type of model layer bounds parameterization.

The definition of model resolution we use is

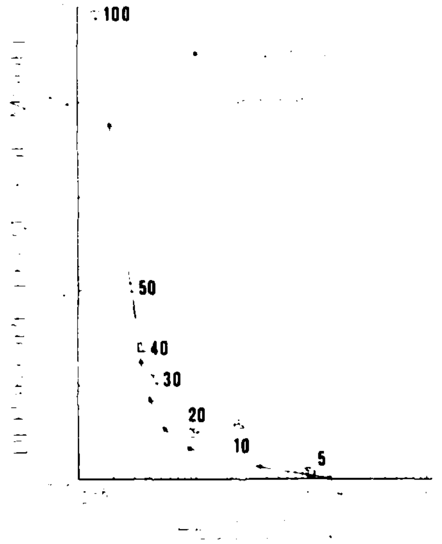

FIG. 5. Departure from the true model as a function of model resolution for 5-, 10-, 20-, 30-, 40-, 50-, and 100-layered, constrained and arbitrary models. This figure demonstrates that solutions obtained from constrained models are closer to the true model than solutions from arbitrary models.

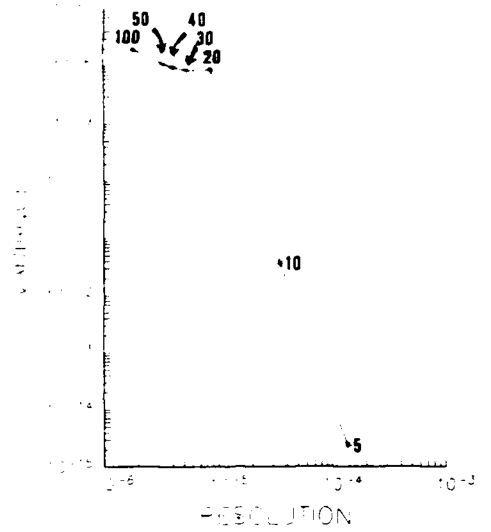

FIG. 6. Solution variance and model resolution trade-off curve for constrained models. Note the existence of a plateau of variance as a function of resolution for highly underdetermined constrained models.

$$\sum_{i=1}^{N}\left[\sum_{j=1}^{N}(p_{ci}-p_j)^2 R_{ij}^2 (p_j - p_{j-1})\right]$$

where p_{ci} is the average slowness in layer i, p_j is the slowness at the lower boundary of layer j, and R_{ij} is the component of the resolution matrix, $\underset{\sim}{V}\underset{\sim}{V}^T$, of the solution, derived from the generalized linear inverse. We have also defined the variance of the inverse velocity gradient solution as

$$\sum_{i=1}^{N}\left[\sum_{j=1}^{N}(p_{ci}-p_j)^2 \operatorname{Cov}(m)_{ij}^2 (p_j - p_{j-1})\right],$$

where Cov $(m)_{ij}$ is the covariance matrix of the model parameters, as determined by the linear inversion process. This value of the model variance is related to the variance of the velocity-depth solution [*Dorman and Jacobson*, 1981, equation (40)].

A comparison between constrained and arbitrary models can be made from an examination of the departure from the true model and the model resolution (Figure 5). The departure from the true model of the arbitrary models is highly dependent upon the relative distribution of layer bounds and data points, as shown partly by the variations in the smoothness of the arbitrary model curve (Figure 5). Of primary importance in Figure 5 is the significant difference in departure from the true model between the constrained and the arbitrary model curves. In all the cases we have examined, the constrained models give a better approximation of the true velocity structure than models with arbitrary parameterization. This result is valid whether the number of layers or model resolution is held constant, strongly indicating that the arbitrary selection of layer bounds is a suboptimal choice of model parameterization.

Given that constrained modeling yields a better solution, we have quantitatively investigated the trade-off between model resolution and solution variance (Figure 6). The figure shows the intuitively expected trade-off between resolution and variance for the even- and overdetermined models, whereas underdetermined models show little change of solution variance as the number of layers increases. This effect is artificial, and is partially caused by the treatment of the covariance matrix of the data, as discussed earlier. There are two contributions to the variance of the solution: the parameter weighting matrix $\underset{\sim}{W}$ and the covariance of the data $\underset{\sim}{S}$, following the notation of *Wiggins* (1972). The variance is related to the reciprocal of the square of the eigenvalues of the generalized inverse matrix, which in turn is weighted by both $\underset{\sim}{W}$ and by the covariance of the data. By artificially restricting the numerical values of the eigenvalues of $\underset{\sim}{S}$ to be no less than some small value, a ceiling is placed upon the contribution of $\underset{\sim}{S}$ to the total, integrated variance of the model. The particular choice of $\underset{\sim}{W}$ we used was a diagonal matrix whose elements were the inverse of the difference of the velocity across each layer (*Jacobson et al.*, 1984). The contribution of $\underset{\sim}{W}$ to the integrated solution variance is independent of the choice of model parameterization and the number of layers.

The departure of Figure 6 from the trade-off curve of Backus and Gilbert (1970) reflects our inadequate treatment of the parameter weighting matrix. This plateau of variance of the model therefore reflects the maximum variance possible for our treatment of this particular data set. The evendetermined (10-layered case in this study) solution, preferred by Jacobson et al. (1984), represents a reasonable compromise between solution variance and model resolution.

CONCLUSIONS

We investigated various combinations of models and their parameterization as used in the tau-zeta traveltime inversion technique of Dorman and Jacobson (1981) for seismic refraction data, by inverting a synthetic traveltime data set.

The best velocity gradient solutions, based on the least deviation of the solution from the starting model, were obtained from constrained models in which the velocities of the layer bounds take on the values of the observed inverse slownesses of the refracted waves. This result implies that, in the tau-zeta inversion, any arbitrary selection of layer bound velocities is a suboptimal choice of model parameterization.

A trade-off curve between model resolution and solution variance was constructed by varying the number of layers of the constrained models. The trade-off curve indicates that an even-determined model (i.e., as many model layers as observed data points) represents a satisfactory compromise between model resolution and solution variance.

We recognize that typical velocity structures of the crust and mantle do not always have velocity-depth functions as simple as the constant velocity gradient model we used in this study. Velocity structures with rapid changes in gradients, including low-velocity zones, can be dealt with by studying one particular traveltime branch at a time. By working from the near-surface downward, stripping the effects of the overlying layers from the deeper traveltime data, one can deal with highly complicated velocity structures. This presupposes that one can identify the secondary arrivals associated with traveltime triplications. We thus feel confident that the results presented here are applicable to traveltime inversion from seismic refraction profiles conducted over more complicated velocity structures.

ACKNOWLEDGMENTS

We thank Leroy Dorman, William Menke, and L. Dale Bibee for many valuable discussions. We also wish to thank two anonymous reviewers for their helpful comments. We gratefully acknowledge the Office of Naval Research under contract number N00014-79-C-0004 for support of this research.

REFERENCES

Backus, G. E., and Gilbert, J. F., 1970, Uniqueness in the inversion of inaccurate gross earth data: Phil. Trans. Roy. Soc. London, Ser. A, **266**, 123–192.

Bessonova, E. N., Fishman, V. M., Ryaboyi, V. Z., and Sitnikova, G. A., 1974, The tau method for inversion of travel times I., Deep seismic sounding data: Geophys. J. Roy. Astr. Soc., **36**, 377–398.

Dorman, L. M., and Jacobson, R. S., 1981, Linear inversion of body wave data—Part I: Velocity structure from traveltimes and ranges: Geophysics, **46**, 138–151.

Jacobson, R. S., Shor, G. G., Jr., and Dorman, L. M., 1981, Linear inversion of body wave data—Part II: Attenuation versus depth using spectral ratios: Geophysics, **46**, 152–162.

Jacobson, R. S., Shor, G. G., Jr., and Bee, M., 1984, A comparison of velocity and attenuation between the Nicobar and Bengal deep sea fans: J. Geophys. Res., **89**, 6181–6196.

Stephen, R. A., and Harding, A. J., 1983, Travel time analysis of borehole seismic data: J. Geophys. Res., **88**, 8289–8298.

Stephen, R. A., Johnson, S. H., and Lewis, B. T. R., 1983, The oblique seismic experiment on Deep Sea Drilling Project leg 65: Initial Rep. Deep Sea Drill. Proj., **65**, 319–327.

Wiggins, R. A., 1972, The general linear inverse problem: Implication of surface waves and free oscillations for earth structure: Rev. Geophys. Space Phys., **10**, 251–285.

Reprinted from Applied Optics, Vol. 24, page 1064, April 1, 1985

Optical analysis of a simulated image of the sea surface

Josué Alvarez Borrego and Marco A. Machado

A simulated sea surface with a Pierson-Neumann power spectrum was generated by a numerical model. The image was recorded on photographic film by means of a microdensitometer with a writing mode. To obtain the bidimensional power spectrum of this simulated image of the sea surface, a coherent optical system was used. This power spectrum has information about frequencies in the highest energy peak and the direction that the waves have at a specific time. The Pierson-Neumann power spectrum used to generate the simulated sea surface was compared with the bidimensional power spectrum obtained with the coherent optical system. Attenuation of the high frequencies in the measured spectrum was observed. This attenuation was probably caused by distribution of density values in the film or by the aperture of the detector used in the coherent optical system. Optical autocorrelations of the simulated sea surface were obtained, and a high degree of correlation in the direction perpendicular to the wind was found.

I. Introduction

Studies of the sea surface using optical and oceanographic methods began by the end of the last century.[1] The radiant energy emanating from the sea surface was the first optical parameter measured. Later, measurements were made of the spectral radiance at different depths. This critical parameter together with other variables such as temperature, salinity, and nutrients determine oceanic productivity.

In the 1930s, measurements of light transmittance and scattering at different depths were made.[1] This research allowed us to understand the particle distribution, which gives information about turbulent flows below the sea surface.

At the same time, physical oceanographers have tried to understand the structural complexities of the sea surface. They have developed techniques which permit us to obtain time series of the waves from which we can derive the power spectrum. With this information we can explain wave generation and propagation and interchanges of energy among volumes of water and also forecast wave behavior. This knowledge is used in the design and construction of harbors. The time series of wave height at a specific point on the sea surface does not give information about the wave direction. Barber[2] used an optical method to find out the direction of the waves on the sea surface. Similar investigations have been carried out by Sugimori.[3] He used an optical method which consists of taking photographs of the sea surface and obtaining its bidimensional optical spectrum. Since this optical method requires only photographs of the sea surface, it can be used for studying waves in deep as well as shallow waters.

The bidimensional optical spectrum contains the same information as the photographic film. There are some problems associated with the method, however, such as limitations arising from film resolution, attenuation of some frequencies, problems with the illumination and contrast in taking the aerial photographs, problems with aberrations present in the optical system, and resolution of the optical system.

The aim of this work is to analyze optically a simulated image of the sea surface (Fig. 1), studying its bidimensional spectrum, and to make a qualitative comparison with a power spectrum obtained from a real sea surface.

II. Simulation of the Sea Surface

Conceptually, the simplest way of generating random surfaces with a specific directional power spectrum is to add many sinusoids in two dimensions, each having a complex amplitude with random phase and magnitude equal to the square root of the power spectrum. Unfortunately, this process generates a small set of independent elevations of the sea surface. The reason behind this is that the method is essentially a Fourier transform of a spectrum of limited wave number con-

---

When this work was done both authors were with Centro de Investigación Científica y de Educación Superior de Ensenada, Departamento de Optica, Apdo. Postal 2732, Ensenada, B.C. México; J. A. Borrego is now with Oregon State University, College of Oceanography, Corvallis, Oregon 97331.

Received 30 November 1984.
0003-6935/85/071064-09$02.00/0.

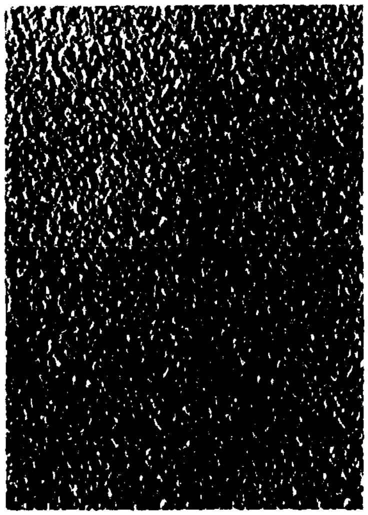

Fig. 1. Four simulated sea surfaces with area of 500,000 m^2 each. The repetition of the surfaces increases the SNR in the optical system.

tent. The filter technique developed in linear system theory[4] does not have this limitation.

A. Generation of the Sea Surface with the Pierson-Neumann Power Spectrum

The technique employed to produce a numerical simulation of the sea surface with a specific power spectrum is based on extension of the 1-D linear system theory to two dimensions.[4] The main idea behind the method consists of applying a bidimensional numerical filter $W(i,j)$ (essentially an impulse response function) to a Gaussian or white surface $X(i,j)$ having uncorrelated random heights. $W(i,j)$ is obtained from a numerical 2-D discrete Fourier transform of the transfer function given by the square root of the ratio of the desired output power spectrum (Pierson Neumann's in our case) to the input power spectrum corresponding to the white surface. This filter modulates the white surface producing an exit surface $Z(i,j)$ with a specific power spectrum $Ez(m,n)$. This power spectrum $Ez(m,n)$ is the theoretical spectrum that has been used in the simulation of the sea surface.[4]

We used the Pierson-Neumann spectrum (Fig. 2), because we had a great deal of information about it. This power spectrum is given by

$$A^2(w,\theta) = \begin{cases} (C/w^6)\exp(-2g^2/w^2u^2)\cos^2\theta \text{ for } w_1 < w < \infty \\ \qquad -\pi/2 < \theta < \pi/2 \\ 0 \qquad \text{otherwise,} \end{cases} \tag{1}$$

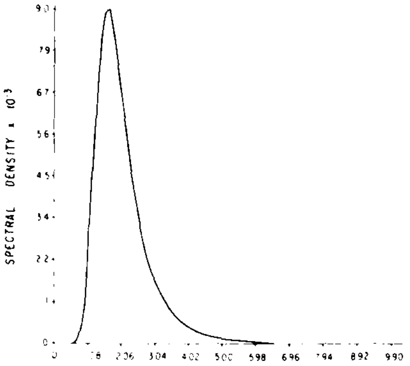

Fig. 2. Directional power spectrum of Pierson-Neumann for a wind velocity of 5.0 m/sec.

where $C = 3.05$ m^2/sec^5, $g = 9.81$ m/sec^2, u(m/sec) is the wind velocity, w(rad/sec) is the angular frequency, w_1 is the angular frequency limit which depends on the fetch and its time duration, $A^2(w,\theta)$ (m^{2}sec/rad) is the power spectral density, θ being the direction of the waves. In this case the wind direction defines $\theta = 0$.[4]

Perhaps the power spectrum is the easier way to characterize a rough surface. When a surface is assumed stationary, as in the case of the sea surface, the power spectrum can be obtained from the Fourier transform of the normalized autocovariance.[4]

The simulated sea surface presented in this work corresponds to fully developed seas in deep waters. (A fully developed sea for a fixed wind speed V is one whose spectrum contains components at all frequencies $0 \leq f < \infty$, each with the maximum energy that can be attained with the given wind speed.)

We can obtain the variance G of the surface elevations in square meters using

$$G = 3C(\pi/2)^{3/2}(u/2g)^5, \tag{2}$$

the significant wave height being $H_{1/3} = 2.83(G)^{1/2}$ (average of the one-third highest waves in the record).

The power spectrum can be written as a function of the wave number components (K_x,K_y). The transformations are

$$w = (gK)^{1/2}, \qquad K = (K_x^2 + K_y^2)^{1/2}, \qquad \theta = \tan^{-1}(K_y/K_x), \tag{3}$$

and the Jacobian is

$$J[(w,\theta)/(K_x,K_y)] = [(g)^{1/2}/2]K^{3/2}. \tag{4}$$

Then the spectrum becomes

$$Ez(K_x,K_y) = J[(w,\theta)/(K_x,K_y)]A^2[w(K_x,K_y),\theta(K_x,K_y)] \tag{5}$$

or

$$Ez(K_x,K_y) = (C/2g^{5/2}K^{9/2})\exp(-2g/u^2K)\cos^2[\tan^{-1}(K_y/K_x)]. \tag{6}$$

We have only considered waves propagating in the wind direction, simplifying the equations. This stochastic model was developed initially by Caruthers and Novarini.[5] In our work, we have amplified the model

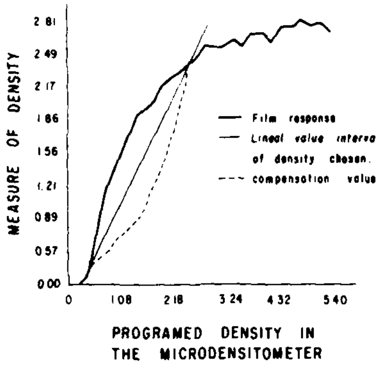

Fig. 3. Film Kodak 2476 response to values of density written with the microdensitometer.

to include much larger areas (as much as 64 times bigger than in the initial model), and we have implemented it with a Prime 400 computer at the Centro de Investigación Científica y de Educación Superior de Ensenada (CICESE).

The numerical results of the simulation consist of a matrix that shows the elevation in centimeters of the surface relative to a mean.

B. Obtaining the Image of the Sea Surface on Photographic Film

The numerical results of the model (wave heights) were expressed as density and using a microdensitometer in the writing mode these values were written on a photographic film.

We found that Kodak Linograph Shellburst film 2476 ESTAR AH BASE gives very high contrast and has high resolution. A range of density values was written on the photographic film with the microdensitometer, and a nonlinear response was observed (Fig. 3). In view of this, the initial values were modified to compensate for the nonlinearities.

The lowest part of the wave (trough) corresponded to the minimum value of density, while the highest part (crest) corresponded to the maximum value of density, and between these extremes a linear interpolation was used to get the intermediate values. This simulation of the sea surface does not make use of the intensity of reflected sunlight as a variable, because our approximation is of the first order only. So the assignment of density values for different heights constitutes only an approximation to the real physical situation.

III. Optical Fourier Transform of the Photographic Image

To get the squared modulus of the optical Fourier transform or power spectrum of the sea images contained in the transparency, it is necessary to use a coherent optical system (Fig. 4). The optical system includes a He–Ne laser 1, a pinhole 2, and a lens L_1 of focal distance f 3. The distance between the pinhole and the lens L_1 is equal to f, thus providing collimated illumination on the object. A circular aperture 4 determines the extent of the illuminated area on the object (transparency), which is placed at 5. The object is put inside a liquid gate to increase the SNR. The lens L_2, placed at a distance f (focal length of L_2) from the object, produces an exact Fourier transform of the object. The power spectrum obtained is measured with a photomultiplier placed at 7.

The 2-D Fourier transform at plane 7 of the complex amplitude transmittance $t_0(x_0,y_0)$ (of the transparency) is given by

$$U_f(x_f,y_f) = \iint_{-\infty}^{+\infty} t_0(x_0,y_0) \times \exp[(-2\pi j/\lambda f)(x_0x_f + y_0y_f)]dx_0dy_0, \quad (7)$$

where λ is the wavelength of the light involved, f is the focal length of the transform lens, j is the imaginary number $(-1)^{1/2}$, and $U_f(x_f,y_f)$ is the complex amplitude at a point (x_f,y_f) in the transformation plane, (x_0,y_0) being coordinates on the object plane.

IV. Optical Correlation of Two Photographic Images

A. Optical System for Correlation

The similitude of two functions can be obtained by performing a cross-correlation analysis. This measure of similitude is effective in finding out the physical structure existing in both functions.

The basic optical configuration of a coherent image-to-image correlator is shown in Fig. 5. Light coming from a laser is collimated and illuminates a section of transparency 1. The transform lens 1 produces an amplitude distribution at its back focal plane (plane 2), which is an exact Fourier transform of transparency 1. A dc block placed on the optical axis in this plane 2 permits removal of the average transmittance of

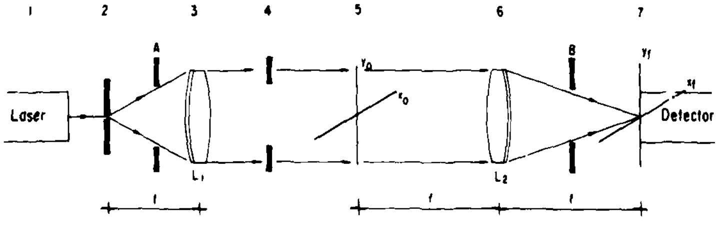

Fig. 4. Coherent optical system for obtaining the power spectrum of the sea images contained in the transparency.

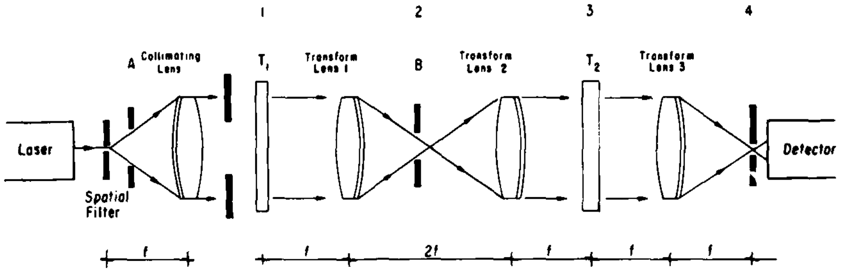

Fig. 5. Coherent optical system for obtaining the correlation between two images.

transparency 1 allowing only the structural information to pass through. The transform lens 2 superimposes the image of transparency 1 on transparency 2 with unit inverted magnification (−1). The transform lens 3 produces the Fourier transform (plane 4) of the amplitude distribution resulting from the illumination of transparency 2 with the filtered image (that is, the image without the dc component) from transparency 1. The correlation signal appears on the optical axis, in the Fourier plane of transform lens 3, and the other light distributions are discriminated by the pinhole in front of the detector.

Correlations between two identical photographic images of the simulated sea surface were performed by illuminating a circular area on transparency 1 (12.56 mm^2) and moving it on its own plane. The displacements were small with intervals $\Delta x = 100$ μm and $\Delta y = 100$ μm. In this way the values of C_{ff} (the correlation function) were obtained.

B. Mathematical Description of the Optical Correlation System

The operation of the system can be described by the following equations.[6] The amplitude distribution in plane 1 is

$$a_1(x_1,y_1) = t_{01} + t_{11}(x,y), \tag{8}$$

where t_{01} is the average amplitude transmittance of transparency 1, and $t_{11}(x,y)$ is the amplitude transmittance corresponding to the structure information. The amplitude distribution in plane 2 is given by

$$a_2(x_2,y_2) = A_1(x_2/\lambda f, y_2/\lambda f), \tag{9}$$

where λ is the wavelength of the light used, f is the focal length of the transforming lens, $A_1(x_2/\lambda f, y_2/\lambda f)$ stands for the Fourier transform of the distribution $a_1(x_1,y_1)$.

The Fourier transform of t_{01} produces a delta function centered on the optical axis in plane 2, which is removed by the dc block. The amplitude distribution on plane 3 is

$$a_3(x_3,y_3) = t_{11}(x_3,y_3)[t_{02} + t_{12}(x_3,y_3)]. \tag{10}$$

Here t_{02} is the average amplitude transmittance of transparency 2, and $t_{12}(x_3,y_3)$ is the amplitude transmittance corresponding to the image structure information. The coordinates (x_3,y_3) are defined in an inverted geometry to avoid the negative signs that occur because of the double transformation process (the image of transparency 1 being inverted).

The amplitude distribution in plane 4 is given by

$$a_4(x_4,y_4) = A_3(x_4/\lambda f, y_4/\lambda f), \tag{11}$$

$$a_4(x_4,y_4) = T_{02}T_{11}(0,0) + T_{11}(x_4/\lambda f, y_4/\lambda f) * T_{12}(x_4/\lambda f, y_4/\lambda f), \tag{12}$$

where T stands for the Fourier transform of t, and $*$ denotes convolution. The first term vanishes since the first dc block in plane 2 has essentially removed the information $T_{11}(0,0)$, and hence the light passing through the pinhole to the detector is essentially given by the second term on the right-hand side of Eq. (12).

When the images corresponding to the two transparencies are identical indicating image matching, the cross correlation becomes an autocorrelation[6]:

$$C_{ff}(x,y) = \iint_{-\infty}^{+\infty} T_{11}(x + \Delta x, y + \Delta y)dxdy. \tag{13}$$

V. Results

The values of the sea surface elevation obtained from the simulation by the computer were calculated for a wind velocity of 5.0 m/sec. The surface area is ~7700 m^2 (Fig. 6).

The computer was programmed to produce a certain density of dots per unit area for each value of height in the waves, giving as a result a normal perspective of the simulated surface (Fig. 1).

First-order linear theory[7] was used to calculate the wavelengths of the deep water waves with periods from 2 to 6 sec. Table I shows the wavelength in microns of the waves present in the photographic film.

Figure 7 shows the bidimensional power spectrum. The power spectrum was obtained in the optical system shown in Fig. 4. The graph of intensity against the wave number along the X_f axis is shown in Fig. 8.

The wave numbers corresponding to the points in the Fourier plane of our optical system, obtained through the relation $X_f = \lambda f f_x$, are listed in Table II (f_x being the associated spatial frequency component).

The theoretical spectrum from the Pierson-Neumann model and the power spectrum obtained with our co-

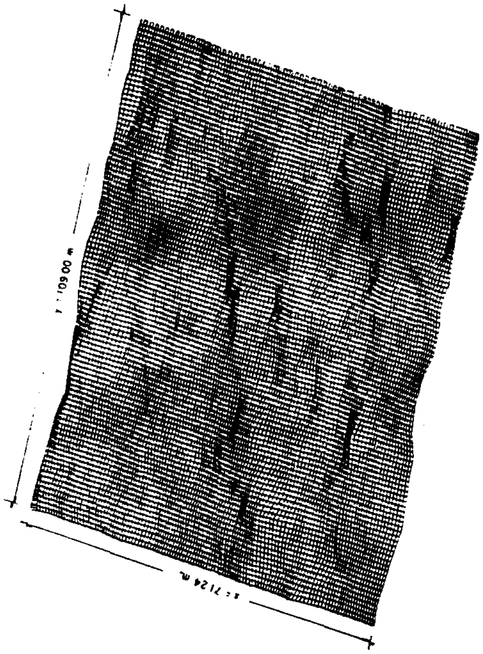

Fig. 6. Simulated sea surface for a Pierson-Neumann power spectrum.

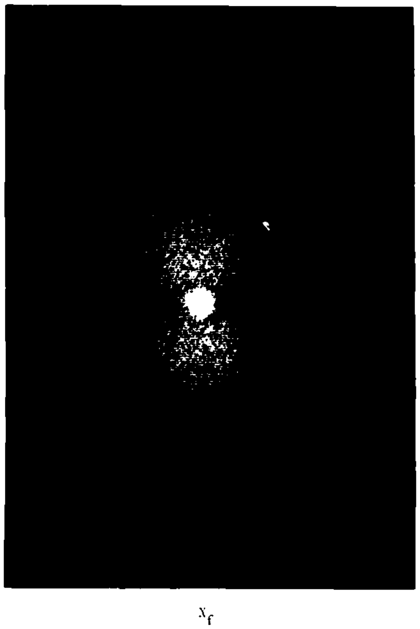

Fig. 7. Power spectrum of the simulated sea surface (Fig. 1). Scale 12:1.

Table I. Wavelength of the Waves

Period (sec)	Wavelength (m)	Wavelength in the film (μm)
2.0	6.27	91.3
3.0	14.05	204.61
4.0	24.98	363.79
5.0	39.03	568.41
6.0	56.20	818.46

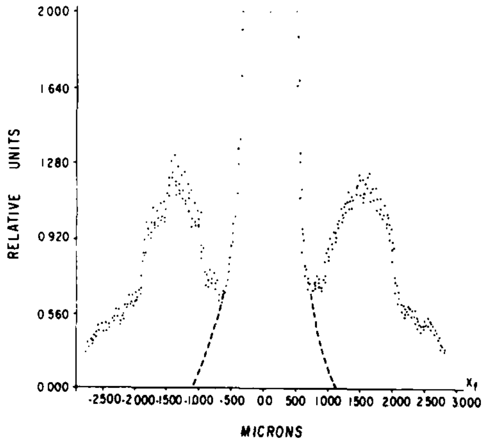

Fig. 8. Result of the measurement of the power spectrum (Fig. 7) obtained in the coherent optical system (Fig. 4).

herent optical processor were normalized and plotted for comparison in Fig. 9.

Figures 10(a) and (b) show the optical autocorrelations of the sea surface along the directions parallel and perpendicular to the wind, respectively.

The correlation area was 133,000 m^2 corresponding to a 4-mm diam limiting aperture in front of the object.

VI. Discussion

We must make clear that the work reported in this paper has had as a main objective to analyze optically a simulated image of the sea surface (Fig. 1), studying its bidimensional spectrum, and to make a qualitative comparison with a power spectrum obtained from a real sea surface.

A calibration of the microdensitometer must be performed each time a different sea is generated on film. Besides, the calibration must be repeated several times over a reasonable period of time to verify possible changes in microdensitometer functioning.

As mentioned before, the marine surfaces were generated using the Pierson-Neumann theoretical spec-

Table II. Localization of Sea Wave Numbers on the Fourier Plane of the Optical System

Period (sec)	Wavenumber ($2\pi/\lambda$)	X_f Fourier plane (mm)
2.0	1.0021	6.99
3.0	0.4472	3.15
4.0	0.2515	1.80
5.0	0.1609	1.17
6.0	0.1118	0.83

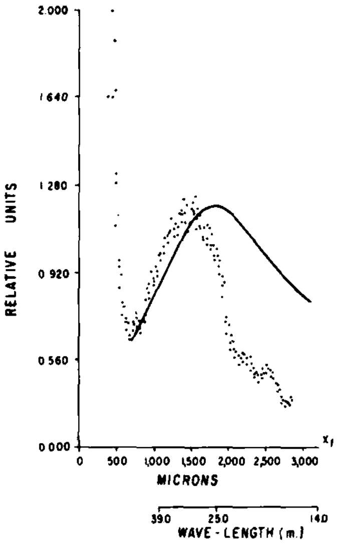

Fig. 9. Comparison between the power spectrum obtained experimentally and the theoretical Pierson-Neumann power spectrum (continue line).

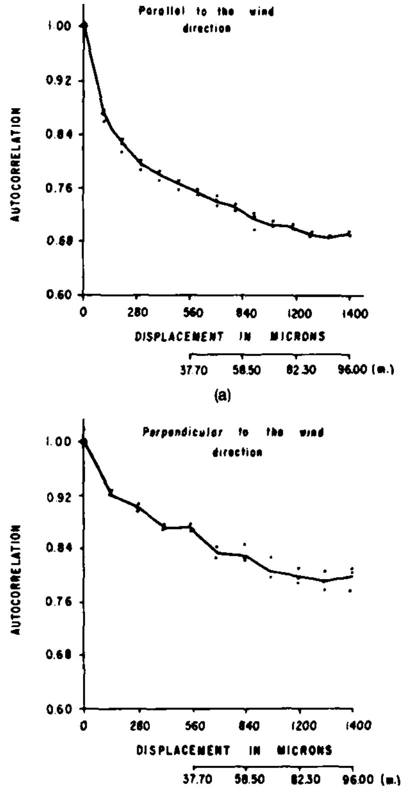

(b)

Fig. 10. Autocorrelations.

trum and for a wind velocity of 5.0 m/sec. The frequency range of importance in the spectrum goes from 0.5 to 0.16 cycles/sec or, in terms of periods, from 2 to 6 sec.

In this work, the modeling of the sea surface has been extended to an approximate area of 500,000 m^2 (Fig. 1) for marine surfaces affected by a wind with a velocity of 5.0 m/sec. This value of wind velocity was chosen in accordance to the real situation existing over a large percentage of the area of interest. (This area is the NW coast of México.) For future work, we intend to take real pictures of the sea surface which would be useful for comparison with the model results. The enlargement of the model is needed to obtain waved surfaces (within important frequency ranges) of 10 cycles minimum, which will improve the optical analysis.

The power spectrum obtained in our optical system is of considerable value because it contains information about the wave number and about the direction of the waves with respect to the given reference system. The intensity, as a function of wave number (Fig. 8), measured in the Fourier plane by the detector is proportional to the energy assigned to the waves in the simulated marine surface,[8] and the location or position in the Fourier plane of the frequencies contained in the spectrum corresponds to the information contained in the simulation.

Tests were made to determine the influence of exposure effects, during recording of the simulated image, on the energy spectrum obtained in the optical processor. If an adequate exposure is not achieved, it is preferable to have an underexposed slide to an overexposed one because the former gives better results for the measurements of the power spectrum by letting more energy through.

The optical system used in this work had a spatial resolution of 104 lines/mm, and it satisfactorily resolves all frequencies contained in the simulated image. Measurements of the spectrum were made only along the X_f axis, because this axis corresponds to the main direction of the waves, and most of the energy is contained here. Attenuation of the high frequencies is observed in the optical power spectrum of the simulated surface when compared to the Pierson-Neumann theoretical spectrum (Fig. 9). This can possibly be caused by the following factors: the designation of density values for each wave height value may have had small errors, and the opening at the detector, even though centered at a certain frequency, also receives energy from neighboring frequencies. To evaluate these aspects, it would be convenient to obtain the power spectrum by means of digital processing. To do this, the microdensitometer should be used to read the information contained in the slide, and the numerical data thus obtained, fed to a computer to perform a numerical Fourier transformation. These results can then be compared with those obtained optically. This would require development of a series of computer programs to carry out the analysis of the very large amount of data arising from a photographic image, in a reasonably short processing time.

The diameter of the limiting aperture gives information about the diameter of the speckle grain existing in our measurement plane and, therefore, about the size of the opening that our detector must have. In our particular case the opening had a 520-μm diameter, and the theoretical diameter of the speckle is 134 μm. The slide containing the simulated marine surface used in the optical system to obtain the power spectrum is considered as an object where the phase changes presented are irrelevant (amplitude object). For this reason we expect the power spectrum to have dual symmetry[9] (as in our case). If this is not the case, the asymmetry in the diffraction pattern could be the result of several factors: first, the detector might not be moving exactly along the X_f axis; second, the diameter of the aperture at the detector might not be uniform; and, finally, there might be asymmetric aberrations in the optical system. If we have no symmetry in the power spectrum, we will have mistakes in the information obtained.

Fortunately, our optical system can satisfactorily resolve the power spectrum for the high energy peak. Seventy-two hours of computing time (Prime 400) are needed to generate a marine surface similar to the one in Fig. 1 with an area of 500,000 m^2.

One of the conditions of the theoretical model is the nonexistence of swell which does not follow the wind direction. This nonexistence can be observed easily in the photograph of the power spectrum of the simulated sea surface (Fig. 7). It can be observed that the power spectrum lies primarily along the X_f axis. If we were to have a sea with crossed waves, a different direction would prominently appear in our Fourier plane. Nevertheless, a certain widening away from the main direction can be observed in the intensity (Fig. 7). This can be easily explained because the locally formed waves have an approximate fluctuation in the direction of ±30° relative to the predominant direction in some cases.[7] This is to be expected because it is included in the model. If local waves were to follow one direction only, the power spectrum would be confined to a very narrow strip in the direction of the waves.

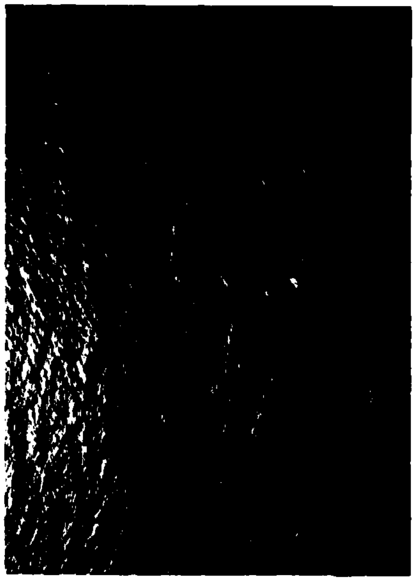
Fig. 11. Real sea surface. Area, 68,900 m^2.

By analyzing the autocorrelation graphs [Figs. 10(a) and (b)], a big decline is observed in the autocorrelation values in the wind direction in comparison with the autocorrelations values in the perpendicular direction. This result coincides with the numerical results obtained by Bruno and Novarini.[4] This gives confidence in the use of the optical correlation method.

For a real sea surface (Fig. 11), uniform sun illumination does not occur. The waves are visible because they tilt the roughened sea surface alternately toward and away from the observer thus modulating the intensity of backscattered sunlight.[10] However, in a real sea surface, the slopes rather than the wave heights are the drivers for the imaged irradiance. Figure 11 shows an aerial picture of the sea surface taken from an altitude of 300 m and from a 45° angle of inclination with respect to the sea surface at 7:00 a.m. The altitude is a very important factor, because the higher altitudes the better the results are when analyzing the power spectrum. For a higher altitude the number of waves present is larger, and the wavelength in the film is smaller. This means that the information in the Fourier plane will appear at a certain distance away from the central Airy pattern (dc component) thus avoiding the noise caused by the rings in the Airy function.

Figure 12 shows the bidimensional power spectrum of the transparency of the real marine surface. We can see that its shape is very similar to the one optically obtained on the basis of the theoretical model (Fig. 7). It should be remembered that with the photographic technique the spectra pertain to a certain very short time interval. To obtain information of the real sea

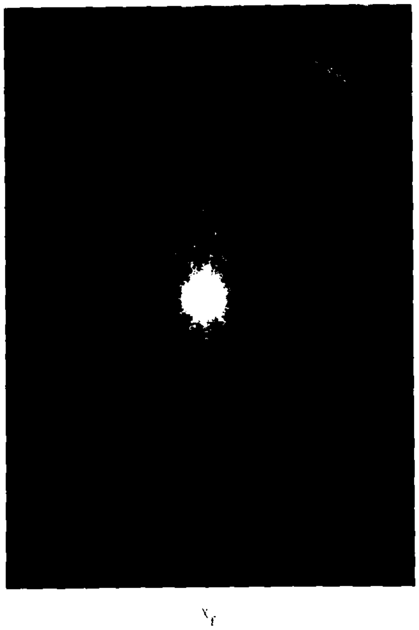

Fig. 12. Power spectrum of a real sea surface (Fig. 11).

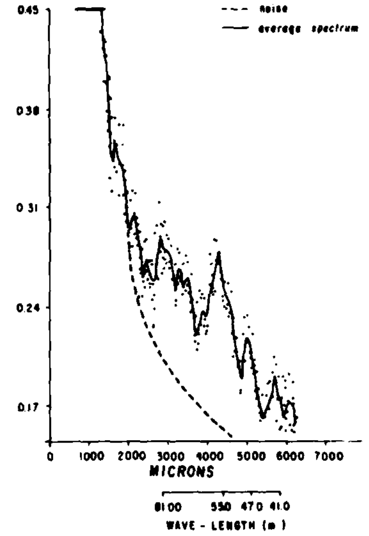

Fig. 13. Result of the measurement of the power spectrum of the real sea surface (Fig. 12).

surface using the spectrum of the photograph, it is necessary to use the method described in Denzil.[8] The difference between both spectra is that in the last one (Figs. 12 and 13) we can observe swell in addition to sea, and swell dominates the power spectrum. In this case the wind velocity was 1.0/sec. The relevant information (Fig. 13) was obtained by measuring the energy distribution in the spectrum along the X_f axis (main wind direction). Three measurements were made along the X_f axis to obtain an average. The diameter of the limiting aperture in front of the object was on this occasion 3 cm.

Finally, to carry out a complete analysis, it is very important to obtain wave data by means of pressure sensors, at the same time and place where the pictures are taken, to allow for a direct comparison between this and the one obtained from the simulated image.

VII. Conclusions

In this work, optical methods for obtaining the frequency distribution contained in a marine surface have been evaluated by means of the analysis of a simulated image. The resolution of the optical system allows the analysis of all frequencies present in the simulated marine surface.

From the obtained results we may conclude that a good optical system for processing can be formed by a pair of achromatic doublets taking the proper alignment precautions.

The only limitation in carrying out this type of optical analysis concerns the size of the simulated surface because the computing time for the simulation increases in a nonlinear fashion. This affects the minimum size of the detector aperture used in scanning the optical spectrum. Also, it was found, because of the running property of the Fourier transform, that the use of several replicas of the simulated image arranged side by side in the object plane allows the use of smaller sampling apertures and increases the SNR in the system

When comparing the power spectrum obtained optically with the Pierson-Neumann theoretical spectrum used in the simulation of the marine surface, a correlation between the two results was found to exist in the higher energy frequency range. A high correlation does not exist for the entire frequency range. It is to be noticed that the measurements have been made on one simulated marine surface only, and it is necessary to repeat the analysis on other simulated surfaces having the same wind velocity, and a different random surface to start the model, and for other seas generated with other wind velocities. The attenuation of the high frequencies in the power spectrum of the simulated sea surface can perhaps be corrected by making a detailed analysis of the relationship between wave heights and density values using this time sunlight as a parameter.

The optical correlation of the simulated marine surface in a direction perpendicular to the wind is larger than in the parallel direction. This result coincides with the numerical results obtained by Bruno and Novarini.[4] This gives confidence in the use of the optical correlation method, allowing us to extend it later to the analysis of aerial pictures of the sea surface.

In this type of analysis it will be useful to develop programs for digital processing to make an analysis similar to the one developed optically. This has the purpose of providing a more solid base for comparison between numerical and optical results.

Having aerial photographs of marine surfaces, taken under similar conditions as those corresponding to the simulated event, is indispensable for the comparison of results. This would give confidence for studying frequency distributions from real marine surfaces.

Subsequent simulations of sea surface should include proper lighting of the studied surface or a demonstration that the sunlight effects do not influence the frequency content and distribution. Besides, it would be convenient if the aerial pictures used include those regions of the sea where tests are made with pressure sensors, since that would give the real frequency distributions.

A larger version of this work was presented by J.A.B. as a MSc. dissertation at CICESE. A scholarship for this MSc. was provided by the National Council of Science and Technology of Mexico. We wish to thank Hugo Peña for a paticularly useful discussion concerning the theoretical model, Hector Escamilla for helpful discussions about the writing of this paper, and Martin Celaya, Head of the Applied Physics Division of CICESE, and the Computer Center of CICESE, for their collaboration in the realization of this work. We are also very grateful to J. Ronald V. Zaneveld for many valuable suggestions in the preparation of the final manuscript. This research was partially supported by the Office of Naval Research under contact N00014-84-C-0218.

References

1. N. G. Jerlov, *Marine Optics, Vol. 14* (American Elsevier, New York, 1976).
2. N. E. Barber, "Finding the Direction of Travel of Sea Waves," Nature London 154, 1048 (1954).
3. Y. Sugimori, "A Study of the Application of the Holographic Method of the Determination of the Directional Spectrum of Ocean Waves," Deep Sea Research and Oceanographic Abstracts, 22(5), May 1975.
4. D. Bruno and J. Novarini, "Análisis comparativo de superficies modeladas numéricamente con distintos espectros de potencia," Junio 1976, Republica Argentina, Servicio de Hidrografia Naval, DOF-ITIO-76 (1976).
5. W. Caruthers and J. Novarini, "Numerical Modeling of Randomly Rough Surfaces with Application to Sea Surfaces," Texas A & M Univ., Dept. Oceanography Tech. Rep. Ref. 71-13-T (1971).
6. D. Casasent, *Optical Data Processing* (Springer, Berlin, 1978).
7. B. Kinsman, *Wind Waves* (Prentice-Hall, Englewood Cliffs, N.J., 1965).
8. S. Denzil, Jr., "Directional Energy Spectra of the Sea from Photographs," J. Geophysical Research, 74, No. 8 (April 15, 1969).
9. R. Bracewell, *The Fourier Transform and its Applications* (McGraw-Hill, New York, 1965), pp. 14–16.
10. C. S. Cox, *Optical Aspects of Oceanography* (Academic, New York, 1974), Chap. 3.

Internal Waves in the Arctic Ocean: Comparison with Lower-Latitude Observations

MURRAY D. LEVINE AND CLAYTON A. PAULSON
College of Oceanography, Oregon State University, Corvallis, OR 97331

JAMES H. MORISON
Polar Science Center, University of Washington, Seattle, WA 98195

(Manuscript received 13 April 1984, in final form 13 November 1984)

ABSTRACT

A thermistor chain was moored below the pack ice from 50–150 m in the Arctic Ocean for five days in 1981. Oscillations in temperature are attributed to the vertical displacement of internal waves. The spectral shape of isotherm displacement is consistent with the Garrett-Munk model and other internal wave observations, but the spectral level is significantly lower. Other observations from the Arctic Ocean also exhibit lower internal-wave energy when compared with historical data from lower latitudes. The lower energy may be related to the unique generation and dissipation mechanisms present in the ice-covered Arctic Ocean. Significant peaks in vertical coherence occur at 0.81 and 2.6 cph. The peak at 2.6 cph coincides approximately with the high-frequency spectral cutoff near the local buoyancy frequency; this feature has been observed in many other internal wave experiments. The coherent oscillations at 0.81 cph exhibit a node in vertical displacement at 75–100 m. This is consistent with either the second, third or fourth vertical mode calculated from the mean buoyancy frequency profile. Evidence is presented which suggests that, contrary to the Garrett-Munk model, the frequency spectrum does not scale with the Coriolis parameter.

1. Introduction

The internal wave field in the mid-latitude ocean is remarkably steady and uniform. This observation motivated Garrett and Munk's universal isotropic model of the internal wave spectrum (Garrett and Munk, 1972; 1975; hereafter referred to as GM). The GM model has served as a useful framework for the analysis and comparison of internal wave observations. While the kinematic description of the internal wave field has continued to improve, our understanding of the physical processes that generate and dissipate the waves remains woefully inadequate (e.g., Olbers, 1983; Levine, 1983).

Wunsch (1975) suggested that deviations of internal wave spectra from universal form may provide clues to sources and sinks of internal waves. However, the identification of variations in the wave field caused by variations in forcing and dissipation has proved difficult. The extensive measurements made during the Internal Wave Experiment (IWEX) agree reasonably well with the GM model except for a peak at low wavenumber and a decrease in the number of modes at high frequency (Müller *et al.*, 1978). Many upper-ocean observations also exhibit a positive deviation from the GM spectrum at high frequency accompanied by an increase in vertical coherence (e.g. Pinkel, 1975; Levine *et al.*, 1983a,b; Käse and Siedler, 1980). Roth *et al.* (1981) found that internal wave spectral levels in the upper ocean tended to fluctuate above the level of the GM spectrum. The influence of the internal tide and its harmonics on the remainder of the spectrum is uncertain (e.g., Pinkel, 1981; Levine *et al.*, 1983b). Better documentation of the temporal variations in the internal wave field with long time series is just beginning (e.g., Briscoe and Weller, 1984). Regions of anomalously high internal wave energy near topographic features have been identified but are apparently due to the kinematic readjustment of the wave field from reflection off the bottom (Eriksen, 1982) or focusing in canyons (Hotchkiss and Wunsch, 1982). In summary, the link between a generation mechanism and observed high energy has not been conclusively established. Perhaps by compiling many more observations in varied environments significant correlation between the wave field and other processes will be found.

In the search for deviations from the universality of the internal wave spectrum, a modest experiment was performed in the Arctic Ocean in May 1981 north of Spitzbergen during the occupation of the FRAM 3 ice camp. A thermistor chain was moored from the ice and time series of vertical displacement of isotherms were obtained. The purpose of this paper is to present the results of an analysis of these observations and to compare spectra and vertical coherence with other Arctic and lower-latitude observations of internal waves. The GM model is used as a convenient framework to aid in making the comparisons. Specifically, we compare spectral energy levels scaled by buoyancy frequency. In addition, the effect of eliminating the Coriolis parameter from the GM scaling is tested.

2. Observations

A single Aanderaa thermistor chain was moored from the pack ice for five days beginning on 1 May, 1981, at 81°50'N, 5°10'E, north of Spitzbergen over the Yermak Plateau (Fig. 1). At the time of recovery on 6 May the mooring had drifted 24 km to the west at an average rate of 7 cm s^{-1}. The chain recorded temperature every 2 minutes at 10 m intervals over a depth range of 49–149 m. Pressure was measured at 48 m to determine the amount of tilt of the mooring caused by the relative velocity between the water and ice.

The sensors were placed in the nearly uniform temperature gradient between the relatively cold Arctic surface water and the deeper warm Atlantic water (Coachman and Aagaard, 1974). Temperature and salinity profiles measured with the APS, profiling current meter–CTD (Morison, 1980), are shown in Fig. 2. The mooring depth was chosen to insure that a large temperature signal would result from any significant vertical displacement of the water. The Aanderaa data logger was modified to record at a resolution of 0.005°C, which corresponds to a vertical displacement of 15 cm in this temperature gradient. The density field over this depth range is dominated by salinity, but the *T–S* relationship was stable enough during this period to tag a density surface by its temperature.

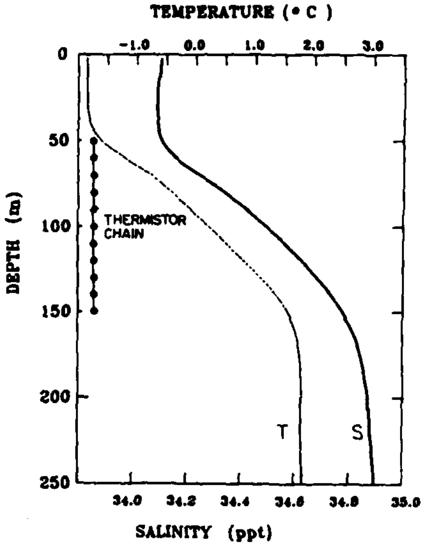

FIG. 2. Average vertical profiles of temperature (thin line) and salinity (bold line) from 20 casts of the APS, profiling current meter–CTD, made concurrently with the thermistor chain deployment. The location of the thermistor chain is indicated.

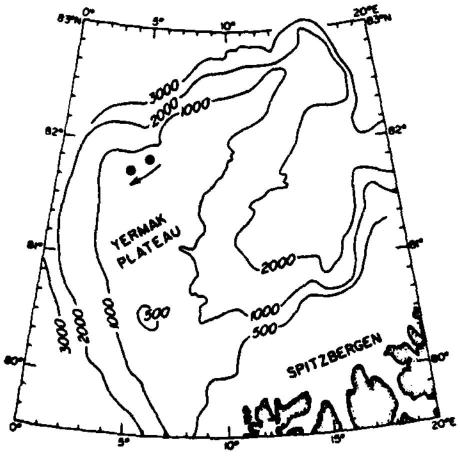

FIG. 1. Map showing the positions of FRAM 3 ice camp (solid dots) at the times of the deployment and recovery of the thermistor chain 5 days later. Bathymetric data, contoured in meters, are from Jackson *et al.* (1984).

Time series of isotherm depth were calculated by linearly interpolating the position of a given isotherm between the appropriate pair of thermistors. The vertical positions of the thermistors were assumed constant because the recorded pressure variation was always less than the 20 cm resolution of the pressure sensor. Sixteen time series of isotherm depth in increments of 0.2°C were obtained. An example of a one-day record of the series is shown in Fig. 3.

The series of isotherm depth were divided into two time segments and pre-whitened by applying a first-difference filter to reduce spectral leakage. Fourier transforms were computed, and the resulting spectra were recolored to restore the signal removed by the filter. Smoothed estimates of auto- and cross-spectra were formed by ensemble-averaging the spectra from the two segments and averaging in non-overlapping frequency bands, equally spaced on a logarithmic frequency scale. Vertical displacement spectra are shown in Fig. 4a for the −0.8° and 1.6°C isotherms which oscillated around average depths of 67 and 137 m, respectively. Vertical coherence estimates between the isotherms at mean depths of 57 and 76 m are shown in Fig. 5.

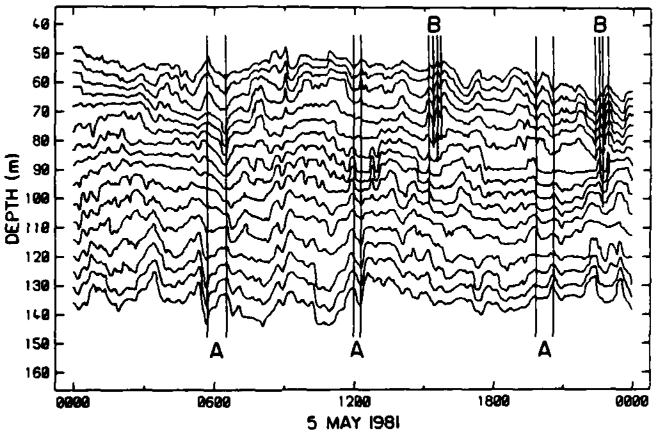

FIG. 3. Isotherm depths as a function of time on 5 May 1981. The 16 isotherms shown are in intervals of 0.2° from −1.4° (shallowest) to 1.6° (deepest). Examples of oscillations that are responsible for the high coherence in the frequency band around 0.81 cph are labeled A. Note the presence of a node at 75–100 m. Higher-frequency fluctuations that contribute to the high coherence at 2.6 cph are labeled B.

A representative vertical profile of the buoyancy frequency $N(z)$ was spliced together from two data sources (Fig. 6). Values in the upper 250 m were obtained by averaging 20 profiles recorded by the CTD during the time the mooring was deployed. The buoyancy frequency increases with depth to a peak of 4 cph at about 75 m followed by a monotonic decrease. Below 250 m values were calculated from water samples taken by scientists from the Lamont-Doherty Geological Observatory (Manley, personal communication, 1982). In this region N was a nearly uniform 1 cph.

3. Spectrum

Frequency spectra of isotherm displacement from 67 and 137 m are presented in Fig. 4a. In the internal wave band between the inertial frequency, f (0.0825 cph), and the local buoyancy frequency N the spectral slopes are between −1.5 and −2.0. To accentuate the internal wave band, the displacement spectra were converted to vertical velocity spectra by multiplying by the square of the frequency (Fig. 4b). A spectral roll-off occurs at frequencies above local N. The spectrum at 67 m is generally lower than the one at 137 m. When the spectra are scaled by multiplying by the local value of N, the difference between the spectra is reduced (Fig. 4c). This is consistent with the $1/N$ scaling of vertical displacement that follows by assuming that $N(z)$ is a "slowly" varying function (WKB approximation).

The spectral form of the Garrett-Munk model is used to compare these spectra with other internal wave observations. The GM model provides a statistical description of the "typical" internal wave observation because it is empirically derived. Specifically, we use the formulation of the spectrum presented by Munk (1981). Desaubies (1976) has shown that the four parameters of the GM model, E (nondimensional energy level), j_* (effective nondimensional mode number), b (vertical depth scale of N in m), and N_0 (buoyancy frequency scale in cph) can be conveniently recast into two independent parameters:

$$r = Eb^2N_0, \tag{1}$$

$$t = \frac{j_*}{2N_0b}. \tag{2}$$

The frequency spectra of vertical displacement and horizontal velocity can then be written

$$S_\zeta(\omega) = \frac{2}{\pi} r \frac{f}{N} \frac{(\omega^2 + f^2)^{1/2}}{\omega^3}, \tag{3}$$

$$S_u(\omega) = S_{u_1} + S_{u_2} = 8\pi r f N \frac{(\omega^2 + f^2)}{\omega^3(\omega^2 - f^2)^{1/2}}, \tag{4}$$

where frequency is expressed in cycles per hour (cph). The vertical displacement and horizontal-velocity spectral levels are proportional to $1/N$ and N respectively, consistent with WKB scaling. Both spectra, and hence the total energy, are scaled by the parameter r. At high frequency, $\omega \gg f$, the frequency dependence is ω^{-2}.

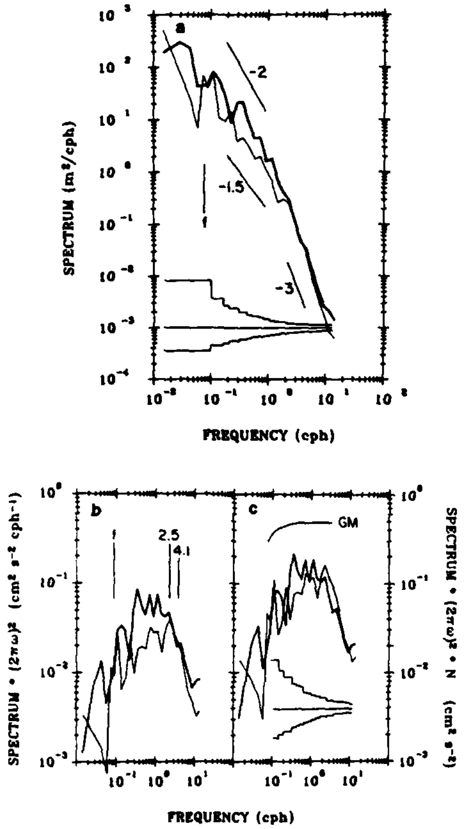

FIG. 4. (a) Autospectra of isotherm displacement for the −0.8° (thin line) and 1.6° (bold line) isotherms which oscillated at average depths of 67 and 137 m respectively. The 95% confidence limits are also plotted. (b) Vertical velocity spectra converted from the displacement spectra plotted in (a) by multiplying by frequency-squared. (c) As in (b) but multiplied by the local buoyancy frequency. N (67 m) = 4.1 cph and N (137 m) = 2.5 cph. Note that the difference between the two spectra in the internal wave band shown in (b) is reduced when scaled by N. The Garrett-Munk spectrum is shown for reference. The 95% confidence limits are also plotted.

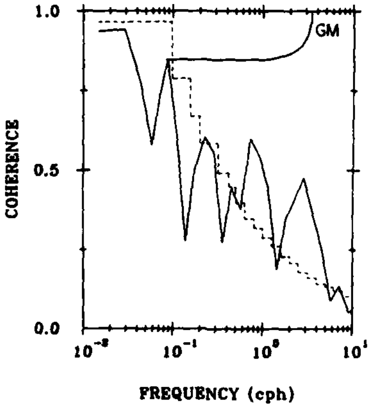

FIG. 5. Vertical coherence between the −1.4° isotherm at 57 m and the −0.4° isotherm at 76 m. Values above the dashed line are nonzero at the 95% significance level. Note the two peaks at 0.81 and 2.6 cph. The coherence from the GM model is also shown [Eq. (6)].

For reference the GM spectrum (Eq. 3) is plotted with the observations (Fig. 4c). The level of the spectrum is set from the canonical GM value of r = 320 m^2 cph, obtained by using the values of E = 6.3 × 10^{-5}, b = 1300 m and N_0 = 3 cph (Garrett and Munk, 1975). The GM spectrum is similar in shape but significantly higher in level than the data (Fig. 4c). A quantitative measure of the observed spectral level was obtained by fitting the GM spectral *shape* (Eq. 3) to the spectra in Fig. 4c by adjusting r so that the model variance equaled the variance in the data over the frequency band from 0.15 to 2.0 cph. The best-fit values of r are 47 and 75 m^2 cph from 67 and 137 m respectively. These values are significantly lower than the GM value.

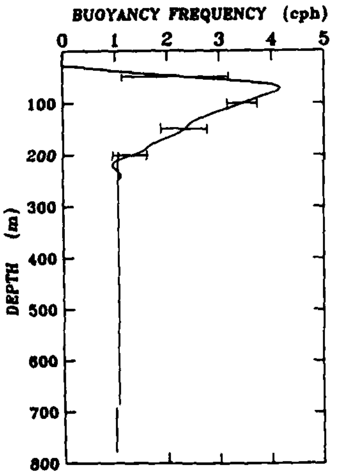

FIG. 6. Average buoyancy frequency profile. Values above 250 m are from measurements made with a CTD. Standard deviations of the 20 profiles used to form the average are shown at selected depths. Estimates from water samples are shown by vertical lines (Manley, personal communication, 1983).

To compare our results with historical observations, estimates of the internal-wave spectral energy from many experiments including other Arctic observations are plotted versus the local buoyancy frequency in Fig. 7a. These values were obtained from both horizontal velocity and vertical displacement data. A complete reference list is given in Table 1. The procedure for estimating the spectral levels varied among investigators; however, nearly all values were obtained by fitting the data to a frequency spectral slope approximating the GM model over a midfrequency range, far from the inertial, tidal and buoyancy frequencies. The spectral level was then converted to a value of r using (3) or (4) with the local values of f and N. Values of E, b, and N_0 were not estimated individually from the data—only the product $r = Eb^2N_0$ was estimated from the spectra. The quantity $r = Eb^2N_0$ is merely the GM notation of the spectral *level* after WKB scaling. If the GM model were truly universal, all observed values of r would lie on a horizontal line. As a group, the values from the Arctic are markedly lower than other observations; varying from factors of 3 to 70 below the canonical GM level. The values from midlatitude generally scatter within a factor of 3 of the GM level. High values occur near topographic features, e.g., Hydrographer Canyon (number 18), Hudson Canyon (number 21), Muir Seamount (number 17) and Ymir Ridge (number 13, highest two values). Values of r at low latitude also tend to be high, e.g., 16°N (number 10), 8.8°N (number 7) and 1.5°N (number 20a), and estimates very near the equator are too large to be plotted, e.g., 0 to 0.05°N (number 20b). Further discussion of the latitudinal scaling of the internal wave energy level is presented below.

What quantities should be considered "universal" in the GM parameterization of the spectrum? If E is constant, can variations in spectral level be described by variations in the stratification parameters b and N_0 alone? The quantities b and N_0 are introduced into the GM model as natural scales for length and time to non-dimensionalize the variables. It is unrealistic to expect that the complexity of internal wave interactions can be characterized by a single

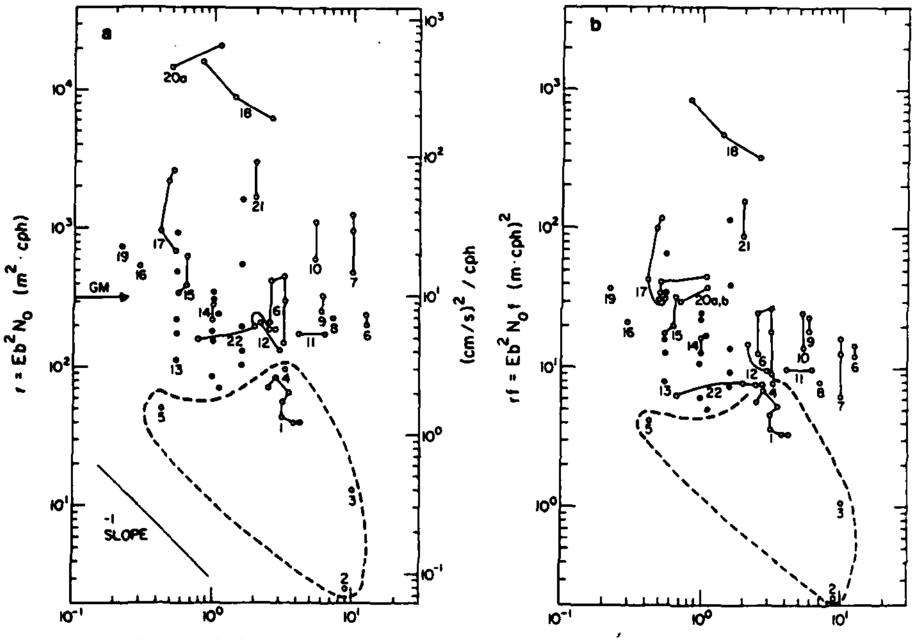

FIG. 7. (a) Estimates of the spectral level, reported in units of $r = Eb^2N_0$, are plotted vs local buoyancy frequency. The numbers refer to the data sources listed in Table 1. The estimates from the Arctic Ocean are enclosed by a dashed line. Lines with slope of −1 are isopleths of total internal-wave energy/volume. The solid dots belong to No. 13. (b) Same data as shown in (a) with ordinate rescaled by $r' = rf$ [m^2 cph^2].

TABLE 1. Source of data displayed in Figs. 7a and 7b. The type of observation is indicated by the abbreviations T and V, representing temperature and velocity, respectively.

Number	Location (Lat. °N, Long. °W)	Primary and additional references	Data type	Duration, days	Instrument depth (m)	Water depth (m)
1	81.8, −4.0 Fram 3	This report Morison (1984)	T	4	50–150	800
2	75.4, 140.3 Ice Island T-3	Yearsley (1966) Morison (1984)	T	4	60	3000
3	85.0, 95.0 Ice Island T-3	Bernstein (1972) Morison (1984)	V	70	40, 60	
4	85.3, 97.8 Ice Island T-3	Neshyba *et al.* (1972) Morison (1984)	T	1	250	
5	89.2, 141.5 Arctic	Aagaard (1981)	V	35	1240, 1415	1500
6	46.6, 145.1 MILE, NE Pacific	Levine *et al.* (1983a)	T, V	19	30–175	4000
7	8.8, 22.9 GATE, Atlantic	Käse and Siedler (1980) Roth *et al.* (1981)	T, V	18–60	18–60	4900
8	25.0, 159.0 Pacific	Pinkel (1975) Roth *et al.* (1981)	T	10	110	4000
9	59.0, 12.5 JASIN, NE Atlantic	deWitt (1981) Levine *et al.* (1983b)	T	40	50	1500
10	16.0, 65.0 St. Croix	Tarbell *et al.* (1977) Roth *et al.* (1981)	T, V	32	95–243	
11	42.0, 70.0 Cape Cod	Zenk and Briscoe (1974) Roth *et al.* (1981)	T, V	21	59, 84	500
12	59.0, 12.5 JASIN, NE Atlantic	Weller (1982) Weller and Halpern (1983)	V	33	82, 100	1550
13	JASIN Area NE Atlantic	Gould *et al.* (1984) Levine *et al.* (1983b)	V	27–52	200–1500	1500
14	46.6, 130.2 MATE, NE Pacific	Levine and Irish (1981)	T, V	23	880–1300	2200
15	38.3, 70.0 39.2, 69.0 Under Gulf Stream	Luyten (1977) Wunsch and Webb (1979)	V	230	200–280	3000
16	28.0, 69.6 MODE Center	Wunsch (1976) Wunsch and Webb (1979)	V		4000	5400
17	33.5, 62.5 Muir Seamounts	Wunsch (1976) Wunsch and Webb (1979)	V	150	2100–3000	3000–4400
18	39.9, 68.9 Hydrographer Canyon	Wunsch (1976) Wunsch and Webb (1979)	V		320–710	350–700
19	38.0, −5.0 Mediterranean	Perkins (1972) Wunsch and Webb (1979)	V	60	1200	2700
20a 20b	1.5, −53.0 0 to 0.05, −50 to −57 Indian Ocean	Wunsch and Webb (1979) Eriksen (1980)	V	60–200	1500, 3600 1500, 3600	5100 4700–5100
21	39.5, 72.3 Hudson Canyon	Hotchkiss and Wunsch (1982)	V	105	100–700	300–700
22	27.7, 69.9 IWEX	Briscoe (1975) Roth *et al.* (1981)	T, V	42	600–2050	6000

length and time scale. One would not expect that an increase in b by a factor of 2 would increase the spectrum by a factor of 4 as (3) suggests. We view the GM formulation as an empirical description rather than a predictive model with the spectral *level* scaled by r. The proper scaling of the spectral level undoubtedly depends on the yet unknown balance of the generation, nonlinear transfer and dissipation processes that maintain the internal wave field.

Instead of r it might be preferable to compare the observations with the total internal-wave energy per unit mass $\hat{E}$. The total kinetic plus potential energy integrated over all frequencies for the GM model in units of J kg^{-1} is

$$\hat{E} = (3600)^{-2} \times 8\pi r N(z) \cos^{-1}[f/N(z)], \qquad (5)$$

where the contribution to the kinetic energy from the vertical velocity has been neglected. For the usual case of f/N much less than 1, $\hat{E} = (3600)^{-2} \times 4\pi^2 rN$. The energy $\hat{E}$ is then proportional to r and N and independent of f. Note that lines of constant $\hat{E}$ are indicated by -1 slope on Fig. 7a. Therefore the total energy levels observed in the upper Arctic Ocean (numbers 1–4) are comparable to some deep-ocean values. However, at comparable values of N, the Arctic values are still lower than at mid-latitude. The only observation from the deep Arctic Ocean (number 5) yields the lowest $\hat{E}$ on the figure.

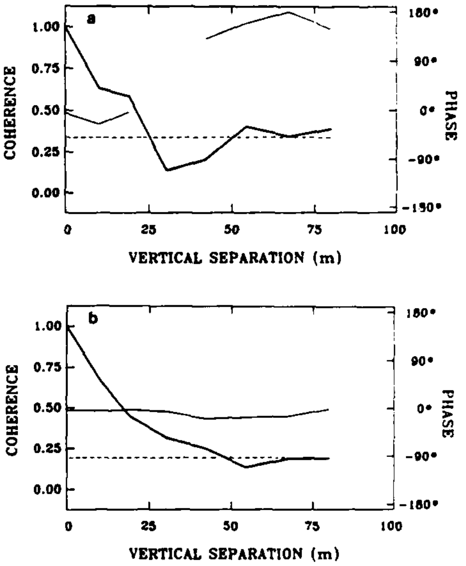

FIG. 8. Coherence (bold line) and phase (thin line) as a function of vertical separation from the mean depth of the −1.4° isotherm at 57 m for frequency bands centered at (a) 0.81 and (b) 2.6 cph. Coherence was calculated between the −1.4°C and adjacent isotherms in increments of 0.2°. Coherence values above the dashed line are non-zero at the 95% significance level. Phase estimates are shown only where the coherence is significant.

4. Coherence

Estimates of coherence between vertically separated isotherm depths are only significantly different from zero in two frequency bands centered around 0.81 and 2.6 cph (Fig. 5). In the GM model the moored vertical coherence (MVC) is independent of frequency and is a function only of vertical separation Δ, and the bandwidth parameter t. The form given by Desaubies (1976) is

$$\mathrm{MVC}(\omega) = \exp[-2\pi t\Delta(N^2 - \omega^2)^{1/2}], \qquad (6)$$

where the approximation made by GM that $(N^2 - \omega^2) \approx N^2$ has not been made, resulting in a rise in coherence near N. The coherence level for the GM value of the parameter $t = 3.8 \times 10^{-4}$ cpm/cph is shown with the data in Fig. 5. The observations do not agree with the model. The statistically significant observed values are much below the predicted, and the variation of coherence below N is not independent of frequency.

The frequency bands of high coherence at 0.81 and 2.6 cph (Fig. 5) were investigated in greater detail. The coherence and phase in these bands are plotted as a function of vertical distance from the −1.4° isotherm at 57 m (Fig. 8). In the band centered around 0.81 cph, which corresponds to a period of 1.1–1.4 h, the coherence decreases with increasing separation until a 30 m separation is reached. At greater separation the coherence increases. The waves are nearly in phase between 57 and 76 m and then jump to nearly 180° out of phase between 57 m and depths deeper than 100 m. This pattern suggests a modal structure with a node located at the depth of the phase shift and coherence minimum, somewhere between 75 and 100 m. The structure of these waves can also be identified in the time series itself; examples of oscillations exhibiting this modal behavior are shown in Fig. 3.

Wavefunctions of vertical displacement $\Psi(z)$ were calculated by solving the boundary value problem

$$\Psi'' + k^2 \frac{(N^2 - \omega^2)}{(\omega^2 - f^2)} \Psi = 0 \qquad (7)$$

with $\Psi = 0$ at the top and bottom of the ocean. The wavefunctions at 0.81 cph for the lowest 4 modes are shown in Fig. 9. The shallowest nodes of modes 2–4 are in reasonable agreement with the depth of the observed phase change at 75–100 m. The cause of the high vertical coherence in this frequency band is not known; it has not been reported previously.

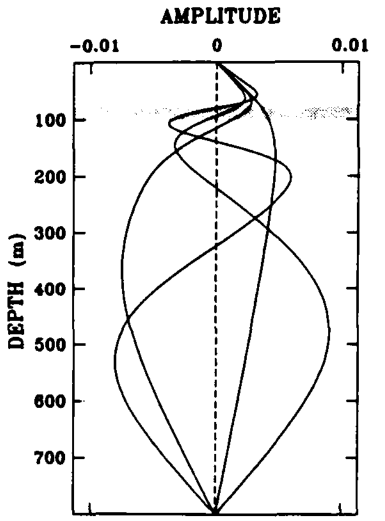

FIG. 9. Vertical wavefunctions for the first four modes at frequency 0.81 cph. A zero-crossing was observed in the data at this frequency at a depth of 75–100 m (shaded).

The coherence pattern at 2.6 cph, near the local value of N, is quite different; coherence decreases monotonically with vertical separation, and the oscillations are nearly in phase at all depths (Fig. 8b). Examples of these fluctuations are also shown in Fig. 3. Although in phase vertically, the scale of the vertical coherence is not large; the oscillations appear to be almost packet-like. This band of high vertical coherence, over the same frequency band as the break in spectral slope, is a feature often found in upper-ocean observations. It has been ascribed to fewer modes at those frequencies than the GM model prescribes (Levine *et al.*, 1983b).

5. f-scaling

The availability of internal wave observations from a wide range of latitudes provides an opportunity to test the dependence of the energy density on f in the GM model. It has been suggested by Munk (1981) that the f-scaling of the frequency spectral density be eliminated from the GM model. To test the validity of this suggestion, the same data from Fig. 7a are replotted as a function of

$$r' = rf \ \mathrm{m}^2 \ \mathrm{cph}^2 \qquad (8)$$

in Fig. 7b. The scatter among the points is significantly reduced. Most noticeably affected are the low-latitude values, from GATE (9°N) and near St. Croix (16°N). The values near large topography are still large, and the low values from the Arctic remain distinct. Therefore, based on this survey of data, it appears reasonable to eliminate f in the scaling of the energy level, while retaining it as the lower limit of the internal-wave frequency band. This modification implies that the internal-wave energy per unit mass $\hat{E}$ is proportional to $1/f$ while the level of the frequency spectrum is independent of f. Further research is needed to determine if the hypothesis of constant spectral level is consistent with the dynamics controlling the energy flow through the internal wave field.

We have indicated that scaling by r' is consistent with observations but have not attempted to reformulate the entire GM model. In contrast to the frequency spectrum this new scaling implies that both vertical and horizontal wavenumber spectra are proportional to $1/f$ (S. Hayes, personal communication, 1983). Therefore, wavenumber spectral levels would increase dramatically as the equator is approached, a feature that is not found in the data. A different formulation is needed to model values near the equator where the f-plane approximation is not valid; a model in the spirit of GM that treats equatorial waves has been developed by Eriksen (1980).

6. Summary and conclusions

Time series of temperature in the upper Arctic Ocean were measured by a thermistor chain hanging from the pack ice for five days in May 1981. The depths of isotherms were tracked in time; it is assumed that the variations in isotherm depth are primarily due to vertical displacement by internal waves.

Spectral analysis of vertical displacement provides a useful description of the internal wave field and allows direct comparison with the GM model and historical data. Between f (0.0825 cph) and N (2–4 cph) the frequency dependence is between $\omega^{-1.5}$ and ω^{-2} (Fig. 4a). This is slightly less steep than the GM model but consistent with other upper-ocean observations (Levine *et al.*, 1983b). Near N, the upper frequency limit for free internal waves, there is a sharp break in the spectral slope followed by a rolloff at higher frequency.

Significant vertical coherence in the internal-wave band occurs at two peaks at 0.81 and 2.6 cph. This does not follow the expectation of a uniform coherence level prescribed by the GM model (Fig. 5). The peak at 2.6 cph is characteristic of peaks found in other upper-ocean observations near local N, the frequency where the break in spectral slope is found (Levine *et al.*, 1983b). The pattern of both the coherence and phase of the oscillations at 0.81 cph indicates the presence of the shallowest node between 75 and 100 m. This is consistent with the location of a node in modes 2 to 4 of the vertical wavefunctions calculated from the mean N profile. The origin of this peak has not been determined. The large-scale circulation in the region of the Yermak Plateau is complicated, and there are numerous fronts that could affect the propagation of internal waves. Perhaps this "high" mode peak is the result of interaction with the low-frequency flow; the lack of data prohibits even a qualitative assessment.

To put these observations into perspective, the energy level r of the internal waves is compared with results from historical data (Fig. 7a). There is considerable variation among the values. When the same data are re-scaled by multiplying by f, the scatter is much reduced (Fig. 7b). This supports the suggestion of Munk (1981) that the latitudinal scaling of the frequency spectral density should be eliminated from the GM model.

The most interesting result of this paper is that spectral levels determined from experiments in the Arctic Ocean are lower than the GM model and those measured at lower latitudes (Fig. 7a). However, one must be cautious in assessing significance. Because the time series are short, some of the ascribed geographical variation may be due to the temporal variability of the internal wave field. Recent multiyear observations in the Sargasso Sea during LOTUS (Long Term Upper Ocean Study) show fluctuations from a half or a third to two or three times the mean energy (Briscoe and Weller, 1984). Perhaps this five-day experiment occurred during a relatively calm period; however, it is more significant that all of the Arctic observations tend to be low compared to spectral levels at lower latitudes. Whether the variations are predominantly geographical or temporal awaits additional observations.

The Arctic observations invite speculation about possible reasons for the relatively low energy levels. The Arctic may be a place where deviations of internal waves from universality can elucidate sources and sinks of internal wave energy. Perhaps the lower energy can be related to the unique forcing and dissipation processes that are present in the Arctic:

1) The ice cover damps the internal wave field via a turbulent boundary layer.

2) Surface forcing is weaker owing to weaker winds and to the loss of momentum to the coast by internal ice stress.

3) The nature of the stress transfer through the ice is different from an ice-free ocean. The generation of internal waves may depend critically on the geometry of the underside of the ice; momentum transfer from surface waves to internal waves is not possible.

4) The internal tides which may transfer energy to other frequency bands in the temperate oceans are generally small in the Arctic or are not able to propagate as free waves (north of 75°N).

The significance of these processes in shaping the internal wave field is not yet known; additional investigations are needed.

Acknowledgments. We thank R. Baumann for his careful processing of the data and S. Gard for his assistance with the preparation of the figures. The support by the Office of Naval Research under codes 422PO (Levine and Paulson) and 425AR (Morison) is gratefully acknowledged.

REFERENCES

Aagaard, K., 1981: On the deep circulation in the Arctic Ocean. *Deep-Sea Res.*, **28A**, 251–268.

Bernstein, R. L., 1972: Observations of currents in the Arctic Ocean. Tech. Rep. No. 7, Contract N-00014-67-A-0108-0016. Lamont-Doherty Geological Observatory of Columbia University, Palisades, NY.

Briscoe, M. G., 1975: Preliminary results from the trimoored internal wave experiment (IWEX). *J. Geophys. Res.*, **80**, 3872–3884.

——, and R. A. Weller, 1984: Preliminary results from the Long-Term Upper-Ocean Study (LOTUS). *Dyn. Atmos. Oceans*, **8**, 243–265.

Coachman, L. K., and K. Aagaard, 1974: Physical oceanography of Arctic and subarctic seas. *Marine Geology and Oceanography of the Arctic Seas*, Y. Herman, Ed., Springer-Verlag, 1–72.

Desaubies, Y. J. F., 1976: Analytical representation of internal wave spectra. *J. Phys. Oceanogr.*, **6**, 976–981.

deWitt, L. M., 1981: Variability of the upper ocean internal wave field during JASIN. M.S. thesis, School of Oceanography, Oregon State University, Corvallis, OR.

Eriksen, C. C., 1980: Evidence for a continuous spectrum of equatorial waves in the Indian Ocean. *J. Geophys. Res.*, **85**, 3285–3303.

——, 1982: Observations of internal wave reflection off sloping bottoms. *J. Geophys. Res.*, **87**, 525–538.

Garrett, C. J. R., and W. Munk, 1972: Space-time scales of internal waves. *Geophys. Fluid Dyn.*, **2**, 255–264.

——, and ——, 1975: Space-time scales of internal waves: A progress report. *J. Geophys. Res.*, **80**, 291–297.

Gould, W. J., A. N. Cutler and D. Weddell, 1984: (Internal report, in preparation). Institute of Ocean Sciences, Wormley, England.

Hotchkiss, F. S., and C. Wunsch, 1982: Internal waves in Hudson Canyon with possible geological implications. *Deep-Sea Res.*, **29**, 415–442.

Jackson, H. R., G. L. Johnson, E. Sundvor and A. M. Myhre, 1984: The Yermak Plateau: Formed at a triple junction. *J. Geophys. Res.*, **89**, 3223–3232.

Käse, R. H., and G. Siedler, 1980: Internal wave kinematics in the upper tropical Atlantic. *Deep-Sea Res.*, **26** (Suppl), 161–189.

Levine, M. D., 1983: Internal waves in the ocean: A review. *Rev. Geophys. Space Phys.*, **21**, 1206–1216.

——, and J. D. Irish, 1981: A statistical description of temperature finestructure in the presence of internal waves. *J. Phys. Oceanogr.*, **11**, 676–691.

——, R. A. deSzoeke and P. P. Niiler, 1983a: Internal waves in the upper ocean during MILE. *J. Phys. Oceanogr.*, **13**, 240–257.

——, C. A. Paulson, M. G. Briscoe, R. A. Weller and H. Peters, 1983b: Internal waves in JASIN. *Phil. Trans. Roy. Soc. London*, **A308**, 389–405.

Luyten, J. R., 1977: Scales of motion in the deep Gulf Stream and across the Continental Rise. *J. Mar. Res.*, **35**, 49–74.

Morison, J. H., 1980: Forced internal waves in the Arctic Ocean. Ph.D. dissertation, Tech. Rep. Ref. M80–10, University of Washington, Seattle, WA.

——, 1984: Internal waves in the Arctic Ocean: A review. *Geophysics of Sea Ice*, N. Untersteiner, Ed. (In press).

Müller, P., D. J. Olbers and J. Willebrand, 1978: The Iwex spectrum. *J. Geophys. Res.*, **83**, 479–500.

Munk, W., 1981: Internal waves and small-scale processes. *Evolution of Physical Oceanography*. B. A. Warren and C. Wunsch, Eds., MIT Press, 264–290.

Neshyba, S. J., V. T. Neal and W. W. Denner, 1972: Spectra of internal waves: *In situ* measurements in a multiple-layered structure. *J. Phys. Oceanogr.*, **2**, 91–95.

Olbers, D. J., 1983: Models of the oceanic internal wave field. *Rev. Geophys. Space Phys.*, **21**, 1567–1606.

Perkins, H., 1972: Vertical oscillations in the Mediterranean. *Deep-Sea Res.*, **19**, 289–296.

Pinkel, R., 1975: Upper ocean internal wave observations from FLIP. *J. Geophys. Res.*, **80**, 3892–3910.

——, 1981: Observations of the near-surface internal wavefield. *J. Phys. Oceanogr.*, **11**, 1248–1257.

Roth, M. W., M. G. Briscoe and C. H. McComas, III, 1981: Internal waves in the upper ocean. *J. Phys. Oceanogr.*, **11**, 1234–1247.

Tarbell, S., S. Payne and R. Walden, 1977: A compilation of moored current meter data and associated mooring action data from mooring 592. Vol XIV (1976 Data), WHOI-77-41, Woods Hole Oceanographic Institution, 122 pp.

Weller, R. A., 1982: The relation of near-inertial motions observed in the mixed layer during the JASIN (1978) experiment to the local wind stress and to the quasi-geostrophic flow field. *J. Phys. Oceanogr.*, **12**, 1122–1136.

——, and D. Halpern, 1983: The velocity structure of the upper ocean in the presence of surface forcing and mesoscale oceanic eddies. *Phil. Trans. Roy. Soc. London*, **A308**, 327–340.

Wunsch, C., 1975: Deep ocean internal waves: what do we really know? *J. Geophys. Res.*, **80**, 339–343.

——, 1976: Geographical variability of the internal wave field: A search for sources and sinks. *J. Phys. Oceanogr.*, **6**, 471–485.

——, and S. Webb, 1979: The climatology of deep ocean internal waves. *J. Phys. Oceanogr.*, **9**, 235–243.

Yearsley, J. R., 1966: Internal waves in the Arctic Ocean. M.S. thesis, Mech. Eng. Dept., University of Washington, Seattle, WA.

Zenk, W., and M. G. Briscoe, 1974: The Cape Cod experiment on near-surface internal waves. WHOI Ref. 74-87, Woods Hole Oceanographic Institution, 52 pp.

Marine Geology, 66 (1985) 323—344
Elsevier Science Publishers B.V., Amsterdam — *Printed in The Netherlands*

CALIBRATION AND COMPARISON OF THE LDGO NEPHELOMETER AND THE OSU TRANSMISSOMETER ON THE NOVA SCOTIAN RISE

WILFORD D. GARDNER[1], PIERRE E. BISCAYE[1], J. RONALD V. ZANEVELD[2] and MARY JO RICHARDSON[3]

[1]*Lamont-Doherty Geological Observatory of Columbia University, Palisades, NY 10964 (U.S.A.)*
[2]*School of Oceanography, Oregon State University, Corvallis, OR 97331 (U.S.A.)*
[3]*City University of New York, Lehman College, Bronx, NY 10468 (U.S.A.)*

(Accepted for publication June 15, 1984)

ABSTRACT

Gardner, W.D., Biscaye, P.E., Zaneveld, J.R.V. and Richardson, M.J., 1985. Calibration and comparison of the LDGO nephelometer and the OSU transmissometer on the Nova Scotian rise. In: A.R.M. Nowell and C.D. Hollister (Editors), Deep Ocean Sediment Transport — Preliminary Results of the High Energy Benthic Boundary Layer Experiment. Mar. Geol., 66: 323—344.

During the survey of the HEBBLE (High Energy Benthic Boundary Layer Experiments) area, two optical instruments were used to determine the spatial and temporal structure of the benthic nepheloid layer. Both instruments showed a linear response to suspended particle mass and volume over the typical range of concentrations found in the ocean (10—250 $\mu g\ l^{-1}$). At higher concentrations the transmissometer response remains linear, but, as previously noted and as shown here by theory, the nephelometer has a predictable second-order response due to multiply scattered light. At the low concentrations found in mid-water, both instruments seem near their limit of sensitivity. Small differences between instruments at low concentrations may result from variations in response to particle types found in mid-water or may be minor second-order effects of temperature or pressure on the instruments. The comparison made here shows that either instrument can be effectively used to study the nepheloid layer, and that data from different study areas using these instruments can consistently be compared. The HEBBLE region was ideal for testing the range of these instruments because it yielded the highest concentrations of particles ever recorded in the deep sea.

INTRODUCTION

In 1979 a search was made for an area where bottom flows were sufficiently active to have an observable geological impact on the seafloor at the present time; an area in which to conduct High Energy Benthic Boundary Layer Experiments (HEBBLE). Based on bottom photos and short-term current records (Zimmerman, 1971; Hollister and Heezen, 1972), the region chosen was the continental rise south of Nova Scotia. It was felt that one of the quickest ways to survey a large area in search of present-day activity was to measure the concentration of particles suspended in the benthic nepheloid layer. Other survey methods included CTD casts (Weatherly and Kelley,

0025-3227/85/$03.30

1982; Spinrad and Zaneveld, 1982), bottom photos (Tucholke et al., this volume), short-term current measurements (Richardson et al., 1981) and sediment trap measurements (Gardner et al., 1983). During September, 1979, a survey of the area in Fig.1 was made using LDGO nephelometers (Thorndike and Ewing, 1967; Thorndike, 1975) and OSU transmissometers (Bartz et al., 1978) in both profiling and moored modes. Data were obtained from 27 profiles where both instruments were on the same wire with a vertical separation of less than 2 m. A nephelometer and transmissometer were also affixed at 1 m above the bottom (mab) to the Lamont Bottom Ocean Monitor tripod (BOM). The BOM was deployed at a depth of 4963 m from July 24 to September 27, 1979 (Fig.1).

The purpose of this paper is to present data used to calibrate both the nephelometer and transmissometer and to show how the outputs of these two instruments compare with each other. Both of these instruments have been used extensively in other parts of the world's oceans to estimate particle concentrations so it is important (1) to determine how the data from the two instruments can be merged; (2) to compare HEBBLE data with those from other areas; and (3) to determine the limitations in data from each instrument.

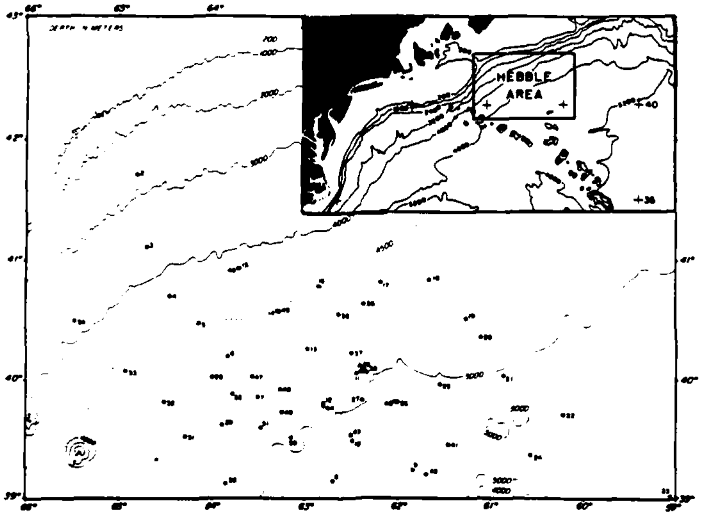

Fig.1. Map of the study area showing ship station numbers for Knorr cruise 74. Contours are in meters. Location of the BOM was at the triangle between stations 11, 38 and 39.

METHODS

Nephelometer

The LDGO nephelometer is a shielded light source, near-forward scattering meter (Thorndike, 1975). The shield is half-way between the white light source and the recording camera, which is focused on the shield. The shield contains three filters and a diffuser which are used to attenuate the direct light. If E_0 is the intensity of the light, the received scattered light signal is given by:

$$E = E_0 \beta_N e^{-cr} \tag{1}$$

where:

$$\beta_N = 2\Pi \int_{\theta_1}^{\theta_2} \beta(\theta) W(\theta) \sin\theta \, d\theta$$

$\beta(\theta)$ is the volume scattering function; $W(\theta)$ is a weighting function that depends on the exact dimensions of the particular design of nephelometer used (this parameter also contains the differential path length traveled by light at different scattering angles, θ); c is the beam attenuation coefficient, and r is the path length between the light source and the camera. For the LDGO nephelometer $\theta_1 = 8°$ and $\theta_2 = 24°$, but the diffuser that is placed in front of the direct light filters also acts as a diffuse light source. Light scattered from the diffuser through angles much less than 8° would thus also be detected as part of the scattered light signal. This is of insignificant magnitude, however, in the relationship between the nephelometer output and total suspended mass, as will be shown later. The direct light travels from the light source to the filter/diffuser and then travels to the camera. Thus the direct light intensity is given by:

$$E_D = E_0 e^{-(c - b_D)r} F_i \tag{2}$$

where b_D is light scattered into the direct beam from the scattered beam (i.e. multiply scattered light), and F_i is a filter factor. The signal E/E_D is then given by:

$$\frac{E}{E_D} = \frac{E_0 \beta_N e^{-cr}}{E_0 F_i e^{-cr} e^{b_D r}} = \frac{\beta_N e^{-b_D r}}{F_i} \tag{3}$$

Equation (3) shows that any fluctuations in the light source, e.g., changes in battery power or dirt on windows, cancel out in the comparison between direct and scattered light.

In the standard vertical profiling mode a white light source shines continuously while film is transported past the lens at a constant rate. The vertical sampling resolution is therefore controlled by the rate of instrument lowering (Eittreim and Ewing, 1972; Thorndike, 1975). Absolute depths of nephelometer measurements are determined by the trace produced by a bourdon tube (0—10,000 psi pressure gauge) and compared with the total water depth (Thorndike, 1975). Accuracy for the data in this study is estimated at ±10 m (based on fit of nephelometer record length to CTD data length) and resolution of the measurements is 10 m in the nepheloid layer (based on lowering rate of instrument). With the continuous light source and continuous film transport, the light scattered from particles is recorded on the film as a general fogging. Data reduction involves digitization of the ratio of the log of scattered light to the log of direct light using a photodensitometer (Thorndike, 1975). The data in this study were digitized at 15 m intervals in the nepheloid layer and 120 m intervals through the rest of the water column. In the moored mode the nephelometer has been modified to use a strobe light source and single-frame advance to obtain an instantaneous measurement (Gardner et al., 1984b). Most of the light scattering is caused by particles smaller than the photographic resolution of the film, so even when a strobe light source is used to obtain discrete measurements, the record still appears as general fogging on the film, but images of some discrete particles can also be seen (Gardner et al., 1984a).

Tests of the temperature effect on the nephelometer film calibration showed no effect between 0° and 27° at the low end of film density, but at a density of $E/E_D = 1.6-1.8$ the low-temperature calibration curve flattened slightly more than the high-temperature curve (Thorndike, 1975). As a result, log E/E_D values from regions with very strong scattering could be too low by as much as 0.1 if calculated using a high-temperature calibration curve (Thorndike, 1975). No internal temperature is measured in the nephelometer from which a temperature correction could be made, so the E/E_D values for these data may be too low in the nepheloid layer and could account for some of the non-linearity in the nephelometer calibration as will be discussed later.

Transmissometer

One-meter pathlength transmissometers were used both for profiling (Spinrad and Zaneveld, 1982; Weatherly and Kelly, 1982; Spinrad et al., 1983; McCave, 1983) and for moored observations from the BOM tripod (Pak and Zaneveld, 1983). In the profiling mode the transmissometer was interfaced with a Neil-Brown CTD and transmission readings were recorded in real time on board the ship. Accuracy of depth is therefore ±1.2 m. The transmissometer moves less than 1 cm while the transmission measurement is made through a 1-m folded path for a 0.5 m resolution. These instruments have solid state electronics and a light-emitting diode light source with a wavelength of 660 nm and a spectral bandwidth of 20 nm. At that wavelength the absorption due to dissolved materials is negligible, so that the signal is due essentially to attenuation by suspended matter and water only. The instrument is well-collimated ($<0.8°$) and is temperature compensated ($<0.1\%$ error in a temperature range of 0°—25°C). Synchronous detection allows the instrument to be operated under ambient light conditions. The instrument has a folded one-meter pathlength with one pressure housing. Transmissometers with similar electronics but a 25 cm pathlength were also extensively used in HEBBLE for profiling and moored observations (Pak, 1983) and with an in-situ settling tube for the determination of particle-size distributions (Zaneveld et al., 1982). Further details regarding the electronics may be found in Bartz et al. (1978).

The output of the transmissometer is 0.5 V DC, and the electronics of each instrument are adjusted so that transmission in air corresponds to the correct transmission in particle-free water. The instrument is then immersed in particle-free distilled water and the value of transmission recorded. The same water is measured using a double pathlength (0.5 and 1.0 m) instrument to determine an absolute water calibration constant, K, for each instrument.

The LED is very stable, but will decrease about 1% in 1000 h of operation. Therefore, air calibrations need to be made during use and the output voltage corrected by:

$$v = [(L/U) \cdot (X - Z)]$$

where v is the corrected output voltage, L is the laboratory air calibration, U is the air calibration at time of use, X is the output voltage measured in water, and Z is the zero offset with the light path blocked. Percent transmission is obtained by:

$$T(\%) = 20 \cdot v \cdot K$$

where K is a calibration constant determined for each instrument. Further compensation for the effects of temperature, salinity and pressure can be made using the method outlined in Zaneveld et al. (1979), but these changes are minor.

The transmissometer measures the loss of light from a well-collimated beam of light over a 1.0 m path. The losses are due to both absorption and scattering events. *If one defines the beam-attenuation coefficient, c, as the* internal attenuance of an infinitesimally thin layer of the medium perpendicular to the medium (Jerlov, 1976), it follows that:

$$T(r) = e^{-cr} \tag{4}$$

where $T(r)$ is the transmission in a pathlength r. We thus find that for a one-meter pathlength:

$$c = -\ln T(1) \tag{5}$$

In practice the transmitted light always contains a small amount of forward scattered light which is denoted by b_s. The parameter measured is thus in actuality:

$$-\ln T(1) = c - b_s \tag{6}$$

RELATION OF OPTICAL PARAMETERS TO PARTICLE MASS

Zaneveld (1973) has shown that if the nature of the particles (i.e. relative size distribution and relative index of refraction distribution) is constant, any inherent optical property of the particles (particle scattering and attenuation) will be proportional to the total suspended volume concentration, C_V, provided multiple scattering is not important. If the particle density is constant, the optical properties will also be proportional to total suspended mass, C_M. With the assumption that the nature of the particles for a given time and space domain is optically constant, or nearly so, we can then relate the nephelometer and transmissometer outputs to suspended particulate volume concentration, C_V or mass concentration, C_M, if density is constant as will be assumed in the following discussion.

If we consider multiple scattering to be unimportant ($b_D = 0$) the output of the nephelometer [eqn.(3)] can be written as:

$$\frac{E}{E_D} = \frac{\beta_N}{F_i} = \frac{1}{F_i}(\beta_{Nw} + \beta_{Np}) \tag{7}$$

where the subscripts w and p refer to water and particles, respectively. Linear regression of E/E_D versus particle concentration will later show that β_{Nw} is very small, on the order of 2 units of E/E_D. Zaneveld (1973) has shown that β_{Np} is proportional to C_M, so that:

$$\frac{E}{E_D} = D\,C_M + G \quad \text{or,} \quad C_M = \frac{1}{D}\left(\frac{E}{E_D} - G\right) \tag{8}$$

where D and G are constants of proportionality.

$$D = \frac{\beta_{Np}}{F_i C_M}$$

and:

$$G = \frac{\beta_{Nw}}{F_i}$$

D is therefore, the scattering per unit volume of particulate matter divided by the filter factor and G is the intercept defined by the water scattering divided by the filter factor.

The transmissometer measures $c - b_s$ which also contains contributions by water ($c_w - b_{sw}$) and particles ($c_p - b_{sp}$). Hence:

$$-\ln T(1) = c_w + c_p - b_{sw} - b_{sp} \tag{9}$$

If we define the constants A and B as

$$A = c_w - b_{sw}$$

and:

$$B = \frac{c_p - b_{sp}}{C_M}$$

then:

$$-\ln T(1) = BC_M + A \tag{10a}$$

and:

$$C_M = -\frac{1}{B}[\ln T(1) + A] \tag{10b}$$

It is thus seen that $-\ln T(1)$ and E/E_D are linearly related to C_M.

For very high particle concentrations, b_D for nephelometers in eqn.(3) cannot be ignored, because significant amounts of multiply scattered light will enhance the direct light. This would decrease the ratio E/E_D. Indeed, as strong nepheloid layers are encountered, E_D increases (Thorndike, 1975). When this occurs, the E_D just above the nepheloid layer is used as E_D in the nepheloid layer. In the case of the transmissometer, high particle concentrations cause the forward scattered light, b_s to increase at a faster rate than c, so that one gets relatively more transmission (less observed attenuation) than the C_M relation [eqns.(10)] would indicate. The relation between C_M and $-\ln T(1)$ continues to increase monotonicly, however. In the case of the nephelometer [eqn.(3)] the exponential term exp $(b_D r)$ eventually decreases faster as a function of C_M than β_N increases. The nephelometer output for very high concentrations of particulate matter then becomes double valued. An example of this is given below in the section on the BOM data. Except for this extreme case the nephelometer output and the transmissometer output track exceedingly well as would be expected from a comparison of eqns.(8) and (10).

These equations show that, if we assume a constant density, the two parameters that are linear with C_M are $\ln T(1)$ (which equals c, beam attenuation) and E/E_D. It is thus appropriate to compare c with E/E_D if one wishes to study sensitivity of the two instruments. If one compares eqns.(8) and (10), it is seen that the constants that relate E/E_D and $\ln T(1)$ to C_M are D and B, respectively. D is essentially the forward scattering per unit particulate volume and B is essentially the beam attenuation per unit particulate volume. Since beam attenuation is by definition larger than the forward scattering, a beam transmissometer is more sensitive than a nephelometer. The actual sensitivity ratio would depend on the shape of the volume scattering function. Sensitivity also depends on the precision of the smallest measurable unit of each instrument.

Examples of profiles from two Knorr 74 stations, one with a moderate and one with a high concentration nepheloid layer, are shown in Fig.2. The profiles are first plotted as log E/E_D and % transmission, which are the variables actually measured. They are then repeated as E/E_D and beam attenuation, the variables which are linearly related to particle concentration as discussed above.

FIELD CALIBRATION

To compare the optical measurements of the nephelometer or transmissometer with either C_M or C_V, calibrations must be made experimentally because the scattering and attenuation properties of particles depend on their size, shape and index of refraction.

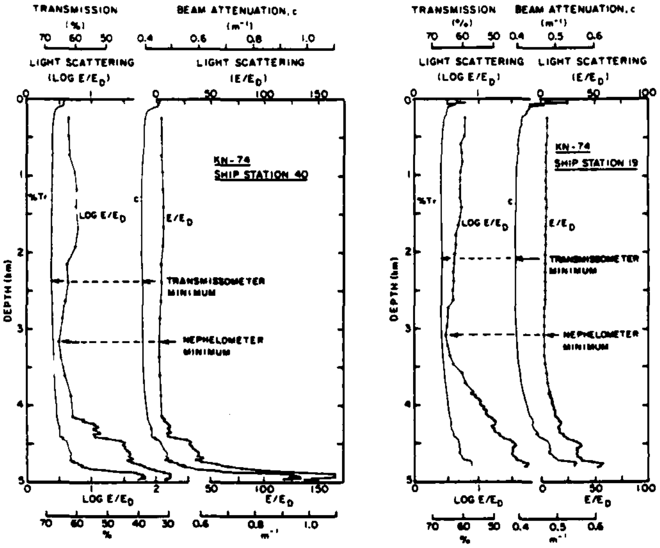

Fig. 2. Nephelometer and transmissometer profiles at stations 19 and 40. Log E/E_D and % transmission are the parameters that are actually measured and initially plotted. A better comparison between the output of the two instruments and also with the concentration of suspended particles comes from plots of E/E_D and c (beam attenuation). Transmissometer readings produce a nearly continuous line, whereas nephelometer readings are made at the points shown.

Suspended particulate matter concentration (SPM)

Water samples were obtained on each hydrocast with ten 10-l Niskin bottles mounted on the CTD rosette and seven 30-l Niskin bottles clamped to the acoustic wire at various heights above the bottom. The 30-l bottles were generally confined to within 250 mab to obtain samples for measurements of excess radon in the benthic boundary layer, but a few bottles were located as much as 400 mab. 18—20 l of water from each bottle were drawn into an evacuated glass bottle through Nuclepore filters with a pore size of 0.4 μm. This water was then analyzed for Rn-222 and Ra-226. The remaining water in the Niskin bottle (usually a total of 7—9 l), including the water below the spigots, was drawn through a separate Nuclepore filter. Water from the 10-l Niskin bottles was occasionally sampled to increase the distribution of samples throughout the water column and was sampled in a similar manner. All filters were immediately washed with 13 aliquots of filtered, distilled water and dried under a laminar-flow hood, sealed and returned to the laboratory to be reweighed. Particle concentrations were calculated separately for the two volumes from each bottle. The second filter from each bottle contained the dregs of particles which settle below the spigots before they can be routinely sampled (Gardner, 1977). These data were combined with the data from the first volume of water to obtain a particle concentration corrected for the dregs. The concentration in the 18—20 l is referred to here as the concentration and the combined data are the corrected concentration.

Concentrations ranged from 5 μg l^{-1} in mid water to 12,700 μg l^{-1} at station 30 — the highest concentration of SPM ever reported in the deep sea. The percent transmission at that station dropped to 0% in the bottom 50 m and filtered concentrations were over 4000 μg l^{-1} up to 90 mab.

Nephelometer and transmissometer measurements were made during the lowering of the CTD (the down trace). Up traces for the nephelometer and transmissometer were recorded, but not processed. The raw transmissometer up trace was plotted on board ship and revealed considerable variability between the down and up trace in the nepheloid layer, so, beginning with station 20, we ran the CTD cast to the bottom, raised the CTD 500 m and again went to the bottom. On station 20 and subsequently the 30-l Niskin bottles were tripped at the end of the second lowering. Typically 30—60 min passed between the time of the nephelometer and transmissometer measurements and the closure of the 30-l bottles at the same depth, so, because of ship drift and currents, it was no longer the same parcel of water as had been analyzed optically. The rosette bottles were tripped at selected depths during the raising of the CTD. Transmissometer values were recorded at the time each rosette bottle was tripped and provided an optical measurement close to the water actually sampled. Time differences between nephelometer measurements (down trace) and sampling with rosette bottles (up trace) were 1—4 h, but these were a small percentage of the total samples.

Aliquots of water (250 ml) were drawn from each bottle as soon as they were on deck to analyze for particle-size distribution and particle volume with a model TA II Coulter Counter on board ship. Two ml of water from each sample was drawn through a 50 μm aperature tube to measure the particle-size distribution from 1 to 24 μm in the manner discussed in Richardson and Gardner (this volume).

Nephelometer and transmissometer calibrations

When the nephelometer was first developed in 1964, it was assumed that the density of the scattered light signal (E/E_D) was proportional to the dry weight of particles in the water. At that time ultrafiltration techniques and sensitive balances were not available to gravimetrically determine the concentration of particles in water. Eittreim and Ewing (1972) filtered water and, with a microscope, counted and measured the sizes of the collected particles. Later, Biscaye and Eittreim (1974, 1977) were able to obtain accurate weights for particles filtered from water and compare log E/E_D with log of particle weight concentration.

Although light scattering and attenuation are functions of particle size and index of refraction, we have plotted and regressed particle volume and mass concentrations against optical properties in Figs.3 and 4 for two mathematical reasons. First, we know E/E_D and c better (i.e., with higher accuracy) than C_M or C_V, both because of measurement techniques and the spatial/temporal separation between optical measurements and sample collection as discussed above. Second, we want to predict C_M or C_V from E/E_D and c, so we want to minimize the variance in C_M or C_V. Data from stations 29, 30 and 31 were omitted from these correlations because there were very large temporal variations between the up and down traces as discussed earlier. As predicted by theory, the nephelometer response to C_M and C_V becomes

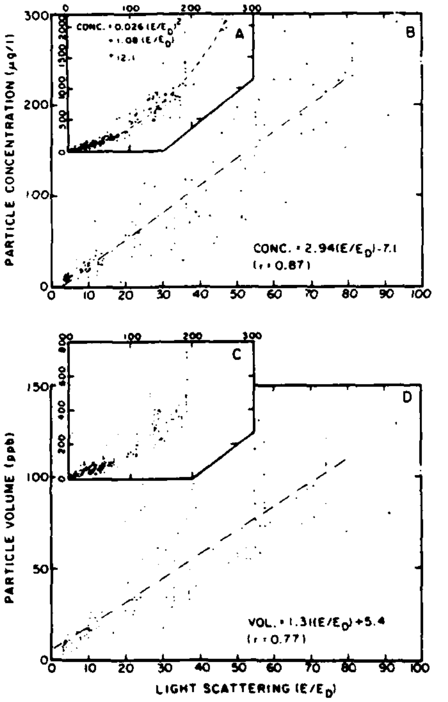

Fig.3. Light scattering versus particle weight concentration (upper) and particle volume concentration (lower) measured with a Coulter Counter for the size range 1—24 μm for HEBBLE stations. Linear least squares fits were made for the data from E/E_D of 0—80 as shown. A second-order least squares fit was made for the entire data set shown in the inset plot A.

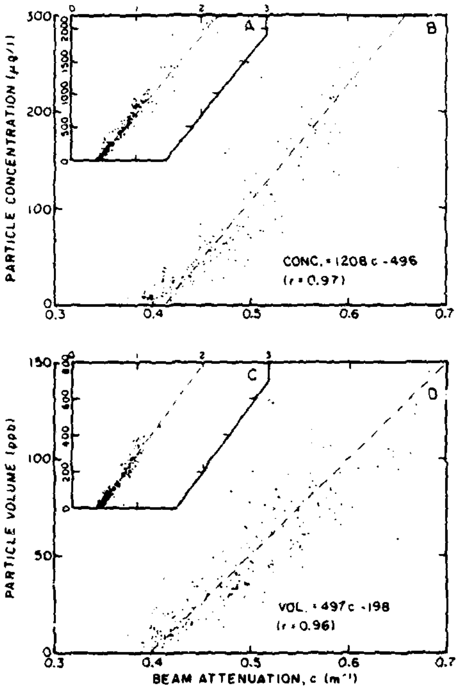

Fig.4. **Beam attenuation versus particle weight concentration (upper) and particle volume (lower) measured with a Coulter Counter in the size range 1—24 μm. Linear least squares fits were made for $c < 1.0$.**

non-linear at higher concentrations due to light being scattered into the direct light beam. Some of the second-order effects at high concentrations could also result from temperature effects in the film response as discussed in the nephelometer methods section. A second-order least squares regression was used to obtain the equation in Fig.3A.

The correlations between beam attenuation, c, and C_M and C_V are much better than between light scattering, E/E_D, and C_M and C_V. Much of this is due to greater accuracy in the depth (±1.2 m for c vs. ±10 m for E/E_D) and resolution (0.5 m for c vs. 10 m for E/E_D) of the transmissometer in nepheloid layers of extreme vertical variability. Scatter in the plots of Figs.3 and 4 could also result from variations in particle size distributions and index of refraction of particles. These factors are known to influence optical measurements (Zaneveld, 1973; Jerlov, 1976) and particle-size distributions vary considerably in this region (McCave, 1983; Richardson and Gardner, this volume). Laboratory calibrations of a transmissometer have been made with natural sediment and glass beads over size ranges from 1—5 to 100 μm and concentrations up to 60 mg l^{-1} and show the slope of the correlation between c and C_M can range from about 0.3 to 40 (Butman and Moody, 1983; Baker and Lavelle, 1984). This is not surprising since particle cross-section increases as r^2, while the particle volume and mass increase as r^3. Particle density also controls particle mass. Similar variations would probably occur for E/E_D.

Biscaye and Gardner (unpublished data) completed a study in the Vema Channel in the South Atlantic that included measurements of particle concentrations and light scattering through the water column. The area is under a mid-ocean gyre, so the particle concentrations were very low. The data from that study showed the relation between light scattering and C_M followed the same linear trend found for low concentrations in the HEBBLE area (Fig.3B) down to particle concentrations as low as 3 μg l^{-1}.

LIGHT SCATTERING VERSUS BEAM ATTENUATION

Profiles through the water column

The purpose of using either a nephelometer or transmissometer in this study was to determine the concentration of particulate matter in the water, especially the benthic nepheloid layer. From the data shown in Figs.3 and 4 it is apparent that one can make a reasonable estimate of C_M with either instrument, although the nephelometer becomes non-linear and has considerably more scatter at extremely high values as noted by Thorndike (1975) and predicted by theory as discussed earlier. Since the two instruments were lowered on the same wire, it is also possible to directly compare readings from the two instruments throughout the water column. Nephelometer values are determined at about 120 m intervals from 250 m down to the top of the nepheloid layer (3000—4000 m in this study). Readings are then made at 25 m intervals and finally at 15 m intervals very near the bottom if much spatial variability is observed in the nepheloid layer. Values of potential beam attenuation (beam attenuation corrected for temperature, salinity, and especially pressure effects) were plotted against values of light scattering (E/E_D) obtained at the same depths (Figs.5A and B). The values are very linear between E/E_D of 7 to about 80 or 100 after which light-scattering values do not rise as fast as beam-attenuation values. It must be remembered that light-scattering values are integrated over a distance of approximately 10 m, and absolute depths for the nephelometer values are good to only ±10 m. The transmissometer resolution is 0.5 m and the error in the absolute depth is 1 m. Nevertheless, the linear correlation between the two measurements is very good between E/E_D of 6.5—80 ($r = 0.93$), which is the range of most nepheloid layers of the ocean (10—250 μg l^{-1}).

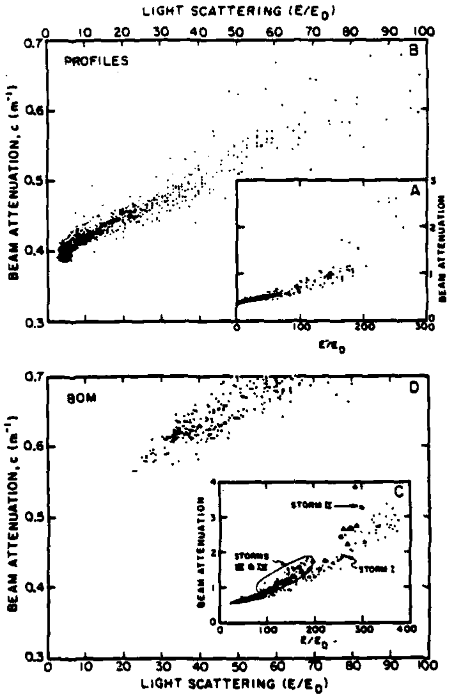

Fig.5. Light scattering versus beam attenuation at depths at which nephelometer readings were made (upper). Light scattering versus beam attenuation *for instruments on the* BOM (lower). Storms were arbitrarily defined as periods during which E/E_D exceeded 100 as seen in Fig.10.

Mid-water comparisons

At the low end of the scales in Fig.5B the relationship between light scattering and beam attenuation deviates from linearity. Although the data below E/E_D of 6.5 and beam attenuation of 0.41 represents a small portion of the range, it accounts for nearly all of the data in the water column between 250 m and about 4000 m in the world's oceans. It is important, therefore, to examine more closely the calibration of and comparison between the two instruments over that range.

Light scattering versus beam attenuation is plotted in Fig.6 for the two stations in Fig.2 plus station 24 with the depths of some measurement indicated. Linearity does not exist over the range plotted (≈250—4000 m).

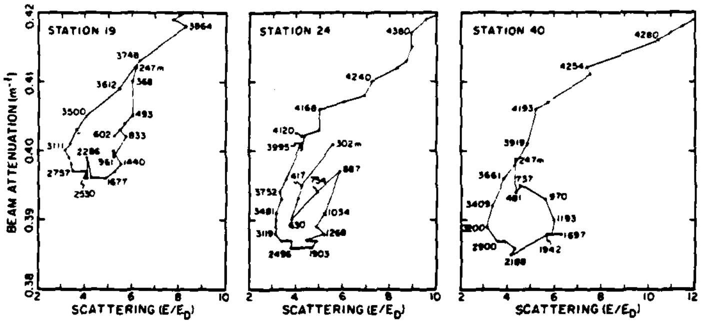

Fig.6. Light scattering versus beam attenuation between 250 m and 4000 m at stations 19, 24 and 40 with highly expanded scales. Both measurements decrease with depth, but reach minimum values at different depths.

The vertical profiles plotted in Fig.2 for stations 19 and 40 look very similar in that they both decrease with depth in the upper water column and gradually increase in the lower water column as the nepheloid layer is encountered. The expanded parameter-parameter plots in Fig.6, however, show that the minimum values occur at different depths for each instrument. Furthermore, there is an apparent offset in beam attenuation between station 19 and stations 24 and 40.

In search of a solution to these two problems, we have plotted certain data for stations from Knorr 74 and also from Conrad 22, another HEBBLE cruise made in the same area a few months prior to Knorr 74. The parameters of interest are the minimum scattering and beam attenuation values during each profile, the deepest depth of the minimum value, and the total water depth at each station (Fig.7). Light-scattering readings were made only once every 250 m for the Conrad data and every 110 m in the Knorr data and therefore contain potential errors of that magnitude for the depth of the minimum. Beyond this, much of the variability in the depth of the minimum is a function of water depth.

The minimum in light scattering is consistently about 800 m deeper than the beam-attenuation minimum in water depths around 5000 m. One possible reason for this is that the two instruments respond differently to changes in the size, shape and index of refraction of particles which might occur in the upper water column. This hypothesis will be further examined later. A second possibility is that either the transmissometer or nephelometer or both are affected by temperature or pressure in some way that has not been compensated for. Although the transmissometer electronics have been temperature compensated, differences have been found in the upper 1500 m between the down and up traces made with a transmissometer identical to the one used in this experiment (Bishop, 1985). The change was correlated with differences

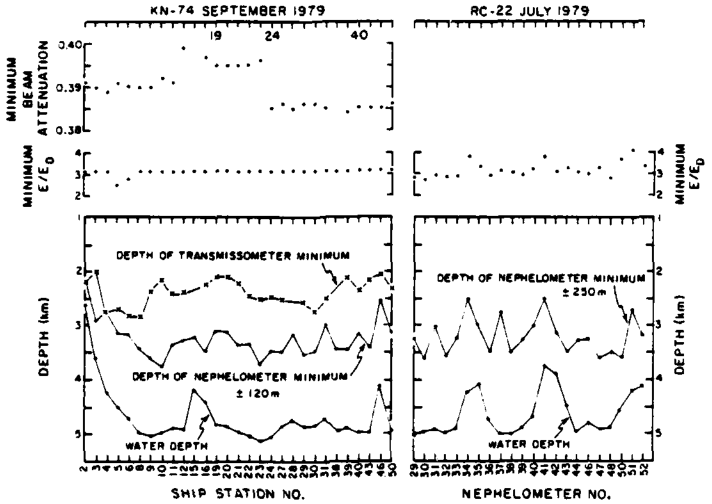

Fig.7. Synopsis of nephelometer and transmissometer minimum values for Knorr 74 and Conrad 22 cruises in the HEBBLE area. The two major changes in the minimum beam-attenuation values reflect calibration changes during the cruise and account for differences in the minimum beam attenuation of stations 19, 24 and 40 as shown in Fig.6. The uniform minimum in E/E_D for most Knorr 74 values resulted from using an average of the minimum log E/E_D values at Conrad 22 stations taken in the same area three months earlier. The depth of minimum beam attenuation was consistently deeper than the depth of minimum beam attenuation. The depth of the minimum was related to total water depth, seen most effectively in the first nine Knorr stations, but also in the correlation between peaks in minimum E/E_D, the depth of the nephel minimum and water depth in the Conrad 22 data.

in temperature measured between the inside and outside of the instrument. This results because, while the transmissometers used in the HEBBLE work had been temperature calibrated, they still were sensitive to temperature "shock". That is, if the instrument is rapidly changing temperature, the temperature throughout the instrument is not constant, so that a slight error resulted.

Beam-attenuation values for profiles throughout the cruise were plotted for the down and up traces at depths where rosette bottles were closed during the up trace (Fig.8). The values on the up trace were consistently lower than those on the down trace to a depth of 2400 m, below which the trend reversed itself. Only samples at least 1000 mab were examined to avoid any influence from variability in the nepheloid layer. The absolute offset (Fig.8, right) appears to be linear with depth, suggesting a pressure effect, but the temperature effect must also be considered. This offset, albeit very small, exists for uncorrected beam attenuation as well as potential beam attenuation.

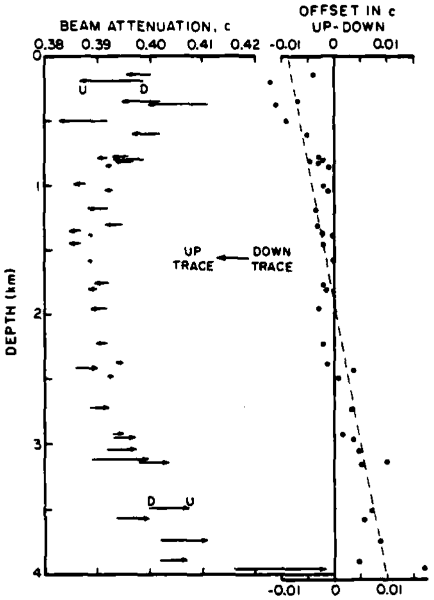

Fig.8. Offset between the down and up traces of beam attenuation decreased down to 2400 m and then increased down to 4000 m (points were taken from profiles made throughout the cruise and all points were at least 1000 mab to avoid the nepheloid layer). On the right is a plot of the absolute offset rather than the relative range with a linear regression of the data. Compare with *c* in Fig.4 to see that the effect is very small.

As mentioned earlier, it was shown by Thorndike (1975) that temperatures can affect log E/E_D by as much as 0.10 units, but only for values greater than about 1.60. No up traces were processed with the nephelometer during the Knorr cruise, but examination of previous data sets shows no consistent offset in the uptrace of nephelometer profiles (Eittreim and Ewing, 1972).

The value for minimum beam attenuation falls in three distinct time ranges within each of which there is little variation (Fig.7). This appears to have resulted from the use of three different air calibrations during the cruise as the instrument windows were cleaned. This is the reason for the offset in minimum beam attenuation between stations in Fig.6. It has little effect on the concentrations in the nepheloid layer, but is important for measurements and comparisons made throughout mid water.

One cannot say much about the minimum E/E_D value throughout the Knorr cruise because an incorrect adjustment in the instrument during that cruise made it necessary to assume a minimum. Rather than use an arbitrary minimum, the average of the log E/E_D values obtained from profiles in the HEBBLE area during the Conrad cruise a few months earlier was used. During the Conrad cruise the minimum E/E_D values did not change much and most of those changes appear to have been a function of water depth. This variability does not cause any change in the depth of the minimum nor does it cause any change in the shape of the log E/E_D curve obtained. Maximum errors for this change are shown in Fig.7.

Another attempt to understand the small, but consistent differences between light scattering and beam attenuation in mid-water was made by plotting the optical values against C_M, corrected C_M (corrected for dregs) and C_V for samples obtained more than 1000 mab, a distance chosen to avoid contamination from nepheloid layer particles (Fig.9). Since the HEBBLE project focused on bottom boundary layers, very few samples were taken more than 1000 mab. Correlation coefficients between the optical measurements and the few values for C_M, corrected C_M or C_V in mid-water samples are less than 0.1 which indicates there is no correlation.

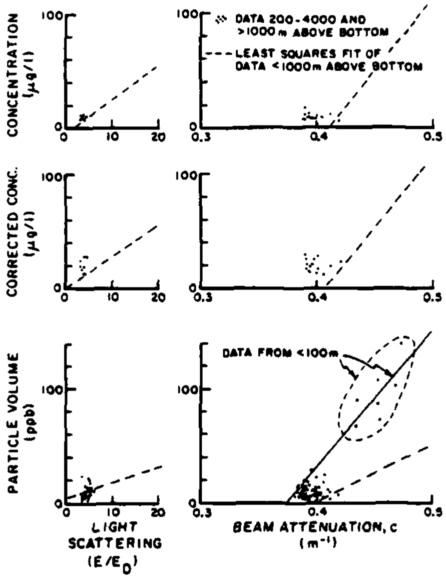

Fig.9. Light scattering and beam attenuation versus concentration, corrected concentration and Coulter Counter volume of particles for water samples between 200 and 4000 m *(all samples taken at least 1000 mab). The dotted lines are the least squares fit of the data* less than 1000 mab. There is no statistical correlation between any of the particle and optical parameters measured in mid-water for these data.

The dotted lines in Fig.9 are the linear least squares fit for the entire data set for particle concentrations from Figs.3B and 4B but for particle volumes the dotted lines are only for data deeper than 4000 m. The seven points of C_V versus c obtained in the surface 100 m do show a trend (solid line in Fig.9) but one that is very different from particles in the nepheloid layer (dotted line in Fig.9); further evidence that particle properties (size, shape, index of refraction) influence optical responses. There is no indication, however, of which instument, if either, accurately reflects the particle concentration above the nepheloid layer. This does not mean the instruments are not sensitive to changes in the water column. For instance at station 24 (Fig.6) both beam attenuation and light scattering decrease down to 630 m, and then both show a slight maximum between 630 and 1268 m.

Another problem in the optical versus C_M comparison lies in accurately determining the particle concentration by filtration methods, since errors can be large at low concentrations (Brewer et al., 1976). Our mid-water concentrations of 5 μg l^{-1} are in the range of variability found for replicate samples in the ocean (Wangersky, 1974; Brewer et al., 1976). The low concentrations are also affected more by the problems of dregs (Gardner, 1977); for the HEBBLE data the particle concentrations double after the dregs correction, but the correlations with E/E_D and c are not improved. The only comparison that is certain for the water column between 250—4000 m is that the two instruments suggest different depths for the deepest particle minimum, but even this could result from different optical responses to changes in particle properties through the water column, or second-order temperature or pressure effects on one or both of the instrument responses.

BOTTOM OCEAN MONITOR (BOM)

The comparison of light scattering and beam attenuation should be better with the units on the BOM because both measurements were instantaneous and very close in time and space. Values produced by the two units tracked each other very well during background levels but during different benthic storms there were different correlations between E/E_D and c (Figs.5C and 10). Differences were small between storms I, III and IV but during storm II transmission went to zero, so beam attenuation was undetermined. The concentrations reached such high values, however, that secondary scattering around the nephelometer began to scatter light in the forward direction and increased the direct light (E_D) reaching the nephelometer film, thus decreasing the value of E/E_D and erroneously indicating lower concentration of particles. This decrease can be seen between August 30th and September 3rd in Fig.10 with the peak of the storm occurring on August 31st, though absolute values are undetermined. The differences in traces of E/E_D versus c between storms are probably due to differences in the size distribution or index of refraction of particles resuspended and therefore, differences in the optical response of light scattering and beam attenuation to particles with different size distributions.

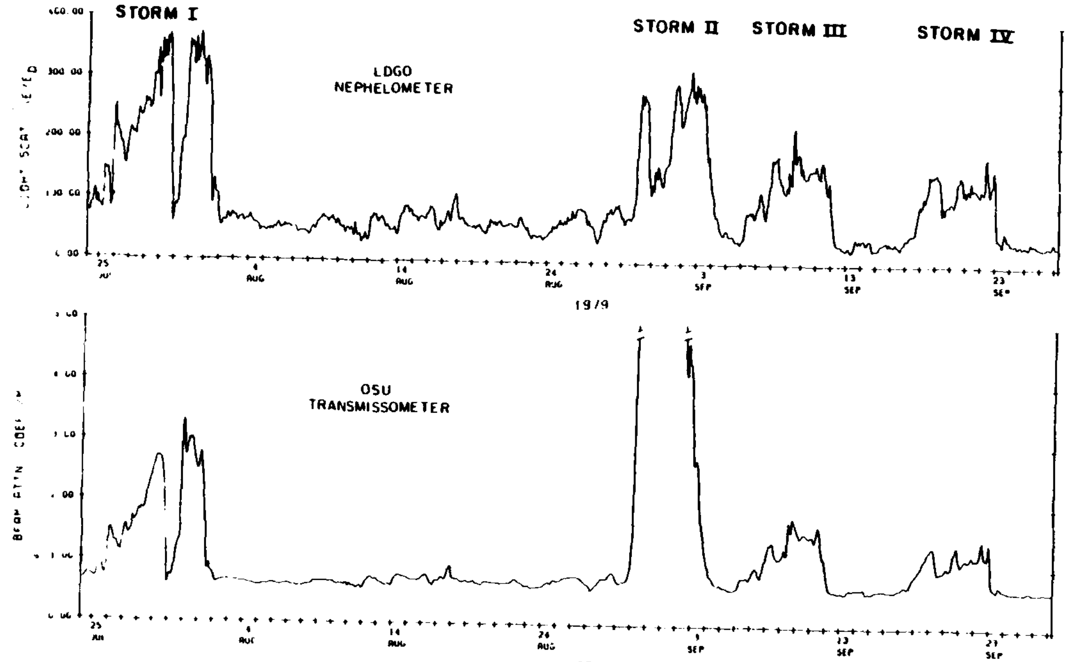

Fig.10. **Time plots of** ***light scattering*** **and beam attenuation from instruments on the BOM tripod.**

Despite the close proximity of the two instruments and the linearity between the two measurements in Fig.5, there is an offset in the plots of E/E_D versus c between the BOM instruments and the profiling instruments (Fig.5B vs. 5D). Based on our calibrations of the two instruments against filtered water, the minimum particle concentration observed during the BOM deployment predicted by the nephelometer is 57 μg l^{-1} whereas the transmissometer data predicts a minimum of 205 μg l^{-1}. No water samples were taken on the BOM, so no direct comparison is available. The only comparison is that three CTD stations were made in the vicinity of the BOM during its deployment. Although there was about 4 km between the stations and the BOM, they were made at times of relatively steady concentrations measured at the BOM. The bottom values of the nephelometer profiles were 32, 12, and 16 units of E/E_D higher than the BOM measurements at corresponding times. Beam attenuation was 0.054 and 0.084 units lower than corresponding BOM measurements. It would thus appear that there were consistent errors in both BOM instruments for undetermined reasons. The nephelometer values should be higher and the transmissometer values should be lower. The offset does not change the shape of the time record of either instrument or the interesting record of benthic storms in the HEBBLE area.

CONCLUSIONS

Both the LDGO nephelometer and the OSU transmissometer can be effectively used to study nepheloid layers in the ocean. Both instruments have a linear correlation between suspended particle mass concentration and light scattering (E/E_D) and beam attenuation (c) for the range of concentrations generally found in the ocean (10—250 μg l^{-1}). At higher concentrations the transmissometer response remains linear, but the response of the nephelometer is described by a second-order equation due to multiply scattered light. Our data for C_M concentrations less than 10 μg l^{-1} are very limited in the study so we cannot state the accuracy of optical measurements for predicting C_M in this range. There is a small systematic difference in the response of E/E_D versus c throughout the upper water column, due either to changes with depth in particle characteristics or to second-order effects of temperature or pressure on one or both of the instruments. Because of this one cannot equate data from the two instruments to determine the depth of the clearest water. This study does make it possible, however, to compare or combine results for the two instruments from independent studies in different parts of the ocean assuming the size distributions and index refraction of particles are similar. The range of particle concentrations in the HEBBLE region included the highest values ever measured in the deep sea (12,700 μg l^{-1}).

ACKNOWLEDGEMENTS

We wish to thank all participants in the HEBBLE Knorr 74 cruise who helped in obtaining the data used in this paper, including Captain Hiller and the crew of the R/V "Knorr". We thank Dr. Charles Hollister for his orchestration of the HEBBLE project. David Menzies, Dr. Rick Spinrad, Dr. Brian Tucholke, Jay Ardai, Greg Bunce and Peter Bruchhausen all helped collect the data. We thank Lawrence G. Sullivan for skillfully managing the nephelometer/BOM data acquisition and reduction, Mary Parsons and Adele Hanley for help in data reduction, and Dr. Edward M. Thorndike for constant attention over the years to details in improving the nephelometer which he originally built. The same thanks go to David Menzies for reduction of the transmissometer data and to Robert Bartz for keeping the electronics of the transmissometer up to the latest state of the art in solid state circuitry. The BOM was constructed with LDGO Industrial Associates funds through Dr. Brian Tucholke. This work was supported at LDGO by the Office of Naval Research contracts N00014-75-C-0210 Scopes R and S and N00014-80-C-0098 Scope D and at OSU by ONR contract N00014-18-0004. This is contribution number 3834 of Lamont-Doherty Geological Observatory.

REFERENCES

Baker, E.T. and Lavelle, J.W., 1984. The effect of particle size on the light attenuation coefficient of natural suspensions. J. Geophys. Res., 89: 8197—8203.

Bartz, R., Zaneveld, J.R.V. and Pak, H., 1978. A transmissometer for profiling and moored observations in water. Soc. Photo Opt. Instrum. Eng., 160: 102—108.

Biscaye, P.E. and Eittreim, S.L., 1974. Variations in benthic boundary layer phenomena. nepheloid layers in the North American Basin. In: R. Gibbs (Editor), *Suspended Solids in Water*. Plenum, New York, N.Y., pp.227—260.

Biscaye, P.E. and Eittreim, S.L., 1977. Suspended particulate loads and transports in the nepheloid layer of the abyssal Atlantic ocean. Mar. Geol., 23: 155—172.

Bishop, J.K.B., 1985. The correction and suspended particulate matter calibration of Sea Tech transmissometer data. Deep-Sea Res. (in press).

Brewer, P.G., Spencer, D.W., Biscaye, P.E., Hanley, A., Sachs, P.L., Smith, C.L., Kadar, S. and Fredericks, J., 1976. The distribution of particulate matter in the Atlantic Ocean. Earth Planet. Sci. Lett., 32: 393—402.

Butman, B. and Moody, J.A., 1983. Observations of bottom currents and sediment movement along the U.S. East Coast continental shelf during winter. In: B.A. McGregor (Editor), Environmental Geological Studies on the United States Mid and North Atlantic Outer Continental Shelf Area, 1980—1982, Vol. II. Mid-Atlantic Region, Ch. 7. BLM Final Rep. AA851-MUO-18.

Eittreim, S. and Ewing, M., 1972. Suspended particulate matter in the deep waters of the North American Basin. In: A.L. Gordon (Editor), Studies in Physical Oceanography. Gordon and Breach, London.

Gardner, W.D., 1977. Incomplete extraction of rapidly settling particles from water samplers. Limnol Oceanogr., 22: 764—768.

Gardner, W.D. and Sullivan, L.G., 1981. Benthic storms: Temporal variability in a deep ocean nepheloid layer. Science, 213: 329—331.

Gardner, W.D., Richardson, M.J., Hinga, K.R. and Biscaye, P.E., 1983. Resuspension measured with sediment traps in a high-energy environment. Earth Planet. Sci. Lett., 66: 262—278.

Gardner, W.D., Bishop, J.K.B. and Biscaye, P.E., 1984a. Nephelometer and current observations at the STIE site, Panama Basin. J. Mar. Res., 42: 207—219.

Gardner, W.D., Sullivan, L.G. and Thorndike, E.M., 1984b. Long-term photographic, current, and nephelometer observations of manganese nodule environments in the Pacific. Earth Planet. Sci. Lett., 70: 95—109.

Hollister, C.D. and Heezen, B.C., 1972. Geologic effects of ocean bottom currents: Western North Atlantic. In: A.L. Gordon (Editor), Studies in Physical Oceanography, Vol. 2. Gordon and Breach, New York, N.Y., pp.37—66.

Jerlov, N.G., 1976. Marine Optics. Elsevier, New York, N.Y.

McCave, I.M., 1983. Particulate size spectra, behavior, and origin of nepheloid layers over the Nova Scotian continental rise. J. Mar. Res., 88. 7647—7666.

Pak, H., 1983. Fluctuations of beam attenuation coefficient in the lowest 2 m on the continental rise off Nova Scotia. Mar. Geol., 51: 77—97.

Pak, H. and Zaneveld, J.R.V., 1983. Temporal variations of beam attenuation coefficient on the continental rise off Nova Scotia. J. Geophys. Res., 88: 4427—4432.

Richardson, M.J., 1980. Composition and characteristics of particles in the ocean: Evidence for present-day resuspension. Ph.D. Thesis, MIT/WHOI Joint Program in Oceanography. 237 pp.

Richardson, M.J., Wimbush, M. and Mayer, L., 1981. Exceptionally strong near-bottom flows on the continental rise of Nova Scotia. Science, 213: 887—888.

Spinrad, R.W. and Zaneveld, J.R.V., 1982. An analysis of the optical features of the near-bottom and bottom nepheloid layers in the area of the Scotian Rise. J Geophys. Res., 87: 9553—9561.

Spinrad, R.W., Zaneveld, J.R.V. and Kitchen, J.C., 1983. A study of the optical characteristics of the suspended particles in the benthic nepheloid layer of the Scotian Rise. J Geophys. Res., 88: 7641—7645.

Thorndike, E.M., 1975. A deep sea, photographic nephelometer, Ocean Eng., 3: 1—15.

Thorndike, E.M. and Ewing, M., 1967 Photographic nephelometers for the deep sea. In: J.B. Hersey (Editor), Deep-Sea Photography, Vol. 3 Johns Hopkins University Press, Baltimore, Md., pp. 113—116.

Wangersky, P.J., 1974. Particulate organic carbon: sampling variability. Limnol. Oceanogr., 19: 980—984.

Weatherly, G.L. and Kelley, E.P., 1982. "Too cold" bottom layers at the base of the Scotian Rise. J. Mar. Res., 40: 985—1012.

Zaneveld, J.R.V., 1973. Variation of optical sea parameters with depth. In: Optics of the Sea (Interface and In-Water Transmission and Imagery). NATO Lecture Ser. Vol. 61: 2.3-1—2.3-22.

Zaneveld, J.R.V., Spinrad, R.W. and Menzies, D.W., 1979. Optical and hydrographic observations in the Congo River and Angola Basin during May 1978. Oregon State University, Tech. Rep. 79—3.

Zaneveld, J.R.V., Spinrad, R.W. and Bartz, R., 1982. An optical settling tube for the determination of particle-size distributions. Mar. Geol., 49. 357—376.

Zimmerman, H.B., 1971. Bottom currents on the New England continental rise. J. Geophys. Res., 76: 5865—5876.

Continental Shelf Research, Vol. 4, Nos 1-2, pp. 159 to 174, 1985.
Printed in Great Britain.

0278-4343/85 $3.00 + 0.00

Geotechnical properties of surface and near-surface deposits in the East China Sea

GEORGE H. KELLER* and YE YINCAN†

(*Received for publication* 8 *August* 1984)

Abstract—Shelf deposits in the East China Sea are primarily relict sands with overlying fine-grained cohesive deposits occurring along the innermost shelf and as a more or less isolated deposit on the midshelf. Considering these surface and near-surface (0 to 1.5 m) cohesive deposits as a unit, the innermost shelf sediments are slightly coarser (more silt) than those of the midshelf which commonly contain more clay-size material. The inner shelf sediments also display higher mean wet bulk densities (1.48 to 1.88 mg m^{-3}) and shear strengths (4.0 to 9.8 kPa), but lower water contents (64 to 81%) and porosities (62 to 66%) than those found associated with the midshelf deposits. Available data indicate that the midshelf mud deposit is primarily derived from the reworking of Huanghe (Yellow River) coastal deposits that were laid down at a time when the river debouched into the Yellow Sea to the north of the Changjiang. Some portion of the midshelf mud may be derived from the Changjiang. These midshelf 'fines' apparently are caught up in a large circulation gyre over the shelf which accounts for their isolated nature. Strong bottom and near-bottom currents, as well as winter storm wave activity, are primary mechanisms resulting in both suspended sediment and bedload transport on the shelf of the East China Sea.

INTRODUCTION

THE ANNUAL suspended sediment load of the Changjiang averages 478 × 10^6 metric tons, which is slightly greater than two times the load carried by the Mississippi River (MILLIMAN and MEADE, 1983). Although the Changjiang's load is considerable, there is no offshore delta comparable to that off the Mississippi. Early sedimentological studies in the East China Sea dealt primarily with the general distribution of surface sediments and their mineralogical composition (SHEPARD *et al.*, 1949; NIINO and EMERY, 1961; CHIN, 1963). In a later study of sediment distribution by CHIN (1979) mention was made of the sources for the fine-grained shelf deposits. The impact of sea-level changes on sediment distribution and paleo drainage on the shelf has been discussed by a number of investigators (GUO, 1979; REN and TSENG, 1980). Until a research program was initiated in 1980 relatively little seems to have been known about the sediment dynamics on the shelf off eastern China. To better understand the impact of the Changjiang on the sedimentary regime of the East China Sea and especially the sediment dynamics on the inner shelf in the vicinity of the river mouth, a cooperative study was initiated by scientists from the United States and the People's Republic of China through the National Bureau of Oceanography and the National Oceanic and Atmospheric Administration of the United States.

---

* College of Oceanography, Oregon State University, Corvallis, OR 97331, U.S.A.
† Second Institute of Oceanography, National Bureau of Oceanography, Hangzhou, People's Republic of China.

This paper presents the results of the geotechnical studies conducted on sediment core samples collected during 1980 and 1981. Particular interest is given to defining the range and distribution of various sediment properties in an attempt to understand the impact of the local energy regime on the transport of the bottom sediments.

METHODS AND FACILITIES

Bottom sediments were collected by means of several coring devices [Kasten corer (Kogler, 1963), Hydroplastic corer (Richards and Keller, 1961), piston, vibracorer, and box corer] as well as with the Peterson grab, at 36 stations extending from the innermost shelf of the East China Sea to the shelf-break (Fig. 1). Piston and vibracore samples, as well as those from the Peterson grab, were used for textural and mineralogical analyses, whereas the Kasten and Hydroplastic core samples provided the high-quality material needed for geotechnical studies. In the majority of cases, measurements of such geotechnical properties as shear strength, water content, and wet bulk density were made in Shanghai immediately after each cruise to minimize alteration of the geotechnical properties due to disturbance and/or water loss. A few select samples were carefully packed, refrigerated, and returned to the United States for consolidation analyses. All consolidation tests were made with an Anteus back pressure unit following the procedures outlined by Lowe *et al.* (1964). An initial load of 0.0293 kg cm^{-2} (2.87 kPa) was applied, and each succeeding load doubled at 24-h intervals, up to 31.3 kg cm^{-2} (3066 kPa). With the exception of the liquid limit test, the standards of the American Society for Testing and Materials were followed in the testing of all samples. Liquid determinations were made using a penotrometer technique (Ministry of Water Conservancy of the People's Republic of China, 1956).

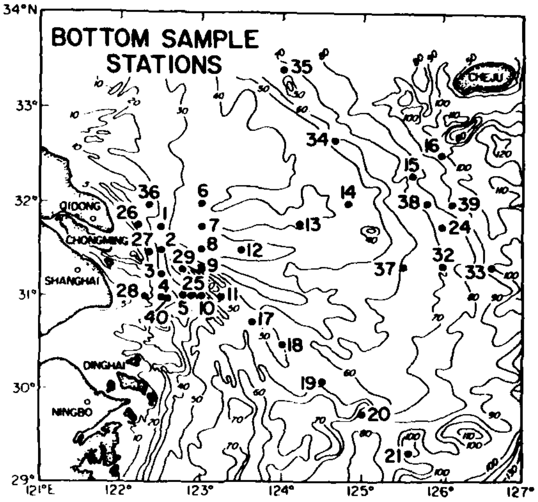

Fig. 1. Sediment coring stations and bathymetry (isobaths in meters).

GEOTECHNICAL PROPERTIES

Texture

Surface deposits of the innermost shelf, particularly in the vicinity of the Changjiang, range in texture from very fine silt to coarse silt (median diameters of 4 to 62.5 μm) with the finer-grained material located to the southeast of the Changjiang's mouth (Fig. 2A). Surface deposits over much of the central shelf are primarily fine to medium sands. Across this portion of the shelf there appears to be a northwest–southeast trending zone of relatively coarse sediment (fine to medium sand) extending from the shelf-break of the East China Sea up into the Yellow Sea which may possibly reflect the effects of stronger currents through this area (Fig. 2A). Along the eastern and northeastern margin of the study area, a pronounced zone of fine-grained material, coarse clay to fine silt, covers a significant portion of the shelf (Fig. 2A). Available data indicate that these deposits represent a tongue of fine-grained material extending from the area of the Yellow Sea down into the East China Sea. This distribution correlates with the circulation pattern for this area (discussed in a later section).

Textural properties within the upper 1.5 m of the seafloor (a common depth reached by the majority of the core samples) reveal that the depositional history has altered little in recent times. The innermost shelf sediments are mainly silts, ranging from very fine to medium silts. As might be expected, the fine-grained material extends in a plume-like pattern onto the shelf from the Changjiang (Fig. 2B). Across the central portion of the shelf, mean grain size for the 0- to 1.5-m interval varies relatively little, being comprised primarily of very fine to fine sand. Mean grain sizes in the upper 1.5 m along the midshelf east of Shanghai indicate that the deposition of clay and silt-size materials has persisted in this area for at least 500 years based on the "apparent ^{210}Pb accumulation rates" of 0.3 cm y^{-1} reported by DEMASTER *et al.* (1983). As will be discussed later, the silts and clays appear to be modern sediments which have and are continuing to be deposited over relict shelf sand of Pleistocene age (BUTENKO *et al.*, 1985). On the innermost shelf these modern sediments blanket semi-consolidated clays representing earlier Changjiang deposits.

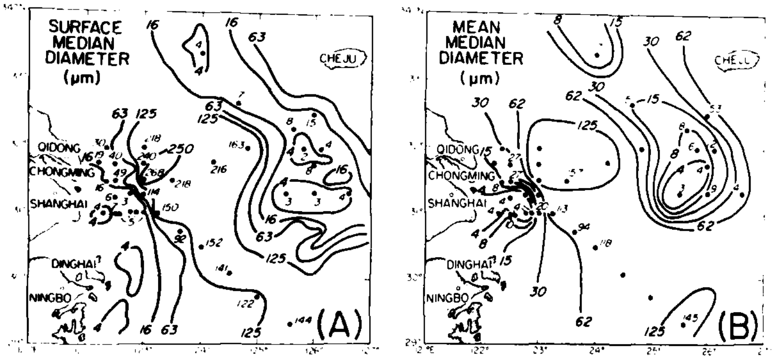

Fig. 2. Distribution of (A) surface sediment median diameter and (B) mean median diameter for the 0- to 150-cm interval.

Percentages of sand, silt, and clay in the 1.5-m interval indicate that relatively little sand is being deposited on the shelf. Although fine-grained sediments predominate along the eastern and northeastern margin of the study area, slightly higher percentages of sand generally occur in these deposits relative to those in close proximity to the Changjiang (Fig. 3A). This increased sand content may possibly be attributed to a combination of factors such as the adjacent sand source, lower dilution owing to significantly lower concentrations of fine grained material reaching this part of the shelf relative to the area just off the Changjiang, or inpart winnowing of the fines. As might be expected, the highest concentrations of silt-size material are located along the innermost margin, where mean values of silt content for the 0- to 1.5-m interval reach as high as 55% (Fig. 3B). Very little clay or silt-size material is found in the central shelf deposits. Those few isolated areas with relatively high percentages of fine-grained material may reflect local variations in the morphology or the outcropping of older

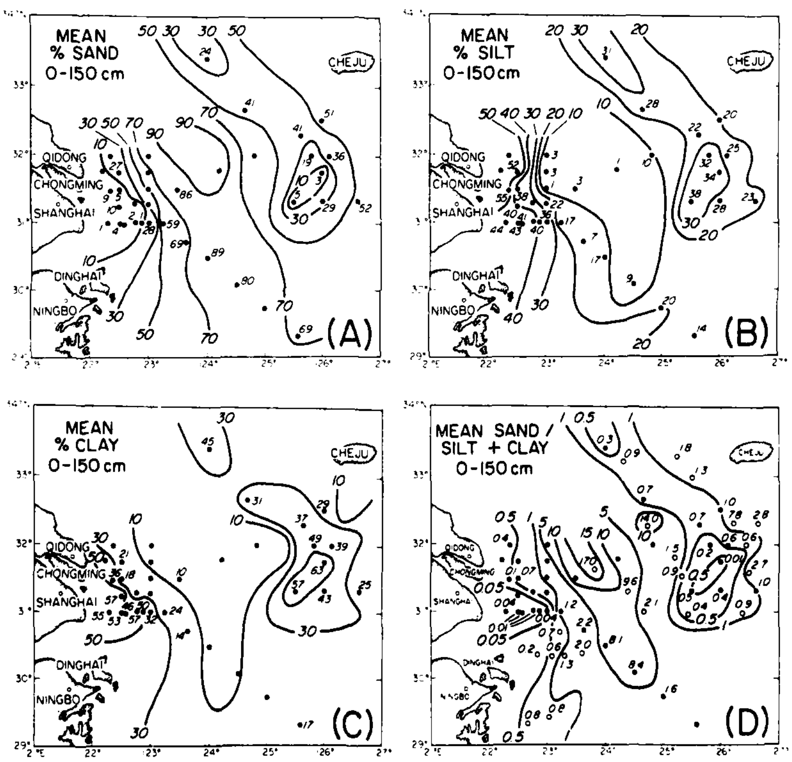

Fig. 3. Distribution of mean values for the 0- to 150-cm interval of (A) sand, (B) silt, (C) clay, and (D) ratio of sand to silt plus clay.

semi-consolidated clays. Although mean concentrations of clay-size material in the 0- to 1.5-m interval in the vicinity of the Changjiang are as high as 57%, slightly higher concentrations occur in the mud deposits blanketing the eastern part of the shelf (Fig. 3C). These relationships are more clearly shown by the ratio of sand to silt and clay (Fig. 3D) which indicates that little or no sand is being deposited in the modern sediment regime. The relict nature of the existing shelf sands has been documented by Niino and Emery (1961) and Butenko *et al.* (1985).

Water content

Higher water contents are commonly associated with finer rather than coarser-grained deposits. The distribution pattern for mean water content in the surficial deposits (0- to 40-cm interval) closely corresponds to the sediment distribution pattern, with clay-dominated sediments displaying the highest water contents and the sands the lowest values (Fig. 4A). Silt-rich sediments of the innermost shelf possess, for the most part, lower water contents (34 to 108% dry wt) than do the silty clay deposits (57 to 111% dry wt) along the eastern margin of the study area.

Although there are only a few mean water content values for the sandy shelf deposits, analysis of a number of surface samples indicates that these deposits have water contents of 30% or less.

Wet bulk density

Commonly wet bulk density (wet wt per unit volume) is inversely proportional to water content; this can be seen in the similarity of the distribution patterns for these two properties (Fig. 4A, B). Although relatively few data are available, the silty sand shelf deposits are found to commonly display wet bulk densities of 1.80 mg m^{-3} or greater. Silty clays of the innermost shelf, however, possess lower densities than do the shelf sands, but not quite as low as the silty clays (1.43 to 1.51 mg m^{-3}) along the eastern portion of the study area (Fig. 4B).

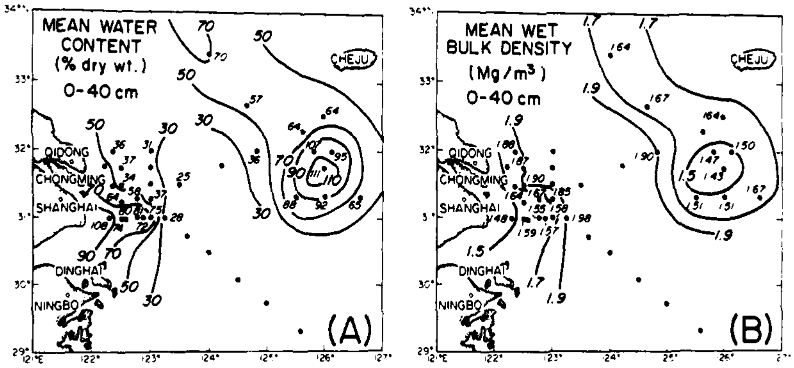

Fig. 4. Mean value distribution of (A) water content and (B) wet bulk density for the 0- to 40 cm interval.

Available data indicate a strong correlation between the density and textural characteristics of the shelf deposits, with no apparent influence from the concentration of particular minerals in these sediments.

Shear strength

Undrained shear strength was measured using a Torvane (SIBLEY and YAMANE, 1965; SILVA and HOLLISTER, 1973) to facilitate a rapid analysis of the samples shortly after they were collected. No attempt was made to measure the strength of the non-cohesive sediments. Mean shear strength in the 0- to 1.5-m interval reveals a gradual increase seaward from the Changjiang. Rapid accumulation of fine-grained, high water content sediment to the southeast of the mouth of the Changjiang (DEMASTER *et al.*, 1983) results in a surface and near-surface deposit of almost fluid consistency and low cohesion. As the sediments are exposed to stronger currents seaward of the coast, they appear to contain less water and be more consolidated. A marked increase in shear strength is noted along the eastern margin of these deposits (Fig. 5). This seaward increase in cohesion may also reflect the age and texture of the sediments. Slight increases in the sand content probably contribute to the noted increase in shear strength. Examination of sediment core 25 to the southeast of the Changjiang (Fig. 1) suggests that the high value of 7.2 kPa (Fig. 5) may be the result of erosion and the sampling of older strata. Silty clay deposits along the eastern and northeastern margin of the study area have anomalously low shear strengths compared to sediments of similar texture and other mass properties. Mineralogy and/or some other geochemical factor may be responsible for these lower strengths.

Comparison of undisturbed to remolded shear strength reveals that the inner shelf deposits have sensitivities ranging from 1 to 12 with an overall mean value of 5. Based on the sensitivity classification of ROSENQVIST (1953), these sediments are classed as being very

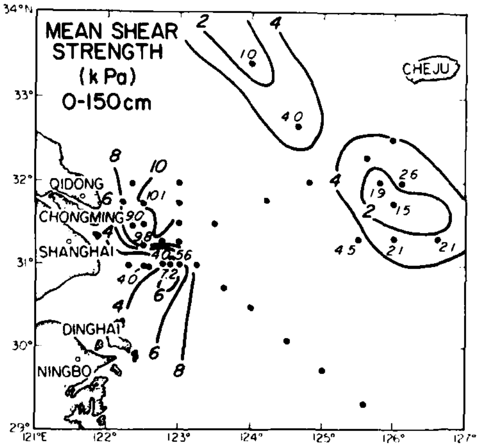

Fig. 5. Shear strength, distribution of mean values for the 0- to 150 cm interval.

sensitive and, upon disturbance, lose approximately 75 to 87% of their natural strength (RICHARDS, 1962). Muds along the eastern margin of the study area are less sensitive to disturbance, displaying values ranging from 1 to 6 with an overall mean value of 3, which is more in line with that found in submarine deposits.

Plastic characteristics

A classification developed by CASAGRANDE (1948) relates plasticity index (range of water content between the liquid and plastic limits of the sediment) to the liquid limit. An "A"-line shown on the plasticity chart (Fig. 6) represents an empirical boundary between inorganic clays above the line, and organic clays and clastic silts below. Based on this classification, cohesive sediments in the East China Sea can be grouped into three classes: the silty clay deposits along the eastern margin of the study area (core 24) are classed as inorganic clays of high plasticity whereas the innermost shelf deposits (cores 3, 4, and 5) are classified as inorganic clays or silty clays of low-to-medium plasticity. Intermediate to these two classes are the sediments (core 25) along the eastern margin of the inner shelf mud deposits, which appear to be older, semi-consolidated material that has been exposed due to erosion.

The plasticity chart also commonly provides a means of identifying sediments according to relative source areas. The occurrence of data points from the innermost and midshelf mud deposits along a line more or less parallel to the "A"-line, suggest that these sediments are derived from a similar source area (TERZAGHI, 1955). As noted earlier, Huanghe sediments are believed to be the primary source for the offshore muds, whereas modern Changjiang sediments appear to be a secondary source. Until the recent study by YANG and MILLIMAN (1983), no distinct difference in composition was reported between the innermost and midshelf fines. Their finding that high concentrations of calcium and an absence of halloysite

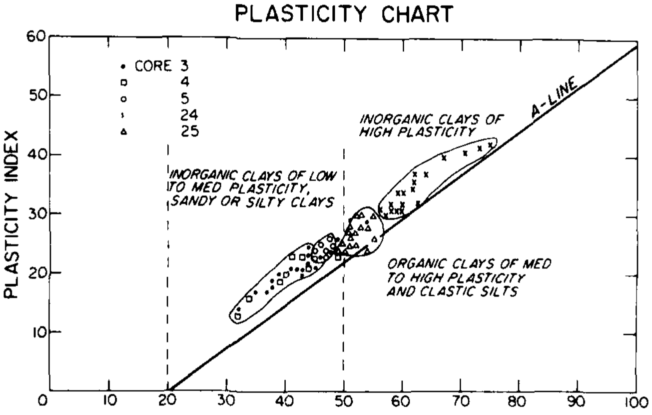

Fig. 6. Plasticity chart showing the classification of the East China Sea cohesive deposits. Values are from subsamples integrated over the entire cored intervals (0 to 150 cm).

is unique to Huanghe suspended sediments and the midshelf muds identifies these fines as being primarily derived from the Huanghe. Since both the Huanghe and the Changjiang drain major portions of eastern China, the plasticity chart indicates a common source area for the shelf muds. The sediment is, however, transported to the sea by two different drainage systems.

Consolidation characteristics

To determine the loading history and strength characteristics of the cohesive sediments sampled on the innermost shelf and along the eastern portion of the study area, consolidation tests were made on 8 subsamples taken from the Kasten cores and one from a Hydroplastic core. Normally consolidated sediments are those in which the present load due to the overburden (overburden pressure) is equal to the preconsolidation pressure or the previous maximum load on the sediment as determined by the consolidation test. Underconsolidated sediments are those in which the present overburden exceeds the preconsolidation pressure; a circumstance which is commonly associated with very rapid deposition where pore water pressures have not come to equilibrium, resulting in excess pore pressures. A third condition is overconsolidation, which occurs when the preconsolidation pressure exceeds the present overburden pressure. On land this situation is commonly observed where erosion has removed overlying material.

All subsamples were taken from depths ranging from 160 to 273 cm below the seafloor and all displayed a slight degree of overconsolidation (Fig. 7). As has been reported by a number of investigators (HAMILTON, 1964; RICHARDS and HAMILTON, 1967; KELLER and BENNETT, 1973), the upper few meters of submarine deposits commonly display 'apparent' overconsolidated characteristics. This 'apparent' overconsolidation has been attributed to, although not substantiated, various factors such as very slow rates of sedimentation and/or some form of bonding or cementation rather than the removal of overburden (TERZAGHI, 1941; HAMILTON, 1964; BJERRUM, 1967; RICHARDS and HAMILTON, 1967). In East China Sea cohesive deposits, overconsolidation ratios (ratio of preconsolidated pressure to overburden pressure) range from 1.2 to 2.4 and are believed to result from the removal of overburden rather than from slow sedimentation or bonding. Core 25 has an overconsolidation ratio of about twice that measured in the other samples tested. Visual inspection and examination of the index properties with depth (see the following section), indicate that the interval 210 to 223 cm in this core represents a stiff, older deposit underlying the soft modern muds of the inner shelf. Assuming that this overconsolidated state results from the erosion of overburden, calculations indicate that approximately 300 cm of sediment has been removed from the area (core 25). In deep sea, overconsolidation is seldom attributed to erosion; however, considering the relatively shallow water depths (16 to 73 cm) of the East China Sea and the episodic nature of deposition and erosion (MCKEE *et al.*, 1983), erosion is probably the primary factor contributing to the overconsolidated state of these deposits. In these shallow depths it is probable that the combination of surface waves and strong bottom shelf currents (up to 48 cm s^{-1}; STERNBERG *et al.*, 1983) do remove considerable quantities of surface and near-surface deposits from time to time (MCKEE *et al.*, 1983; DEMASTER *et al.*, 1983). Calculations based on the consolidation test data indicate that along the innermost shelf (cores 3, 4, and 5), on the order of 35 to 85 cm of sediment column has been eroded. In the fine-grained deposit along the eastern margin of the study area, assuming an erosion model, approximately 100 to 125 cm of sediment has been removed.

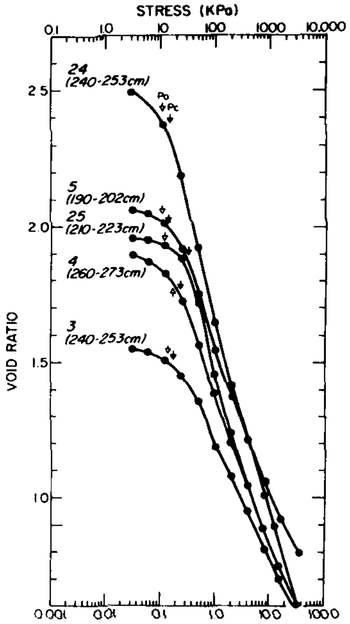

Fig. 7. Void ratio vs logarithm of pressure curves for five subsamples, intervals noted within ( ), from cores 3, 4, 5, 24, and 25. P_0 denotes overburden pressure and P_c the preconsolidation pressure.

Variations with depth

Examination of the vertical variations in the geotechnical properties within the upper 1.5 to 3 m of the seafloor reveal an offshore decrease in variations of these properties. As might be expected, the closer to the Changjiang, the greater the occurrence of coarser-grained layers and the greater the variation in the textural properties. This seaward gradation is especially evident in the vertical distribution of the geotechnical properties in cores 3, 4, 5, 25, and 24 (Fig. 8). The mud deposit on the midshelf shows the least variation of these properties with depth (core 24). Changes in sediment water content and bulk density in the vicinity of the Changjiang, are indicative of variations in the textural properties. Increase in sand and/or silt content is commonly reflected in decreases in water content and increases in bulk density.

Owing to the increased degree of variation in the textural properties in the vicinity of the Changjiang, the sediments do not display a distinct decrease in water content and porosity or an increase in bulk density with depth as would be commonly expected. Such a gradient begins to appear in cores 5 and 25, and is particularly pronounced in core 24 (Fig. 8) where the least degree of textural variation is found.

All cohesive deposits sampled display an increase in shear strength with depth below the seafloor which is attributed to the effect of overburden. Shear strength gradients are greatest in the vicinity of the Changjiang and the lowest in the midshelf mud deposit (Fig. 8). Predicting any geotechnical property with depth by use of a gradient model is more reliable in the case of the midshelf mud deposit because of its more homogenous character.

All the sampled cohesive sediments of the East China Sea possess water contents distinctly higher than their liquid limit. The difference between these two parameters is significantly greater in the midshelf mud than in the innermost shelf deposits. Such a relationship would indicate that upon disturbance all these deposits would tend to fluidize to some degree.

Core 25, from the seaward margin of the brown modern day fluidized mud zone, displays slightly different geotechnical properties than those found in the other cohesive deposits (Fig. 8). The upper few centimeters are composed of the brown fluid-like mud which blankets the seafloor off the Changjiang. Below about 10 cm, the remainder of the core consists of a stiff gray silty clay. This underlying clay layer is characterized by considerably higher bulk densities and shear strengths, and lower water contents than those sediments with a comparable texture found to the east on the midshelf (Fig. 8). Examination of consolidation test data, as discussed earlier, also reveals that this gray clay displays a preconsolidation pressure (a measure of the prior maximum load applied) that is considerably greater than the preconsolidation pressures determined at similar depths in the other cores. These data tend to support the supposition that this gray clay represents an older sediment, possibly deposited during a lower stand of the sea or a period of different dynamic conditions. Based on high resolution seismic profiles data from BUTENKO *et al.* (1985), it appears that this semiconsolidated horizon extends over much of the innermost shelf as well as seaward for some distance under the adjacent sand deposits.

SEDIMENT TRANSPORT

Long-term apparent sediment accumulation rates of 0.3 to 5.4 cm y^{-1} in the study area (DEMASTER *et al.*, 1983) as well as the presence of great expanses of sand across the shelf in an area into which approximately 500×10^6 metric tons of sediment is discharged annually, clearly indicates that the majority of the sediment coming to the area is also being transported out of the area. A significant portion of the sediment entering from the Changjiang is transported out of the area as a suspended load, principally along the coast to the south (LIMEBURNER *et al.*, 1983). Of these sediments that are deposited on the adjacent shelf considerable quantities are eroded in time as revealed by comparing the short-term (100 day) accumulation rates (53 cm y^{-1}) to the long-term (100 y) rates (5.4 cm y^{-1}) (DEMASTER *et al.*, 1983). Since there is no evidence of sediment mass failure or slumping due to gravity the removal of these bottom sediments off the Changjiang is attributed to current activity. In considering a combination of factors such as sediment physical properties, cyclic wave loading, and excess pore pressure, plus the presence of strong bottom currents, there is good reason to believe that much of the fine-grained deposits are resuspended and transported out of the area by the currents from time to time.

Owing to the shallow nature of the inner and midshelf (<75 m) the fine-grained, cohesive deposits are readily affected by storm waves and the cyclic loading imposed by these waves. Such loading brings about an increased pore pressure within the bottom sediments (BENNETT

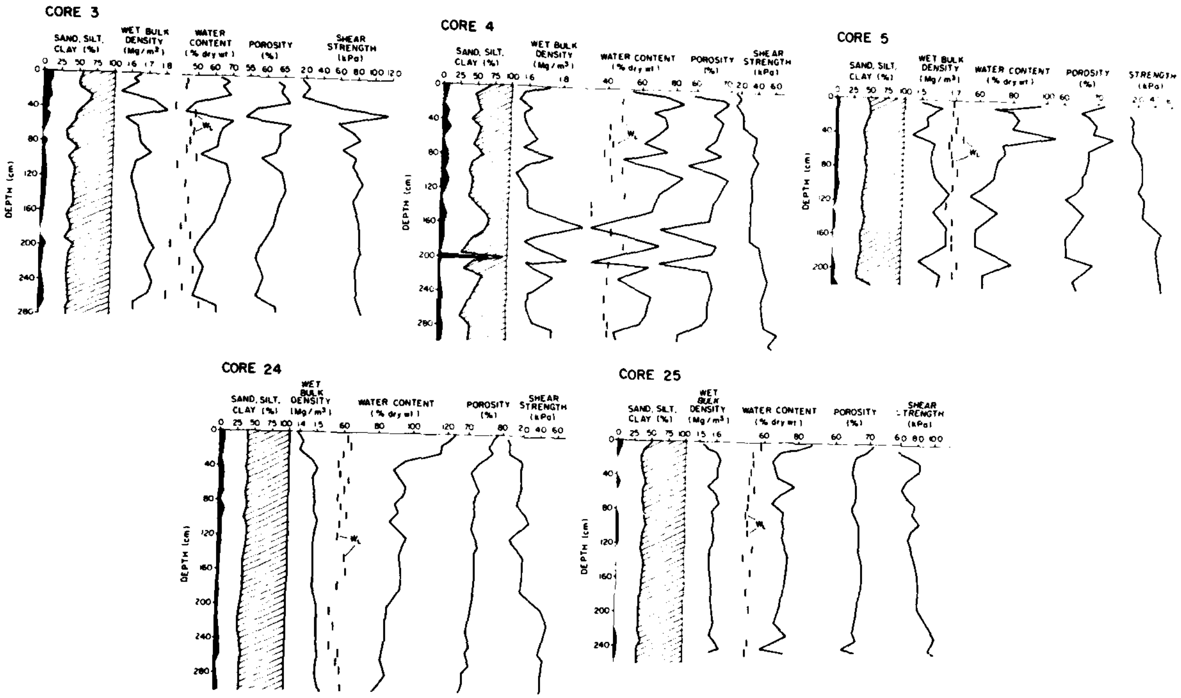

Fig. 8. Distribution of geotechnical properties with depth within the inner shelf deposits (cores 3, 4, 5, and 25) and in the midshelf mud deposit (core 24).

and FARIS, 1979; YAMAMOTO, 1981) which in turn results in sediment particle separation and disturbance to the sediment mass. In cohesive sediments such as those in the East China Sea where sensitivities are relatively high and water contents are greater than the liquid limit, disturbance to the sediment by cyclic loading may cause a significant loss of shear strength or cohesion (perhaps as much as 85%) that the sediment actually fluidizes. Such a change in state in the presence of strong bottom currents may be an important mode of bottom sediment transport along the western margin of the East China Sea. In the summer of 1981, STERNBERG *et al.* (1983) found from their *in situ* sediment transport experiment on the inner shelf that during peak tidal current flow the silty bottom material was resuspended and eroded. During the winter months when storm activity intensified resuspension and transport of the bottom deposits may be expected to increase considerably.

DISCUSSION AND CONCLUSION

Using representative samples from the cohesive shelf deposits of the East China Sea reveals a distinct difference in geotechnical properties between the innermost shelf deposits and those along the eastern margin of the study area (Table 1). Using Shephard's classification (SHEPARD, 1954) and the average textural properties of the upper 3 m, the inner and midshelf fine-grained deposits are classified as silty clays. Of the mass physical properties, the textural properties appear to display the least amount of variance between the two areas of fine-grained deposits. There does appear, however, to be a slightly higher concentration of silt in the inner shelf and relatively more clay-size material in the mud deposits in the northeast and eastern parts of the study area. Sand is present only in relatively small amounts in all mud deposits, averaging 1 to 5% for the 0- to 3-m interval (Table 1). A comparison of the inner and midshelf muds, however, indicates that there is slightly more sand present in the muds of the midshelf (Fig. 3A). Data shown in Table 1 appear to contradict the prior statement. Since core 24 (from the midshelf) is located nearly in the center of the mud deposits, it contains relatively little sand compared to other samples from this area. This slight difference in relative sand content may possibly be attributed to three factors: (a) a high dilution of the sands by the large concentrations of fines being deposited off the Changjiang, (b) the presence of sand surrounding the midshelf muds which then become mixed with the fines as a result of storm-wave and current activity, or (c) winnowing of the fines along the margin of the midshelf deposit.

Sediment wet bulk densities are considerably higher in the nearshore deposits, with average values for the cored interval ranging from 1.55 to 1.64 mg m^{-3}, whereas midshelf mud zone sediments display a much lower average wet bulk density (1.43 to 1.47 mg m^{-3}). Water content and porosity are, however, considerably higher in the offshore deposit, with average values of 111 and 72%, respectively; in contrast, the innermost shelf deposits possess average water contents of 64 to 81% and porosities ranging from 52 to 66% (Table 1). Average shear strengths for the cored interval are correspondingly higher in the innermost shelf deposits, as might be anticipated from the relatively high bulk densities and lower water contents found off the Changjiang.

Although additional samples and analyses are needed, available data indicate that the difference in the geotechnical properties might be attributed to the slightly greater concentration of coarser-grained material in the innermost shelf deposits relative to those of the midshelf muds. Thus, despite the relatively small textural differences between the two mud deposits, grain size appears to be distinct enough to influence the geotechnical properties.

Table 1. Geotechnical properties and range of values

Kasten core	Core length (cm)	Water depth (m)	Bulk density (mg m^{3})	Water content (% dry wt)	Porosity (%)	Shear strength (kPa)	% Sand	% Silt	% Clay	Texture
03	274	26								
Max			1.69	70	67	11.6	11	53	67	
Min			1.45	43	54	1.6	0	33	42	
Ave			1.64	64	62	9.8	5	40	56	Silty clay
04	294	16								
Max			1.77	85	70	7.0	11	61	68	
Min			1.53	50	47	1.4	0	30	32	
Ave			1.59	74	63	4.0	4	43	53	Silty clay
05	238	27								
Max			1.69	105	75	5.3	8	48	64	
Min			1.45	56	62	1.2	0	34	50	
Ave			1.55	81	66	4.0	2	41	57	Silty clay
25	248	33								
Max			1.64	88	71	10.4	5	45	68	
Min			1.52	60	65	5.8	0	30	50	
Ave			1.57	72	66	7.2	1	36	60	Silty clay
24	305	73								
Max			1.59	124	78	5.2	7	40	68	
Min			1.39	78	68	0.2	0	29	59	
Ave			1.43	111	72	1.5	3	34	63	Silty clay

Other factors such as mineralogy, organic carbon, and carbonate content also may contribute to the observed variations, but the available data are too limited to be conclusive.

The majority of the East China Sea is floored by relict sands (Niino and Emery, 1961). Along the innermost continental shelf and in an area on the midshelf centering around 32°00'N, 126°00'E, modern silty clays and clayey silts blanket the sands. Indications are that about half of the sediment load of the Changjiang is deposited in the immediate vicinity of its mouth (Milliman *et al.*, 1983). The remainder of the sediment appears to be transported to the south by the coastal currents (Beardsley *et al.*, 1983). Varying intensities in the coastal currents between the summer and winter seasons may result in limited transport of sediment to the northeast on occasion (Beardsley *et al.*, 1983). The predominant transport of these fine sediments is clearly to the south.

The large area of silty clay deposits along the eastern portion of the study area appears to be a finer grain version of the inner shelf deposits; however, evidence indicates that most of these sediments are derived from Huanghe deposits now exposed along the coast of the Yellow Sea rather than from the Changjiang (Yang and Milliman, 1983). This concept is supported by satellite images which reveal plumes of suspended sediment extending out from the vicinity of an ancient mouth of the Huanghe to the north of the Changjiang to the site of the present midshelf mud deposit (R. Limeburner, personal communication). Studies by Cai (1982) and Milliman *et al.* (1983) also report suspended sediment and low-salinity plumes extending southeasterly to the area of the midshelf mud deposit. The general circulation pattern of surface currents in the Yellow and East China Seas reveals the presence of a large current gyre over the midshelf to the east of Shanghai (Niino and Emery, 1961). Such a gyre undoubtedly serves to localize the suspended sediments coming from the northeast and thus accounts for the isolated deposit of fine-grained sediment found on the midshelf. The infrequent extensions of a Changjiang sediment plume to the northeast (Beardsley *et al.*, 1983) may result in some Changjiang sediments being incorporated into the midshelf mud deposit. These, however, are believed to be less important than the contribution from Huanghe coastal deposits along the western margin of the Yellow Sea.

Although the major portion of the sediment discharged into the East China Sea from the Changjiang bypasses the immediate shelf and is transported south along the coast, approximately 40% of this sediment can be accounted for in the fine-grained deposits of the inner shelf (DeMaster *et al.*, 1983). Strong evidence is found indicating that these deposits undergo resuspension and considerable erosion by strong bottom currents over time.

Acknowledgements—We wish to acknowledge the help provided to us during both the field and part of the laboratory work by Jorge Butenko. Funding support for the senior author from the National Oceanic and Atmospheric Administration and the Office of Naval Research under Contract N00014-79-C-0004 is gratefully acknowledged.

REFERENCES

Beardsley R. C., R. Limeburner, L. Kentage, H. Dunxin, G. A. Cannon and D. J. Pashinski (1983) Structure of the Changjiang river plume in the East China Sea during June 1980. In: *Proceedings of the International Symposium on Sedimentation on the Continental Shelf, with Special Reference to the East China Sea*, Vol. 1. L. Yuru, editor, China Ocean Press, pp. 265–284.

Bennett R. H. and J. Faris (1979) Ambient and dynamic pore pressures in fine-grained submarine sediments in the Mississippi Delta. *Applied Ocean Research*, 1, 115–123.

Bjerrum L. (1967) Progressive failure in slopes of overconsolidation plastic clay and clay shales. *Journal of Soil Mechanics and Foundations, Division of American Society of Civil Engineers*, 93, 1–49.

Butenko J., J. D. Milliman and Y.-c. Ye (1985) Geomorphology, shallow structure, and geological hazards in the East China Sea. *Continental Shelf Research*, **4**, 121–141.

Cai A. (1982) Diffusion of sediment of the Changjiang River discharging into the sea. *Acta Oceanologica Sinica*, **4**, 78–88.

Casagrande A. (1948) Classification and identification of soils. *American Society of Civil Engineers Transactions*, **113**, 901–931.

Chin Y. S. (1963) A preliminary study on the topography and bottom sediment types of the Chinese continental shelf. *Oceanologia et Limnologia Sinica*, **5**, 1.

Chin Y. S. (1979) A study on sediment and mineral compositions of the sea floor of the East China Sea. *Oceanic Selections*, **2**, 130–137.

DeMaster D. J., B. A. McKee, C. A. Nittrouer, J. Qian and G. Cheng (1983) Rates of sedimentary processes based on radiochemical profile from continental shelf deposits in the East China Sea. In: *Proceedings of the International Symposium on Sedimentation on the Continental Shelf, with Special Reference to the East China Sea*, Vol. 2, L. Yuru, editor, China Ocean Press, pp. 581–589.

Guo X. (1979) Sea level changes since Late Pleistocene in China. *Scientia Geologica Sinica*, **10**, 330–341.

Hamilton E. (1964) Consolidation characteristics and related properties of sediments from experimental Mohole (Guadalupe site). *Journal of Geophysical Research*, **69**, 4257–4269.

Keller G. H. and R. H. Bennett (1973) Sediment mass physical properties—Panama Basin and northeastern equatorial Pacific. In: *Initial reports of the deep sea drilling project*, Vol. 16, T. H. van Andel *et al.*, editors, U.S. Government Printing Office, Washington, D.C., pp. 499–512.

Kogler F. C. (1963) Das Kastenlot. *Meyniana*, **13**, 1–7.

Limeburner R., R. C. Beardsley and Z. Jinson (1983) Water mass and circulation in the East China Sea. In: *Proceedings of the International Symposium on Sedimentation on the Continental Shelf, with Special Reference to the East China Sea*, Vol. 1, L. Yuru, editor, China Ocean Press, pp. 285–294.

Lowe J. P., F. Zaccheo and H. S. Feldman (1964) Consolidation testing with back pressure. *Journal of Soil Mechanics and Foundations. Division of American Society of Civil Engineers*, **90**, 69–86.

McKee B. A., C. A. Nittrouer and D. J. DeMaster (1983) Concepts of sediment deposition and accumulation applied to the continental shelf near the mouth of the Yangtze River. In: *Proceeding of the International Symposium on Sedimentation on the Continental Shelf, with Special Reference to the East China Sea*, Vol. 2, L. Yuru, editor, China Ocean Press, pp. 631–633.

Milliman J. D. and R. H. Meade (1983) World-wide delivery of river sediment to the oceans. *Journal of Geology*, **91**, 1–21.

Milliman J. D., Y. Zuosheng and R. H. Meade (1983) Flux of suspended sediment in the Changjiang Estuary. *In: Proceedings of the International Symposium on Sedimentation on the Continental Shelf, with Special Reference to the East China Sea*, Vol. 1, L. Yuru, editor, China Ocean Press, pp. 413–430.

Ministry of Water Conservancy of the People's Republic of China (1956) *Operating rules for geotechnical analyses*. Water Conservancy Press, Peking, pp. 38–40.

Niino H. and K. O. Emery (1961) Sediments of shallow portions of the East China Sea and South China Sea. *Geological Society of America, Bulletin*, **72**, 731–762.

Ren M. O. and C. K. Tseng (1980) Later Quaternary continental shelf of East China. *Acta Oceanologia Sinica*, **2**, 1–9.

Richards A. F. (1962) Investigations of deep-sea sediment cores. II. Mass physical properties. Technical Report TR-63, Washington, D.C., U.S. Navy Hydrographic Office, 70 pp.

Richards A. F. and G. H. Keller (1961) A plastic-barrel sediment corer. *Deep-Sea Research*, **8**, 306–312.

Richards A. and E. Hamilton (1967) Investigations of deep-sea sediment cores. III. Consolidation. In: *Marine geotechnique*, A. F. Richards, editor, University of Illinois Press, Urbana, pp. 93–117.

Rosenqvist I. Th. (1953) Considerations on the sensitivity of Norwegian quick-clays. *Geotechnique*, **3**, 195–200.

Shepard F. P. (1954) Nomenclature based on sand–silt–clay ratios. *Journal of Sedimentary Petrology*, **24**, 151–158.

Shepard F. P., K. O. Emery and H. R. Gould (1949) Distribution of sediments on East Asiatic continental shelf: Allan Hancock Foundation. Occasional Paper 9, 64 pp.

Sibley E. A. and G. Yamane (1965) A simple shear test for saturated cohesive soils. Paper presented at Fifth Pacific Area National Meeting of the American Society of Testing Materials, Philadelphia, PA, 10 pp.

Sternberg R. W., L. H. Larsen and Y. T. Miao (1983) Near bottom flow conditions and associated sediment transport on the East China Sea continental shelf. In: *Proceedings of the International Symposium on Sedimentation on the Continental Shelf, with Special Reference to the East China Sea*, Vol. 2, L. Yuru, editor, China Ocean Press, pp. 522–535.

Terzaghi K. (1941) Undisturbed clay samples and undisturbed clays. *Journal of the Boston Society of Civil Engineers*, **28**, 211–231.

Terzaghi K. (1955) Influence of geological factors on the engineering porperties of sediments. *Economic Geology*, 50th Anniversary volume, 1905–1955, 557–618.

YAMAMOTO T. (1981) Wave-induced pore pressures and effective stresses in inhomogeneous seabed foundations. *Ocean Engineering*, **8**, 1–16.

YANG Z. S. and J. D. MILLIMAN (1983) Fine-grained sediments of Changjiang and Huangho Rivers and sediment sources of the East China Sea. In: *Proceedings of the International Symposium on Sedimentation on the Continental Shelf, with Special Reference to the East China Sea*, Vol. 1, L. YURU, editor, China Ocean Press, pp. 436–446.

Eos, Vol. 66, No. 6, Page 52, February 5, 1985

Some Personal Observations on the Status of Marine Sciences in the People's Republic of China

Chen-Tung A. Chen

Owing to the long hiatus in communication with the People's Republic of China (PRC) during the Cultural Revolution and the inability of most westerners to read the original Chinese literature, a great deal of marine science research in PRC is not known to the outside world. I have felt that progress in marine science in general could be accelerated with better awareness of the existence of a large Chinese data base. Also, duplication of efforts caused by lags in communication could be averted if a review of the status of marine science research in PRC were available.

At the invitation of Shandong College of Oceanography in April 1983, I visited eight oceanographic institutions in PRC for a month with the primary goal of ensuring a thorough and efficient acquisition of marine chemistry publications, particularly items published in the "gray literature." A report "Marine Chemistry in the People's Republic of China" with extensive bibliography has been prepared for the Office of Naval Research (ONR) (C.-T. A. Chen, Marine Chemistry in the People's Republic of China, *Doc. 454 158 19338*, U. S. Government Printing Office, Washington, D. C., 1984), and a limited number of copies are available from the author. In the following report, I give only my impressions of oceanographic research in PRC obtained from my site visit and from my conversations with visiting PRC marine chemists in America. I must point out at once, however, that exceptions to my description, given below, certainly exist.

Marine Scientific and Technological Information

Scientific and technological information is flowing relatively freely in PRC, albeit at a slow pace and with certain restrictions. I will discuss the availability of scientific information in three categories.

Exchange of Information Within PRC

Every major research or teaching institute seems to publish at least one technical journal that is widely distributed in PRC. All institutes have their own libraries, and the current publications are displayed. Researchers can check out only a limited amount of material. Copying machines are all but unavailable and expensive to use; there are also few microfilm readers, and no national computer data base. IBM 1620–type computers are used in several of the oceanographic centers. Most tasks are still performed manually. For instance, monthly hand-written tidal tables from 51 ocean stations are tabulated and plotted by hand at the Institute of Marine Scientific and Technological Information A Chinese-made computer is available there (which uses paper tape), but a modern minicomputer is being imported. Understandably, printed hard copy is normally used to transmit numerical data. Nationwide technical meetings, where researchers exchange information freely, are held frequently.

Information Flow Into PRC

Major foreign oceanographic journals are available in all oceanographic institutions. Most of the journals are reproduced in Beijing and later distributed, with a delay of 8 to 18 months. Reports published by foreign institutions are available through exchange. There is a large number of Russian publications, but Japanese and English publications seem to be expanding at a faster rate. In order to improve the information flow, many foreign scientists visit and lecture at the PRC oceanographic institutions. Foreign visitors are generally treated exceedingly well.

Information Flow Out of PRC

This is the area that has received the most restrictions. The policy of PRC, apparently, is to classify all information unless specifically unclassified. For example, very few journals published in Chinese before 1980 can be taken out. There are signs, however, that information is beginning to flow out of PRC more freely. Several journals changed names in 1982. These "new" journals are not classified, whereas the "old" ones were. The China National Publishing Industry Trading Corporation, which is in charge of exporting PRC publications, accepts orders for some marine science publications.

A data center similar to the National Oceanographic Data Center (NODC) (see *Eos*, May 4, 1982, p. 275) is being established, with NODC's assistance, in the Institute of Marine Scientific and Technological Information, National Bureau of Oceanography (NBO), in Tianjin. The institute collects, processes, stores, and provides marine scientific and technological information and data from PRC and abroad. It also functions as an International Oceanographic Committee depository center and exchanges a limited amount of information with NODC. U.S. scientists attempting to gain access to Chinese data and results will have a better chance if they send their requests through official channels.

Instrumentation

The use of advanced instrumentation is now widespread. The Chinese manufacture various spectrophotometers, anodic stripping voltimeters, and mass spectrometers. Development of marine instruments and equipment is carried out at essentially all marine research and teaching institutions. These efforts seem to be focused on instruments such as *p*H meters. Chinese-made versions of large instruments such as autoanalyzers and spectrophotometers are available, but the higher-priced major instruments are mainly purchased from Japan and western countries. Procurement of foreign items receives much review. All approved requests are finally funneled through a central Instruments Import and Export Corporation. It takes 2–3 years to receive an item after a successful request. Passage of the patent law in 1984 may open the way for licensing or joint production with foreign manufacturers of state-of-the-art equipment.

Ship Operations

PRC has an oceanographic research and survey fleet of 150 vessels totaling over 100,000 tons. Some are quite large, with several exceeding 3000 tons. Until recently, the ships have been operating in coastal and continental shelf regions, as even the large ships sometimes do not yet have deep-water sampling capability. On-board instrumentation is scarce, but laboratory space is ample. Shandong College of Oceanography's 2740-ton *East is Red* even has a lecture hall which seats at least 50. Some recent geophysical survey vessels are equipped with state-of-the-art instrumentation, perhaps reflecting PRC's strong emphasis on offshore exploration for petroleum. The three subbureaus of the NBO operate the NBO ships, whereas the Academia Sinica and the Ministry of Education ships are run by the institutions that own them.

Surveys

China maintains long records of coastal salinity data, some dating back more than 100 years. Continuous water chemistry data for the Huanghe ("Yellow River"), in Jiaozhou Wan (Bay), and in the Changjiang ("Yangtze") estuary date back several decades. Most of the ocean surveys have been performed in the PRC territorial waters. PRC, however, has started to make routine surveys in the Taiwan Strait, which until recently was totally controlled by the Republic of China on Taiwan.

Deep ocean surveys began only recently. Early blue water measurements were all part of international multiship programs. The first single-ship expedition was carried out by the PRC-built 4000-ton R/V *Xiangyanghong 16* in the Western Pacific (7–13°N, 167–178°W) between May 7 and July 10, 1983. Manganese modules were recovered from depths of 5000 m.

Research on and around Antarctica has recently begun. Initial efforts were in collaboration with Australian and New Zealand scientists and concentrated on marine biological studies and living resources. PRC achieved a form of observer status under the 1959 Antarctic Treaty in June 1983, and it plans to send a 14,000-T research vessel (R/V *Xiangyanghong 10*) on a circum-Antarctic expedition between December 1984 and March 1985.

Funding for Research

Most research is supported by block operational funding to the institutions, which in turn provide "hard" salary and research funding internally to the staff. Research money competes internally with all other expenses, such as salaries, building and maintenance, ship operation, etc. A selected few obtain research funding from the Academia Sinica Science Fund. More money per grant is available from this source, but competition is strong. A small amount of money is provided to a faculty member for research if he has graduate students under his guidance. All research topics must be approved by the Office of Scientific Research at each institution.

0096–3941/85/6606–0049$01.00

Serving the needs of the people carries a lot of weight in regard to whether a research topic is approved.

Students

Formal college entrance examinations resumed in 1977, after the Cultural Revolution. The first group of students entered in early 1978 and graduated in early 1982. Students (20% female) are highly motivated: they must be younger than 30 years old, are not allowed to marry while in school, and must live in dormitories. They receive free room and board plus stipends.

Both teaching and research institutions admit graduate students, but only Shandong College of Oceanography, the Department of Oceanography of Xiamen University, the Institute of Estuarine and Coastal Research (East China Normal University), and the Institute of Oceanology currently have oceanography graduate students. The three institutes of NBO may soon admit graduate students too.

Study in Foreign Countries

Most of the marine scientists at the professorial level in PRC received advanced education from western countries before 1950. Since the end of the Cultural Revolution, researchers are again allowed to study abroad (mostly on PRC fellowships).

Initially, only faculty members went abroad, because the first class of college students for over a decade did not graduate until 1982. Generally speaking, faculty members or research scientists who go abroad are expected to learn a selected research topic and transfer the knowledge back quickly in order to fill an existing gap. On the other hand, the cream of recent college graduates are sent abroad (on 1-year PRC fellowships) to receive a more balanced training and to earn an advanced degree.

Competition for fellowships is fierce (about 10% of the faculty have been sent abroad). After passing tests and other considerations, those who would stay abroad for a year or longer, faculty and students alike, are sent to foreign language institutes for 6 months of intensive language training.

International Collaborative Field Program

The scientists and administrators to whom I talked all agreed that international collaborative programs are beneficial to all parties concerned. They appreciate that joint field programs would greatly accelerate their transition from a laboratory-confined marine sciences program to a balanced laboratory and field oceanographic program. It is clear that possibilities of substantive collaborative research do exist, but lengthy discussion must be expected. Agreement to transfer advanced technology, especially instrumentation, during and after the completion of a collaborative program would be most welcome. As a possible aid to such exchanges, it should be noted that the United Nations Development Program has had an office in Beijing since 1979 and is offering assistance to international collaborative programs.

Chen-Tung A. Chen *is with the College of Oceanography, Oregon State University, Corvallis.*

reprinted from EOS
with permission from
AGU

Perspective:

Personal Observations on the Status of Marine Sciences in the People's Republic of China

Chen-Tung A. Chen

Owing to the long hiatus in communication with the People's Republic of China (PRC) during the Cultural Revolution and the inability of most westerners to read the original Chinese literature, a great deal of marine science research in PRC is not known to the outside world. I have felt that progress in marine science in general could be accelerated with better awareness of the existence of a large Chinese data base. Also, duplication of efforts caused by lags in communication could be averted if a review of the status of marine science research in PRC were available.

At the invitation of Shandong College of Oceanography in April 1983, I visited eight oceanographic institutions in PRC for a month, with the primary goal of ensuring a thorough and efficient acquisition of marine chemistry publications, particularly items published in the "gray literature." A report "Marine Chemistry in the People's Republic of China" with extensive bibliography has been prepared for the Office of Naval Research (ONR) (C.-T. A. Chen, Marine Chamistry in the People's Republic of China, *Doc. 454 158 19338,* U.S. Government Printing Office, Washington, D.C., 1984), and a limited number of copies are available from the author. In the following report, I give only my impressions of oceanographic research in PRC obtained from my site visit and from my conversations with visiting PRC marine chemists in America. I must point out at once, however, that exceptions to my description, given below, certainly exist.

MARINE SCIENTIFIC AND TECHNOLOGICAL INFORMATION

Scientific and technological information is flowing relatively freely in PRC, albeit at a slow pace and with certain restrictions. I will discuss the availability of scientific information in three categories.

Exchange of Information Within PRC

Every major research or teaching institute seems to publish at least one technical journal that is widely distributed in PRC. All institutes have their own libraries, and the current publications are displayed. Researchers can check out only a limited amount of material. Copying machines are all but unavailable and expensive to use; there are also few microfilm readers, and no national computer data base. IBM 1620-type computers are used in several of the oceanographic centers. Most tasks are still performed manually. For instance, monthly hand-written tidal tables from 51 ocean stations are tabulated and plotted by hand at the Institute of Marine Scientific and Technological Information. A Chinese-made computer that uses paper tape is available there, but a modern minicomputer is being imported. Understandably, printed hard copy is normally used to transmit numerical data. Nationwide technical meetings, where researchers exchange information freely, are held frequently.

Information Flow Into PRC

Major foreign oceanographic journals are available in all oceanographic institutions. Most of the journals are reproduced in Beijing and later distributed, with a delay of 8 to 18 months. Reports published by foreign institutions are available through exchange. There is a large number of Russian publications, but Japanese and English publications seem to be expanding at a faster rate. In order to improve the information flow, many foreign scientists visit and lecture at the PRC oceanographic institutions. Foreign visitors are generally treated exceedingly well.

Information Flow Out of PRC

This is the area that has received the most restrictions. The policy of PRC, apparently, is to classify all information unless specifically unclassified. For example, very few journals published in Chinese before 1980 can be taken out. There are signs, however, that information is beginning to flow out of PRC more freely. Several journals changed names in 1982. These "new" journals are not classified, whereas the "old" ones were. The China National Publishing Industry Trading Corporation, which is in charge of exporting PRC publications, accepts orders for some marine science publications.

A data center similar to the National Oceanographic Data Center (NODC) (*See Eos*, May 4, 1982, p. 275) is being established, with NODC's assistance, in the Institute of Marine Scientific and Technological Information, National Bureau of Oceanography (NBO), in Tianjin. The institute collects, processes, stores and provides marine scientific and technological information and data from PRC and abroad. It also functions as an International Oceanographic Committee depository center and exchanges a limited amount of information with NODC. U.S. scientists attempting to gain access to Chinese data and results will have a better chance if they send their requests through official channels.

INSTRUMENTATION

The use of advanced instrumentation is now widespread. The Chinese manufacture various spectrophotometers, anodic stripping voltmeters and mass spectrometers. Development of marine instruments and equipment is carried out at essentially all marine research and teaching institutions. These efforts seem to be focused on instruments such as *p*H meters. Chinese-made versions of large instruments such as autoanalyzers and spectrophotometers are available, but the higher-priced major instruments are mainly purchased from Japan and western countries. Procurement of foreign items receives much review. All approved requests are finally funneled through a central Instruments Import and Export Corporation. It takes 2-3 years to receive an item after a successful request. Passage of the patent law in 1984 may open the way for licensing or joint production with foreign manufacturers of state-of-the-art equipment.

SHIP OPERATIONS

PRC has an oceanographic research and survey fleet of 150 vessels totaling over 100,000 tons. Some are quite large, with several exceeding 3,000 tons. Until recently, the ships have been operating in coastal and continental shelf regions, as even the large ships sometimes do not yet have deep-water sampling capability. On-board instrumentation is scarce, but laboratory space is ample. Shandong College of Oceanography's 2,740-ton *East is Red* even has a lecture hall which seats at least 50. Some recent geophysical survey vessels are equipped with state-of-the-art instrumentation, perhaps reflecting PRC's strong emphasis on offshore exploration for petroleum. The three sub-bureaus of the NBO operate the NBO ships, whereas the Academia Sinica and the Ministry of Education ships are run by the institutions that own them.

SURVEYS

China maintains long records of coastal salinity data, some dating back more than 100 years. Continuous water chemistry data for the Huanghe ("Yellow River"), in Jiaozhou Wan (Bay), and in the Changjiang ("Yangtze") estuary date back several decades. Most of the ocean surveys have been performed in the PRC territorial waters. PRC, however, has started to make routine surveys in the Taiwan Strait, which, until recently, was totally controlled by the Republic of China on Taiwan.

Deep ocean surveys began only recently. Early blue water measurements were all part of international multiship programs. The first single-ship expedition was carried out by the PRC-built 4,000-ton R/V *Xiangyanghong 16* in the Western Pacific (7-13°N, 167-178°W) between May 7 and July 10, 1983, Manganese modules were recovered from depths of 5,000 m.

Research on and around Antarctica has recently begun. Initial efforts were in collaboration with Australian and New Zealand scientists and concentrated on marine biological studies and living resources. PRC achieved a form of observer status under the 1959 Antarctic Treaty in June 1983, and it plans to send a 14,000-T research vessel (R/V *Xiangyanghong 10*) on a circum-Antarctic expedition between December 1984 and March 1985.

FUNDING FOR RESEARCH

Most research is supported by block operational funding to the institutions, which in turn provide "hard" salary and research funding internally to the staff. Research money competes internally with all other expenses, such as salaries, building and maintenance, ship operation, etc. A selected few obtain research funding from the Academia Sinica Science Fund. More money per grant is available from this source, but competition is strong. A small amount of money is provided to a faculty member for research if he has graduate students under his guidance. All research topics must be approved by the Office of Scientific Research at each institution. Serving the needs of the people carries a lot of weight in regard to whether a research topic is approved.

STUDENTS

Formal college entrance examinations resumed in 1977, after the Cultural Revolution. The first group of students entered in early 1978 and graduated in early 1982. Students (20% female) are highly motivated: they must be younger than 30 years old, are not allowed to marry while in school and must live in dormitories. They receive free room and board, plus stipends.

Both teaching and research institutions admit graduate students, but only Shandong College of Oceanography, the Department of Oceanography of Xiamen University, the Institute of Estuarine and Coastal Research (East China Normal University), and the Institute of Oceanology currently have oceanography graduate students. The three institutes of NBO may soon admit graduate students too.

STUDY IN FOREIGN COUNTRIES

Most of the marine scientists at the professorial level in PRC received advanced education from western countries before 1950. Since the end of the Cultural Revolution, researchers are again allowed to study abroad (mostly on PRC fellowships).

Initially, only faculty members went abroad, because the first class of college students for over a decade did not graduate until 1982. Generally speaking, faculty members or research scientists who go abroad are expected to learn a selected research topic and transfer the knowledge back quickly in order to fill an existing gap. On the other hand, the cream of recent college graduates are sent abroad (on 1-year PRC fellowships) to receive a more balanced training and to earn an advanced degree.

Competition for fellowships is fierce (about 10% of the faculty have been sent abroad). After passing tests and other considerations, those who would stay abroad for a year or longer, faculty and students alike, are sent to foreign language institutes for 6 months of intensive language training.

INTERNATIONAL COLLABORATIVE FIELD PROGRAM

The scientists and administrators to whom I talked all agreed that international collaborative programs are beneficial to all parties concerned. They appreciate that joint field programs would greatly accelerate their transition from a laboratory-confined marine sciences program to a balanced laboratory and field oceanographic program. It is clear that possibilities of substantive collaborative research do exist, but lengthy discussion must be expected. Agreement to transfer advanced technology, especially instrumentation, during and after the completion of a collaborative program would be most welcome. As a possible aid to such exchanges, it should be noted that the United Nations Development Program has had an office in Beijing since 1979 and is offering assistance to international collaborative programs.

Chen-Tung A. Chen is with the College of Oceanography, Oregon State University, Corvallis, Oregon. His article is reprinted from Eos, *Vol. 66, No. 6, a publication of the American Geophysical Union.*

Bulletin of the Seismological Society of America, Vol. 75, No. 5, pp. 1383-1393, October 1985

LABORATORY TEST OF APPARENT ATTENUATION FORMULAS

BY WILLIAM MENKE, DEAN WITTE, AND ROLIN CHEN

ABSTRACT

We measure the apparent attenuation of *P* waves propagating through a three-dimensional scattering medium (a three-dimensional aluminum block containing a random assemblage of cylindrical voids). The observed apparent attenuation is compared to that predicted by a single scattering approximation. At low frequencies, both the amount of attenuation and its variation with frequency are well predicted. At intermediate and high frequencies, the agreement is poorer. Observed phase shifts are very different from those predicted by the Kramers-Krönig relations.

INTRODUCTION

Apparent attenuation is the diminution in amplitude of a semismic wave caused by the scattering of energy from the wave front by heterogeneities in the medium of propagation (O'Doherty and Anstey, 1971). The mechanism of apparent attenuation is very different from the mechanism of intrinsic attenuation. In the intrinsic attenuation case, energy is removed from the wave field by frictional absorption. In the apparent attenuation case, the energy is only redistributed between different parts of the wave field. Nevertheless, in practice, both these mechanisms cause a propagating wave to lose amplitude and are therefore difficult to descriminate.

There are two general methods that have been proposed to distinguish between these two attenuation mechanisms. One method relies on the fact that energy is only redistributed in the apparent attenuation case and can potentially be observed later in the seismogram or at different observation points. Thus, for example, waves that have strong coda should tend to have strong apparent attenuation. Studies of coda can therefore potentially quantify the amount of apparent attenuation (see, e.g., Gao *et al.*, 1983). If, indeed, the problem were only to descriminate cases where apparent or intrinsic attenuation were exclusively involved, this method would be very easy to apply. Unfortunately, most realistic cases involve some combination of the two cases. Any intrinsic attenuation will tend to suppress the coda, since it consists of waves with relatively long pathlengths (Richards and Menke, 1983).

The second method relies on the fact that, at least at low frequencies, apparent attenuation should be very strongly frequency dependent, while intrinsic attenuation should be less so. As is well known, intrinsic attenuation can often be described by a frequency independent quality factor, Q. On the other hand, when the wavelength of the seismic waves is larger than the size of the scatterers, the energy scattered from a single scatterer is a strong function of frequency. If there is not too much interaction between scatterers, then at long wavelengths the apparent Q has a simple frequency dependence, which can be shown to be $Q(f) \sim f^{-n}$, where f is frequency and n is the dimensionality of the scatterers (i.e., $n = 1$ for thin layers, $n = 2$ for cylinders, and $n = 3$ for spheres; Menke, 1984). At intermediate frequencies, when the wavelength is on the order of the scatterer size, the scattering can be particularly strong, hence the apparent Q should have a minimum at these frequencies. At higher frequenciess, wave propagation can be described by simple geometrical optics, hence $Q(f) \sim f$ (Dainty, 1981). The practical difficulty in applying this method is in properly accounting for the frequency dependence of the seismic source, which affects the frequency dependence of the observed waves as much as does the attenuation

The efficacy of this second method ultimately depends upon the ability to predict the apparent attenuation expected from any given heterogeneous medium. This subject is still an area of active research and has two outstanding problems. The first concerns precisely what is meant by apparent attenuation. Much of the mathematical theory of scattering in random media concerns the properties of ensemble averages of seismograms. On the other hand, what seismologists observe is not ensemble averages but individual seismograms. The apparent attenuation of an ensemble average need not equal the apparent attenuation of the individual seismograms in the ensemble (see, e.g., Wu, 1982). (Consider, for example, a set of media which are homogeneous but have randomly chosen velocities. Since each medium is homogeneous, each individual seismogram experiences no apparent attenuation. Nevertheless, the ensemble average is attenuated, since it consists of a sum of waves with different arrival times which can therefore destructively interfere with one another.) The second problem concerns the effect of multiple scattering. Energy that is scattered out of a propagating wave can later be scattered back in by subsequent scattering interactions. This effect, which is very difficult to treat theoretically, becomes very important in strongly heterogeneous media. Theoretical treatments of apparent attenuation have ranges from very approximate treatments that ignore some of these problems (e.g., Wu, 1982), to very complicated ones that try to include them (e.g., Varadan *et al.*, 1983).

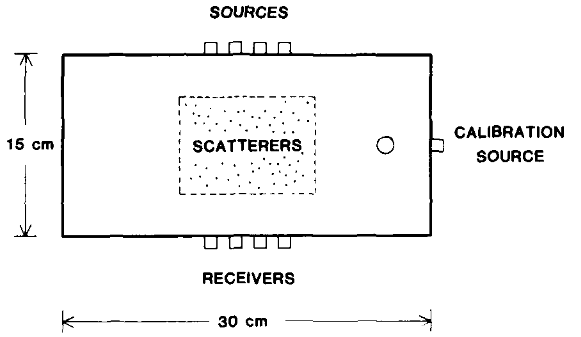

FIG. 1. Schematic of model used in experiments. The aluminium block measures 15 × 30 × 3.75 cm. The effect of the scatterers (a random assemblage of parallel cylindrical voids) on the transmitted P wave was measured using ultrasonic transducers as sources and receivers. In some experiments, a calibration source and reflecting hole were positioned at the edge of the model. Measurements of the amplitude of the calibration transducer, as measured by the other sources and receivers, were used to control relative amplitudes.

In this paper we use laboratory measurements of apparent attenuation in scattering media with known heterogeneities to test some of these predictions of apparent attenuation. In particular, we are interested in the simplest class of theories, typified by the work of Wu (1982), which ignore multiple scattering. These theories have the advantage of being analytical and of yielding relatively simple formulas for the apparent attenuation. Furthermore, they are applicable to individual seismograms as well as ensemble averages. The relevant question is whether or not they can adequately predict the processes that are occurring, or whether recourse to some more complicated, possibly numerical, theory is necessary.

EXPERIMENT DESIGN

Our approach is to record a P wave that has passed through a three-dimensional aluminium block, before and after heterogeneities are placed in the block (Figure 1). The heterogeneities are parallel cylindrical voids that pass through the entire thickness of the model, thus the scatterer distribution is two-dimensional, even though the model is three-dimensional. We examine several different ratios between scatterer radius, A, and seismic wavelength, λ, including the Rayleigh scattering limit ($A \ll \lambda$) and the geometrical optics limit ($A \gg \lambda$). Since we are comparing the homogeneous and the scattering cases, the effect of the source function is completely eliminated, and the effect of the material's intrinsic attenuation ($Q_{intrinsic} \approx 100$) is greatly reduced. The sources and receivers are Panametrics M110 piezoelectric crystals that produce highly reproducible pulses in the megaHertz band, and the recordings are made with a digital oscilloscope with about 12 bits of effective resolution. The only complication that arises with this experimental configuration is that P waves reflected from the sides of the model can interfere with the direct P wave. At high frequencies, these secondary arrivals are distinct and can be edited from the signal. It is only at low frequencies that they pose a problem. However,

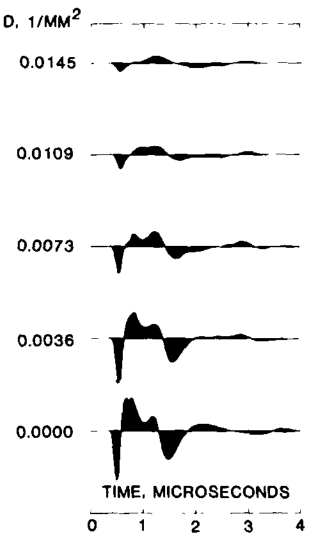

FIG. 2. P-wave seismograms derived from the model of Figure 1 with void radius $A = 0.66$ mm and various scatterer densities, D. The relative amplitude between these seismograms is accurate to within about 10 per cent. Note that the attenuation increases as the density of scatterer per unit area, D increases. A concentration of $D = 0.0145$ mm^{-2} corresponds to 200 voids in the model, or a volume fraction of 2.0 per cent. Each of these seismograms is an average of four measurements made a small distance apart on the model. This ensemble averaging tends to reduce the coda, making the apparent attenuation more visible.

since they are present in both the homogeneous and scattering case, we expect that they will not significantly change our measurements of the apparent attenuation even at low frequencies.

The theory to which we compare our results is due to Wu (1982). This approximate theory computes the apparent attenuation by the single scattering approximation. Any energy that is scattered in a direction outside a small cone centered about the propagation direction is assumed lost. The effect of many scatterers is computed by multiplying the effect of single scatterers. Apart from the single scattering approximation, the most important simplification comes in deciding what scattered energy is lost from the wave, i.e., the size of the cone (measured, say, by its angle Ω). Wu chooses an $\Omega = 90°$ cone, assuming only backscattered energy is lost. This approximation ignores the fact that the forward-scattered energy need not add to the incident wave. Under some circumstances it might destructively interfere with it. We therefore also compute the result of an $\Omega = 0°$ cone, for comparison. Finally, our treatment differs from Wu's in that he uses the Born approximation to calculate the scattered energy, while we, recognizing that the Born approximation will not work well for cylindrical voids, use the exact expressions given by Mow and Pao (1971).

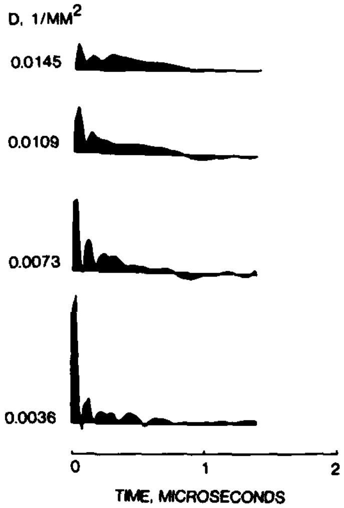

FIG. 3. Empirical attenuation operators derived by finding the damped least-squares filter that when convolved with the unattenuated seismogram of Figure 2 yields the attenuated seismogram. Note that as the concentration of voids, D, increases, the overall width of the attenuation operators increases. The high-frequency (~5 MHz) oscillations in the operators are an artifact of a narrow high-frequency peak in the source spectrum.

LONG WAVELENGTH SCATTERING

In our first set of experiments, we examine the effect of a random set of cylindrical voids (all with the same radius, A and with axes parallel to one another and perpendicular to the propagation direction). The wavelength is in the range of 6 to 30 mm, compared to a scatterer diameter of 1.3 mm. In these experiments, the absolute amplitude of the waves was preserved to within about 10 per cent.

Measurement of waves transmitted through the scattering medium are then analyzed for evidence of apparent attenuation. We are interested in the attenuation of the leading pulse of the signal (which is deterministic), rather than the coda (which randomly oscillates). We therefore average the signals for several paths. While we could, in principle, remove the coda completely by averaging sufficient number of paths, practical considerations limit us to only a few paths (four). The coda is therefore not completely suppressed and we must taper it from the signal manually. While this procedure is *ad hoc*, it leads to only a few per cent changes in the spectral amplitudes.

As the density of voids, D is increased, the amplitude of the transmitted P wave rapidly diminishes (Figure 2). The amplitude is reduced by a factor of 5 by a volume fraction of voids of about 2 per cent. The pulse width also increases, as can be seen by computing empirical attenuation operators (Figure 3). The spectra of these signals, computed after tapering the coda from the direct pulse, clearly exhibits a frequency-dependent attenuation (Figure 4). Spectral ratios of the attenuated signals with the unscattered wave demonstrate that the attenuation increases rapidly with frequency, and have the correct sense of curvature. As mentioned above, $Q(f) \sim f^{-2}$ for cylindrical scatterers, so the log-spectral ratio should be proportional to f^3. Least-squares fits of polynomials to these data (not shown) indicate that a cubic fits the data much better than either a quadratic or quartic. Theoretical predictions of the apparent attenuation, based on Wu's theory with $\Omega = 0°$ and $\Omega = 90°$ are shown in Figure 5. The $\Omega = 90°$ agree best with the data. Although only one of the four observed curves exhibits the leveling off of the attenuation predicted at high frequencies, this effect can be attributed to the poor signal-to-noise ratio at the edge of the source spectrum.

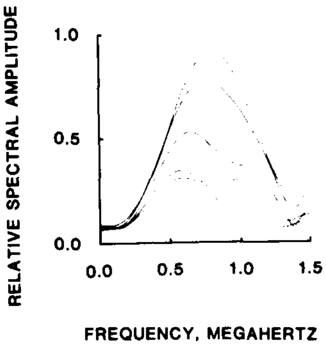

FIG. 4. Spectra for the P waves in Figure 2, after their coda has been removed by tapering after about 1 μsec from the first arrival.

The attenuation also increases as the diameter of the voids are increased slightly to 1.5 mm (Figures 6 to 8). Once again, the theoretical curves for $\Omega = 90°$ fit the

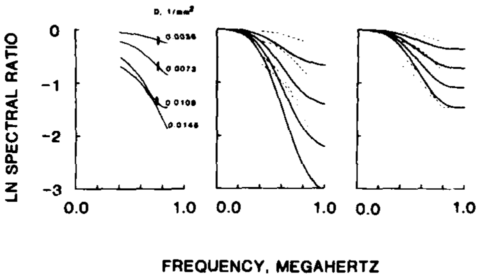

FIG. 5. (*Left*) Spectral ratios of the attenuated signals of Figures 2 and 3, referenced to the unattenuated signal. Relative amplitudes were measured to within about 10 per cent accuracy, so each curve can be moved vertically by as much as the vertical error bar. Note that the attenuation increases strongly with both frequency and density of scatterers, D. These frequencies correspond to wavelengths smaller than the scatterer size. (*Middle*) Comparison of the observed spectral ratios (dashed) with the predictions of the single scattering theory with scattering angle of $\Omega = 0°$. (*Right*) Comparison with theory when $\Omega = 90°$.

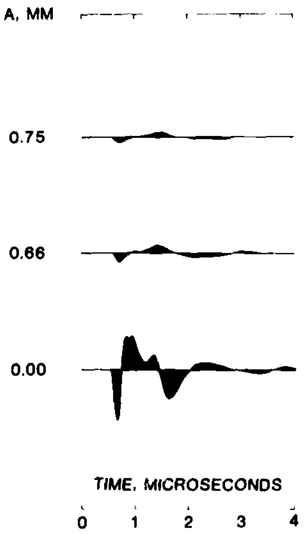

FIG. 6. P-wave seismograms derived from the model of Figure 1 with scatterer density $D = 0.0145$ mm^{-1} and varying void radius A. Note that the attenuation increases as the scatterer size increases. Each of these seismograms is an average of four measurements made a small distance apart on the model. The relative amplitude between the seismograms is correct to within about 10 per cent.

data best, and the predicted leveling of the attenuation at high frequencies is not observed.

SCATTERING AT HIGHER FREQUENCIES

At high frequencies, the scattering can be analyzed purely in terms of geometrical ray theory. Each of the cylindrical voids blocks part of the propagating energy, so the attenuation at high frequencies is independent of frequency (and hence, $Q \propto f$). We performed a second set of experiments, with a high-frequency source, to observe the scattering in this frequency range (Figures 9 and 10). Through the use of a calibration transducer (see Figure 1), we are able to measure amplitudes to within about 1 per cent. The spectral ratio of the attenuated to unattenuated wave does show a flattening at high frequencies, although it tends to oscillate about a mean value (an effect that might be due to interference from the early part of the coda).

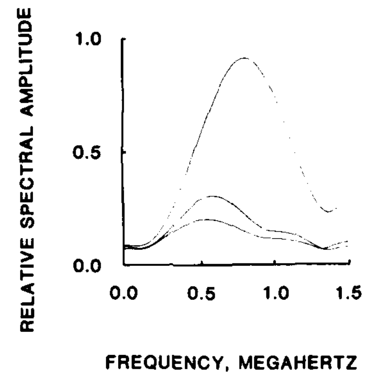

FIG. 7. Spectra for the P waves in Figure 5, after their coda has been removed by tapering after about 1 μsec from the first arrival.

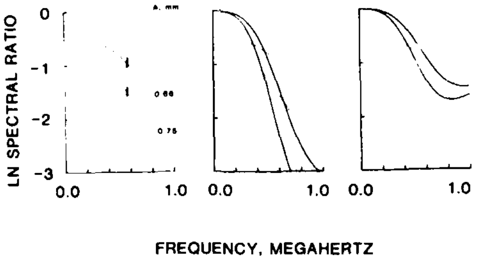

FIG. 8. (*Left*) Spectral ratios of the attenuated signals of Figures 5 and 6, references to the unattenuated signal. Relative amplitudes were measured to within about 10 per cent accuracy, so each curve can be moved vertically by as much as the vertical error bar. Note that the attenuation increases strongly with both frequency and radius of scatterers, A. These frequencies correspond to wavelengths smaller than the scatterer size. (*Middle*) Comparison of the observed spectral ratios (dashed) with the predictions of the single scattering theory with scattering angle of $\Omega = 0°$. (*Right*) Comparison with theory when $\Omega = 90°$.

At high frequencies, the $\Omega = 0°$ predicted curve seems to fit the data better than the $\Omega = 90°$ curve (Figure 11). However, we feel that this is a fortuitous result caused by two approximations in the theory happening to cancel out this particular case: the theory underestimates the effect of the shadows from the cylindrical voids, since the single scattering approximation cannot represent the fact that above some critical density of voids, 100 per cent of the incident wave is shadowed. On the other hand, the theory, in ignoring the phase of the scattered waves by dealing only with energy, overestimates the energy scattered from a single void by a factor of two (it counts the energy scattered into the shadow, which in fact is completely canceled out by the incident wave). We feel that in cases where the scatterers have less impedance contrast with the surrounding material than the voids we are using, the $\Omega = 90°$ may well produce the better fit. This conclusion is in agreement with the results from the low-frequency experiments, in which shadowing and phase effects are unimportant.

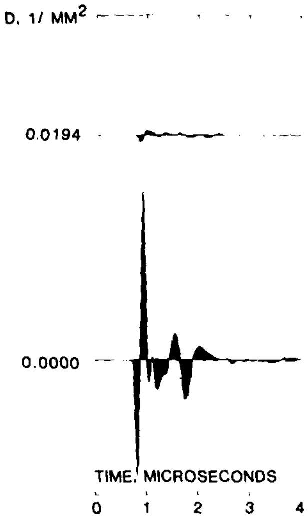

FIG. 9. *P*-wave seismograms made with a higher frequency source than previous experiments and using a calibration transducer that enabled measurements of relative amplitude to within 1 per cent. The void diameter was kept constant at $A = 0.66$ mm and the density of voids, D, was varied.

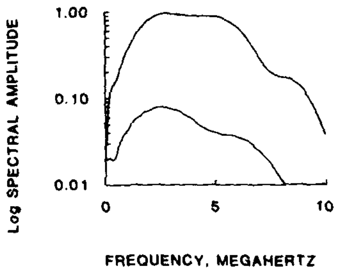

FIG. 10. Spectra of the seismograms in Figure 8.

PHASE SHIFTS DUE TO SCATTERING

The presence of scatterers affects not only the amplitude, but also the phase of the seismic waves (Figure 12). These two effects are related by causality (see, e.g., Banik *et al.*, 1985). Energy can propagate from source to receiver no faster than by the fastest ray connecting source to receiver. The Kramers-Krönig relationship shows that the phase velocity, $c(f)$ is related to the quality factor $Q(f)$ by $c^{-1}(f) - c^{-1}_{\infty} = H[\frac{1}{2}c^{-1}(f)Q^{-1}(f)]$, where c_{∞} is a reference velocity, and H is the Hilbert transform (see, e.g., Aki and Richards, chapter 5, 1980). Since the Hilbert transform contains an integral over all frequencies, measurements of phase in a given frequency band contain different information about the scattering than measurements of the attenuation in that band alone.

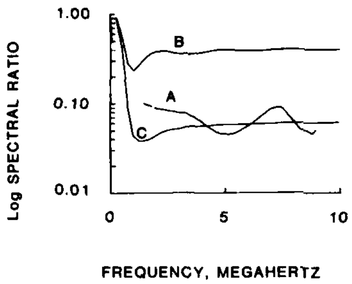

FIG. 11. Spectral ratio of the seismograms of Figure 8 (curve A) compared with the prediction of the single scattering model with scattering angles of $\Omega = 90°$ (curve B) and $\Omega = 0°$ (curve C).

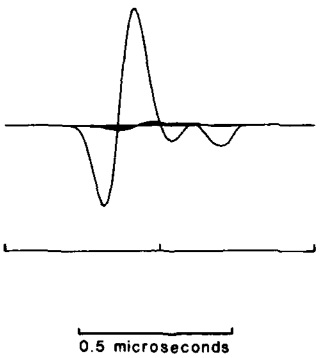

FIG. 12. Initial part of seismograms of Figure 8. Note the phase delay of the attenuated (filled) seismogram, which arrives about 0.1 μsecond later than the unattenuated (unfilled) one.

We examine the phase of the high-frequency data only, since it is only in this case that we can completely remove internal reflections within the propagation medium from the signal (by selecting only the first pulse) that might otherwise interfere with measurements of phase. The presence of the scatterers causes a phase delay that is as much as $\pi/2$ at some frequencies (Figure 13). The theoretical prediction of this phase shift does not agree particularly well with the data (Figure 13). The overall magnitude of the phase delay is underestimated by a factor of 5 to 10 at frequencies between 2 and 8 MHz.

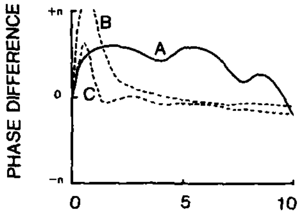

FIG. 13. Phase difference between the seismograms shown in Figure 11 (curve A), compared with prediction of the single scattering approximation with scattering angles of $\Omega = 0°$ (curve B) and $\Omega = 90°$ (curve C).

CONCLUSIONS

These laboratory measurements of apparent attenuation are in reasonably good agreement with Wu's (1982) single scattering theory (with scattering angle $\Omega = 90°$) for wavelengths longer than the scatterer dimension. The overall magnitude of the attenuation and its f^3 behavior are both predicted. At wavelengths small compared to the scatterer dimension, the predicted frequency-independent attenuation is observed, but the attenuation seems about a factor of two larger than is predicted. This discrepancy is interpreted in terms of the preculiarities of the particular scatterers in this experiment (cylindrical voids) and may not be as large in models with weaker heterogeneities.

The Kramers-Krönig relations permit the phase shift caused by the apparent attenuation to be predicted from the attenuation cure. When this is done, the results are in very poor agreement with the data. This discrepancy can be understood in terms of the way the Hilbert transform constructs the phase at one frequency from the attenuation at all frequencies. The poor fit of the attenuation data at high frequencies translates into a poor fit of the phase at all frequencies.

ACKNOWLEDGMENTS

We appreciate Bruce Dubendorff's help in performing some of the experiments. We thank Dallas Abbott for helpful discussion. This research was supported by the Office of Naval Research under Contract N00014-84C-0218 and the National Science Foundation under Grant EAR-8319104.

REFERENCES

Aki, K. and P. G. Richards (1980). *Quantitative Seismology, Theory and Methods*, W. H. Freeman and Co., San Francisco, California.

Banik, N. C., I. Lerche, and R. T. Shuey (1985). Stratigraphic filtering, Part 1: Derivation of the O'Doherty-Anstey formula, *Geophysics* (in press).

Dainty, A. M. (1981). A scattering model to explain seismic observations in the lithosphere between 1 and 30 Hz, *Geophys. Res. Letters* **8**, 1126–1128.

Gao, L. S., L. C. Lee, N. N. Biswas, and K. Aki (1983). Comparison between the effects of single and multiple scattering on the coda of earthquakes, *Bull. Seism. Soc. Am.* **73**, 377–390.

Menke, W. (1984). Asymptotic formulas for the apparent Q of weakly scattering three-dimensional media, *Bull. Seism. Soc. Am.* **74**, 1079–1081.

Mow, C.-C. and Y.-H. Pao (1971). The diffraction of elastic waves and dynamic stress concentrations. Rand Corporation Report R-482-PR, Rand Corp., Santa Monica, California.

O'Doherty R. F. and N. A. Anstey (1971). Reflections on amplitudes, *Geophys. Prosp.* **19,** 430-458.

Richards, P. G. and William Menke (1983). The apparent attenuation of a scattering medium, *Bull. Seism. Soc. Am.* **73,** 1005-1021.

Varadan, V. K., V. N. Bringi, V. V. Varadan, and Y. Ma (1983). Coherent attenuation of acoustic waves by pair-correlated random distribution of scatterers with uniform and Gaussian size distributions. *J. Acoust. Soc. Am.* **73,** 1941-1947.

Wu, R. S. (1982). Attenuation of short period seismic waves due to scattering, *Geophys. Res. Letters* **9,** 9-12.

COLLEGE OF OCEANOGRAPHY
OREGON STATE UNIVERSITY
CORVALLIS, OREGON 97331
(W.M., R.C.)

LAMONT-DOHERTY GEOLOGICAL OBSERVATORY AND
DEPARTMENT OF GEOLOGICAL SCIENCES OF
COLUMBIA UNIVERSITY
PALISADES, NEW YORK 10964 (D.W.)

Manuscript received 15 March 1985

GEOPHYSICAL RESEARCH LETTERS, VOL. 12, NO. 10, PAGES 721-724, OCTOBER 1985

DISCRIMINATING INTRINSIC AND APPARENT ATTENUATION IN LAYERED ROCK

William Menke and Bruce Dubendorff

College of Oceanography, Oregon State University

Abstract. The spectra of normal incidence transmitted compressional and shear waves are inverted to yield intrinsic (frictional) and apparent (scattering) attenuation factors as a function of frequency. This inversion is made possible by the observation that, to a first approximation, scattering and intrinsic attenuation are additive [Spencer, 1982 and Richards and Menke, 1983]. Two additional assumptions are needed; that poisson's ratio is constant and that intrinsic attenuation is mainly due to shear. The technique is tested against numerical calculations, and is shown to work at least for wavelengths larger than the scale length of the layering. The inversion requires wide-band observations and is quite sensitive to noise in the data.

Introduction

Apparent attenuation is the diminution in the amplitude of a seismic wave caused by the scattering of energy from a propagating pulse by heterogeneities in the medium of propagation [O'Doherty and Anstey, 1971]. The mechanism of apparent attenuation is very different from the mechanism of intrinsic attenuation. In the intrinsic attenuation case, energy is removed from the wavefield by internal friction. In the apparent attenuation case, energy is only redistributed to other parts of the wavefield. Nevertheless, both of these mechanisms cause a propagating seismic pulse to lose energy, and are therefore difficult to discriminate.

Considerable attention has been given to the relationship between the statistics of the heterogeneities and the apparent attenuation, especially in media consisting of very finely laminated plane layers with no intrinsic attenuation [eg. O'Doherty and Anstey, 1971; Schoenberger and Levin, 1974; Spencer et al., 1982; Richards and Menke, 1983; Menke, 1983a; Menke, 1984; Banik et al., 1985]. This relationship is now well established for normally incidence waves (with no intrinsic attenuation, and with the statistics of the layers assumed stationary):

$$\alpha(\omega) = \frac{1}{2\langle c\rangle}\,\omega^2 A(2\omega) \tag{1}$$

Here the attenuation factor, $\alpha(\omega)$, measures the decay of amplitude with distance, x, and angular frequency, ω, as $\exp(-\alpha(\omega)\,x)$. The medium has mean velocity, $\langle c\rangle$, and impedance flucuations with autocorrelation function A(t), measured as a function of one-way travel time, t. The autocorrelation function has fourier transform, $A(\omega)$. If it were possible to measure the attenuation factor, $\alpha(\omega)$ as a function of frequency for a layered rock, then it would be easy to use equation 1 to deduce the autocorrelation function, A(t). (Inverting the fourier transform requires wide-band measurements of $\alpha(\omega)$. As pointed out by Menke [1983a], low-frequency measurements of $\alpha(\omega)$ specify only the first moment of A(t). Below we show that the problem is worse than this: even the process of separating the intrincic and apparent parts of the attenuation factor requires wide band data).

In realistic experiments both apparent and intrinsic attenuation are likely to be present, so equation 1 no longer holds. One must first remove the effect of the intrinsic attenuation. We show below that this can be done if both compressional and shear wave attenuation is measured and if certain restricting assumptions are made about the nature of the attenuation.

Paper number 5L6635W.
0094-8276/85/005L-6635$3.00

Derivation

The separation of the two types of attenuation is made possible by the observation that the intrinsic and apparent attenuation factors are approximately additive:

$$\alpha(\omega)_{t,c} = \alpha(\omega)_{i,c} + \alpha(\omega)_{a,c} \tag{2a}$$

$$\alpha(\omega)_{t,s} = \alpha(\omega)_{i,s} + \alpha(\omega)_{a,s} \tag{2b}$$

Here the subscripts t, i, and a denote total, intrinsic, and apparent, respectively, and the subscripts c and s denote compressional and shear, respectively. The total attenuation, $\alpha(\omega)_t$, is the observed attenuation in the presence of both scattering and internal friction. The intrinsic attenuation factors, $\alpha(\omega)_i$, are defined as that attenuation that would be observed if the medium was homogeneous, and the apparent attenuation factors, $\alpha(\omega)_a$, are defined as that attenuation that would be observed if the medium was perfectly elastic. This approximation is valid as long as the total travel time of the scattered energy in the attenuated pulse is not substantially longer than the travel time of the direct wave. The relationship has been tested numerically by Spencer, et al. [1982] and Richards and Menke [1983] and is further substantiated in this paper. Equation 2 has four unknowns: $\alpha(\omega)_{i,c}$, $\alpha(\omega)_{a,c}$, $\alpha(\omega)_{i,s}$, and $\alpha(\omega)_{a,s}$, and only two observable quantities: $\alpha(\omega)_{t,c}$, and $\alpha(\omega)_{t,s}$. The unknowns are therefore underdetermined.

We must therefore supplement the data with *some prior information*. Two equations, in addition to equation 2, are needed.

The first equation is derived from the assumption that poisson's ratio is constant within the layer stack. The normal incidence

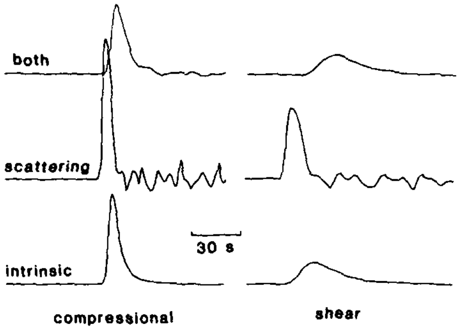

Fig. 1. Transmission response for compressional (left) and shear (right) waves propagating through a stack of 500 thin layers. Seismograms are shown for the cases where only intrinsic or scattering attenuation mechanisms are operating, and for the case that both are operating.

reflection coefficients of the compressional waves then equals those of the shear waves and the travel times of all the compressional and shear arrivals are proportional. The transmission response of the medium to a normally incident compressional wave is then the same as to a normally incidence shear wave, up to a scale factor in time. This equivalence implies:

$$\alpha(\omega)_{a,s} = \alpha(r\omega)_{a,c} \tag{3}$$

where r is the ratio of the compressional and shear wave velocities. In the real earth, poisson's ratio may flucuate from layer to layer. Nevertheless, our calculations (not shown) indicate that equation 3 is still approximately valid (in the mean) as long as the fluctuation is small (<5%).

The second equation is derived from the assumption that the intrinsic attenuation is due mainly to shear, a hypothesis *usually true for* rocks. This assumption implies that the intrinsic attentuation factors for compression and shear are proportional [Aki and Richards, p.513, 1980]:

$$\alpha(\omega)_{i,s} = \frac{3}{4}\, r^3\, \alpha(\omega)_{i,c} \tag{4}$$

Equations 2, 3, and 4 can now be solved simultaneously for the four unknown functions. The equation for $\alpha(\omega)_{i,c}$ is:

$$\alpha(\omega)_{i,c} - (3r^3/4)\, \alpha(\omega/r)_{i,c} = \alpha(\omega)_{t,c} - \alpha(\omega/r)_{t,s} \tag{5}$$

Note that this equation is implicit in the unknown function $\alpha(\omega)_{i,c}$. We solve this equation in the *Appendix*. The four unknowns are then given by:

$$\alpha(\omega)_{i,c} = \sum_{p=0}^{\infty} (3r^3/4)^{-p-1} \left[\alpha(\omega r^p)_{t,s} - \alpha(\omega r^{p+1})_{t,c}\right] \tag{6a}$$

$$\alpha(\omega)_{a,c} = \alpha(\omega)_{t,c} - \alpha(\omega)_{i,c} \tag{6b}$$

$$\alpha(\omega)_{i,s} = (3r^3/4)\, \alpha(\omega)_{i,c} \tag{6c}$$

$$\alpha(\omega)_{a,s} = \alpha(\omega)_{t,s} - \alpha(\omega)_{i,s} \tag{6d}$$

In order to determine the intrinsic and apparent attenuation factors at a given frequency, ω, measurements must be made at a set of frequencies higher than ω. In principle, the inversion requires infinite bandwidth. Fortunately, the series (equation 6a) contains the term $(3r^3/4)^{-p-1}$, which rapidly decreases with p. If the total attenuation is reasonably well behaved at high frequencies, then only two or three terms are needed in the sum to give, say, 10% accuracy. Once $\alpha(\omega)_{a,c}$ and $\alpha(\omega)_{a,s}$ have been determined, equation 1 can be used to invert for the autocorrelation function of the impedance flucuations.

Example

We have calculated the normal incidence compressional *and shear* wave transmission response of a stack of 500 layers. Each of these layers has the same one-way travel time, 1.0 s for compressional waves. The compressional velocity is randomly chosen to be either 0.9 km/s or 1.1 km/s, and the density and poisson's ratio are held constant at 1.0 gm/cm^3 and 0.25 respectively. The medium is assumed to have intrinsic attenuation described by a constant quality factor, $Q_c=100$ for compressional waves and $Q_s=44.4$ for shear waves. Compressional and shear wave seismograms for one realization of this medium, and for the cases when either only intrinsic or apparent attenuation is acting are shown in figure 1. The attenuation factor as a function of frequency for the leading pulse of each of these seismograms is shown in *figure* 2. *Also shown is* the total attenuation predicted by equation 2, which *matches* the observed data quite well.

We then invert these data using equations 6a-d. We have found that noise in the data can lead to poor results, so we first smooth the

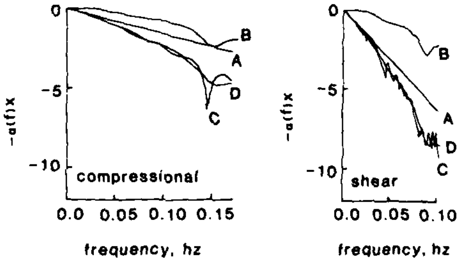

Fig. 2. Attenuation factor, $\alpha(f)$, as a function of frequency f, for the compressional and shear waves shown in figure 1. The attenuation has been scaled by the propagation distance, x. A) Only intrinsic attenuation is operating. B) Only scattering attenuation is operating. C) Both mechanisms are operating. D) Prediction of curve C by equation 2. Note that the prediction of equation 2 is quite accurate.

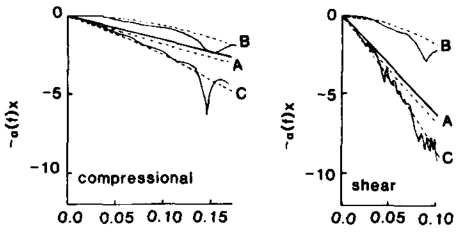

Fig. 3. Attenuation factor, α(f), as a function of frequency, f, for the compressional and shear waves shown in figure 1. The attenuation has been scaled by the propagation distance, x. The solid lines are the attenuation factors observed for the seismograms of figure 1; A) intrinsic, B) scattering, and C) both. The dashed curves labeled C are the polynomial fits to the data. The dashed curves labeled A and B are the reconstructed intrinsic and scattering attenuation factors. The slight misfit arises from the sensitivity of the method to noise in the data, as discussed in the text.

data by fitting low order least-squares polynomials to it. This procedure is somewhat ad hoc, since changing the order of the polynomials can lead to subtle, but important, changes in the smoothed data, and can have substantial effects on the inversion. Nevertheless, the results (figure 3) are in reasonably good agreement with the observed attenuation when only one of the two attenuation mechanisms is active.

Conclusions

Our main result is that the observed attenuation factors for compressional and shear waves transmitted at normal incidence through a randomly layered medium may be inverted for the individual contribution of apparent (scattering) attenuation and intrinsic (frictional) attenuation. The scattering attenuation factor may then be used to construct the autocorrelation function of the impedance of the layers. Two assumptions must be made to make the inversion possible: that poisson's ratio is constant throughout the medium, and that the intrinsic attenuation is due mainly to shear.

While the transmission response of the medium may be difficult, in practice, to determine, some work has recently been done in relating the spectrum of the transmission response to that of the reflection response [B. White, *personal communication*, 1985; J. Resnick, *personal communication*, 1985]. The reflection response is routinely measured in seismic reflection profiling.

The inversion method described in this paper is unique. Unfortunately, substantial bandwidth is required. Furthermore, since fairly subtle differences in the observed compressional and shear wave attenuation factors allow the effects of apparent and intrinsic attenuation to be separated, the method is sensitive to noise. While very little work has been done examining apparent attenuation at oblique angles of incidence (but see Menke, 1983), it may be that these data will eventually provide further constraints that will make the inversion more robust.

Appendix

Here we prove that the solution to equation 5 is equation 6a. For the sake of brevity, let the $a(\omega)=\alpha(\omega)_{i\ c}$ and the right hand side of equation 5 be called $g(\omega)$. Then equation 5 can be written as:

$$a(\omega) - (3r^3/4)\, a(\omega/r) = g(\omega) \qquad \text{(A1)}$$

and its solution, equation 6a can be written as:

$$a(\omega) = -\sum_{p=0}^{\infty} g(\omega r^{p+1})\ (3r^3/4)^{-p-1} \qquad \text{(A2)}$$

Replacing ω with ω/r, equation A2 becomes:

$$a(\omega/r) = -\sum_{p=0}^{\infty} g(\omega r^{p})\ (3r^3/4)^{-p-1}$$

$$= -g(\omega)(3r^3/4)^{-1} - \sum_{p=1}^{\infty} g(\omega r^{p})\ (3r^3/4)^{-p-1} \qquad \text{(A3)}$$

We then change the limits of the sum by setting $p=p'+1$, and then ignoring the prime:

$$a(\omega/r) = -g(\omega)(3r^3/4)^{-1} - \sum_{p=0}^{\infty} g(\omega r^{p+1})(3r^3/4)^{-p-2}$$

$$= -g(\omega)\ (3r^3/4)^{-1} + (3r^3/4)^{-1} a(\omega) \qquad \text{(A4)}$$

We now insert this expression for $a(\omega/r)$ into equation A1, and note that it is satisfied uniquely.

Note that equation 6a will converge as long as $a_{t,c} \sim \omega^q$ and $a_{t,s} \sim \omega^z$ for large ω, with $p,z<3$. Since all the transmission responses are causal (that is, satisfy the Kramers-Kronig theorem), this condition is always satisfied. We have tested equation 6a numerically, and have found the convergence is usually very rapid.

Acknowledgements. We thank Gunnar Bodvarsson for helpful discussion. Ian Lerche provided some very helpful comments on the original manuscript. This work was supported by the Office of Naval Research under contract N00014-~~80C~~-0218.
84C

References

Aki, K. and P.G. Richards, Quantitative Seismology, Theory and Methods, W.H. Freeman and Co., San Francisco, 1980.

Banik, N.C., I. Lerche, and R.T. Shuey, Stratigraphic filtering, part 1, derivation of the O'Doherty-Anstey formula, in press in Geophysics, 1985.

Menke, W., A formula for the apparent attenuation of acoustic waves in randomly layered media, Geophys. J. R. Astr. Soc., 75, 541-544, 1983a.

Menke, W., On the effect of P-S coupling on the apparent attenuation of elastic waves in randomly layered media, Geophys. Res. Lett., 10, 1145-1147, 1983b.

O'Doherty, R.F. and N.A. Anstey, Reflections on amplitudes, Geophys. Prospecting, 19, 430-458, 1971.

Richards, P. G. and W. Menke, The apparent attenuation of a scattering medium, Bull. Seism. Soc. Am., 73, 1005-1021, 1983.

Schoenberger, M. and F.K. Levin, Apparent attenuation due to interbed multiples, Geophysics, 39, 278-291, 1974.

Spencer, T.R., J.R. Sonnand, and T.M. Butler, Seismic Q - stratigraphy or dissipation, Geophysics, 47, 16-24, 1982.

William Menke and Bruce Dubendorff, College of Oceanography, Oregon State University, Corvallis, OR 97331.

(Received July 9, 1985;
Accepted July 18, 1985.)

Journal of Marine Research, 43, 793–824, 1985

Wind-driven mid-ocean baroclinic gyres over topography: A circulation equation extending the Sverdrup relation

by **R. A. de Szoeke**[1]

ABSTRACT

What is the circulation driven by wind stress in a stratified ocean above topography? This question was answered by Sverdrup (1947) for vertically integrated transport over flat topography only. By applying the ideas and methods of Rhines and Young (1982a,b), a modified form of the Sverdrup transport relation can be derived for the case of stratification and topography in certain circumstances. This circulation equation is, in quasigeostrophic form,

$$J(\Psi, \beta y + \chi f_0 h'_T/H) = -\chi f_0^{-1} gAH\, J(\beta y, h'_T) + \hat{z} \cdot \nabla \times \tau/\rho_0,$$

where most symbols have their usual meanings, while χ is a parameter no larger than 1 that depends on stratification, bottom friction and horizontal diffusivity. The effect of topography is attenuated (χ is reduced) by strong stratification, strong bottom friction, or weak horizontal diffusivity. The circulation equation applies strictly to uniform bottom slope or other topographies obeying $\nabla^2 h'_T = 0$, though it approximately holds for $\nabla^2 h'_T \simeq 0$, a criterion for which is that the scale of bottom topography greatly exceeds the baroclinic Rossby radius of deformation. It holds only above deep closed circulations. It is remarkable for the form of the characteristic lines for transport, $\beta y + \chi f_0 h'_T/H =$ constant, and the extra forcing term on the right, which depends on topography.

Examples are given of two-layer flows driven by wind-stress curl over east-west and north-south sloping topography. The determination of the boundary of the deep gyre is an implicit nonlinear problem. The solution for the case of east-west slope illustrates the general method for solving such a problem.

1. Introduction

The basis of modern understanding of wind-driven ocean circulation remains a simple relation derived by Sverdrup (1947) between the vertically integrated meridional mass transport and the curl of the wind stress. A question that remains open despite much theoretical work concerns the nature of the distribution of this transport with depth, and its relation to stratification. This question has received new attention recently with the appearance of two somewhat complementary theories of ocean circulation by Luyten *et al.* (1983; hereafter LPS) and Rhines and Young (1982a,b; hereafter RYa,b). The former take the view that parcels of water of a given density in

---

[1] College of Oceanography, Oregon State University, Corvallis, Oregon, 97331, U.S.A.

anticyclonic gyres acquire their potential vorticity from the wind in the latitudes in which their density horizon outcrops, and that the ensuing circulation is determined by geostrophy and the conservation of potential vorticity as parcels sink along their isopycnals. Density layers not in contact with the surface anywhere in the subtropical gyre are taken to be motionless. This is a theory of 'ventilated motion'. Rhines and Young examine the question of motion in unventilated layers, the possibility of which there seems no reason to exclude. Now the classical result is that motion conserves potential vorticity but there is a difficulty in determining the functional relationship between streamfunction and potential vorticity in closed unventilated gyres. Rhines and Young propose that friction and diffusion, however slight, link circulation in adjoining density layers in such a way as to determine uniquely this functional relation. A novel prediction is that potential vorticity in interior unventilated gyres is uniform throughout the gyre. Both LPS and RY theories retain the Sverdrup relation for vertically integrated transport.

The Sverdrup relation holds strictly only for flat, level bottom topography or where bottom flow is zero or along isobaths. Bottom flows across isobaths, where bottom slopes are of order 10^{-3}, must be smaller than $0(1 \text{ mm/s})$ to be negligible in the Sverdrup relation, compared to typical wind-stress curls of $0(10^{-7} \text{ N m}^{-3})$. Nonetheless, though such bottom slopes are pervasive and cross-isobath mean flows of such magnitude cannot be ruled out *a priori*, experience shows that meridional Sverdrup transport integrated across the North Atlantic agrees well with the Gulf Stream return flow at subtropical latitudes (Leetmaa *et al.*, 1977). The question is, why should this be so? This is part of a larger outstanding question, how are bottom flows determined by the wind stress in the presence of topography? In this paper, I attempt a partial answer to this larger question of geophysical fluid dynamics, limited to uniformly sloping topography, or other topographies satisfying $\nabla^2 h = 0$.

In Section 2, we derive the relationship between circulation at different levels in the vertical in the simplest context, a two-layer model with bottom topography, using the method of RYb. This allows us to derive important extensions of the Sverdrup relation in the presence of topography, stratification, and nonzero bottom flows. Generalization of the method to an arbitrary number of layers, and even the continuous limit, is taken up again in Section 7 and the Appendix. The result is a circulation equation, stated in the Abstract, which is an extension of the classical Sverdrup relation, that relates vertically integrated flow to wind-stress curl and topography, and depends on stratification and turbulent friction and diffusion. Also in Section 7, we obtain a criterion for how strictly $\nabla^2 h = 0$ must be obeyed: roughly, topography varying on scales much larger than the baroclinic Rossby radius of deformation will satisfy this criterion.

In Section 3 we apply the circulation equation to determine the wind-driven flow in the case of north-south slope for some simple examples. For north-south slope, as for no slope at all, the natural characteristics are latitude lines. In Sections 4, 5 and 6 we consider circulation over east-west slope in two layers, and find that the natural characteristics intersect both latitude lines and isobaths in regions where the wind-driven flow penetrates to the bottom. We obtain a criterion for closed lower layer circulation which states that the integrated Ekman pumping across a lower layer gyre along any characteristic, biased by a term which represents the effect of vortex stretching by flow across isobaths, must be zero (Section 4). This places constraints on the orientation of lower layer gyres with respect to the wind forcing and topography. We obtain a similar, though not essential, criterion for closed upper layer circulation.

In Section 5 we obtain the circulation driven by an east-west oriented 'dipole' wind-stress curl field over east-west slope. This example is important for it illustrates how the problem of solving the circulation in the general case should be attacked. An interesting result is that, even for compact wind-stress curl field with no net Ekman pumping, remote zonal currents are forced to the east and west of the forcing region, different on either side of it, with a net zonal throughput.

Section 6 examines, by some illustrative examples, shapes of wind-stress curl fields for closed circulation in both upper and lower layers. The required shapes depend, through the criteria derived in Section 4, on the bottom slope, the strength of forcing, and the orientation of the natural characteristics. The examples we consider assume some truly bizarre shapes. This contrasts with the deceptively simple forcing field that RYb used to drive close circulation over flat bottom.

2. A two-layer model

We show how to obtain the circulation driven by wind-stress curl in two layers over topography. In the unventilated lower layer streamfunction is a function of potential vorticity. This function is specified through consideration of frictional and diffusive linkage of circulation around closed gyres between adjoining layers. This method closely follows RYb.

a. The governing equations. Consider two layers of fluid of equal mean depth H_1 with the upper layer in contact with the base of an Ekman layer driven by a wind-stress distribution, the lower layer lying above topography whose variation is given by $h'_T(x, y)$ (positive h'_T corresponds to elevated bottom). Then the steady quasigeostrophic potential vorticity equations for the two layers on a β-plane are:

$$J(\psi_1, q_1) = W_o/H_1 - R'\nabla^2(\psi_1 - \psi_2) + K\nabla^2 q'_1 \tag{2.1a}$$

$$J(\psi_2, q_2) = R'\nabla^2(\psi_1 - \psi_2) - D\nabla^2\psi_2 + K\nabla^2 q'_2 \tag{2.1b}$$

where

$$q_1 = \beta y + F(\psi_2 - \psi_1) \tag{2.1c}$$

$$q_2 = \beta y + h_T + F(\psi_1 - \psi_2) \tag{2.1d}$$

$$F = \rho_o f_o^2/g\Delta\rho H_1 = (\text{Rossby radius of deformation})^{-2} \tag{2.1e}$$

$$W_o = \hat{z} \cdot \nabla x\, \tau/\rho_o \tag{2.1f}$$

$$h_T = f_o\, h'_T/H_1. \tag{2.1g}$$

Subscript 1 refers to the upper layer, 2 to the lower layer, ψ_i, q_i are the streamfunctions and potential vorticities of the two layers. The scale of the flow is assumed to be much larger than the Rossby radius, so that relative vorticity is neglected in the potential vorticity. Vorticity is transferred between layers by a simple drag law with coefficient R', and to the bottom by a similar drag law with coefficient D. Referring to a vertical eddy exchange coefficient A for momentum, we can write these coefficients as

$$R' = A/H_1^2,\ D = f_o\delta_E/H_1,$$

where $\delta_E = (2A/f_o)^{1/2}$ is the bottom Ekman layer thickness (Pedlosky, 1979). Note that $R'/D = \delta_E/2H_1 \ll 1$. q'_1, q'_2 are the horizontally diffusible parts of potential vorticity; since relative vorticity is neglected, these will be $\pm\ F(\psi_2 - \psi_1)$. This represents temperature, or buoyancy, so the appropriate turbulent diffusivity K to use is that for heat. The R' and K terms in (2.1a,b) are of identical form and can be combined into terms of the form

$$\pm\ R\nabla^2(\psi_1 - \psi_2),$$

where $R = R' + FK$. Hence

$$\frac{R}{D} = \frac{\delta_E}{2H_1} + \frac{FH_1K}{f_o\delta_E}. \tag{2.2}$$

For $\Delta\rho/\rho_o = 10^{-3}$, $\delta_E = 10$ m, $f_o = 10^{-4}$ s^{-1}, $K = 10^3$ m^2 s^{-1}, the second term is 1.0, though the first is quite small. In this paper, we shall assume $R \sim D$. This presumes that vortex stretching accomplished by horizontal diffusion of buoyancy is of the same order as that accomplished by bottom Ekman pumping balancing frictionally driven boundary layer divergences. These equations and their underlying assumptions are identical to RYb's except for the addition of topography to the lower layer potential vorticity. W_o is the Ekman layer divergence, which stretches vortices in the interior and acts as a source of vorticity; it is given by the curl of the wind stress.

Add equations (2.1a), (2.1b); the baroclinic terms cancel, so that

$$\beta\psi_{Bx} + J(\psi_2, h_T) = W_o/H_1, \tag{2.1h}$$

where $\psi_B = \psi_1 + \psi_2$, and bottom friction is neglected.

b. The motion in the lower layer. Consider layer 2. To the extend that frictional and diffusive processes on the right of (2.1b) can be neglected, streamlines must coincide with potential vorticity trajectories ('isostrophes'), i.e.,

$$\psi_2 = A_2(q_2), \tag{2.3}$$

where $A_2(\cdot)$ is a function to be determined. In a closed ocean basin, the lower layer flow on any isostrophe that can be tracked back to an ocean boundary must vanish, hence $A_2 = 0$ for such trajectories. The upper layer flow in such regions is simply the Sverdrup flow:

$$H_1\psi_1 = -\beta^{-1}\int_x^{x_e} W_o(x', y)dx'. \tag{2.4}$$

Of more interest are isostrophes that do not intersect the boundaries but close on themselves, and the flow in the volumes they enclose. RYb suggested how flow on such trajectories can be determined. Without friction, no more information can be obtained about the flow than is contained in (2.3): any flow along isostrophes is possible. However, friction and diffusion, no matter how small, transmit information about the neighboring flow between layers and across the isostrophes. This serves to link the circulation in neighboring layers and isotrophes and specify the potential vorticity-streamfunction relation for the flow in the closed region. To see this, integrate (2.1b), including friction and diffusion, over an area bounded by a closed q_2 contour. The left-hand side is precisely zero, and applying Stokes' theorem to the frictional terms, remembering that $\mathbf{u}_i = \hat{z} \times \nabla\psi_i$, we obtain

$$R \oint (\mathbf{u}_1 - \mathbf{u}_2) \cdot d\mathbf{s} = D \oint \mathbf{u}_2 \cdot d\mathbf{s}. \tag{2.5}$$

This states that, for steady flow on a closed isostrophe, the vertical divergence of circulation must vanish. On the other hand, using (2.3), which is correct to $O(R)$, and the definition of q_2, (2.1d), we can calculate the circulation on a q_2-contour in the lower layer to be

$$\begin{aligned}\oint \mathbf{u}_2 \cdot ds &= \oint \hat{z} \times \nabla\psi_2 \cdot d\mathbf{s}\\ &= \frac{dA_2}{dq_2}\oint \hat{z} \times \nabla q_2 \cdot d\mathbf{s}\\ &= \frac{dA_2}{dq_2}\left\{F \oint (\mathbf{u}_1 - \mathbf{u}_2) \cdot d\mathbf{s} + \oint \hat{z} \times \nabla(\beta y + h_T) \cdot d\mathbf{s}\right\}.\end{aligned} \tag{2.6}$$

Application of Stokes' theorem to the second integral in the last expression shows this to be $\int \nabla^2 (\beta y + h_T) dA$, where the integration is over the area enclosed by the q_2 isostrophe. As long as planetary vorticity, including the effect of topography, is *harmonic*, i.e., $\nabla^2(\beta y + h_T) = 0$, this contribution vanishes. In particular, this is true for uniformly sloping topography.

From (2.5), (2.6), we must have

$$\frac{dA_2}{dq_2} = \frac{1}{F}\frac{R}{D} \tag{2.7}$$

so that the arbitrary function A_2 in (2.3) is determined:

$$\psi_2 = \frac{q_2}{F}\frac{R}{D} + \text{const.} \tag{2.8}$$

Using (2.1d), this can be written

$$\psi_2 = \frac{R/D}{1 + R/D}\left\{\frac{1}{F}(\beta y + h_T) + \psi_1\right\} + \text{const.}, \tag{2.9}$$

or, in terms of $\psi_B = \psi_1 + \psi_2$,

$$\psi_2 = \frac{R/D}{1 + 2R/D}\left\{\frac{1}{F}(\beta y + h_T) + \psi_B\right\} + \text{const.} \tag{2.10}$$

This is valid in any region with closed q_2 isostrophes. Except for the inclusion of topography, which seems almost inconsequential up to this point, the reasoning hardly differs from *RYb*.

Substitution of (2.10) into (2.1h) gives

$$J(\psi_B, \beta y + [f_R^{-1}h_T]) = [(f_RF)^{-1}J(h_T, \beta y)] + W_o/H_1, \tag{2.11}$$

where $f_R = 2 + D/R$. Or, in terms of ψ_2,

$$J(\psi_2, \beta y + f_R^{-1}h_T) = (f_RF)^{-1}J(h_T, \beta y) + W_o/f_RH_1. \tag{2.12}$$

The circulation equation (2.11) should be compared to the classical Sverdrup transport relation which omits the terms in braces [ ]. These terms are present only where there is lower layer motion. The extra term on the right represents vorticity input by stretching due to topography variations. The extra term on the left forces characteristics to deviate from latitude lines over topography. Both terms contain the factor $f_R^{-1} = R/(2R + D)$, which depends on the ratio of bottom friction to horizontal diffusivity D/R. If $D/R \gg 1$, the bottom flow ψ_2 is arrested, and the simple Sverdrup relation holds despite topography.

3. North-south bottom slope

We shall describe the flow over topography of the form

$$h_T = \delta y, \tag{3.1}$$

driven by a symmetric circular dipole wind stress curl field, similar to the one used by

RYb:

$$W_o/H_1 = -\alpha x, \text{ inside circle,} \tag{3.2}$$
$$= 0, \text{ outside circle.}$$

Substitute into (2.12). This gives

$$(f_R\beta + \delta)\psi_{2x} = -\alpha x, \tag{3.3}$$

to determine the flow in the layer wherever it is not zero. Notice that the extra forcing term in (2.12) is absent with north-south slope, and that the characteristics of (3.3) are latitude lines, as they would be without topography. A simple solution of (3.3), consistent with the requirement of closed lower layer circulation, upon which the reasoning of Section 2 that leads to (3.3) depends, is

$$\psi_2 = \frac{1}{2}\alpha(\beta f_R + \delta)^{-1}(r_0^2 - x^2 - y^2), \quad x^2 + y^2 < r_0^2, \tag{3.4a}$$
$$= 0, \quad x^2 + y^2 > r_0^2, \tag{3.4b}$$

where r_0 is arbitrary, except that it should be small enough that the nonzero circulation of the lower layer be contained within the dipole-forcing circle. Eq. (2.9) can be used to find ψ_1 above the lower layer circulation:

$$\psi_1 = \frac{1}{2}(1 + D/R)\alpha(\beta f_R + \delta)^{-1}\{x^2 + (y + y_1)^2\} + \text{const.}, x^2 + y^2 < r_0^2, \tag{3.5}$$

where $y_1 = (1 + D/R)^{-1}(\beta f_R + \delta)(\beta + \delta)/\alpha F$. On the boundary of validity of (3.5), $x^2 + y^2 = r_0^2$,

$$\psi_1 = -(\beta + \delta)y/F + \text{const.} \tag{3.6}$$

For $x^2 + y^2 > r_0^2$, because $\psi_2 = 0$, the upper layer flow satisfies

$$\beta\psi_{1x} = W_o/H_1. \tag{3.7}$$

Integrating this equation out from the circle bounding the lower layer flow, where (3.6) is the boundary condition, we obtain

$$\psi_1 = -\alpha(2\beta)^{-1}\{x^2 + (y + y_0)^2\} + \text{const.}, x^2 + y^2 > r_0^2, \tag{3.8}$$

where $y_0 = \beta(\beta + \delta)/\alpha F$. The upper layer streamlines are circles or segments of circles, centered on $y = -y_0$. The first such circle that can completely close on itself outside the lower layer gyre has radius $r_1 = |y_0| + r_0$. If we take this circle to define the domain of the circular dipole forcing (3.2), then there is no flow beyond it, and the circulation forced by it is given by (3.4), (3.5), and (3.8) in the appropriate domains.

The calculation of ψ_1 and ψ_2 illustrates that the transport in the gyres is reduced by a factor of $(1 + \delta/f_R\beta)^{-1}$ for an upslope to the north ($\delta > 0$) compared to flat bottom.

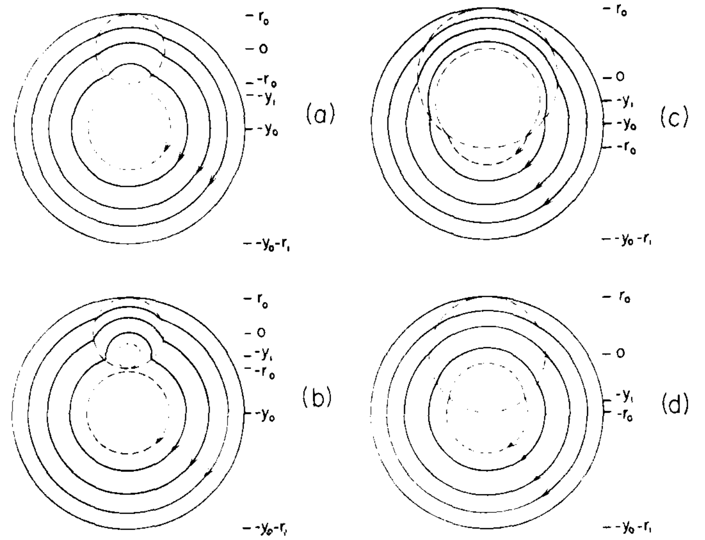

Figure 1. Circulation patterns driven by the circular dipole wind over north-south sloping topography. Streamlines in the upper layer are shown. The region of lower layer circulation (dot-dashed) is displaced to the north for $\delta/\beta > -1$. (a) $y_0/r_1 = 0.7$, $r_0/r_1 = 0.3$, $y_1/r_1 = 0.4$, $\delta/\beta = 0.5$; (b) $y_0/r_1 = 0.7$, $r_0/r_1 = 0.3$, $y_1/r_1 = 0.2$, $\delta/\beta = 4.0$; (c) $y_0/r_1 = 0.4$, $r_0/r_1 = 0.6$, $y_1/r_1 = 0.2$, $\delta/\beta = 1.0$; (d) $y_0/r_1 = 0.5$, $r_0/r_1 = 0.5$, $y_1/r_1 = 0.4$, $\delta/\beta = -0.5$; $f_R = 2 + D/R = 3.0$, in all cases.

Conversely, it is increased by a downslope to the north ($\delta < 0$). Also, the lower layer gyre is further offset to the north and is correspondingly smaller for $\delta > 0$, and conversely.

Examples of such flows are shown in Figures 1 and 2 for various values of y_0, y_1. Each panel shows the circulation in the upper layer, with the outline of the lower layer gyre dot-dashed in. For $\alpha > 0$, the upper layer circulation is anticyclonic, as shown. For all the examples shown, lower layer flow is anticyclonic, too. (Only for $\delta/\beta < -f_R$ is the lower layer gyre opposite to the upper layer.) Figure 1 shows circulation for $\beta + \delta > 0$, Figure 2 for $\beta + \delta < 0$. For the former, $0 < y_1 < y_0$, while for the latter, $0 < -y_0 < y_1$. For $\beta + \delta > 0$, the lower layer gyre is displaced north of the upper layer gyre, while for $\beta + \delta < 0$, it is displaced south. The amount of displacement is inversely proportional, *paris paribus*, to the strength α of the forcing. For $\beta + \delta = 0$, when topography exactly opposes β in the lower layer, the upper and lower layer gyres are perfectly circular and

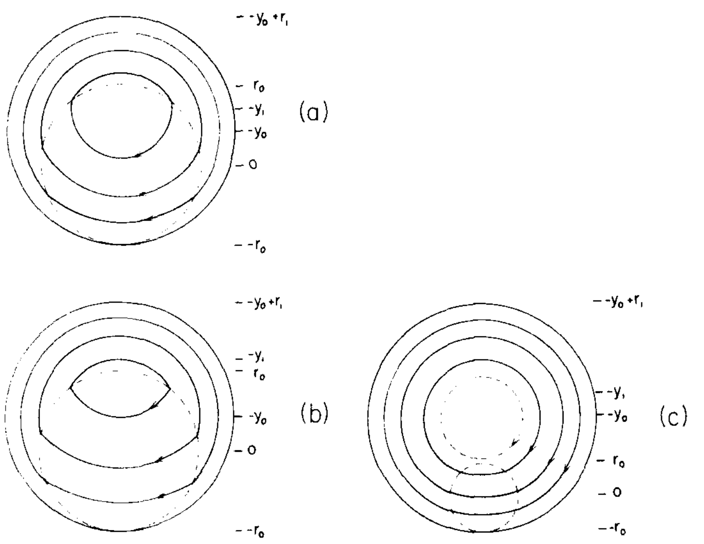

Figure 2. Like Figure 1. The region of lower layer circulation is displaced south for $\delta/\beta < -1$. (a) $y_0/r_1 = -0.3$, $r_0/r_1 = 0.7$, $y_1/r_1 = -0.5$, $\delta/\beta = -1.8$; (b) $y_0/r_1 = -0.3$, $r_0/r_1 = 0.7$, $y_1/r_1 = -0.8$, $\delta/\beta = -2.25$; (c) $y_0/r_1 = -0.7$, $r_0/r_1 = 0.3$, $y_1/r_1 = -0.9$, $\delta/\beta = -1.44$; $f_R = 3.0$ in all cases.

coincide. The strength of the lower layer circulation, compared to the upper layer, is smaller by a factor of $(1 + D/R)$.

4. Integral conditions for closed circulation over topography

Next, we would like to consider east-west sloping topography, and perhaps find examples of wind-stress curl fields that drive closed gyres in both layers. Compared to the simplicity of the case of north-south topography this proves unexpectedly complicated. The reason for this is rooted in two integral conditions that the wind forcing must satisfy along the natural characteristics over the domain of closed circulation in each layer. For the north-south sloping topography, the characteristics are constant-latitude lines in both layers, and the integral conditions merely require simple east-west anti-symmetry in the forcing, which the circular dipole readily satisfies. For east-west topography the natural characteristics slope obliquely across the closed lower layer gyre, and are constant-latitude lines outside it. This distortion of the characteristics, and other asymmetries, means that the integral conditions put peculiar demands

AD-A167 102 COMPILATION OF REPRINTS NUMBER 63(U) OREGON STATE UNIV 3/3
CORVALLIS COLL OF OCEANOGRAPHY MAR 86 REF-83-12
N00014-76-C-0067 86 PAT-APPL-825 107

UNCLASSIFIED F/G 8/10 NL

END
DATE
FILMED
6-86
DTIC

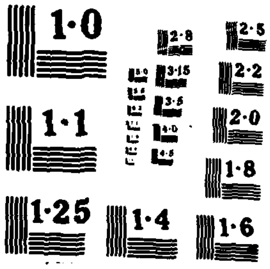
1·0
2·8
2·5
3·15
2·2
3·5
1·1
4·0
2·0
4·5
1·8
1·25
1·4
1·6

on the distribution of wind forcing necessary for closed gyres in both layers. In this Section, we shall derive these two conditions. In Section 6, we shall construct some peculiar wind-stress curl fields that satisfy these conditions, and obtain the circulations that they drive. But first, in Section 5, we shall relax the condition of closed flow in the upper layer, and consider circulation driven by the circular dipole over topography.

We consider east-west sloping topography of the form

$$h_T = \gamma x. \tag{4.1}$$

If this is substituted into (2.12) and (2.11), one obtains

$$f_R \beta \psi_{2x} - \gamma \psi_{2y} = \gamma \beta / F + W_o / H_1, \tag{4.2}$$

$$\beta \psi_{Bx} - \frac{1}{f_R} \gamma \psi_{By} = \frac{\gamma \beta}{f_R F} + W_o / H_1, \tag{4.3}$$

where $f_R = 2 + D/R$.

It is convenient to introduce a tilted coordinate frame given by

$$\xi = (f_R \beta x - \gamma y)/B, \qquad \eta = (\gamma x + f_R \beta y)/B, \tag{4.4a,b}$$

where $B = (\gamma^2 + f_R^2 \beta^2)^{1/2}$, in terms of which (4.2) and (4.3) may be written

$$B \psi_{2\xi} = \gamma \beta / F + W_o / H_1 \tag{4.5}$$

$$\frac{1}{f_R} B \psi_{B\xi} = \gamma \beta / f_R F + W_o / H_1. \tag{4.6}$$

The characteristics of (4.5), (4.6) are lines of constant η The relation of the tilted coordinate frame to the geographic frame is illustrated in Figure 3. Suppose there exists a region of closed circulation in the lower layer (closed q_2 and ψ_2; shown schematically as a circle in Fig. 3) and that the right and left boundaries of the region are given by $\xi_+(\eta)$, $\xi_-(\eta)$. Integrate (4.5) across this region. Then

$$\int_{\xi_-}^{\xi_+} (W_o(\xi', \eta)/H_1 + \gamma \beta / F)\, d\xi' = 0, \tag{4.7}$$

since $\psi_2 = 0$ on the boundaries. This condition places restrictions on the location of lower layer gyres relative to the forcing field W_o. Sometimes this condition serves to forbid closed recirculation. For instance, if $W_o/H_1 + \gamma\beta/F$ is of one sign along a characteristic, only the trivial solution $\xi_+ = \xi_-$ of (4.7) is possible. Conversely, any recirculating region must straddle regions with opposite signs of $W_o/H_1 + \gamma\beta/F$. For $\gamma = 0$, $\xi = x$ and $\eta = y$, so that (4.7) becomes $\int_{x_-}^{x_+} W_o dx = 0$. This means that the closed lower layer gyre must straddle the wind-stress curl field in the east-west direction in such a way that there is no net vortex stretching on any latitude.

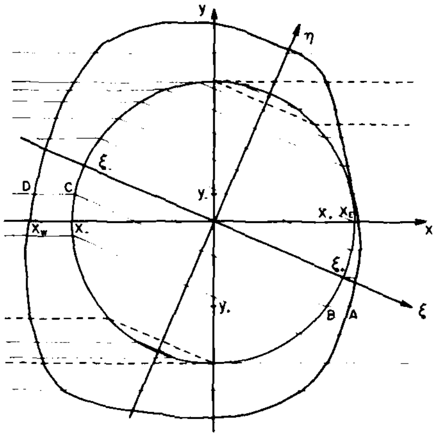

Figure 3. Lines of constant topography-modified planetary vorticity $\beta y + \chi f_0 h'_T/H = \beta y + \gamma x/f_R$ for westward, upward sloping topography. These correspond to latitudes outside the region bounded by the circle where wind-driven circulation penetrates to the bottom.

On the boundaries where ψ_2 vanishes,

$$\psi_1 = -\frac{1}{F}(\beta y + \gamma x) + \psi_0, \tag{4.8}$$

by (2.9), where ψ_0 is an arbitrary constant.

Outside the boundary, $\psi_2 = 0$ everywhere and the usual Sverdrup relation applies to the upper layer,

$$\beta\psi_{1x} = W_o/H_1, \tag{4.9}$$

for which the characteristics are constant-latitude lines. For the joint system (4.6), (4.9), the characteristics are lines of constant η and lines of constant y, joined at the boundaries between the regions (Fig. 3). Integrating (4.9) and (4.6) across the forcing region along such characteristics gives a condition on the forcing field for closed circulation, in the upper layer namely,

$$\underset{(y = \text{const})}{\int_{x_W}^{x_\cdot} H_1^{-1}\beta^{-1}W_o dx} + \underset{(\eta = \text{const})}{\int_{\xi}^{\xi_\cdot}\left(\frac{\gamma\beta}{FB} + f_R H_1^{-1}B^{-1}W_o\right)d\xi} + \underset{(y = \text{const})}{\int_{x_\cdot}^{x_E} H_1^{-1}\beta^{-1}W_o dx} = 0 \tag{4.10}$$

where the coordinates $x_\cdot, \xi_\cdot, x_E, x_W$ are defined graphically in Figure 3. There can exist places where the characteristic lines emerge from the region of closed lower layer circulation and head off in the same direction whence they came. Examples are the areas enclosed by dashed lines in the upper right and lower left of Figure 3. For the former, for example, it must be remembered that in the first integral of (4.10) $x_W > x_-$.

When $\gamma = 0$, condition (4.10) reduces to

$$\int_{x_W}^{x_E} W_o dx = 0, \tag{4.11}$$

which means that, to achieve closed circulation in the upper layer, the net input of vorticity by the wind along any latitude must be zero.

Eq. (4.7) is the condition for closed circulation in the lower layer, while (4.10) is the condition for closed circulation in the upper layer. The former is more fundamental because without it (2.9), upon which the whole line of reasoning depends, is invalid. The latter condition (4.10) is not at all crucial to the existence of lower layer recirculation. If it is not satisfied, however, there must be a net zonal transport through the forcing region. We shall see an example of this in the next Section.

5. The east-west oriented circular dipole over topography

We show first that the east-west dipole does not satisfy the conditions of Section 4 for closed flow in both layers over topography. But if one relaxes the requirement of closed flow in the upper layer, one can obtain steady solutions with closed lower layer circulation. A feature of these solutions is that a zonal flow passes through the forcing region and is meridionally redistributed.

Let us attempt to apply conditions (4.7), (4.10) to the forcing field defined by (3.2), inside the circle $x^2 + y^2 = r_1^2$. These give

$$(\xi_+ - \xi_-)\left\{-\frac{\alpha}{2B}(f_R\beta(\xi_+ + \xi_-) + 2\gamma\eta) + \frac{\gamma\beta}{F}\right\} = 0, \tag{5.1}$$

$$(\xi_+ - \xi_-)\left\{\frac{\alpha}{2\beta}(\xi_+ + \xi_-) - (f_R - 1)\frac{\gamma\beta}{FB}\right\} = 0. \tag{5.2}$$

These are incompatible unless $\xi_+ = \xi_-$, which merely denotes that there be no lower layer recirculation. If condition (5.2) were relaxed, then (5.1) asserts that any closed recirculating region in the lower layer symmetrically straddles

$$\xi = \frac{1}{2}(\xi_+ + \xi_-) = -\frac{\gamma}{f_R\beta}\eta + \frac{\gamma B}{f_R F\alpha}, \tag{5.3}$$

or $x = x_0 = \gamma\beta/F\alpha$, along lines of constant η (see Fig. 4).

Let us calculate the flow driven by (3.2). Solve first for ψ_2. This is done most easily

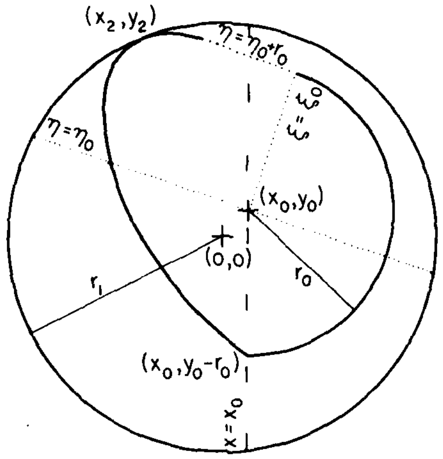

Figure 4. A schematic of the lower layer gyre inscribed within the region of wind forcing given by (3.2). Topography slopes up from west to east. The various points and lines marked are explained in the text.

from Eq. (4.5) in the tilted coordinate frame:

$$B\psi_{2\xi} = \gamma\beta/F - \alpha B^{-1}(f_R\beta\xi + \gamma\eta).$$

Integration with respect to ξ gives

$$\psi_2 = -\alpha/(2f_R\beta B^2)\,\{(f_R\beta\xi + \gamma\eta - \gamma\beta B/F\alpha)^2 - fn(\eta)\}, \tag{5.4}$$

where $fn(\eta)$ is an arbitrary function of η, to be determined. Upper layer streamfunction ψ_1 is related to this by (2.9). In particular, on the outer edge of the lower layer gyre, given by $x = x_\Gamma(y)$, where ψ_2 must be zero,

$$\psi_1 = -(\beta y + \gamma x)/F + \text{constant}. \tag{5.5}$$

Between x_Γ and the eastern edge of the forcing region, $x_E(y) = +(r_1^2 - y^2)^{1/2}$, where it is assumed that $\psi_1 = 0$, the simple Sverdrup relation applies to the upper layer flow:

$$\beta\psi_{1x} = W_o/H_1. \tag{5.6}$$

Integration gives

$$\beta(\beta y + \gamma x_\Gamma)/F + \text{const.} = -1/2\,\alpha(x_E^2 - x_\Gamma^2),$$

that is,

$$(x_\Gamma - x_0)^2 + (y - y_0)^2 = r_0^2, \tag{5.7}$$

where $x_0 = \beta\gamma/F\alpha$, $y_0 = \beta^2/F\alpha$, and r_0 is an arbitrary constant. This describes part of the boundary of the lower layer gyre east of the line $x = x_0$; evidently this segment is an arc of the circle, radius r_0, centered on (x_0, y_0). Setting $\psi_2 = 0$ in (5.4) and comparing to (5.7), after transformation to a common coordinate frame, permits the determination of $fn(\eta)$, namely:

$$fn(\eta) = \{\gamma(\eta - \eta_0) + f_R\beta[r_0^2 - (\eta - \eta_0)^2]^{1/2}\}^2. \tag{5.8}$$

The $\psi_2 = 0$ streamline is therefore given by

$$f_R\beta(\xi - \xi_0) + \gamma(\eta - \eta_0) = \pm\{fn(\eta)\}^{1/2}, \tag{5.9}$$

(where (ξ_0, η_0) is the same point as (x_0, y_0) in the tilted coordinate frame), or

$$B(x - x_0) = \pm\left\{fn\left(\frac{\gamma x + f_R\beta y}{B}\right)\right\}^{1/2}. \tag{5.10}$$

The positive root describes the arc of the circle (5.7); the negative root describes an ellipse centered on (x_0, y_0), with axis tilted at an angle $\pi/4 + 1/2$ arc tan $(\gamma/f_R\beta)$ clockwise to the x-axis, and joining on to the arc of the circle at $(x_0, y_0 - r_0)$; see Figure 4. These two branches of the streamline serve to cut off equal lengths on either side of $x = x_0$ along any line of constant η, thereby ensuring the satisfaction of condition (4.7). The $\psi_2 = 0$ streamline is not yet closed, for $fn(\eta)$ is not defined for $\eta > \eta_0 + r_0$. We shall address this point in a moment.

The constant r_0 is chosen so that the combined circle-ellipse shape is inscribed within the forcing circle of radius r_1. Some examples of r_0 for various parameter settings are given in Table 1. It can be shown that

$$r_0^2 \leq r_1^2 - x_0^2 - y_0^2, \tag{5.11}$$

so that $x_0^2 + y_0^2 < r_1^2$ is a necessary condition for the existence of the closed lower layer gyre. This means that

$$W_{\max}/H_1 = \alpha r_1 > \frac{\beta}{F}(\beta^2 + \gamma^2)^{1/2}, \tag{5.12}$$

which may be compared to RYb's condition $\alpha r_1 > \beta^2/F$ for $\gamma = 0$. The maximum Sverdrup transport of the gyre that would be driven by (3.2) without topography is $H_1\alpha r_1^2/2\beta$. Inequality (5.12) suggests that this must be larger than $H_1 r_1(\beta^2 + \gamma^2)^{1/2}/2F$ to drive bottom circulation. Taking $H_1 = 2000$ m, $r_1 = 1000$ km, $\beta = \gamma = 10^{-11}$ m^{-1} s^{-1}, $F = (30 \text{ km})^{-2}$, this threshold value is about 13×10^6 m^3 s^{-1}, not an unreasonable figure for the magnitude of typical wind forcing on ocean gyres.

Table 1. Circulation driven by circular dipole wind-stress curl over east-west topography. First line of each entry gives parameters for westward throughput, second line for eastward throughput. In all cases, $f_R = 3.0$.

x_o/r_1	y_o/r_1	r_o/r_1	$\frac{2\beta}{\alpha r_1^2}\psi_{1W}(y_2)$	$\frac{2\beta}{\alpha r_1^2}\psi_{2\max}$	x_2/r_1	y_2/r_1
0.25	0.5	.441	.041	.065	.111	.965
		.468	.046	.073	.398	.006
0.125	0.25	.701	.104	.164	−0.097	.989
		.742	.116	.184	.360	−0.532
0.0625	0.125	.787	.131	.207	−0.186	.954
		.873	.161	.254	.339	−0.795
0.5	0.5	.293	.065	.029	.338	.852
		.366	.101	.045	.703	.060
0.25	0.25	.619	.288	.128	−0.093	.993
		.697	.365	.162	.637	−0.588
0.125	0.125	.685	.353	.156	−0.255	.949
		.726	.396	.176	.528	−0.748
0.8	0.4	.106	.027	.004	.716	.576
		.183	.081	.011	.946	.095
0.5	0.25	.441	.470	.065	.147	.985
		.426	.439	.060	.841	−0.460
0.25	0.125	.518	.649	.089	−0.164	.988
		.507	.621	.086	.656	−0.720

The elliptical segment of the boundary of the lower layer gyre attains its maximum northern extent at the point (x_2, y_2), shown on Figure 4. Between the latitude of this point and the latitude y_2' of its reflection in $\xi = \xi_0 - \gamma r_0/f_R\beta$, the characteristics enter from, and double back toward, the east (as shown schematically in Fig. 3). Since ψ_1 can be specified to be zero only on one end of these characteristics, it will in general differ from zero on the other end. Hence, there must be a relatively narrow zonal jet in the upper layer below latitude y_2 impinging on the forcing region and drawn by it from the east. We shall presently compute the transport of this jet. Above y_2 and below y_2', all characteristics pass through the forcing region from east to west. The values of ψ_1 on either end of characteristics that pass over the lower layer gyre must differ. This is a restatement of the failure of condition (4.10). This means that the zonal jet incident from the east emerges, redistributed meridionally, in the west.

Between the ellipse, where (5.5) applies, and the western boundary of the forcing region $x_W = -(r_1^2 - y^2)^{1/2}$, the conventional Sverdrup relation (5.6) holds, from which $\psi_{1W}(y) = \psi_1(x_W, y)$ can be computed. This is not zero. Integrating (5.6) from x_2 to $x_W(y_2)$ along $y = y_2$, we obtain

$$\beta[\psi_1(x_2, y_2) - \psi_{1W}(y_2)] = 1/2\,\alpha(r_1^2 - x_2^2 - y_2^2).$$

Since (x_2, y_2) and $(x_0, y_0 - r_0)$ lie on $\psi_2 = 0$, (5.5) can be used to calculate the difference

$$\beta[\psi_1(x_0, y_0 - r_0) - \psi_1(x_2, y_2)] = \alpha x_0(x_2 - x_0) + \alpha y_0(y_2 - y_0 + r_0).$$

At $y = y_0 - r_0$, (5.6) can be used to compute

$$\beta[\psi_{1w}(y_0 - r_0) - \psi_1(x_0, y_0 - r_0)] = 1/2\, \alpha(x_0^2 + (y_0 - r_0)^2 - r_1^2).$$

(Note that $\psi_{1w}(y_0 - r_0) = \psi_1(-[r_1^2 - (y_0 - r_0)^2]^{1/2}, y_0 - r_0) = \psi_1(+[r_1^2 - (y_0 - r_0)^2]^{1/2}, y_0 - r_0) = 0$.) Addition of these three equations gives

$$\psi_{1w}(y_2) = \frac{\alpha}{2\beta}[(x_2 - x_0)^2 + (y_2 - y_0)^2 - r_0^2]. \tag{5.13}$$

This formula gives the volume transport in the upper layer emerging from the forcing region on the western side, whence it proceeds in a zonal flow toward the west. The volume transport of the narrow zonal jet impinging on the eastern side must be exactly the same.

Above latitude y_2, ψ_1 = constant = $\psi_{1w}(y_2)$ on both western and eastern limbs of the forcing boundary. Between $y = y_2$ and $y = y_0 + f_R\beta r_0/B$ (which corresponds to the latitude of the northernmost sweep of the circular arc boundary of the lower layer gyre, at $\eta = \eta_0 + r_0$, $\xi = \xi_0$), ψ_1 changes from this value to zero, which it maintains along the remainder of the western boundary of the forcing region. We remarked above that ψ_2 is not defined by (5.4), (5.8) for $\eta > \eta_0 + r_0$. This merely reflects the fact that the $\psi_1 = 0$ condition on the eastern forcing boundary cannot be sustained for larger η. The lower layer gyre can be closed by connecting the ends of the ellipse and the circle at $\eta = \eta_0 + r_0$ by any curve that cuts equal lengths on either side of $x = x_0$ along lines of constant η, so that condition (4.7) is maintained. This flexibility affects the precise distribution of the zonal flow incident from the east between $y_0 + f_R\beta r_0/B$ and y_2, though not its total transport. This minor indeterminacy is settled by an appropriate upstream condition.

So, to sum up, the circular dipole draws a narrow zonal jet from the east in the upper layer, circulates it anticyclonically around the forcing region, and expels it in a much broader zonal flow to the west. Presumably the rest of the ocean can organize itself in some way, by means of boundary layers, etc., to close the mass flow circuit. Examples of such flows are shown in Figures 5 and 6. The latter corresponds to twice the east-west slope of the former. Note the weak counterflows in the broader zonal jets in the west. The lower layer gyre is offset to the north by β-effect and to the east by topography. The eastward offset increases with slope and, because the lower gyre must be contained within the forcing region, becomes more constricted and weaker. Despite this, the zonal throughput increases from $\psi_{1w}(y_2) = 0.353$ to $\psi_{1w}(y_2) = 0.649$, in scaled units (Table 1). (The slight irregularities in these figures are artifacts of the contouring programs.)

It is remarkable that it is impossible to construct a solution that has $\psi_1 = 0$ everywhere to the east of the forcing region. This contradicts conventional wisdom,

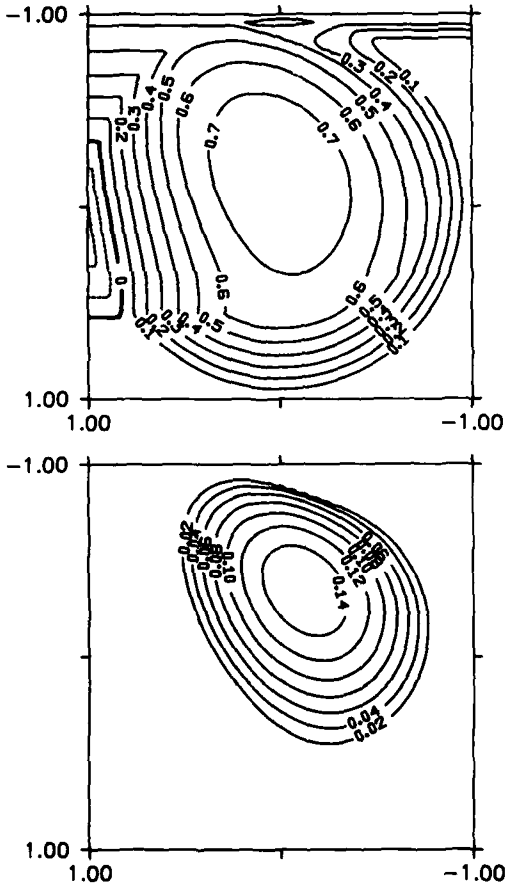

Figure 5. Upper layer streamfunction ψ_1, (a), and lower layer streamfunction ψ_2, (b), for $x_0/r_1 = y_0/r_1 = 0.125, f_R = 3$. A solution giving a westward throughput is shown, with $r_0/r_1 = 0.685$. Both streamfunctions are scaled by $\alpha r_1^2/2\beta$.

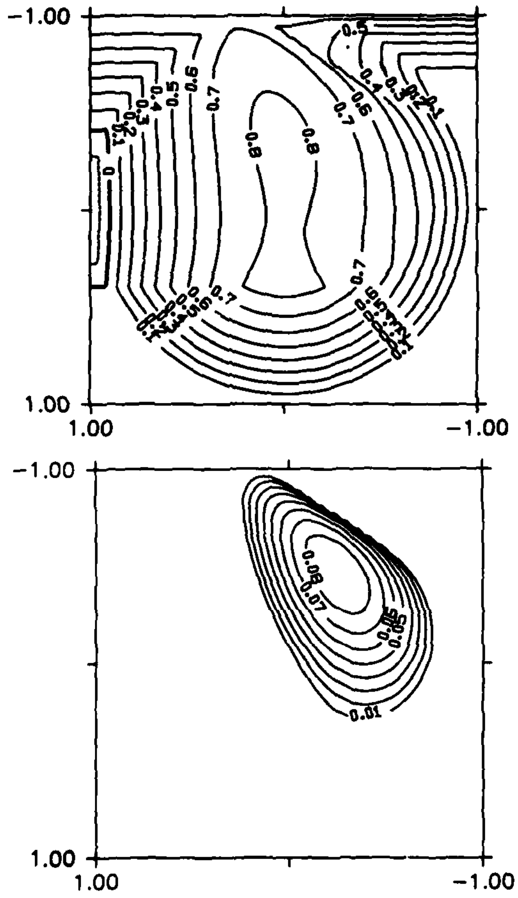

Figure 6. Like Figure 5, for $x_0/r_1 = 0.25$, $y_0/r_1 = 0.125$, $f_R = 2$, A solution for westward throughput is shown, with $r_0/r_1 = 0.518$.

based on flat-bottom assumptions, about computing Sverdrup interior flows by assuming zero flow in the eastern boundary. Of course, it is not at all necessary to demand $\psi_1 = 0$ on the eastern boundary. However, a different choice will in general affect the shape of the closed lower layer circulation. For example, in setting up the solution for the lower layer flow, we chose to orient the segment with the circular boundary in the east and the segment with the tilted elliptical boundary in the west. There is no reason not to reverse this choice, putting the circular segment in the west and satisfying $\psi_1 = 0$ along the western boundary of the forcing region opposite this segment. This corresponds to taking the negative root of the radical, $-[r_0^2 - (\eta - \eta_0)^2]^{1/2}$, instead of the positive, in the definition of $fn(\eta)$, Eq. (5.8), and amounts to rotating the pattern of Figure 4 through 180°. The constant r_0 has to be readjusted to inscribe this reversed shape into the forcing circle. The intense zonal jet now finds itself flowing in from the west in the southwestern sector of the gyre, and emerging in the east, more diffuse and displaced to the north. Examples of such flows with eastward throughput are shown in Figures 7 and 8, corresponding respectively to Figures 5 and 6. Again, note the counterflows in the broader zonal flows now found in the east. The same remarks can be made about eastward shift, constriction and weakening of the lower layer gyre with increasing slope; and about the increasing zonal throughput (see Table 1).

Table 1 lists some vital statistics of the solutions for various settings of the dimensional parameters γ, β, α, F, r_1 in the nondimensional groups $x_0/r_1 = \gamma\beta/F\alpha r_1$, $y_0/r_1 = \beta^2/F\alpha r_1$; with $f_R = 3$ throughout. The first line for each setting corresponds to westward throughflow; the second line to eastward throughflow. The geometrical meanings of $x_0, y_0, r_0, r_1, x_2, y_2$ are clear from the discussion and from Figure 4. $\psi_{1W}(y_2)$ is the transport of the zonal jet being pumped through the forcing region in the upper layer. It is scaled in Table 1 by $\alpha r_1^2/2\beta$, the magnitude of the gyral transport that would be forced if there were no lower layer flow. For weak forcing (small αr_1, large x_0, y_0), $\psi_{1W}(y_2)$ is quite small: only a few percent for the examples in Table 1. For strong forcing (large αr_1, small x_0, y_0) $\psi_{1W}(y_2)$ can be substantial: for $x_0 = y_0 = 0.125r$, $\psi_{1W}(y_2)$ is 40%; with stronger topography (larger x_0), $x_0 = 0.25r$, $y_0 = 0.125r$, for example, $\psi_{1W}(y_2)$ is 62%. The scaled strength of the lower layer gyre, $\psi_{2\max}$, is also tabulated. It depends, roughly, on the size of the gyre that can be inscribed within the forcing region. The largest $\psi_{2\max}$ by no means correspond to the largest $\psi_{1W}(y_2)$. Values of $\psi_{2\max}$ as large as 25% are achieved for $x_0/r_1 = 0.0625$, $y_0/r_1 = 0.125$, i.e., strong forcing, weak topography.

Table 1 reflects results, and Figures 5–8 show flow patterns, for situations where $\gamma > 0$ (topography sloping up to the east) and $\alpha > 0$ (dipole forcing with upwelling in the western half-disc, downwelling in the eastern). Reversed topographic slope and reversed forcing can be easily considered from symmetry considerations. For negative γ, the entire flow pattern for the corresponding positive value need only be reflected in the y-axis, while the anticyclonic sense of circulation in both layers is maintained, as is

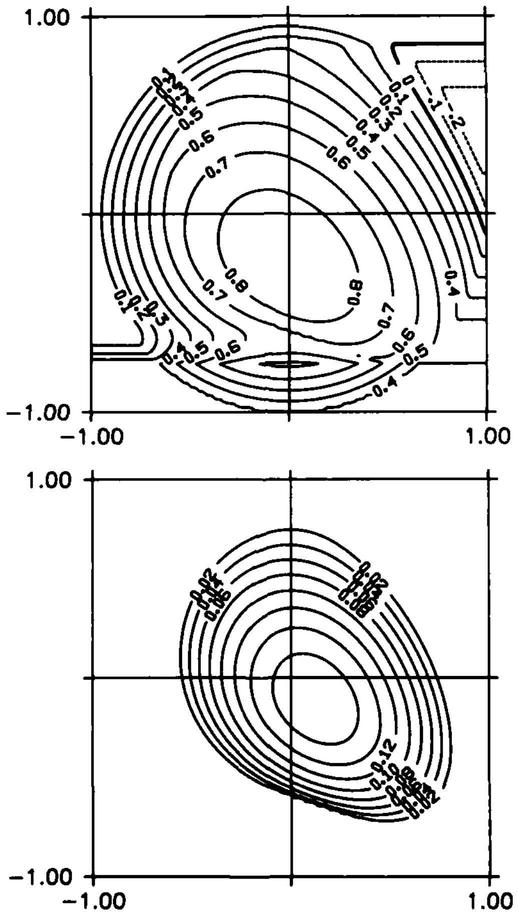

Figure 7. Like Figure 5 for $x_0/r_1 = y_0/r_1 = 0.125$, $f_R = 3$, except showing eastward throughput with $r_0/r_1 = 0.726$.

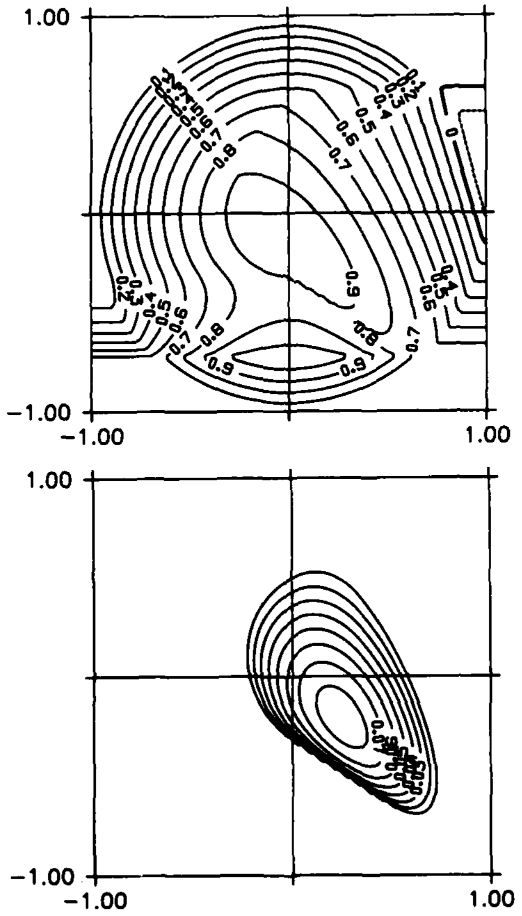

Figure 8. Like Figure 6, for $x_0/r_1 = 0.25$, $y_0/r_1 = 0.125$, $f_R = 3$, except showing eastward throughput with $r_0/r_1 = 0.507$.

the sense of zonal throughflow. For reversed forcing, $\alpha < 0$, the corresponding $+ |\alpha|$ flow pattern must be rotated through 180°, although the sense of circulation and the zonal throughput must be reversed.

6. Circulation over east-west bottom slope driven by a 'bizarre' dipole

In this Section, we shall construct examples of wind-stress curl fields that produce closed circulation in both layers. The method is to deduce an incomplete W_o-field that is necessary to drive, according to (4.7) and (4.10), a recirculating gyre in the lower layer. Next the W_o-field is extended beyond the lower layer gyre until it is defined out to boundaries $x_E(y)$, $x_w(y)$ within which the upper layer circulation is closed, consistent with (4.10). This backward reasoning, from lower layer gyre to forcing field, leads to very peculiarly shaped forcing fields, which we shall term the 'bizarre dipoles'.

The tilted dipole forcing field given by

$$W_o/H_1 = -\gamma\beta/F - \alpha\xi \tag{6.1}$$

satisfies condition (4.7) within a circle of radius r_0, say, centered on the origin. If, in (4.7) and (4.10), we use

$$\xi_\pm = \pm(r_0^2 - \eta^2)^{1/2} \quad \text{or} \quad x_\pm = \pm(r_0^2 - y^2)^{1/2}, \tag{6.2}$$

then, from (4.5) with $\psi_2 = 0$ on and beyond these boundaries:

$$\psi_2 = \frac{\alpha}{2B}(r_0^2 - x^2 - y^2), \qquad x^2 + y^2 < r_0^2. \tag{6.3}$$

In the same region the streamfunction in the upper layer can be calculated from (2.9):

$$\psi_1 = -\frac{R + D}{2R}\frac{\alpha}{B}\{(x - x_*)^2 + (y - y_*)^2 - x_*^2 - y_*^2 - r_0^2\} + \psi_0, \quad x^2 + y^2 < r_0^2, \tag{6.4}$$

where

$$x_* = -\frac{R}{R + D}\frac{\gamma}{\beta}y_1, y_* = -\frac{R}{R + D}y_1, y_1 = \frac{\beta B}{F\alpha}.$$

Hence, the streamlines in the upper layer above the lower layer gyre are segments of concentric circles set off to the west (for $\gamma > 0$) and south from the center of the streamline circles in the lower layer.

Outside the lower layer gyre, we take the wind-stress curl distribution (6.1) to continue, and integrate (4.9) outward along latitude lines to obtain

$$\psi_1 = \frac{\alpha f_R}{2B}\left\{\left[x_+ - \frac{\gamma}{f_R\beta}(y - y_1)\right]^2 - \left[x - \frac{\gamma}{f_R\beta}(y - y_1)\right]^2\right\}$$
$$- \frac{1}{F}(\beta y + \gamma x_+) + \psi_0, \qquad (6.5)$$

for $x > x_+(y) = +(r_0^2 - y^2)^{1/2}$. For $x < x_-(y) = -(r_0^2 - y^2)^{1/2}$, $x_+(y)$ is replaced by $x_-(y)$ in (6.5). The arbitrary function of y from the integration has been chosen to match (6.4) on the circumference of the lower layer gyre.

To obtain closed circulation in the upper layer, the outer boundary of the forcing region must coincide with a streamline ψ_1 = constant. The streamline $\psi_1 = -r_0(\beta^2 + \gamma^2)^{1/2}/F + \psi_0$ is tangential to the circle containing the lower layer gyre at $(x, y) = r_0(\gamma, \beta)/(\beta^2 + \gamma^2)^{1/2}$, and does not approach the circle anywhere else for $|y| < r_0$ in either the eastern or western sector. We choose this streamline to define the boundary of the forcing region. (Choosing $\psi_0 = r_0(\beta^2 + \gamma^2)^{1/2}/F$ makes this the $\psi_1 = 0$ streamline.) For $\gamma = 0$, (6.5) reduces to

$$\psi_1 = \frac{\alpha f_R}{2\beta}\left[\left(r_0 + \frac{\beta^2}{F\alpha f_R}\right)^2 - x^2 - \left(y + \frac{\beta^2}{F\alpha f_R}\right)^2\right] \qquad (6.6)$$

within a circle centered on $(0, -\beta^2/F\alpha f_R)$ with radius $r_0 + \beta^2/F\alpha f_R$. This is precisely RYb's circulation associated with the circular dipole. The streamlines defined by (6.5) do not close in the strip $|y| < r_0$, beyond which (6.5) is not defined. To complete the description of the forcing and to close the flow beyond $y = \pm r_0$, simply extend the $\psi_1 = 0$ streamline and the forcing boundary along any curve that cuts off equal lengths at any latitude on either side of the $W_0 = 0$ line. Any such choice guarantees the closure of the upper layer streamlines through the region $|y| > r_0$. One simple choice is straight line segments from $y = \pm r_0$ to points on the line $f_R\beta x - \gamma(y - y_1) = 0$. This is the choice made in Figures 9 and 10. RYb's choice for the case $\gamma = 0$ amounts to extending the circular shape of the $\psi_1 = 0$ streamline beyond $y = -r_0$ until it recloses; nothing is required north of $y = +r_0$.

Figures 9, 10 show the upper layer streamline patterns and the specially tailored forcing fields necessary to force a circular lower layer gyre for a selection of settings of y_1/r_0, γ/β and R/D (or f_R). Only positive values of y_1, γ/β are shown in Figures 9, 10. The sense of circulation is anticyclonic. For corresponding negative values of γ (upward slope to the west) the pictures must be reflected in the y-axis, while retaining the anticyclonic sense of motion. For $\alpha < 0$, which represents reversed forcing, so that $y_1 < 0$, the pictures must be reflected in $\gamma x + \beta f_R y = 0$, with the sense of circulation reversed. Also shown in Figures 9, 10 are the dashed lines $\beta f_R x - \gamma(y - y_1) = 0$, and $\beta x - \gamma y = 0$. The first is the line of zero wind-stress curl, with positive curl in the northwest region, negative in the southeast. The second line is perpendicular to the

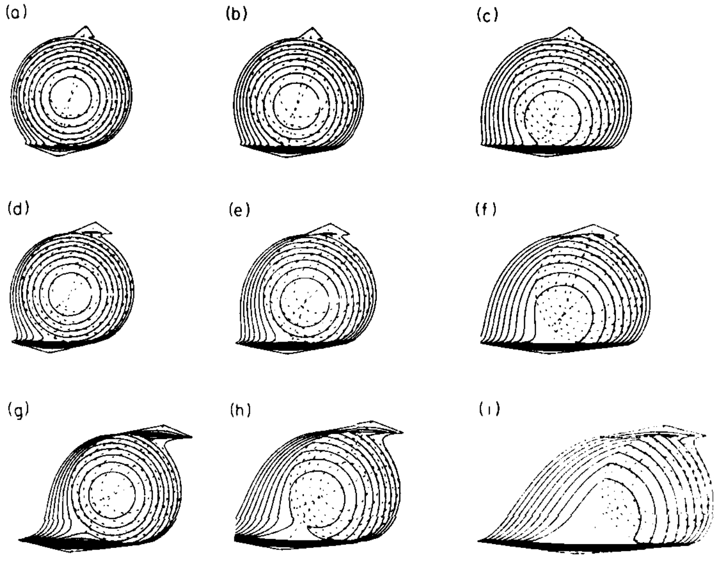

Figure 9. Upper and lower layer circulation patterns for various forcing fields and varying topography. Solid lines are upper layer streamlines, dashed circles are lower layer streamlines. Wind stress curl is positive to left of longer dashed straight line, negative to the right. Sense of circulation is anticyclonic (clockwise). Contouring interval (nondimensional) for lower layer flow is $B\Delta\psi_2/\alpha r_0^2 = 0.2$ on all panels; for upper layer flow, $\Delta\psi_1$ varies. The lower layer gyre has nondimensional radius 1 on all panels. (a) $y_1/r_0 = 0.25$, $\gamma/\beta = 0.5$, $B\Delta\psi_1/\alpha r_0^2 = 0.144$; (b) $y_1/r_0 = 0.5$, $\gamma/\beta = 0.5$, $B\Delta\psi_1/\alpha r_0^2 = 0.182$; (c) $y_1/r_0 = 1.0$, $\gamma/\beta = 0.5$, $B\Delta\psi_1/\alpha r_0^2 = 0.270$; (d) $y_1/r_0 = 0.25$, $\gamma/\beta = 1.0$, $B\Delta\psi_1/\alpha r_0^2 = 0.154$; (e) $y_1/r_0 = 0.5$, $\gamma/\beta = 1.0$, $B\Delta\psi_1/\alpha r_0^2 = 0.204$; (f) $y_1/r_0 = 1.0$; $\gamma/\beta = 1.0$, $B\Delta\psi_1/\alpha r_0^2 = 0.324$; (g) $y_1/r_0 = 0.25$, $\gamma/\beta = 2.0$, $B\Delta\psi_1/\alpha r_0^2 = 0.182$; (h) $y_1/r_0 = 0.5$, $\gamma/\beta = 2.0$, $B\Delta\psi_1/\alpha r_0^2 = 0.270$; (i) $y_1/r_0 = 1.0$, $\gamma/\beta = 2.0$, $B\Delta\psi_1/\alpha r_0^2 = 0.498$; $R/D = 1.0$ throughout.

lines of constant f/h (where $h = H - h'_T$), to within the quasigeostrophic approximation. It also forms a diameter of the circular gyre in the lower layer, whose extent and streamlines are indicated by the dashed circles. The center of the upper-layer circulation, whose streamlines are the solid lines, is at the intersection (x_*, y_*) (defined after Eq. (6.4)) of these two lines. The outermost upper layer streamline shown is $\psi_1 = 0$, beyond which the wind-stress curl is set to zero. The upper layer streamline interval is indicated on each panel. Figure 9 shows all combinations of $y_1/r_0 = 0.25, 0.5, 1.0$ and $\gamma/\beta = 0.5, 1.0, 2.0$ for $R/D = 1.0$. Figure 10 shows $R/D = 0.125, 0.25, 1.0, 2.0, 8.0$ for $y_1/r_0 = 0.5$, $\gamma/\beta = 1.0$. Comparing panels in Figure 9 with

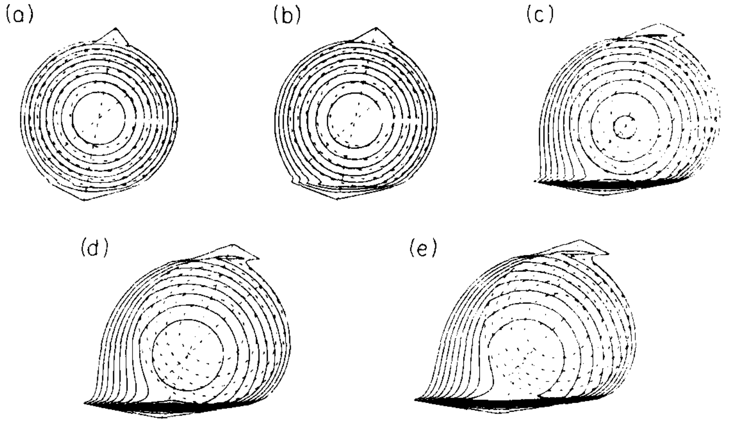

Figure 10. Upper and lower layer circulation patterns as in Figure 9. (a) $R/D = 0.125$, $B\Delta\psi_1/\alpha r_0^2 = 0.58$; (b) $R/D = 0.25$, $B\Delta\psi_1/\alpha r_0^2 = 0.362$; (c) $R/D = 1.0$, $B\Delta\psi_1/\alpha r_0^2 = 0.200$; (d) $R/D = 2.0$, $B\Delta\psi_1/\alpha r_0^2 = 0.180$: (e) $R/D = 8.0$, $B\Delta\psi_1\alpha r_0^2 = 0.166$; $y_1/r_0 = 0.5$, $\gamma/\beta = 1.0$ throughout.

the same γ/β and R/D but differing y_1/r_0, one sees the effect of varying the strength of the forcing, upon which y_1/r_0 depends inversely: the weaker the forcing (large y_1/r_0), the more the lower layer gyre is skewed away from the upper layer gyre along $\beta x - \gamma y = 0$. The effect of increasing γ/β (increasing topography) is to skew the displacement of the lower layer gyre more to the west than to the north, compared to when the β-effect acts alone. Figure 10 shows the effect of varying R/D for the same y_1/r_0, γ/β. For large R/D the lower layer flow is more nearly comparable in magnitude to the upper layer flow. (Note the decreasing contouring intervals for ψ_1 employed in Figure 10 as R/D increases.) Conversely, for small R/D the bottom flow is weak, in accord with the intuitive notion of the arresting effect of large bottom friction. As RYb note, potential vorticity in the lower layer tends to become uniform for large R/D, that is, for horizontal diffusion dominating vertical diffusion of vorticity; this can be confirmed from Eq. (2.7) as $R/D \rightarrow \infty$, i.e.,

$$dq_2/d\psi_2 = 1/(dA_2/dq_2) \rightarrow 0.$$

The shapes of the forcing fields shown on Figures 9, 10 are rather bizarre. There are sharp cusps in the northeast and southwest corners of the forcing field. These features are an artifact of the insistence, not essential, on a perfect circular form for the gyre in the lower layer, and the linear growth of forcing away from the dipole axis, coupled to the conditions (4.7) and (4.10) for closed lower and upper layer circulation. Relaxation of the inessential requirements may permit smoother, more aesthetically pleasing, forcing fields.

The essential, germane features of our solutions are the following. The center of the lower layer gyre is set off from the center of the upper gyre along the line $\beta x - \gamma y = 0$, across f/h contours in effect, by an amount inversely proportional to the strength α of the forcing. This offset is similar to the effect noted by RYb. The direction of offset is a consequence of the occurrence in (2.9) in equal proportion of the planetary vorticity βy and topographic vorticity $h_T = \gamma x$. The slope of the characteristic lines of the circulation equation (4.3), however, is $f_R\beta/\gamma$. This f_R-fold amplification of β over γ in the proportional relation of ψ_2 to ψ_B depends on the ratio R/D of the frictional coefficients. When $R = D$, for example, $f_R = (2R + D)/R = 3$. These features should survive whatever form of forcing field, consistent with (4.7) and (4.10), is adopted.

Subsidiary features in Figure 9 include the occurrence of weak secondary anticyclonic gyres in the upper layer in the northeast and southwest regions in some cases. These are associated with characteristic lines that reverse direction after crossing the lower layer gyre, as was shown schematically in Figure 3. We have already remarked on the unappealing character of the cusps at $y = \pm r_0$. A given cusp can be smoothed by an appropriate choice of the forcing boundary outside the lower layer recirculation region. Usually, if (4.7) and (4.10) are to be met, this only transfers the cusp from the eastern to the western side, or vice versa. Conversely, if a cusp on the western side is smoothed, condition (4.10) will not be fulfilled (while (4.7) is met, however). This means that a zonal jet with westward and eastward bands and zero net transport, must emerge from the forcing region in the upper layer between the latitudes where (4.10) is violated on its western edge. The role of this jet is to export the excess vorticity being generated by the forcing and by the topographic stretching. This excess vorticity can be dumped, possibly, at a solid western boundary in a frictional boundary current. As long as these vigorous frictional effects are confined to the upper layer, the validity of the reasoning of Section 2 is unaffected.

7. Extensions of the theory

a. N layers and the continuous limit. The theory given for two layers can be readily extended to an arbitrary number of layers. Indeed, the limit can be taken of a large number of layers, which approaches the description of a continuous model. This treatment is related to the Appendix. In summary, continuous (or discrete) solutions, analogous to and extending (2.11), (2.12), can be written down for an arbitrary background distribution of density $\bar{\rho}(z)$. This is that potential vorticity is uniform on isopycnal surfaces in the interior (Eq. (A5), Appendix),

$$\frac{\partial}{\partial z}\left(\frac{f_0^2 \partial\psi}{N^2 \partial z}\right) + \beta y = Q(\bar{\rho}) \qquad (7.1)$$

(cf. RYa), and that the barotropic (vertically integrated) transport stream function

$\Psi = \int_h^0 \psi dz$ is governed by (Eq. (A12), Appendix)

$$J(\Psi, \beta y + \chi f_0 h'_T/H) = -\chi f_0^{-1} gAHJ(\beta y, h'_T) + W_o, \tag{7.2}$$

where $\chi = (1 + gB\delta_E/f_0K)^{-1}$, and A and B are parameters determined by the stratification, given by (A11). The factor χ is the generalization of $2/f_R$, which appears in (2.11). Note that $\chi < 1$. There is a curious additional forcing term in (7.2) which depends on the part of topography that slopes across the gradient of planetary vorticity, and on the stratification through the factor A. For large horizontal diffusivity K, χ approaches 1, so that the characteristic lines for the transport are

$$\beta y + f_0 h'_T/H = \text{constant},$$

in effect f/h contours, like the result for a homogeneous ocean, except for the additional forcing term in (7.2). For a homogeneous ocean, A and B vanish, and the same characteristic lines are recovered, whatever the diffusivity. For $B = (\bar{\rho}(-H) - \hat{\rho})/\rho_0 = 10^{-3}$, $\delta_E = 10$ m, $K = 10^3$ m^2 s^{-1}, $f_0 = 10^{-4}$ s^{-1},

$$gB\delta_E/f_0K = 1.0,$$

so that the attentuation factor χ is 0.5. Smaller diffusivity or strong stratification reduces χ, and so reduces the influence of topography in (7.2). An equation corresponding to (7.2) for the streamfunction ψ_N just above the bottom frictional boundary layer is derived in the Appendix. It is

$$J(\psi_N, \beta y + \chi f_0 h'_T/H) = -\chi gBf_0^{-1} J(\beta y, h'_T) + \chi W_o/H. \tag{7.3}$$

Eqs. (7.2), (7.3) share the same characteristic lines,

$$\eta(x, y) = \beta y + \chi f_0 h'_T/H = \text{const}. \tag{7.4}$$

Both equations hold only in regions where there is a nonvanishing closed bottom flow, $\psi_N \neq 0$. If $\xi\,(x, y) =$ constant describes a family of lines orthogonal to (7.4), then the boundaries $\xi_*(\eta)$ of the region of closed bottom circulation, where $\psi_N(\xi_*, \eta) = 0$, η must satisfy

$$\int_{\xi}^{\xi_*} (-gBf_0^{-1} J(\beta y, h'_T) + W_o/H) d\xi = 0 \tag{7.5}$$

(cf. 4.7).

Eq. (7.2) is a useful practical relation for determining the barotropic transport ψ above topography. Subtlety is required in its correct application, however: it applies only above *closed* bottom circulation. This must be checked with Eq. (7.3). Where the lower layer circulation cannot close, we take it to be stagnant, so that the simple Sverdrup balance holds:

$$\beta \Psi_x = W_o. \tag{7.6}$$

The barotropic transport of the two regions must be matched at their common boundary. Since this boundary depends implicitly on the flow and the forcing, the solution of (7.2) and (7.6), despite their linear appearance, is subtly nonlinear. The process of solution for a given wind stress curl field, albeit a very simple one, is illustrated for the dipole forcing in Section 5.

The dependence of the barotropic transport on turbulent exchange coefficients through the parameter χ is noteworthy. This comes about because the bottom flow which determines the topographic vortex stretching, is related to the barotropic flow through subtle considerations on the turbulent diffusion of potential vorticity. This dependence is a practical disadvantage in the application of (7.4) because of the large uncertainties of estimates of turbulent eddy diffusivities, especially on quasi-horizontal surfaces (Freeland *et al.*, 1975).

b. Weakly nonharmonic topography. A major restriction of the theory is that topography $h_T(x, y)$ must be harmonic, $\nabla^2 h_T = 0$. (The example of uniform slope in the calculations given above is convenient for illustration, though not essential.) It is not easy to relax this restriction, for on it depends the cancellation of $\oint \mathbf{u}_2 \cdot ds$ on both sides of Eq. (2.6), from which follows the simple specification of the function $A_2(q_2)$; otherwise, A_2 is specified in terms of a nasty circulation integral whose path and value depend *implicitly* on q_2 in a manner not obvious.

What if $\nabla^2 h_T$ is approximately zero? More precisely, how small must it be to the negligible? The expression in curly brackets in Eq. (2.6) can be written

$$\int [F(\omega_1 - \omega_2) + \frac{f_0}{H_1} \nabla^2 h'_T]\, dA \tag{7.7}$$

where ω_1, ω_2 are the relative vorticities of the upper and lower layer. These must be of order ϵf_0 where $\epsilon = U/f_0 L$ is the Rossby number of the gyral scale flow. If variations of h'_T are of order H_1 on scales L_T, then a scaling condition for the neglect of the topographic term in the integral is

$$L_T \gtrsim (\epsilon F)^{-1/2}, \tag{7.8}$$

which is $\epsilon^{-1/2}$ times the Rossby radius of deformation. Were this condition to be met, as it might be for large-scale topographic variation ($F^{-1/2}$ is typically 10–100 km), then extensions of (2.10) and (4.3) would hold (in the simplest two-layer theory):

$$\psi_2 = \frac{1}{f_R}\left(\frac{\beta y + h_T}{F} + \psi_B\right) + \text{const.}, \tag{7.9}$$

$$\beta \psi_{Bx} - \frac{1}{f_R}\left\{J(h_T, \psi_B) + \frac{\beta}{F} h_{Tx}\right\} = W_o/H_1, \tag{7.10}$$

where $h_T = f_0 h'_T/H_1$. If bottom friction is much stronger than internal diffusivity, $D \gg$

R, so that $1/f_R \rightarrow 0$, then the bottom flow ψ_2 is arrested, the second term in (7.10) is small, and the simple Sverdrup relation holds, despite topography. Otherwise, if condition (7.8) is met, or even a weaker condition that ensures that the second term in (7.7) is small compared to the first, and the lower layer flow is closed in the ocean interior away from side boundaries, so that (7.9) holds, then the modified circulation equation (7.10) holds.

8. Summary

We have derived a circulation equation (7.2) which is a generalization of the Sverdrup relation between wind-stress curl and vertically integrated transport for the case of stratified ocean flowing over topography. The circulation equation holds only for wind forcing sufficiently strong to drive circulation that penetrates to the bottom.

For the simple wind-stress curl patterns of Sections 3, 4 and 5, it was possible to determine precisely what 'sufficiently strong' means. While more complicated wind-stress curl distributions have to be evaluated by individual computations, it seems that curl distributions with length scales of order 100 km and sufficiently strong to drive ocean gyre transports of order $20 \times 10^6\ \mathrm{m^3\,s^{-1}}$ without topography are necessary. Such magnitudes are not impossible to achieve over the ocean. The new circulation equation holds over the closed deep gyre. Elsewhere the deep flow is stagnant and the standard Sverdrup relation applies. While Eq. (7.2) and the Sverdrup relation appear linear, the determination of the boundary between the regions of applicability of the two is implicit and nonlinear. The method of determining this boundary and the flows in the various density strata of the ocean is illustrated for two layers and a simple wind-stress curl pattern in Section 5.

The theory of the circulation equation depends on quasigeostrophic vorticity dynamics, though we showed that it can readily be extended to an arbitrary number of layers or even the continuous case (Section 7 and Appendix A). According to this theory, unventilated layers not in direct contact with the surface or the bottom achieve homogeneous potential vorticity, as in the theory of RYa,b.

A troubling restriction of the theory is that it applies only to uniformly sloping topographies or to topographies satisfying the harmonic condition, $\nabla^2 h = 0$. In Section 7 we advanced a scaling argument for the criterion that scales of topography be large compared to the Rossby radius of deformation, in which case $\nabla^2 h$ is approximately zero.

A factor χ multiplies the topography in the circulation equation. This factor depends on the stratification, the bottom friction and the horizontal turbulent diffusivity (of heat). It is troubling that the large-scale circulation might be sensitive to so ill-defined and crudely known a quantity as horizontal turbulent diffusivity. Nevertheless this dependence is quite fundamental: it is the frictional and diffusive processes, however they are parameterized, that determine the circulation in closed gyres.

Acknowledgments. This work has been supported under National Science Foundation grants OCE-8117700, OCE-8316930 and Office of Naval Research contract number N00014-84-C-0218.

APPENDIX

N layers; the continuous limit

The extension of the treatment of an arbitrary number N of layers is so straightforward that it suffices to state the problem and results in the sparest detail. Suppose the mean thickness and density of the n-th layer are H_n, ρ_n. The total mean depth of the ocean is $H = \Sigma H_n$. The vorticity equations for the layers are

$$J(\psi_n, q_n) = \delta_{n1} W_o/H_1 + K\nabla^2\left(q_n - \beta y - \delta_{nN} f_0 \frac{h'_T}{H_n}\right) - \delta_{nN} D\nabla^2\psi_N, \tag{A1}$$

for $n = 1, \ldots, N$, where $W_o = \hat{z} \cdot \nabla x\tau/\rho_0$, $\delta_{nm} = 1$ for $n = m$, $\delta_{nm} = 0$ for $n \neq m$, and $\delta'_{nm} = 1 - \delta_{nm}$. The potential vorticities of the layers are

$$q_n = \beta y + \frac{f_0^2\rho_0}{gH_n}\left\{\delta'_{nN}\frac{\psi_{n+1} - \psi_n}{\rho_{n+1} - \rho_n} - \delta'_{n1}\frac{\psi_n - \psi_{n-1}}{\rho_n - \rho_{n-1}}\right\} + \delta_{nN} f_0 \frac{h'_T}{H_N}\Bigg\}. \tag{A2}$$

K is the horizontal turbulent exchange coefficient. The frictional coefficient at the bottom is $D = f_0\delta_E/H_N$, where $\delta_E = (2A_v(-H)/f_0)^{1/2}$ is the Ekman boundary layer thickness (Pedlosky, 1979). Neglecting friction, we see that in all layers but the first

$$q_n = Q_n(\psi_n). \tag{A3}$$

The functions Q_n can be determined in each layer by RYb's method of examining the line integral of the vorticity equations around a q_n isostrophe. It may then be shown that in every layer but the first and N-th, these functions are mere constants, that is, potential vorticity is constant in each layer:

$$q_n = \frac{f_0^2\rho_0}{gH_n}\left\{\frac{\psi_{n+1} - \psi_n}{\rho_{n+1} - \rho_n} - \frac{\psi_n - \psi_{n-1}}{\rho_n - \rho_{n-1}}\right\} + \beta y = Q_n. \tag{A4}$$

By passing to the limit in which all the H_n and $\Delta\rho$'s → 0, we recover the continuous result

$$\frac{\partial}{\partial z}\left(\frac{f^2}{N^2(z)}\frac{\partial\psi}{\partial z}\right) + \beta y = Q(\bar{\rho}), \tag{A5}$$

where $N^2(z) = -(g/\rho_0)\, d\bar{\rho}/dz$. This is valid except near the top and bottom boundaries. Eqs. (A4), (A5) state Rhines and Young's (1982a, b) startling deduction that potential vorticity is homogenized in the interior of gyres. The arbitrary function $Q(\bar{\rho})$, like the Q_n in (A4), is inconsequential in determining the flow, as it entails merely a purely z-dependent contribution to ψ. In the N-th layer, similar reasoning leads to

$$\frac{f_0^2\rho_0}{gH_N(\rho_N - \rho_{N-1})}(\psi_{N-1} - \psi_N) - \frac{D}{K}\psi_N + \beta y + f_0\frac{h'_T}{H_N} = Q_N, \text{ constant.} \qquad \text{(A6)}$$

(cf. (2.9))

We can obtain another equation by summing the vorticity balances (A1) in each layer, multiplied by the layer thickness H_n:

$$\beta\Psi_x + f_0 J(\psi_N, h'_T) = W_o, \qquad \text{(A7)}$$

where $\Psi = \Sigma_1^N H_n\psi_n$ is the total (barotropic) transport stream function. The continuous limit of (A7) has the identical form, with $\Psi = \int_{-H}^0 \psi dz$, and with ψ_N interpreted as the stream function on the bottom. (A4) and (A6) form $(N - 1)$ linear relations among $\psi_1, \ldots, \psi_N$; these can be used to eliminate all variables in favor of Ψ. In particular,

$$\Psi = -\frac{gH^2}{f_0}\left(A\frac{\beta y}{f_0} + B\frac{h'_T}{H}\right) + \left(1 + \frac{gB\delta_E}{f_0 K}\right)H\psi_N, \qquad \text{(A8)}$$

where

$$A = H^{-2}\sum_{n=1}^{N-1}\sum_{j=1}^{n} H_j(\rho_{n+1} - \rho_j)\rho_0^{-1} H_{n+1}, \qquad \text{(A9a)}$$

$$B = H^{-1}\sum_{j=1}^{N-1} H_j(\rho_N - \rho_j)\rho_0^{-1}. \qquad \text{(A9b)}$$

In the continuous limit, $N \to \infty$, the latter become

$$A = H^{-2}\int_{-H}^{0}\int_{z}^{0}(\bar{\rho}(z) - \bar{\rho}(z'))\rho_0^{-1}\, dz'dz, \qquad \text{(A10a)}$$

$$B = H^{-1}\int_{-H}^{0}(\bar{\rho}(-H) - \bar{\rho}(z))\rho_0^{-1}dz. \qquad \text{(A10b)}$$

A little manipulation shows that

$$A = -H^{-2}\int_{-H}^{0}(2z + H)\bar{\rho}(z)\rho_0^{-1}\, dz; \qquad \text{(A11a)}$$

this establishes that only the part of $\bar{\rho}(z)$ asymmetric about the midpoint of the water column contributes to A. Even more simply,

$$B = (\bar{\rho}(-H) - \hat{\rho})/\rho_0, \qquad \text{(A11b)}$$

where $\hat{\rho}$ is the vertically averaged density. Then, use of (A8) eliminates ψ_N from (A7):

$$J(\Psi, \beta y + \chi f_0 h'_T/H) = -\chi f_0^{-1} gAHJ(\beta y, h'_T) + W_o \qquad \text{(A12)}$$

where $\chi = (1 + gB\delta_E/f_oK)^{-1}$. For $N = 2$, $H_1 = H_2 = 1/2\,H$, $B = 1/2\,\Delta\rho/\rho_0$, $A = 1/4\,\Delta\rho/\rho_0$, $F = f_0^2\rho_0/g\Delta\rho H_1$, and $\chi = (1 + 1/2\,D/R)^{-1} = 2/f_R$, where $D = f_0\delta_E/H_1$, $R = FK$, and f_R is defined after Eq. (2.11). In this case, recalling that $\Psi = H_1\psi_B$, $h'_T = H_1 f_0^{-1} h_T$, in the notation of Section 2, Eq. (2.11) is easily recovered from (A12).

Eliminating Ψ instead of ψ_N from (A7), we obtain

$$J(\psi_N, \beta y + \chi f_0 h'_T/H) = -\chi g B f_0^{-1} J(\beta y, h'_T) + \chi W_0/H. \qquad \text{(A13)}$$

In the continuous limit, $N \to \infty$, ψ_N is simply the streamfunction, or pressure, on the bottom, just outside the frictional boundary layer.

REFERENCES

Freeland, H. J., P. B. Rhines and T. Rossby. 1975. Statistical observations of trajectories of neutrally buoyant floats in the North Atlantic. J. Mar Res., *33*, 383–404.

Ierley, G. R. and W. R. Young. 1983. Can the western boundary layer affect the potential vorticity distribution in the Sverdrup interior of a wind gyre? J. Phys. Oceanogr., *13*, 1753–1763.

Leetmaa, A., P. Niiler and H. Stommel. 1977. Does the Sverdrup Relation account for the Mid-Atlantic circulation? J. Mar. Res., *35*, 1–10.

Luyten, J. R., J. Pedlosky and H. Stommel. 1983. The ventilated thermocline. J. Phys. Oceanogr., *13*, 292–309.

Pedlosky, J. 1979. Geophysical Fluid Dynamics. Springer-Verlag, NY, 624 pp.

Rhines, P. B. and W. R. Young. 1982a. Homogenization of potential vorticity in planetary gyres. J. Fluid Mech., *122*, 347–367.

—— 1982b. A theory of wind-driven circulation. I. Mid-ocean gyres. J. Mar. Res., *40* (Suppl), 559–596.

Sverdrup, H. U. 1947. Wind-driven currents in a baroclinic ocean; with application to the equatorial currents of the eastern Pacific. Proc. Natl. Acad. Sci. U.S.A. *33*, 318–326.

Young, W. R. and P. B. Rhines. 1982. A theory of wind-driven circulation. II. Gyres with western boundary layers. J. Mar. Res., *40*, 849–872.

Received: *11 February, 1985*; revised: *14 August, 1985*.

END

DATE
FILMED

6 - 86

DTIC